UNIVERSITY OF OKLAHOMA

GRADUATE COLLEGE

DIAGNOSTIC ANALYSIS OF TERRESTRIAL GROSS PRIMARY PRODUCTIVITY USING REMOTE SENSING AND *IN SITU* OBSERVATIONS

A DISSERTATION

SUBMITTED TO THE GRADUATE FACULTY

in partial fulfillment of the requirements for the

Degree of

DOCTOR OF PHILOSOPHY

By

YAO ZHANG
Norman, Oklahoma
2017

Downloaded from SHAREOK. Persistent Handle URL: https://hdl.handle.net/11244/52420

DIAGNOSTIC ANALYSIS OF TERRESTRIAL GROSS PRIMARY PRODUCTIVITY USING REMOTE SENSING AND *IN SITU* OBSERVATIONS

A DISSERTATION APPROVED FOR THE
DEPARTMENT OF MICROBIOLOGY AND PLANT BIOLOGY

BY

Dr. Xiangming Xiao, Chair

Dr. Jeffrey Basara

Dr. Heather McCarthy

Dr. Lara Souza

Dr. Yang Hong

© Copyright by YAO ZHANG 2017
All Rights Reserved.

This dissertation is dedicated to my wife Sha Zhou, to my parents for their understanding, encouragement, and unconditional love and support.

Acknowledgements

I still remember the day I got the offer from Prof. Xiangming Xiao three years ago, I accepted his offer without any hesitation. Now, three and half years later, I am still glad that I made a wonderful choice at that time. Ever since I decided to come to OU, Prof. Xiao has been guiding me on the way to be an independent thinker and a trained scientist. He guided me into the study of carbon cycle, ecological modelling and the satellite remote sensing. He also gave me a lot of freedom and support on the research project that I'm interested in. Without his support, I would not be able to finish these research projects and my dissertation. He also encouraged me to get a balance between work and life. I still remembered during the first years in OU, we played badminton a lot with Jinwei, Yuanwei. This really helped me to relax myself and better concentrate on my research.

I would also like to thank Prof. Heather McCarthy. She taught me the plant physiological ecology in the first semester of my Ph.D. study. I had no background in physiology and my English is not good, I asked a lot of "foolish" questions and she was always patient answering them. I also learnt a lot from her through further discussions and collaborations. I would like to thank my other committee members, Dr. Jeffery Basara, who helped me to build the SIF observation site in KAEFS. I learnt a lot about instrumentations and field work from him. Dr. Yang Hong and Dr. Lara Souza, they helped me a lot with my dissertation.

I also thank Dr. Yiqi Luo, who taught me ecological modelling class, I learn how to use data assimilation to solve problems and how to think in an interdisciplinary way. He also helped me get rid of the fear to complex mathematical equations.

I extend my heartful thanks to all EOMF members. They include (but certainly not limited to): Dr. Jinwei Dong, Dr. Geli Zhang, Dr. Yuanwei Qin, Dr. Fang Liu,

Dr. Pradeep Wagle, Dr. Cui Jin, Dr. Jie Wang, Dr. Yuting Zhou, Dr. Shiyun Tang, Mr. Delong Zhao, Mr. Rajen Bajgain, Mr. Michael Menarguez, Ms. Jin Liu, Ms. Xiaocui Wu, Mr. Zhenhua Zou, Mr. Russell Doughty, and Ms. Qing Chang. I had a wonderful time working and living with you!

I would give my special thanks to Dr. Guangzhi Di and Dr. Weiheng Xu, they went out to the field for the entire summer to help me collect samples and do the field measurements. It's a really a challenge to work under the sun in Oklahoma and they helped me make this process less painful.

Dr. Luis Guanter, Dr. Yongguang Zhang, Dr. Xi Yang, Dr. Joanna Joiner, Dr. Sebastian Wolf, Dr. Georg Wohlfahrt, Dr. Kaiyu Guan and I shared the same research interests and I got a lot of help from them, which helped me better understand the origin of SIF. Their scientific integrity also inspired me and set me a good example.

Last by not least, I would like to thank my wife and my parents. Sha and I met in the 2014 AGU meeting, during my Ph.D. study, we had more time being separated than being together. She is not only a good wife, a good mother, but also a good friend, a good collaborator. We discussed a lot of scientific questions together and we learned from each other. I'm so fortunate to have such a soulmate to enjoy the rest of my life. My parents supported me a lot during my Ph.D. studies. Their unconditional love will always be remembered.

Table of Contents

Acknowledgements **iv**

List of Figures **xiii**

List of Tables **xvi**

Abstract **xxvi**

Chapter 1: Introduction **1**

1.1 Background 1

1.2 Overall research objectives 9

1.3 Organization of the dissertation 9

1.4 List of publication from the dissertation 12

Chapter 2: Seasonal variation and drought responses of gross primary productivity and solar induced chlorophyll fluorescence for a South Great Plain grassland **14**

Abstract 14

2.1 Introduction 15

2.2 Materials and Methods 18

2.2.1 Site description 18

2.2.2 Climate data measurement from Mesonet station and eddy covariance flux tower site . . . 19
2.2.3 Leaf level gas exchange and fluorescence measurements . . . 21
2.2.4 Canopy level vegetation reflectance and solar induced chlorophyll fluorescence measurement . . . 23
2.2.5 Leaf and canopy biophysical parameter measurements . . . 25
2.2.6 Contributing factors for the seasonal variation of canopy SIF . 25
2.3 Results . . . 26
2.3.1 Seasonal variation climate and vegetation photosynthesis at different scales . . . 26
2.3.2 Relationship between chlorophyll fluorescence and CO_2 assimilation . . . 27
2.3.3 Vegetation response to drought using SIF and optical vegetation indices . . . 29
2.4 Discussion . . . 30
2.4.1 Seasonal variation of vegetation photosynthetic capacity and relationship with biophysical variables . . . 30
2.4.2 Solar induced chlorophyll fluorescence as an indicator of vegetation drought stress . . . 33
2.5 Conclusion . . . 34
2.A Appendix . . . 36
2.A.1 Data acquisition using SpecFluo system and processing . . . 36

Chapter 3: On the relationship between sub-daily instantaneous and daily total gross primary production: implications for interpreting satellite-based SIF retrievals 39

Abstract 39
3.1 Introduction 40
3.2 Materials and Method 44
3.2.1 GPP from FLUXNET data base and preprocessing 44
3.2.2 Relationship between instantaneous and daily GPP at seasonal scale across sites 45
3.2.3 Relationship between instantaneous and daily LUE at seasonal scale across sites 46
3.2.4 Analytical conversion from instantaneous to daily APAR 47
3.2.5 SCOPE model simulation 48
3.2.6 Comparison of satellite retrieved SIF and GPP at global scale . 49
3.3 Results 51
3.3.1 Comparison between instantaneous GPP and daily GPP at seasonal scale 51
3.3.2 Comparison between sub-daily instantaneous LUE and daily LUE at seasonal scale 54
3.3.3 Comparison between simulated instantaneous and daily SIF from the SCOPE model 56
3.3.4 GPP-SIF comparison at global scale 59
3.4 Discussion 59
3.4.1 The relationship between daily GPP and instantaneous SIF across space and time 59
3.4.2 Potential uncertainty for phenological analysis using GOME-2 SIF 64
3.5 Conclusions 67
3.A Appendix 69

Chapter 4: Spatio-temporal convergence of maximum daily light use efficiency based on radiation absorption by chlorophylls of the canopy **75**

Abstract 75

4.1 Introduction 76

4.2 Materials and Methods 81

4.2.1 Solar-induced chlorophyll fluorescence as a proxy of $APAR_{chl}$ 81

4.2.2 FLUXNET data processing and light use efficiency calculation 85

4.2.3 Remote sensing observations at flux tower sites 88

4.2.4 Land cover dataset for major biome types 91

4.2.5 Error propagation 91

4.3 Results 93

4.3.1 Relationship between $fPAR_{SIF}$ and OVAIs 93

4.3.2 LUE estimation at different scales across biomes based on flux tower GPP 95

4.3.3 Using $fPAR_{chl}$ approximations to track seasonal dynamic of photosynthetic capacity 97

4.4 Discussion 99

4.4.1 Advantages and biophysical interpretation of $fPAR_{chl}$ 99

4.4.2 Potential of using SIF and $fPAR_{chl}$ for GPP estimation and data assimilation 101

4.4.3 Implications for PEMs 102

4.A Appendix 105

4.A.1 Relationship between SIF and $fPAR_{chl}$ 105

4.A.2 Error propogation in each approximation 106

Chapter 5: Canopy and physiological controls of GPP during drought and heat wave **122**

Abstract 122

5.1 Introduction 122

5.2 Materials and Methods 125

5.2.1 Data 125

5.2.2 Method 126

5.3 Results 129

5.3.1 Sensitivity of GPP anomalies to changes in vegetation indices and climate over the entire drought period 129

5.3.2 Sensitivity of GPP anomalies to changes in vegetation indices and climate at 8-day intervals during the drought period . . . 131

5.4 Discussion 134

5.4.1 Differences between forest and non-forest ecosystems in response to drought and heatwave 134

5.4.2 A conceptual model for canopy and physiological limitation on forest and non-forest during drought and heatwave 135

5.4.3 Implication and limitation of the canopy and physiological control analysis 136

5.5 Conclusions 138

5.A Appendix 138

Chapter 6: Consistency between sun-induced chlorophyll fluorescence and gross primary production of vegetation in North America **153**

Abstract 153

6.1 Introduction 154

6.2 Materials and Methods . . . 158
6.2.1 Regional datasets for VPM simulations across North America . 158
6.2.2 Datasets used to evaluate and compare VPM simulations across North America . . . 162
6.2.3 A brief description of the Vegetation Photosynthesis Model (VPM) . . . 163
6.3 Results . . . 165
6.3.1 Seasonal dynamics of GPP at individual flux tower sites . . . 165
6.3.2 Spatial patterns of GPP_{VPM} across North America in 2010 at 500-m spatial resolution . . . 169
6.3.3 Spatial-temporal comparison between GPP_{VPM} and SIF across NA in 2010 at 0.5° spatial resolution . . . 171
6.4 Discussion . . . 174
6.4.1 The relationship between SIF and GPP . . . 174
6.4.2 Comparison of SIF and GPP estimates in North America from several models . . . 175
6.4.3 Sources of uncertainty for VPM simulations in North America 179
6.5 Conclusions . . . 184
6.A Appendix . . . 185

Chapter 7: Precipitation and carbon-water coupling jointly control the interannual variability of global land primary production 187

Abstract . . . 187
7.1 Introduction . . . 187
7.2 Materials and Methods . . . 190
7.2.1 GPP from 14 models . . . 190

7.2.2 Solar-induced chlorophyll fluorescence from GOME-2 190
7.2.3 The ensemble of GPP using SIF 191
7.2.4 The Budyko framework 193
7.3 Results and Discussion 194
7.A Appendix 205
7.A.1 GPP product 205
7.A.2 Evapotranspiration and potential evapotranspiration dataset . 208
7.A.3 Climate dataset 208
7.A.4 Aggregation of MODIS land cover map 209
7.A.5 Rationale of GPP ensemble using SIF as a reference 209
7.A.6 Comparing GPP ensemble using SIF as a temporal proxy and spatial proxy 210
7.A.7 Interannual variation of SIF 210
7.A.8 Decompose ET variation from precipitation variation and potential evapotranspiration variation 212
7.A.9 Verification of the stability and robustness of the weighted ensemble method 213

Chapter 8: Conclusions and perspectives **228**

Bibliography **232**

List of Tables

Table 2.1 The start and end time of the five period and the average climate variables (maximum temperature, average VPD, and average FWI) for each period. 29

Table 3.A.1 Flux tower sites used in this study. 72

Table 4.1 Optical vegetation activity indices (OVAIs) used in this study. ρ with a subscription number indicate the satellite retrieved band reflectance centered at this wavelength. 90

Table 4.2 The uncertainties of approximations used in our study. 92

Table 4.A.1 Parameters settings used in the second run of the SCOPE model with fixed irradiance but variable parameters which result in different f_{esc} values. 117

Table 4.A.2 Flux tower sites used in this study. 117

Table 4.A.3 Root mean square error (RMSE) for the regressions between LUE_{PAR} and OVAI or $OVAI_m$, with all biome types combined together. 121

Table 4.A.4 Coefficient of determination (R^2) for the regressions between LUE_{PAR} and OVAI or $OVAI_m$, with all biome types combined together. 121

Table 5.1 Parameters of the regression models for both absolute anomalies (Δ) and relative anomalies (δ). 133

Table 5.A.1 Flux tower sites used in our analysis. $\overline{\Delta_{GPP}}$ and $\overline{\delta_{GPP}}$ stand for the absolute and relative GPP anomaly for the drought period (June 2^{nd} to November 16^{th}) compared to the normal year average. 147

Table 5.A.2 Same as Table 5.1, but using NDVI as the canopy control and VPD as the physiological control. 148

Table 5.A.3 Same as Table 5.1, but using LSWI as the canopy control and VPD as the physiological control. 149

Table 5.A.4 Same as Table 5.1, but using EVI as the canopy control and LST as the physiological control. 150

Table 5.A.5 Same as Table 5.1, but using NDVI as the canopy control and LST as the physiological control. 151

Table 5.A.6 Same as Table 5.1, but using LSWI as the canopy control and LST as the physiological control. 152

Table 6.1 Descriptions of the 39 flux tower sites used in this study. 165

Table 6.2 The magnitudes and annual sums of simulated gross primary production (GPP_{VPM}) of different biomes in North America (170°–50°W, 20°–80°N) for year 2010. 170

Table 6.3 Annual gross primary production (GPP) of North America (170°–50°W, 20°–80°N) estimated from different models for year 2010. . . . 177

Table 6.A.1 Biome specific lookup-table (LUT) used in the VPM model. . . 186

Table 7.A.1 Classification scheme of aridity regions based on aridity index (AI). 226

Table 7.A.2 The biome area weighted correlation between GPP and SIF ($score_i$) using SIF as a temporal reference. 226
Table 7.A.3 The biome area weighted correlation between GPP and SIF ($score_i$) using SIF as a spatial reference. 227

List of Figures

Figure 1.1 The global carbon cycle. All numbers are shown in Pg C year^{-1}. This figure is adopted from IPCC (2013) 2

Figure 1.2 Observation of plant photosynthesis at leaf or canopy/ecosystem level using different techniques. 4

Figure 1.3 NASA Earth Science Division Operating Missions. 6

Figure 2.1 The location of the study site. 19

Figure 2.2 Climate variables for the study site between DOY 120 to 240. . 20

Figure 2.3 The seasonal variation of canopy level mean daily SIF, three vegetation indices (NDVI, EVI, MTCI) from FluoSpec system and leaf level assimilation rate, photochemical yield (ϕ_{PSII}) and chlorophyll content. And the leaf area measurements for the vegetation near the FluoSpec site. 27

Figure 2.4 Comparison between the SIF and the product of PAR at 750 nm (as a proxy of PAR) and VI (as a proxy of fraction of PAR). 28

Figure 2.5 (a) Comparison between the chlorophyll fluorescence estimated photochemical yield (ϕ_{PSII}) and the corresponding leaf level gas exchange at different time of the measurement. (b) comparison between the product of photochemical yield and chlorophyll content (ϕ_{PSII}×Chl. content) and the leaf level gas exchange. 28

Figure 2.6 diurnal variation of SIF (a,f), fPAR× SIF_{yield} (b,g), NDVI (c,h), EVI (d,i), and PRI (e,j) during five different period as indicated by different colors and symbols. 31

Figure 2.A.1 A work flow for FluoSpec system to obtain irradiance and radiance measurement of the canopy from HR2000+ and QE-PRO. . 37

Figure 2.A.2 Comparison between spectral flux density of irradiance at 750 nm and the cosine of the sun zenith angle. 38

Figure 2.A.3 The seasonal and diurnal variation for SIF during the peak growing season. 38

Figure 3.1 Schematic graph showing the diurnal course of GPP or SIF normalized by their daily maximum values. 44

Figure 3.2 Seasonal variation of (a) GPP_{inst}, GPP_{daily}, and (b) γ_{GPP} of different time of day from a savanna flux tower site CG-Tch. (c) The regression between GPP_{daily} and GPP_{inst} from different times of the day (TOD). 53

Figure 3.3 Boxplots of bi-hourly (a) coefficient of determination (R^2) and (b) linear regression slope between the daily and instantaneous GPP (γ_{GPP}) at seasonal scale across 135 flux tower sites. 54

Figure 3.4 Latitudinal distribution of regression slopes between daily and instantaneous GPP (γ_{GPP}). 55

Figure 3.5 Comparison between bi-hourly LUE_{inst} and LUE_{daily} across flux tower sites at the seasonal scale. 56

Figure 3.6 (a) Dynamic of sub-daily GPP, APAR, and LUE, and (b) the relationship between APAR and GPP at sub-daily scale. 57

Figure 3.7 Latitudinal pattern of regression slopes between daily and instantaneous SCOPE simulated GPP, SIF, and GPP derived from EC tower (open circles). 58

Figure 3.8 Scatter diagrams showing the relationship between the instantaneous (upper panels) and daily (bottommost panel) SIF with daily GPP as computed with the SCOPE model for the five sites (color coded) as indicated in the legend. 60

Figure 3.9 Comparison between SIF_{inst} and SIF_{daily} from GOME-2 (a, b) and OCO-2 (c,d) with GPP from FluxCom. 61

Figure 3.10 Schematic diagram showing the relationships between PAR, APAR, SIF and GPP at sub-daily and daily scales. 64

Figure 3.11 (a) Relationship between instantaneous PAR at GOME-2 and OCO-2 satellite overpass and the daily average PAR for site US-Ivo (latitude=68.49°N). Correction factor for (b) GOME-2 and (c) OCO-2 at different latitude throughout the year. 66

Figure 3.A.1 The spatial distribution of the 136 flux tower sites used in this study. 69

Figure 3.A.2 The coefficient of determination (R^2) for the correlation between instantaneous and daily GPP estimates from flux tower. 69

Figure 3.A.3 Comparison between the SCOPE simulated GPP and eddy covariance flux tower derived GPP. 70

Figure 3.A.4 Comparison between the SIF simulated from the SCOPE model and from the GOME-2 satellite. 71

Figure 4.1 Idealized representation of the radiation partitioning in plant canopies for light use efficiency models. 77

Figure 4.2 A flowchart showing the evaluation of spatio-temporal convergence of ε_{max} based on radiation absorption of chlorophyll of the canopy. 81

Figure 4.3 Relationships between $fPAR_{SIF}$ and four OVAIs for Northern (a-d) and Southern Hemisphere (e-h). 94

Figure 4.4 Spatial distribution and frequency distribution of the regression slopes between $fPAR_{SIF}$ and four optical vegetation activity indicators (OVAIs) with fixed intercepts (c in equation 4.6) for the period 2007 to 2015. 96

Figure 4.5 Relationship between different OVAIs and LUE_{eco} for peak growing season using GPP_{EC} from clear days (left panel) and cloudy days (right panel). 98

Figure 4.6 The variation of maximum daily LUE as represented by the coefficient of variation. 99

Figure 4.7 Comparing EVI, NDVI, MTCI and their approximation of $fPAR_{chl}$ (EVI_m, $NDVI_m$, $MTCI_m$) with PC at K67 and K34 sites in Amazon forest. 100

Figure 4.A.1 The relationship between (a) fluorescence efficiency and $APAR_{chl}$, and (b) SIF740 and $APAR_{chl}$ using the simulation from the SCOPE model. 110

Figure 4.A.2 The variation of (a) fluorescence efficiency (in J nm^{-1} sr^{-1} mol^{-1}) and (b) $fPAR_{chl}$ under all possible combination of LAI, Cab and Cdm values in Table 4.A.1. 111

Figure 4.A.3 Comparison between the estimated iPAR at 9:30 am using cos(SZA) and observed iPAR from flux tower sites. 111

Figure 4.A.4 The linear regression with fixed OVAI intercept, same dataset from Figure 4.3 is used. 112
Figure 4.A.5 The spatial distribution of the flux tower sites used in this study. 113
Figure 4.A.6 The land cover type at the resolution of 0.5°× 0.5° for year 2007. 113
Figure 4.A.7 Spatial pattern (left column) and frequency distribution (right column) of the regression intercept (c in Eq. 4.6). 114
Figure 4.A.8 Spatial distribution (left column) and frequency distribution (right column) of regression slopes without fixing the intercept. . . . 115
Figure 4.A.9 Spatial pattern (left column) and frequency distribution (right column) of the coefficient of determination (R^2) between $fPAR_{SIF}$ and three optical vegetation activity indicators (OVAIs). 116

Figure 5.1 Location of the flux tower sites used in this study, and the averaged drought intensity from June to October in 2003. 130
Figure 5.2 Partial correlation between anomalies in GPP and anomalies in EVI (a, c) and VPD (b, d). 132
Figure 5.3 The conceptual model for vegetation canopy and physiological controls on (a) forest and (b) non-forest during the drought period. 135
Figure 5.A.1 Gap-filled results of NDVI (a), EVI (b), and LSWI (c) for site DE-Tha for year 2003. 141

Figure 5.A.2 Relationship of averaged absolute anomalies ($\overline{\Delta_\gamma}$) between GPP and vegetation indices (EVI, NDVI, LSWI), land surface temperature (LST), and vapor pressure deficit (LST) for the entire drought and heatwave period (a-e). GPP decrease for forest (F) and non-forest (NF) in absolute anomaly (f). 141

Figure 5.A.3 Pearson correlation between anomalies in absolute value for GPP (Δ_{GPP}) and EVI (Δ_{EVI}) with different lags applied. 142

Figure 5.A.4 Pearson correlation between anomalies in absolute value for GPP (Δ_{GPP}) and VPD (Δ_{VPD}) with different lags applied. 142

Figure 5.A.5 Relationship of average anomalies between GPP and air temperature for the entire drought and heatwave period. 143

Figure 5.A.6 Same as Figure 5.2, but for NDVI instead of EVI. 143

Figure 5.A.7 Same as Figure 5.2, but for LSWI instead of EVI. 144

Figure 5.A.8 Same as Figure 5.2, but the climate indicator was replaced with land surface temperature instead of VPD. 144

Figure 5.A.9 Same as Figure 5.A.8, but for NDVI instead of EVI. 145

Figure 5.A.10 Same as Figure 5.A.8, but for LSWI instead of EVI. 145

Figure 5.A.11 Box plot of the absolute and relative sensitivity of canopy control (CC) and physiological control (PC) for forest (F) and non-forest (NF). 146

Figure 6.1 A list of different approaches and models (as examples) to estimate gross primary production (GPP) of vegetation. 156

Figure 6.2 Flowchart of the data processing procedures for vegetation photosynthesis model (VPM). 164

Figure 6.3 Seasonal dynamics and interannual variations of the tower-based (GPP_{EC}) and the modeled (GPP_{VPM}) gross primary production at 39 flux sites at 8-day intervals. 167

Figure 6.4 A comparison of the tower-based (GPP_{EC}) and the modeled (GPP_{VPM}) gross primary production by biome types. 168

Figure 6.5 Spatial distribution of modeled (A) annual GPP_{VPM} and (B) maximum daily GPP_{VPM} for year 2010. 169

Figure 6.6 The frequency distribution of GPP_{VPM} of the (A) annual GPP and (B) maximum daily GPP compared to the flux site distribution and their distribution in the climate space defined by mean annual temperature (MAT) mean annual precipitation (MAP) (C, D). 172

Figure 6.7 A comparison of seasonal average solar-induced fluorescence (SIF) from the GOME-2 satellite instrument and simulated gross primary production (GPP_{VPM}) during the period of March 2010 through February 2011. 173

Figure 6.8 Relationship between SIF and GPP_{VPM} (A, E, I, M), $APAR_{chl}$ (EVI×PAR) (B, F, J, N), APARNDVI (NDVI×PAR) (C, G, K, O) and APARf-PAR (fPAR×PAR) (D, H, L, P) for four seasons (by row from first to fourth: spring, summer, autumn, winter) in North America in 2010. . 176

Figure 6.9 Comparison of annual gross primary production (GPP) from different LUE-based models (A, C), data-driven model (D), process-based models (E, F, G, H), and with solar-induced fluorescence (SIF) (B). Data are shown for the year 2010. 178

Figure 6.10 A comparison for relationship between GPP_{VPM} and SIF (A), GPP_{MPI} and SIF (B), GPP_{PSN} and SIF (C), $APAR_{chl}$ (EVI×PAR) and SIF (D), SIF_{yield} (SIF/APAR) and LUE_{VPM} (E) for different biome types in North America in 2010. 180

Figure 6.11 Seasonal dynamics and interannual variations of the tower-based (GPP_{EC}) and the modeled (GPP_{VPM}) gross primary production at two flux tower sites at 8-day intervals at a maize/soybean rotation site (US-Bo1) (A) and a continuous maize site (US-Ne1) (B). 182

Figure 6.12 Comparison between no gap-filled and gap-filled enhanced vegetation index (EVI) and the corresponding modeled gross primary production (GPP_{VPM}). 184

Figure 6.A.1 (A) A comparison between GPP_{EC} and $APAR_{chl}$ for all 39 sites using 8-day data. (B) comparison between the coefficient of determination (R2) between GPP_{EC} vs. GPP_{VPM}, and GPP_{EC} vs. $APAR_{chl}$ for individual sites. 185

Figure 7.1 Mean and variability of GPP and SIF (2000-2011). 195

Figure 7.2 (a) The aridity map calculated as a ratio between precipitation and potential evapotranspiration. (b) IAV of GPP ensemble. (c) The contribution of total GPP variability from different aridity classes. (d) Detrended GPP anomaly for global and 5 individual aridity regions, from 2000 to 2011. 196

Figure 7.3 Relationship among GPP and GPP IAV, climate variables, and ET. 198

Figure 7.4 Decomposition of GPP IAV into ET IAV and precipitation IAV, and their relationship with aridity index. 200

Figure 7.5 Difference in variation between the unweighted average and the weighted ensemble methods. 204
Figure 7.A.1 Spatial patterns of annual mean GPP from 3 data-driven models, and 11 DGVMs from the Trendy-V4 project. 214
Figure 7.A.2 Latitudinal pattern (1° bands) of annual GPP. 215
Figure 7.A.3 Spatial patterns of inter-annual variability (standard deviation, s.d.) of GPP from the 3 data-driven models and the 11 DGVMs from the Trendy-V4 project. 216
Figure 7.A.4 Land cover map (80% threshold value) from MODIS MCD12Q1 for 2007 (a) and the 'pure' pixel numbers for each land cover type at different threshold values(b). 217
Figure 7.A.5 Average model contribution of spatial GPP ensemble (see Methods) with different orders. 217
Figure 7.A.6 Average model contribution of temporal GPP ensemble (see Methods) with different orders. 218
Figure 7.A.7 Spatial pattern of annual GPP ensemble from all models (first column), data-driven models (second column), and DGVMs (third column). 218
Figure 7.A.8 Latitudinal pattern (1° bands) of annual GPP. 219
Figure 7.A.9 Spatial pattern of GPP IAV from all models ensemble (first column), data-driven models (second column), DGVMs (third column). 219
Figure 7.A.10 The calculated SIF variability from 2007 to 2015 using annual mean SIF value (a) and the average SIF error from each year (b). . . . 220
Figure 7.A.11 Detrended GPP anomaly from the ensembles of data-driven models (a) and process-based models (b). 220

Figure 7.A.12 Regression slope between GPP and ET. 221
Figure 7.A.13 Correlation distribution between 2^{nd} order GPP ensemble and MTE ET across different aridity index. 221
Figure 7.A.14 Relationship between ET variability and aridity index. 222
Figure 7.A.15 The spatial pattern of precipitation variation from GPCC and PET variation. 223
Figure 7.A.16 σ_{ET}/σ_P estimated from 12 ET models and the GPCC precipitation for 2000-2011. 224
Figure 7.A.17 The variation of (a, c, e, g) annual GPP and (b, d, f, h) GPP s.d. using unweighted average (a, b) and weighted ensemble (c, d, e, f, g, h) with different order factor (γ in Eq. 7.2). 225

Abstract

Vegetation play a critical role in the interactions between atmosphere and biosphere. CO_2 fixed by plants through photosynthesis process at ecosystem scale is termed as gross primary production (GPP). It is also the first step CO_2 entering the biosphere from the atmosphere. It not only fuels the ecosystem functioning, but also drives the global carbon cycle. Accurate estimation of the ecosystem photosynthetic carbon uptake at a global scale can help us better understand the global carbon budget, and the ecosystem sensitivity to the global climate change. Satellite observations have the advantage of global coverage and high revisit cycle, hence, are ideal for global GPP estimation. The simple production efficiency model that utilize the remote sensing imagery and climate data can provide reasonably well estimates of GPP at a global scale. With the solar induced chlorophyll fluorescence (SIF) being retrieved from satellite observations, new opportunities emerge in directly estimating photosynthesis from the energy absorption and partitioning perspective. In this thesis, by combining observations from both *in situ* and remotely acquired, I tried to (1) investigate the GPP SIF relationship using data from observations and model simulations; (2) improve a production efficiency model (vegetation photosynthesis model, VPM) and apply it to the regional and global scale; (3) investigate the GPP and SIF sensitivity to drought at different ecosystems; (4) explore the global interannual variation of GPP and its contributing factors. Chapter 2 uses site level observations of both SIF and GPP to explore their linkage at both leaf and canopy/ecosystem scale throughout a growing season. Two drought events happened during this growing season also highlight the advantage of SIF in early drought warning and its close linkage to photosynthetic activity. Chapter 3 compares the GPP and SIF relationships using both instantaneous and daily integrated

observations, the daily GPP and satellite retrieved SIF are latitudinal dependent and time-of-overpass dependent. Daily integrated SIF estimation shows better correlation with daily GPP observations. Chapter 4 compares different vegetation indices with SIF to get an empirical estimation of fraction of photosynthetically active radiation by chlorophyll ($fPAR_{chl}$). By comparing this $fPAR_{chl}$ estimation with ecosystem light use efficiency retrieved from eddy covariance flux towers, the light use efficiency based on light absorption by chlorophyll shows narrower range of variation that can be used for improving production efficiency models. Chapter 5 investigates the drought impact on GPP through the change of vegetation canopy optical properties and physiological processes. Forest and non-forest ecosystems shows very different responses in terms of these two limitation and need to be treated differently in GPP modelling. Chapter 6 applies the improved VPM to North America and compared with SIF retrieval from GOME-2 instrument. The comparison shows good consistency between GPP and SIF in both spatial and seasonal variation. Chapter 7 uses an ensemble of GPP product to explore the cause of hot spots of GPP interannual variability. GPP in semiarid regions are strongly coupled with evapotranspiration and show high sensitivity to interannual variation of precipitation. The results demonstrate the importance of precipitation in regional carbon flux variability.

Chapter 1: Introduction

1.1 Background

Earth is Breathing. Every day, every hour, every minute, plants on earth are absorbing carbon dioxide (CO_2) through the photosynthesis and respiration processes. Photosynthesis happens when there is light and suitable environment (temperature, humidity, etc.). The outcome of this process is so strong that changes the CO_2 concentration in the boundary layer where the terrestrial and atmosphere interacts. At a broader scale, since the Northern Hemisphere have larger land area and more vegetation, during the Northern Hemisphere growing season (typically from May to October), the global average atmosphere CO_2 concentration will be dragged down by around 10 ppm in equator and 15 ppm close to North Article Circle compared to the winter time (Keeling et al., 1996). Because of the increasing vegetation activity in the Northern Hemisphere, this number is still increasing (Graven et al., 2013; Gray et al., 2014; Zeng et al., 2014). As the CO_2 is absorbed by the vegetation through stomata, water loss is inevitable. This water loss, known as "Transpiration", together with evaporation, consists a very important flux of the global water cycle. In some humid regions, the transpiration from the vegetation is so strong that even changed the local weather (Findell et al., 2011; Wright et al., 2017).

Gross primary productivity (GPP), the total plant photosynthesis at the ecosystem scale, is the driving step of the terrestrial carbon cycle. Every year, about 120 Pg C enters the terrestrial ecosystem from the atmosphere (Beer et al., 2010). Most of these carbons are released back to the atmosphere through autotrophic and heterotrophic respiration, while a small percentage is retained in the ecosystem which either supports plant growth or is stored in the soil (Figure 1.1). Over the past years, this amount of carbon is continuously increasing and offsets around 33% of the an-

thropogenic carbon emission (Le Quéré et al., 2015). Most of the increased carbon stock is attributed to increased vegetation activity in the Northern Hemisphere because of the extended growing season, and the CO_2 fertilization (Baldocchi et al., 2016; Forkel et al., 2016; Graven et al., 2013; Keenan et al., 2016).

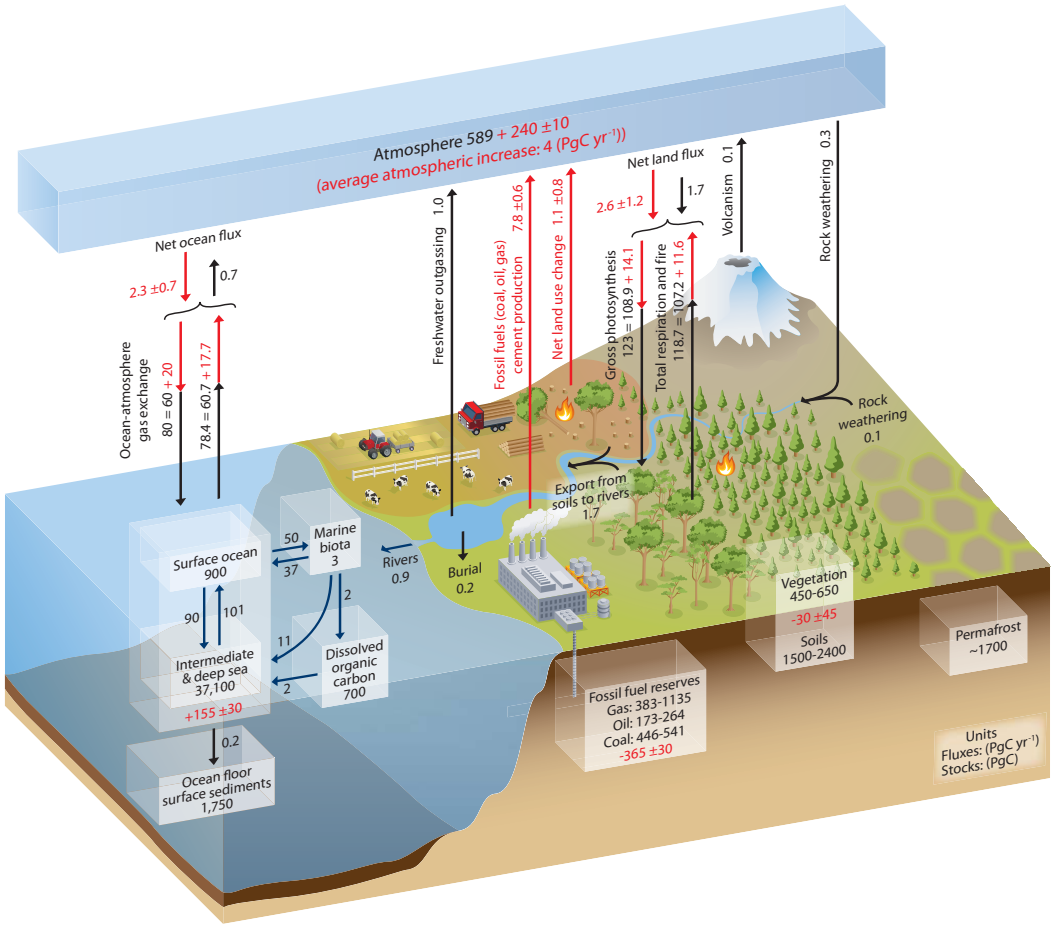


Figure 1.1: The global carbon cycle. All numbers are shown in Pg C year^{-1}. This figure is adopted from IPCC (2013)

Accompanied with the global warming, drought severity and frequency also increased over the past years (Dai, 2012; Easterling et al., 2000b; Trenberth et al., 2013). Other disturbances, e.g., flood, heatwave, fire, are also projected to increase in frequency (Christidis et al., 2014; IPCC, 2013), and will have significant impacts on

the GPP, hence the global carbon cycle (Ciais et al., 2005; Reichstein et al., 2013). Understanding the climate change impact on global carbon cycle is critical to a better projection of global warming and ecosystem functioning and services. Accurate estimation of GPP of terrestrial ecosystems is the first step to solve this problem. Multiple approaches have been made to estimate GPP including the process based modeling approach and data-driven models. However, a large discrepancy still remains (Anav et al., 2015), which make our projection of future global warming even more difficult.

The study of plant photosynthesis has a long history. Photosynthesis combines a series of biochemical processes starting from the capture of light by chlorophyll molecules. From the energy perspective, the light absorbed by the chlorophyll either forms the electron transport chain, be reemited as solar-induced chlorophyll fluorescence (SIF), or be dissipated as heat (Govindjee, 2004). The electron transport chain transfers the biochemical energy to the light independent reaction and fix the CO_2. Therefore, the observation of plant photosynthetical activity can be based on two aspects, from the gas exchange, i.e., the CO_2 fixation; or the energy partition, i.e., electron transportation rate (ETR). Leaf chamber combined with gas analyzer, or eddy flux measurements are based on the gas exchange (Figure 1.2). However, the direct measurement of the ETR can be challenging. By using the pulse amplitude modulation (PAM) technique, ETR can be indirectly calculated, which offers a means to study the photosynthesis process through energy perspective (Genty et al., 1989). Recently, many studies suggest that SIF positively correlated to ETR at moderate or high level of solar radiation, which makes direct estimates of energy partition for plant photosynthesis possible (Yang et al., 2015). With the help of hyper-spectral resolution spectrometers, this leaf level fluorescence measurement can be extended to canopy or ecosystem level using unmanned aerial vehicles

(UAVs) or satellites.

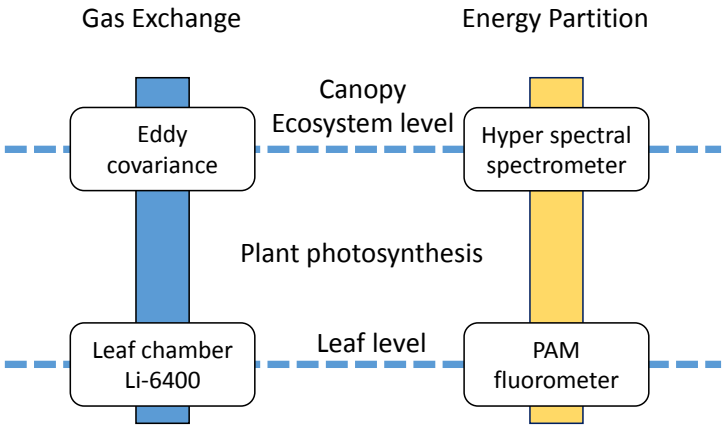


Figure 1.2: Observation of plant photosynthesis at leaf or canopy/ecosystem level using different techniques.

Based on these observations, scientists also developed different models to simulate plant photosynthesis. The models with equations representing each biophysical or physiological process are known as process-based models, and the models which based on empirical relationships are known as data-driven models. The most well-known process-based model for GPP simulation is the Farquhar model Farquhar et al. (1980), which consider the leaf level plant photosynthesis as the minimum of Rubisco carboxylation limited (J_c) and Ribulose-1,5,-bisphosphate (RuBP) regeneration limited (J_e) carbon assimilation. Both of which can be calculated with Michaelis-Menten formed functions. Although these models have a explicit representation of the processes during photosynthesis, they requires a lot of parameters to drive the model. These parameters often varies in space and time (Xu & Baldocchi, 2003; Lin et al., 2017; Wu et al., 2016), and may not be measured for all ecosystems.

Another kind of models, the production efficiency models (PEM) or light use efficiency (LUE) models, are based on the concept that light is used at a constant rate

by the plants to fix carbon dioxide (Monteith, 1972; Hilker et al., 2008). Previous studies have shown that given longer period of time, the averaged LUE becomes more stable, which suggest that these models can perform well at least for daily to monthly time scale (Song et al., 2013). These models have very simple form, but still considered different forms of environmental limitation (temperature, water, radiation, etc). The resultant GPP can well capture the spatial, seasonal variation, but most models does not perform well for the interannual variation (Anav et al., 2015). Compared with the process-based models, LUE models omit many complicated processes and just use an empirical LUE factor to include different kinds of limitations (typically water and temperature). One critical issue is the difficulties in models parameterization, as the empirical relationship may change for different biomes, species, or even specific plants. Specifically, the maximum light use efficiency (ε_0) is hard to parameterize as it varies both spatially and temporally. The environmental limitations also face problems during drought or other disturbances. How to improve the estimations of these parameters is critical to a better estimation of GPP using LUE models.

The simulation of GPP has two major objectives. The first one is to investigate the GPP response to the climate change related events, e.g., global warming, increase drought frequencyintensity, plants adaptation and acclimation. The second objective is to evaluate the global total carbon stock and its spatial and temporal variation. For the first objective, a single site data with *in situ* measurements can be used. Albeit lacking of spatial coverage, this site level simulations can still help us understand the response of vegetation to climate change for a specific ecosystem. To get a global total GPP simulation, we need to run the model at each grid box. The driving data may not be directly measured for each grid box. The total GPP for all the grid boxes can represent the total GPP at one specific time step. In this way, we

can get the spatial variation of the global GPP. These two objectives are not mutually exclusive, and they are often combined so that they can be used to investigate the climate change effects on vegetation and the feedbacks of the vegetation to climate. These are often called fully coupled Earth system models "online" mode.

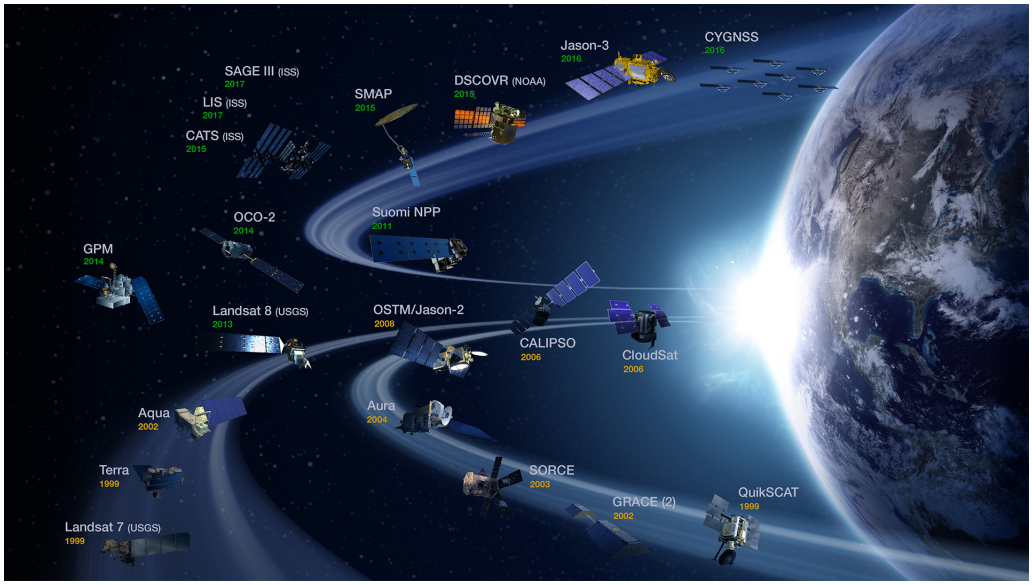


Figure 1.3: NASA Earth Science Division Operating Missions (from NASA website). This dissertation uses datasets from Terra, Aqua, OCO-2 satellites.

To use the models at global scale, global coverage datasets are necessary either to drive the model or to validate the model outputs. Remote sensing play an very important role to obtain data with a regional or global coverage. These satellite can provide various information about the Earth systems including radiation, surface temperature, precipitation, water storage, and most relevant to this dissertation, information about vegetation. Since vegetation have very distinct spectral signatures in both the visible and near-infrared band, multi-spectral sensors onboard different satellites can use these signatures to derive vegetation information.

Over the past years, a lot of vegetation indicators have been developed, the most well-known ones, normalized difference vegetation index (NDVI) and enhanced

vegetation index (EVI) uses the spectral signature of low reflectance in red band and high reflectance in the near infrared band. These indices are sensitive to vegetation physical and biophysical properties and can be good indicators for vegetation activities. Specifically, vegetation reflectance at ~ 531 nm is highly sensitive to photoprotective xanthophyll cycle and can be used to estimate the light use efficiency and track vegetation phenology (Gamon et al., 1992, 1997, 2016). Microwave remote sensing also provide information about the vegetation water content (a proxy of biomass (Liu et al., 2013)) since water in the vegetation has high dielectric constant and will decrease the brightness temperature signal emitted by Earth surface at microwave band (Guan et al., 2017). Although this water content data or biomass data cannot be directly used for GPP simulation, they can serve as a validation for plants growth models. In addition to the reflectance in visible and near infrared band and brightness temperature at microwave band, vegetation also emits a small amount of energy as fluorescence in the red and near infrared band. This energy, albeit small in total amount, can be detected by ultra high spectral resolution sensors onboard some satellites. SIF can be retrieved using a signal decomposition algorithm based on the solar Fraunhofer lines at ~ 740 or 680 nm wavelengths (Joiner et al., 2016). For most satellites that can be used for SIF retrievals (e.g., OCO-2, GOSAT), they are designed for atmospheric column CO_2 concentration retrievals. The atmospheric CO_2 data can be used for net ecosystem exchange (NEE) inversion, which also include information of photosynthesis activities at regional scale and the transportation of the traced gases. To conclude, with the development of new sensors and technologies onboard the satellite, remote sensing can provide increasingly numbers of direct and indirect observations for carbon cycle related studies.

Although a lot of dataset have been derived from remote sensing and other types of measurement, the GPP prediction from different models still have a very large un-

certainty. Even for data driven models which uses similar input datasets, the GPP accuracy is still not satisfactory (Wang et al., 2017; Sims et al., 2014; Yuan et al., 2014b; Verma et al., 2014), especially during drought periods (Wagle et al., 2014; Dong et al., 2015). This less satisfactory performance can be attributed to several aspects: (1) Models are abstraction of the real world, and the data-driven models are too simple to represent the real world processes. For example, based on plant physiological studies, drought affects plant photosynthesis from a variety of ways, including change of vapor pressure deficit that affect the stomatal conductance (Oren et al., 1999); change of soil moisture that decreases the hydraulic conductance and increased stomata sensitivity to VPD (Novick et al., 2016; Martinez-Vilalta & Garcia-Forner, 2017). Plants also have various ways to adapt and compensate drought effect (CAM photosynthesis pathway, change of leaf inclination, etc.). Because data-driven models do not have an explicit representation of these physiological processes, they do not fully capture the plant responses to drought. (2) A numbers of parameters are needed to drive the model, these parameters are mostly considered stable either across ecosystems or non-variant along time. However, this assumption either fails to consider the change of the plant species composition within a ecosystem type, or the seasonal dynamic of vegetation growth stage. For example, several studies have demonstrate that many photosynthesis related parameters are related to the vegetation phenology (Xu & Baldocchi, 2003; Lin et al., 2017), or related to the leaf age and demography (Wu et al., 2017, 2016). The changes of these variables directly affect the seasonal and spatial variation of GPP simulations. However, concurrent LUE models did not have good solutions for these problems. With the accumulation of global eddy covariance (EC) flux tower dataset (Baldocchi et al., 2001), solar induced chlorophyll fluorescence from both *in situ* canopy level and remotely sensed ecosystem level observations, we have access to unprecedently large

amount of datasets of GPP observations from leaf, canopy, to ecosystem, continental and global scale. These observations also provide continuous coverage with a temporal resolution from seconds to several days. For many satellite and *in situ* site level observations, they can provide as long as decades of data, allowing us to investigate the interannual variation and response to extreme events and climate change (Keenan et al., 2013; Zhang et al., 2014a).

1.2 Overall research objectives

The goal of this dissertation is to improve GPP estimations from multiple approaches and explore the spatial, temporal, and interannual variability of GPP. Specifically, this dissertation focuses on the data-driven approach. I use one specific LUE model, the Vegetation Photosynthesis Model (VPM), as an example to improve the LUE models. I also try to explore the possibility of using solar induced chlorophyll fluorescence (SIF) from both *in situ* observations and satellite retrievals as a direct observation of GPP, and how to use SIF to improve the LUE models. Finally, I would like to use these information and generate a global GPP dataset to explore the regional and global GPP variation at different time scales. This dissertation involves both *in situ* observations (e.g., vegetation biophysical and physiological parameters), and model simulations (both data-driven and process-based) using a variety of datasets. The ultimate goal of this dissertation is to improve the use of models and data to get a better understanding of global carbon cycle and impact of climate change.

1.3 Organization of the dissertation

My proposed dissertation will include six chapters as briefly outlined below:

Chapter 2. Seasonal variation and drought responses of gross primary productivity and solar induced chlorophyll fluorescence for a South Great Plain grassland. Many studies have showed that the relationship between GPP and SIF have a very high consistency at seasonal scale. However, most of these studies are at either forest or cropland, where drought rarely happens. In this chapter, I would like to investigate the relationship between GPP and SIF at seasonal scale. The SIF and GPP data will be obtained from both *in situ* observation and satellite retrievals. This study will also investigate the drought effect on GPP and SIF, and the sensitivity of SIF and optical vegetation indices to drought. The results of this study will provide evidence to build models to simulate GPP and SIF at a seasonal cycle and allow us to give early drought warning using satellite based SIF measurement.

Chapter 3. On the relationship between sub-daily instantaneous GPP and daily total GPP: implication for SIF measurement. As most satellite measurements are instant and does not represent the daily average value if a diurnal cycle exist for the targeted variable. For both GPP and SIF, these two are both driven by the solar radiation and the diurnal relationship changes across time. In this chapter, I would like to investigate the relationship between instantaneous GPP and daily GPP, and their relationship with the corresponding SIF measurements. This will help us better understand the relationship between GPP and SIF, thus build new models to predict GPP from SIF.

Chapter 4. Spatio-temporal convergence of maximum daily light use efficiency based on radiation absorption by chlorophylls of the canopy. The maximum daily light use efficiency is a very important parameter in production efficiency models (PEMs) or light use efficiency (LUE) models. However, based on the light absorption at different scales, the LUE can also vary significantly. I compare the LUE defined at ecosystem, leaf and chlorophyll scales and try to find if the maximum daily LUE

has less spatial and season variation at the scale which light is more directly used for photosynthesis. This will help us parameterize LUE models and provide better GPP estimates.

Chapter 5. Canopy and physiological controls of GPP during drought and heat wave. GPP response to drought and heat wave is a critical issue in global carbon cycle under the background of increasing drought frequency. In this chapter, I try to identify the two limitations of drought on photosynthesis, i.e., the canopy and the physiological limitations. I would also like to explore the role of these two limitations among different biome types. This will give us better understanding of how drought affects plant photosynthesis and improve the GPP simulation during drought and heat wave.

Chapter 6. Consistency between sun-induced chlorophyll fluorescence and gross primary production of vegetation in North America. The relationship between GPP and SIF have been long studied and but mostly at leaf level or at ecosystem level for cropland. In this chapter, I want to compare the GPP estimates from a light use efficiency model, the vegetation photosynthesis model (VPM) with the SIF observation from the GOME-2. This study will provide a new regional GPP product (GPP_{VPM}) and help us better understand the GPP-SIF relationship at seasonal scale.

Chapter 7. Precipitation and carbon-water coupling jointly control the interannual variability of global land primary production. The interannual variation (IAV) or the year to year variation of the terrestrial carbon uptake is very critical to our understanding of the global carbon cycle under climate change. In this chapter, by using the GPP estimates from multiple datasets, I would like to investigate the hotspot where highest IAV of GPP can be found, and what is the possible reason for this high GPP IAV. This study will help us better understand the water carbon cou-

pling and the variability of carbon cycle under climate change.

1.4 List of publication from the dissertation

Chapter 2

Zhang, Y., Xiao, X., et al. Seasonal variation and drought responses of gross primary productivity and solar induced chlorophyll fluorescence for a South Great Plain grassland. (in preparation)

Chapter 3

Zhang, Y., Xiao, X., Zhang, Y., Wolf, S., Zhou, S., Joiner, J., Guanter, L., Verma, M., Sun, Y., Yang, X., Paul-Limoges, E., Gough, C., Wohlfahrt, G., Gioli, B., van der Tol, C., Yann, N., & Lund, M. On the relationship between sub-daily instantaneous and daily total gross primary production: implications for interpreting satellite-based SIF retrievals. (in revision for Remote Sensing of Environment)

Chapter 4

Zhang, Y., Xiao, X., Wolf, S., Wu, J., Wu, X., Gioli., B., Wohlfahrt, G., Cescatti, A., van der Tol, C., Zhou, S., Gough, C., Gentine, P., Zhang Y., Steinbrecher, R., & Ardö, J. Spatio-temporal convergence of maximum daily light use efficiency based on radiation absorption by chlorophylls of the canopy. (prepare for submission)

Chapter 5

Zhang, Y., Xiao, X.M., Zhou, S., Ciais, P., McCarthy, H., & Luo, Y.Q. (2016). Canopy and physiological controls of GPP during drought and heat wave. Geophysical Research Letters, 43, 3325-3333

Chapter 6

Zhang, Y., Xiao, X.M., Jin, C., Dong, J.W., Zhou, S., Wagle, P., Joiner, J., Guanter, L.,

Zhang, Y.G., Zhang, G.L., Qin, Y.W., Wang, J., & Moore, B. (2016). Consistency between sun-induced chlorophyll fluorescence and gross primary production of vegetation in North America. Remote Sensing of Environment, 183, 154-169

Chapter 7

Zhang, Y., Xiao, X.M., Guanter, L., Zhou, S., Ciais, P., Joiner, J., Sitch, S., Wu, X.C., Nabel, J., Dong, J.W., Kato, E., Jain, A.K., Wiltshire, A., & Stocker, B.D. (2016). Precipitation and carbon-water coupling jointly control the interannual variability of global land gross primary production. Scientific Reports, 6 39748. DOI:10.1038/srep39748

Zhang, Y., Xiao, X., Wu, X., Zhou, S., Zhang, G., Qin, Y., & Dong, J. (2017) A global moderate resolution dataset of gross primary production of vegetation for 2000-2016. Scientific Data, 4 170165. DOI:10.1038/sdata.2017.165

Chapter 2: Seasonal variation and drought responses of gross primary productivity and solar induced chlorophyll fluorescence for a South Great Plain grassland

Abstract

Semi-arid grassland ecosystems have high drought sensitivity and interannual variability of carbon fixation, therefore, play an important role in the global carbon cycle. The compensatory effect of early start growing season and summer drought accompanied with global warming also highlights the importance of accurately estimate seasonal dynamic of ecosystem photosynthesis. Chlorophyll fluorescence (ChlF) has been demonstrated to be a promising technology in monitoring vegetation photosynthesis from a non-destructive way. However, the underlying mechanism of its relationship with ecosystem total gross primary production (GPP) and plant responses to drought is not clear. Using data from a integrated solar-induced chlorophyll fluorescence (SIF) measurement system (FluoSpec) together with *in situ* leaf level ChlF and assimilation measurement, we investigated the seasonal dynamic and of SIF and other plant biophysical variables, and their responses to drought. The results suggested that the light absorption by chlorophyll and energy partitioned to photochemistry can well track the leaf level assimilation rate. The canopy level SIF variation can be explained to a large extent by radiation and vegetation indices (r>0.83, p<0.001). Canopy level SIF also exhibited higher sensitivity than optical vegetation indices and captured the midday depression during drought period. The chlorophyll related vegetation (MERIS Terrestrial Vegetation Index, MTCI) also showed larger decrease than enhanced vegetation index (EVI) and normalized difference vegetation index (NDVI) after drought. The results of this study highlighted the importance of using SIF to track the seasonal dynamic of

vegetation photosynthetic activity and the physiological and canopy limitation of drought.

2.1 Introduction

Plants uptake carbon through photosynthesis and provide food, fiber, and wood for human beings (Beer et al., 2010). This carbon flux, known as gross primary productivity at ecosystem level, also drives the ecosystem functioning. Over the past decades, increasing vegetation carbon uptake offsets one third of the anthropogenic CO_2 emissions, most of which comes from the climate change-induced GPP increase (Le Quéré et al., 2016). Plants benefit from the CO_2 fertilization, extended growing season caused by global warming (Zhu et al., 2016; Mao et al., 2016). On the other hand, extreme climate events are also projected to increase in both frequency and severity along with global climate change, which may greatly affect the carbon sequestration (Ciais et al., 2005; Zhao & Running, 2010). Recent studies suggest that semi-arid ecosystems contribute most of the interannual variability to the global carbon uptake and is very vulnerable to extreme climate event such as drought or heatwave (Ahlstrom et al., 2015; Poulter et al., 2014). A comprehensive understanding of the vegetation photosynthesis response to climate change and disturbances are critical to global carbon cycle.

Multiple approaches have been made to measure plant photosynthesis at different scales (Zhang et al., 2016e). At leaf scale or plant scale, static chamber combined with gas analyzer are used to investigate the physiological processes including the temperature sensitivity, stomatal conductance, etc. (Luo et al., 2001). When extended to ecosystem level, eddy covariance technology has become increasingly important to investigate the water, carbon, energy exchanges which are closely re-

lated to the ecosystem productivity and respiration. Global flux network spanning across various ecosystem types and long-term observation period greatly contributed to both physiological and phenological studies (Baldocchi et al., 2001; Schimel et al., 2015). These methods can be regarded as direct observations since they measure the CO_2 exchange, one of the most important substrates for the photosynthesis process. At global scale, satellites that can monitor the CO_2 column concentration have been launched (Butz et al., 2011). They can act as a complementary data source since the relative longer revisit cycle and sparse spatial resolution.

In addition to these CO_2-based gas exchange measurements of GPP, scientists also developed different indirect methods to estimate plant photosynthesis so that GPP can be estimated at a larger scale. Ever since 1970s, people have found that during the light reaction of photosynthesis process, when light is absorbed by the chlorophyll pigments (Porcar-Castell et al., 2014), most light goes to photochemistry and provide ATP and NADPH for dark reaction; some energy dissipate as heat; and a very small amount of energy is re-emitted as fluorescence. This small amount of energy is known as chlorophyll fluorescence (ChlF). Previous studies use pulse amplitude-modulated (PAM) technique to measure the chlorophyll fluorescence (ChlF) at leaf level (Genty et al., 1989). PAM fluorometry has shown a close linkage between ChlF and CO_2 assimilation. This close linkage is explained by the ChlF as an indicator of electron transportation rate (ETR), which is further used in the Calvin Cycle (Krause & Weis, 1991). Many studies also showed that ChlF is very sensitive to vegetation stress, e.g., drought, salinity, diseases (Christen et al., 2007; Vankooten & Snel, 1990; Schreiber et al., 1995; Lichtenthaler & Rinderle, 1988).

In addition to PAM based ChlF measurement, recent studies have successfully retrieved sun-induced chlorophyll fluorescence (SIF) from satellite, using hyperspectral resolution remote sensing spectroscopy, and the SIF caused in-filling of

Fraunhofer Lines (Frankenberg et al., 2011; Guanter et al., 2012; Joiner et al., 2012). This measurement does not trigger the plant response to saturating light, and can reflect the plant photosynthesis at normal conditions. Many *in situ* and modeling studies also show a clear positive correlation of CO_2 assimilation or stomatal conductance with SIF, because the heat dissipation increase with light under stress conditions while the SIF and photochemistry declines simultaneously (Kooten & Snel, 1990). Although with the evidences from the leaf level that PAM measured ChlF is sensitive to photosynthetic activities, at canopy level or ecosystem level, this relationship may be affected by many other factors, e.g., the canopy structure, the atmospheric conditions. The direct comparison between the satellite retrieved SIF measurement and the ChlF at leaf level is restricted because the different footprint sizes, the inconsistent measurement time, and relative large errors for each individual satellite measurement (Joiner et al., 2014). How to evaluate the SIF measurement from canopy level and compare with satellite measurement, leaf level measurement and the CO_2 assimilation at different scales is vital to understand the mechanism of plant photosynthesis and improve the accuracy of global carbon cycle.

Southern great plain (SGP) is one of the major agroecosystems in U.S. This region is also experiencing frequent droughts in recent years (Gu et al., 2007). The SGP ecosystems are mostly in semi-arid and are sensitive to drought disturbances. Drought of 2011 greatly decreases the vegetation productivity and caused more than $5.2 billion loss. In many regions, the drought induced tree mortality also induced huge ecological impact, especially on the carbon cycle (Anderegg et al., 2015). We choose to investigate the GPP and SIF relationship for a typical grassland in SGP, which can be a good representative of grassland in SGP and other regions that are suspected to drought impact.

This study uses an integrated observation system to estimate photosynthesis us-

ing both gas exchange and chlorophyll fluorescence measurement at different scale (e.g., leaf, canopy, ecosystem). In this study, we try to answer the following questions which may greatly advance our knowledge about the seasonal cycle of photosynthesis processes and their responses to drought: (1) what are the seasonal variations of CO_2 assimilation rate and chlorophyll fluorescence at leaf and ecosystem scale and what are the relationship between them? (2) what controls the seasonal chlorophyll fluorescence variations? (3) how do GPP and SIF respond to drought?

2.2 Materials and Methods

2.2.1 Site description

Kessler Atmospheric and Ecological Field Station (KAEFS) locates in the central of Oklahoma, USA, approximately 28 km southwest of the University of Oklahoma, Norman campus (Figure 2.1). KAEFS has a mixed grass prairie ecosystem with tall grass prairie, woodland, riparian, and pastures. The major grass species include switchgrass (*Panicum virgatum*), Indiangrass (*Sorghastrum nutans (L.) Nash*), smooth brome (*Bromus inermis* Leyss.), little bluesterm (*Schizachyrium scoparium*), etc. The grass species composition changes within a growing season: C3 grasses (e.g. smooth brome) make up a proportion of grass species during early and late growing season, while C4 grasses dominated the mid-growing season (May to July). The annual average temperature is around 16°C, with a highest monthly average temperature in July and August of 27°C, and a lowest in January of 3°C. The annual precipitation is around 850 mm, with higher precipitation in May and June. Summer time (July and August) are often considered as dry season due to the lower precipitation but higher temperature and evapotranspiration demand.

2.2.2 *Climate data measurement from Mesonet station and eddy covariance flux tower site*

Both the EC flux tower and the Mesonet station provide a variety of climate variables measurements including air temperature, radiation, air humidity, wind speed, precipitation and soil moisture, since Mesonet site provide more robust and detailed measurements for the climate variables. Unless specified, all climate variables in this paper are from Mesonet measurements. The fractional water index (FRI) is a unitless soil water indicator with 0.00 indicating very dry soil to 1.00 for soil at field

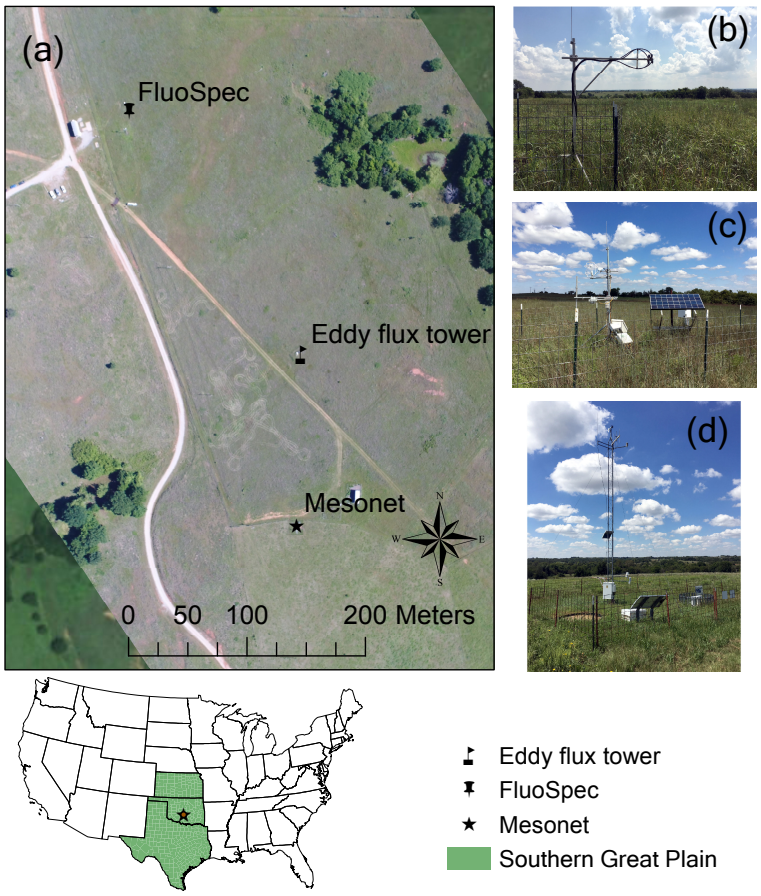


Figure 2.1: The location of the study site. The integrated observation system includes a FluoSpec solar-induced chlorophyll fluorescence measurement site (b), a eddy covariance flux tower site (c) and a Mesonet site (d).

capacity (Schneider et al., 2003). It was calculated using three Campbell Scientific 229 - L sensors at 5cm, 25cm, and 60cm depth, which covers most of the root zone for the grassland ecosystems (Illston et al., 2008). In 2017, two drought event happened during the growing season (Figure 2.2).

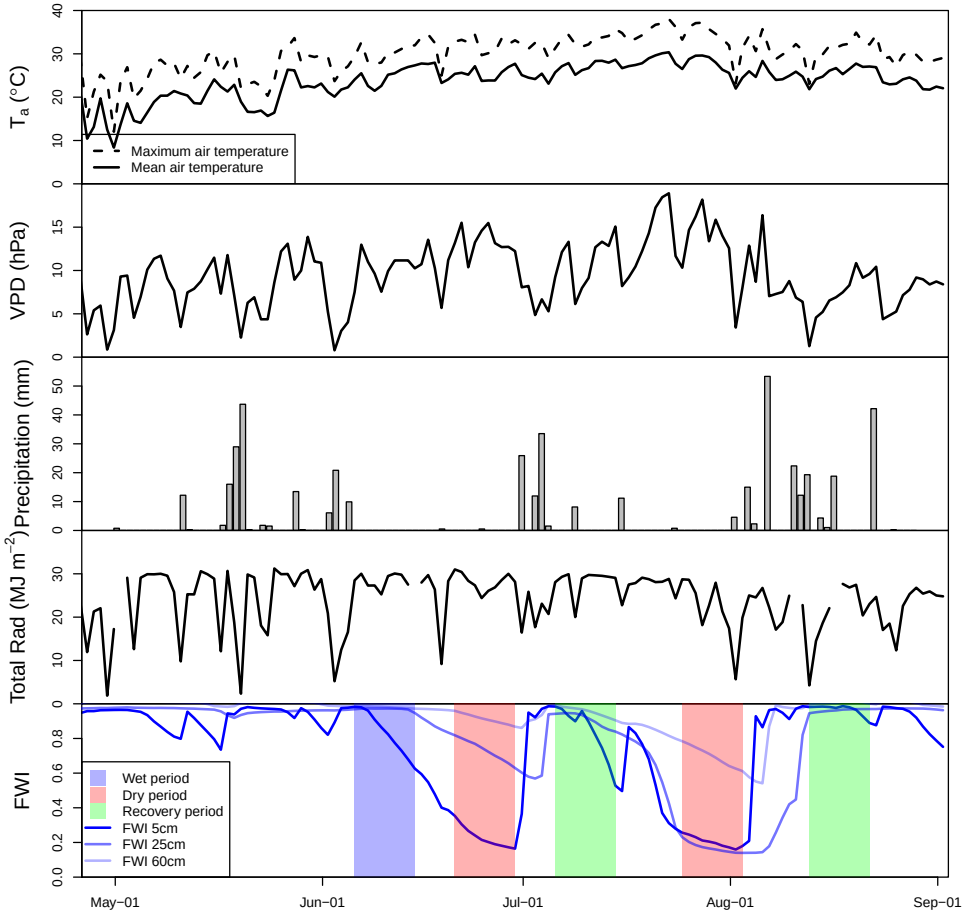


Figure 2.2: The variation of air temperature (T_a), vapor pressure deficit (VPD), precipitation, total daily radiation (Total Rad), and fractional water index (FWI) at different depth (5cm, 25cm, 65cm) during the peak growing season from DOY 120 to 240. Five period of wet, dry and recovery are identified based on fractional water index.

2.2.3 Leaf level gas exchange and fluorescence measurements

Leaf level measurement were acquired every week using a LI-6800 portable photosynthesis system (LI-COR Corporate). LI-6800 is the succedent of the widely used LI-6400 system. We used the fluorometer chamber which allows the simultaneous measurement of assimilation (A) and chlorophyll fluorescence (ChlF) using a pulse amplitude modulation (PAM) technique. Each week, three switchgrass leaves were chosen and A and ChlF were measured under ambient (400 ppm) and elevated (1000 ppm) CO_2 environment. Other environmental conditions are under control: temperature is set to 25°C, relative humidity is set to 50%, photosynthetically active radiation (PAR) is set to 2000 μ mol m^{-2} s^{-1}. for each leaf, we made three assimilation measurements together with three PAM ChlF measurements at both ambient and elevated CO_2 level.

The ChlF measurement can be used as an indicator of energy partitioning after being absorbed by plants. After light is harvested by the antenna pigment chlorophyll, it will ends up in three destinations: (1) be used for photochemistry to fix CO_2 (ϕ_P), (2) be dissipated as heat (or non-photochemical quenching, NPQ), and (3) be reemmited as chlorophyll fluorescence (ϕ_F). We further partitioned NPQ to heat loss in light-adapted condition (ϕ_N) and dark-adapted condition (ϕ_D) (van der Tol et al., 2014). These four processes compete with each other and summed up to unity (Eq. 2.1).

$$\phi_P + \phi_N + \phi_D + \phi_F = 1 \tag{2.1}$$

At steady state, the rate constant for these three process (κ_P, κ_N, κ_D, κ_F, respectively) are invariant within a small period of time:

$$\phi_P = \frac{\kappa_P}{\kappa_P + \kappa_N + \kappa_D + \kappa_F} \tag{2.2}$$

$$\phi_N = \frac{\kappa_N}{\kappa_P + \kappa_N + \kappa_D + \kappa_F} \tag{2.3}$$

$$\phi_D = \frac{\kappa_D}{\kappa_P + \kappa_N + \kappa_D + \kappa_F} \tag{2.4}$$

$$\phi_F = \frac{\kappa_F}{\kappa_P + \kappa_N + \kappa_D + \kappa_F} \tag{2.5}$$

when plant leaf is exposed to a saturating light (>8000 μmol $m^{-2}s^{-1}$), the reaction center will close and κ_P drops to zero. This correspond to an increase of ϕ_F which is termed as maximum fluorescence yield ($\phi_{F_m^{'}}$):

$$\phi_{F_m^{'}} = \frac{\kappa_F}{\kappa_N + \kappa_D + \kappa_F} \tag{2.6}$$

by combining Eq. 2.2, 2.5, and 2.6, Genty et al. (1989) demonstrate that the fraction of light used for photochemistry can be estimated as:

$$\phi_P = \frac{\phi F_m^{'} - \phi_F}{\phi F_m^{'}} \tag{2.7}$$

In our study, ϕ_P is termed as ϕ_{PSII} to be consistent with LI-6800 terminology, and the ϕ_{PSII} is recorded every time a leaf gas exchange measurement is recorded by measuring the steady state fluorescence and 1 second of fluorescence under saturating light.

Leaf level assimilation rate can then be calculated as:

$$A = PAR \times fPAR \times \phi_{PSII} \tag{2.8}$$

2.2.4 *Canopy level vegetation reflectance and solar induced chlorophyll fluorescence measurement*

We deployed a continuous canopy-level solar induced chlorophyll fluorescence measurement system — FluoSpec at our station. This system consists two high spectral resolution spectrometers, for SIF and vegetation reflectance measurements. The first spectrometer, QE-Pro, was customized by OceanOptics, Inc., Dunedin, Florida with a full width half maximum (FWHM) of around 0.04nm and a spectral range from ~730 nm to ~788 nm. This spectrometer is used for SIF retrieval at ~760 nm. The second spectrometer, HR2000+ (OceanOptics, Inc., Dunedin, Florida), has a FWHM of 0.5nm and a spectral range from ~187 nm to ~1105 nm. The spectral measurement from this spectrometer can be used to calculate various reflectance based vegetation indices:

$$EVI = 2.5 \times \frac{\rho_{860} - \rho_{655}}{\rho_{860} + (6 \times \rho_{655} - 7.5 \times \rho_{470}) + 1} \tag{2.9}$$

$$NDVI = 2.5 \times \frac{\rho_{860} - \rho_{655}}{\rho_{860} + \rho_{655}} \tag{2.10}$$

$$PRI = \frac{\rho_{531} - \rho_{570}}{\rho_{531} + \rho_{570}} \tag{2.11}$$

where the ρ with a number subscript represents the vegetation canopy reflectance at this specific wavelength.

The FluoSpec system uses two optical fibers and one shutter (FOS-2×2-TTL, OceanOptics, Inc.) to switch the light path so that the spectrometers can measure the solar irradiance and vegetation radiance in turns. One of these two optical fibers with a opaline glass cosine corrector (CC-3, OceanOptics, Inc.) is mounted facing up to the sky to get the downwelling irradiance of the sun; the other bare optical fiber

with a field of view (FOV) of 25° is facing down to get the upwellling radiance of the vegetation. The vegetation in the FOV of the bare fiber is dominated by switchgrass (>80%). The shutter can be controlled by the spectrometer and switches between these two fibers, so that each spectrometer can get observations of both irradiance and radiance measurements.

Both spectrometers are controlled by a Raspberry Pi 3 (RP3) and the measurement cycle is conducted every 15 minutes between 6:00 to 20:00 everyday. With in each measurement cycle, two spectrometers operate in turns, and get 5 pairs of irradiance and radiance measurements. The 5 pairs of irradiance and radiance are conducted in turn to minimize the effect of change in radiation. All measurements use optimum integration time that maximize the signal to noise ratio. For a detailed operating procedure, please refer to the Appendix text 2.1 and Figure 2.A.1. The code used to control the spectrometers are available online (https://github.com/zhangyaonju/seabreeze_control). The two spectrometers are radiometric calibrated using a light source (HL-2000-CAL, OceanOptics, Inc) in the lab before the growing season. The system is also calibrated using a white reference every two months after being deployed to the field.

The Original data we get from these two spectrometers are digit number (DN) values, these DN values were then processed with a dark current calibration and a non-linearity corrections, before converting to absolute radiance or irradiance. After we get the absolute irradiance and radiance, we can use the spectral fitting methods (SFM) to calculate SIF (Meroni et al., 2009). The relationship between irradiance ($E(\lambda)$) and upwellling radiance ($L(\lambda)$) is affected by the fluorescence emission ($F(\lambda)$ red and far-red spectral range) and reflectance ($r(\lambda)$). Both of which are regarded as

a linear function of wavelength λ in oxygen A (O_2A) band.

$$L(\lambda) = \frac{r(\lambda) \times E(\lambda)}{\pi} + F(\lambda) + \epsilon(\lambda) \qquad \lambda \in [759.00, 767.76] \tag{2.12}$$

2.2.5 Leaf and canopy biophysical parameter measurements

For each leaf we measured during the growing season, we also use a CCM-300 chlorophyll content meter (Opti-Science, Inc) and measure the chlorophyll content at five different places along the leaf (Gitelson et al., 1999). The average of those five values were considered the chlorophyll content for that leaf. Every time, at least three leaves were measured and represent the average chlorophyll content for that day.

We also used the LAI-2200C (LI-COR) to measure the leaf area index (LAI) near the FluoSpec Site. Five individual measurements were averaged to represent the average LAI for the site. Both the leaf level measurements and the LAI measurements were obtained in the morning between 9:00 to 12:00.

2.2.6 Contributing factors for the seasonal variation of canopy SIF

At canopy scale, SIF at a specific wavelength can be represented as a function of APAR, fluorescence efficiency (ϕ_F) and the escape factor (f_{esc}) (Joiner et al., 2014):

$$SIF = PAR \times fPAR \times \phi_F \times f_{esc} \tag{2.13}$$

sometimes the last two factors are combined together and termed $_{yield}$. Since canopy level gross primary productivity (GPP) can also be calculated as:

$$GPP = PAR \times fPAR \times LUE \tag{2.14}$$

where LUE represent the light use efficiency which convert the radiation to photochemical carbon fixation. Since both SIF and GPP shared the APAR (=PAR×fPAR), we used several vegetation indices to investigate how much variance of SIF can be explained by each component. This will help us better understand the relationship between SIF and GPP and can be used to improve the LUE models.

2.3 Results

2.3.1 Seasonal variation climate and vegetation photosynthesis at different scales

Figure 2.3 shows the seasonal dynamic of the canopy level SIF and vegetation indices measurement combined with the leaf level chlorophyll fluorescence, gas exchange and biophysical measurements. A very strong seasonal dynamic of canopy SIF can be observed, while all three vegetation indices only tracks the start of the growing season. When comparing three vegetation indices, NDVI showed relative stable day to day variation while EVI showed larger fluctuation and MTCI exhibited largest. These fluctuations are mostly continuous therefore may not be affected by the weather conditions, on the other hand, they may represent higher sensitivity to the plant pigments changes while the canopy structure remains unchanged.

We further compared the correlation between SIF and the proxies of APAR. These proxies of APAR are calculated based on PAR at 750 nm (as a proxy of PAR) and different vegetation indices (as proxies of fPAR). Figure 2.4 shows that all three indices have very significant correlation with SIF. A clear upper bounary can be found for these comparisons, the slope of which corresponds to the maximum SIF_{yield}. Points below this upper bourdary have a lower SIF_{yield} can may be caused by stress. These mostly happens in the mid- to late-growing season. We try to added the average of FWI as a stress indicator into the APAR term, but the correlation only slightly

increases.

2.3.2 Relationship between chlorophyll fluorescence and CO_2 assimilation

We compared the leaf level photochemical yield of photosystem II (ϕ_{PSII}) with assimilation rate (A) for all leaf level measurements across the growing season (Figure 2.5). We found that when comparing ϕ_{PSII} directly with A, a clear lower boundary

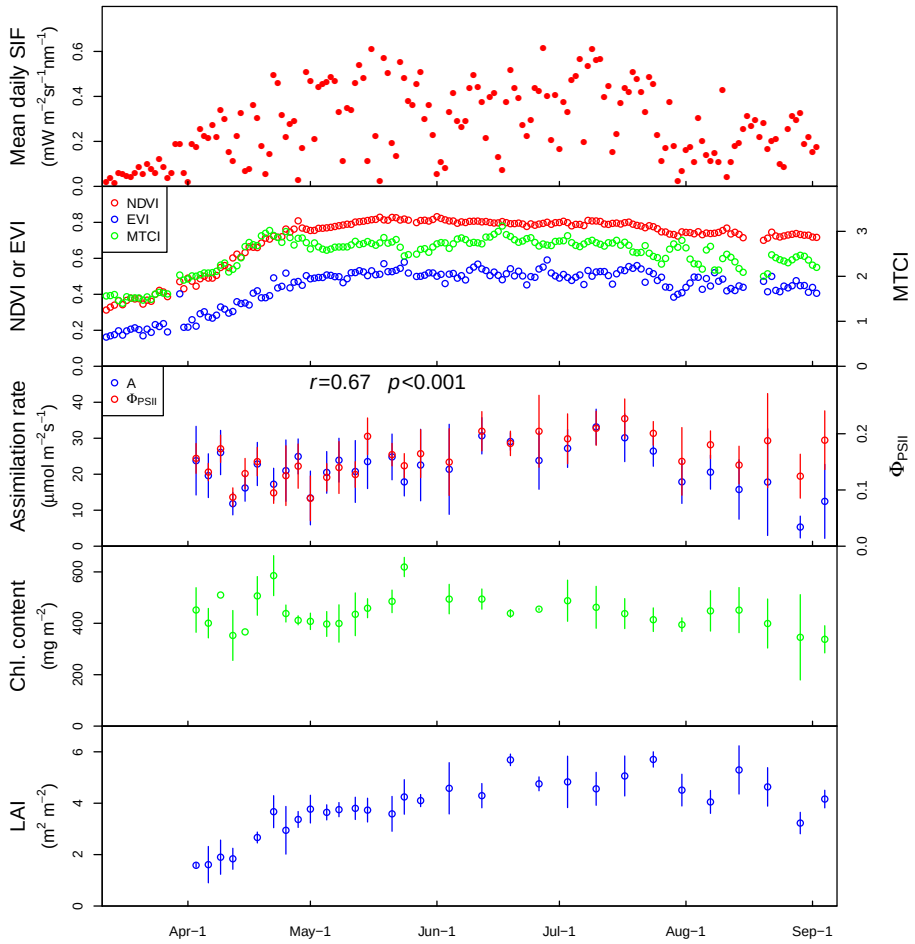


Figure 2.3: The seasonal variation of canopy level mean daily SIF, three vegetation indices (NDVI, EVI, MTCI) from FluoSpec system and leaf level assimilation rate, photochemical yield (ϕ_{PSII}) and chlorophyll content. And the leaf area measurements for the vegetation near the FluoSpec site.

can be observed, most of which are in the mid growing season. While for early (dark blue) or late (dark red) growing season, the A is much lower when same percent of energy is partitioned for photochemistry. When we compared the A with the product of ϕ_{PSII} and chlorophyll content, the correlation increased and the upper dots merged into the linear relationship.

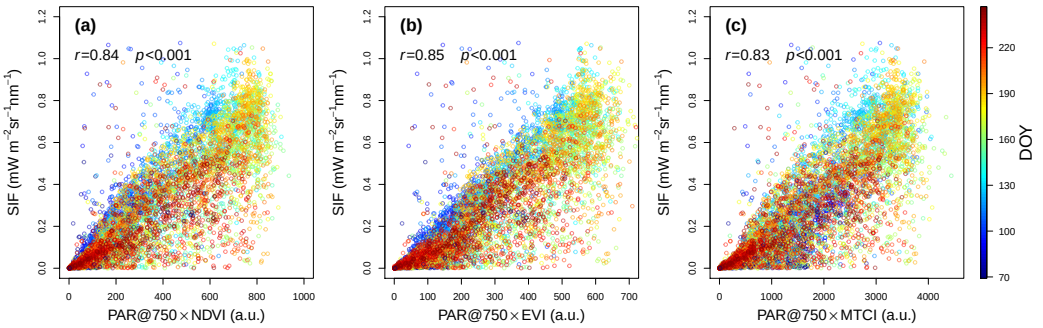


Figure 2.4: Comparison between the SIF and the product of PAR at 750 nm (as a proxy of PAR) and VI (as a proxy of fraction of PAR). (a) NDVI, (b) EVI, (c) MTCI.

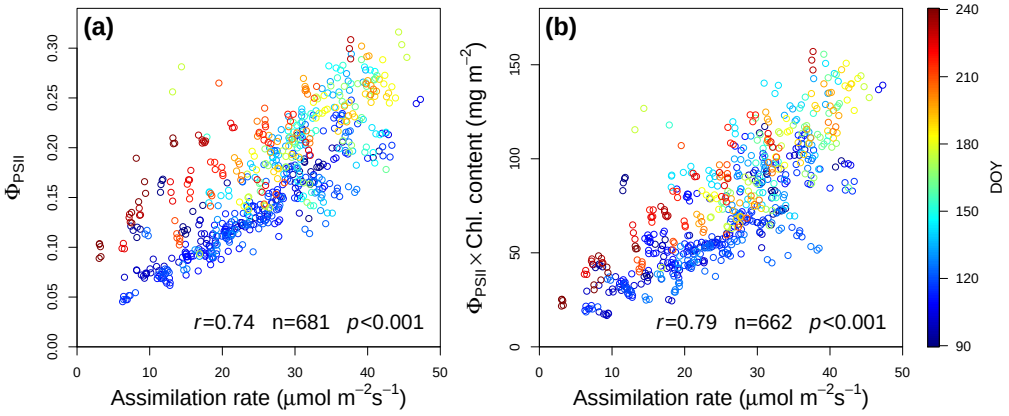


Figure 2.5: (a) Comparison between the chlorophyll fluorescence estimated photochemical yield (ϕ_{PSII}) and the corresponding leaf level gas exchange at different time of the measurement. (b) comparison between the product of photochemical yield and chlorophyll content (ϕ_{PSII}×Chl. content) and the leaf level gas exchange.

2.3.3 Vegetation response to drought using SIF and optical vegetation indices

We also assessed the drought impact on SIF and various vegetation indices by comparing the diurnal variation for the five phase of drought as identified by FWI in Figure 2.2. A summary of the climate conditions for the five periods can be found in Table 2.1. The two drought events are mostly caused by low soil moisture while the air temperature and VPD is not extremely high. It should also be noted that the first drought event (D1) only depleted the surface soil mosture (5cm), and the average of FWI is still high (0.64), while for the second drought event (D2), both the surface soil and root zoon soil moisture greatly decreased and created a stress for the vegetation.

Table 2.1: The start and end time of the five period and the average climate variables (maximum temperature, average VPD, and average FWI) for each period.

	Wet period 1 (W1)	Dry period 1 (D1)	Recovery period 1 (R1)	Dry period 2 (D2)	Recovery period 2 (R2)
Start (DOY)	156	170	188	205	224
End (DOY)	165	179	197	214	233
Average T_{max} (°C)	30.1	32.1	33.6	33.4	31.0
Average VPD (hPa)	10.2	13.2	10.8	12.7	7.0
Average FWI	0.93	0.64	0.87	0.36	0.98

Figure 2.6 showed the diurnal variation of SIF and other vegetation indices for clear and cloudy day. SIF mostly followed the diurnal variation of the solar radiation for the first three period (W1, D1, R1) during the clear day, while no clear pattern can be found for cloudy days. It can be seen a clear decrease of SIF for the D2 and R2. A detailed daily and diurnal vairation can be found in Figure 2.A.3. When excluded the contribution from diurnal variation of PAR, the product of fPAR×SIF_{yield} also showed much lower value compared to the first three period. And it can be seen

that the fPAR×SIF_{yield} exhibited a "U" shaped with close to normal values for early morning and late afternoon during D2. However, the fPAR×SIF_{yield} was alwasys lower than average from early morning (Figure 2.6(b)).

All vegetation indices showed slight decrease for the D2 and R2 period. For the first three period, the difference if minor except PRI (Figure 2.6(c-f)). The cloudy days exhibited a similar pattern while the diurnal variation of the indices are much smaller. The MTCI showed a higher sensitivity with a 24% decrease for the R2 compared to NDVI (12%) and EVI (15%) which may indicate a decrease of the chlorophyll or the greenness of the leaves. PRI exhibited an asymmetrical pattern at a diurnal scale, and the low or high values for the 5 periods are different compared to other indices.

2.4 Discussion

2.4.1 Seasonal variation of vegetation photosynthetic capacity and relationship with biophysical variables

The importance of the pigments in the leaves in controlling the seasonal variation of canopy photosynthetic capacity have been emphasized by many previous studies (Wu et al., 2016; Croft et al., 2017; Alton, 2017; Gitelson et al., 2014). Our studies suggested that the assimilation rate at leaf level can be improved when considering the total light absorption by chlorophyll in addition to the energy partitioning for photochemistry. Some other studies suggested that the photochemical yield can track the seasonal variation of the ecosystem photosynthesis (Yang et al., 2016). However, the relationship between the seasonal variation of GPP and ChlF estimated photochemical yield is different for spring and autumn. This can be explained by the variation of the leaf area and the photosynthetic pigments concentration in the

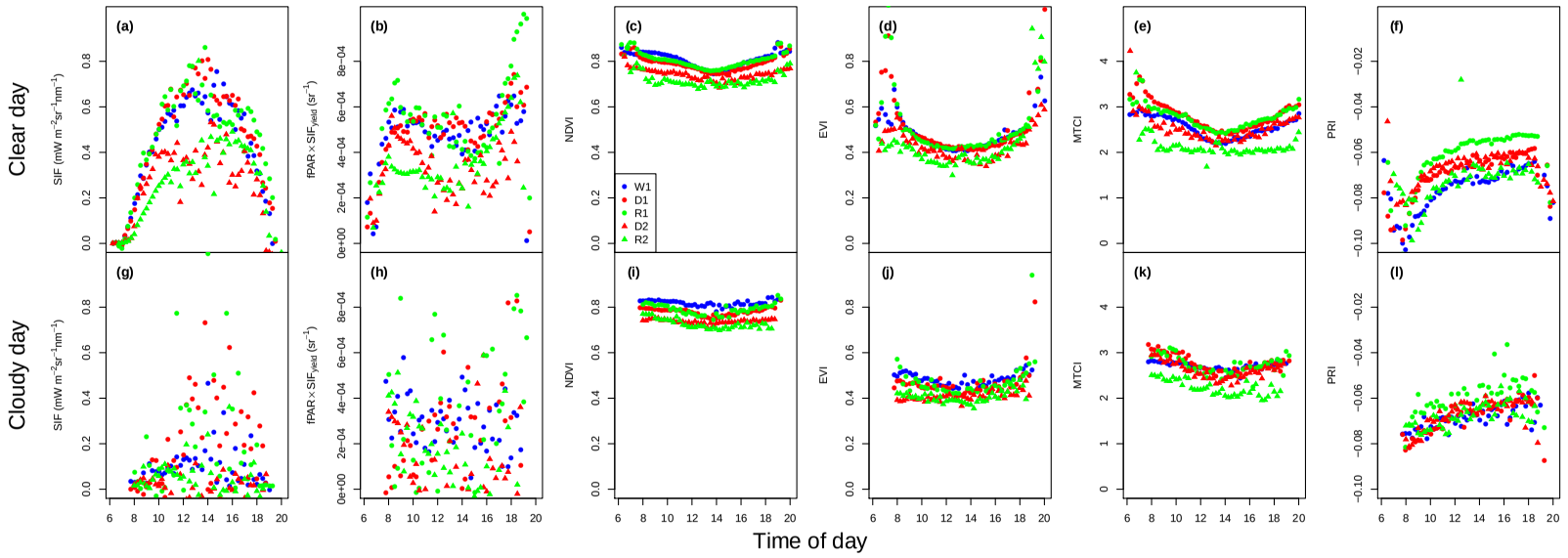


Figure 2.6: diurnal variation of SIF (a,f), fPAR×SIF_{yield} (b,g), NDVI (c,h), EVI (d,i), and PRI (e,j) during five different period as indicated by different colors and symbols. The upper panel shows the variation for clear days. The lower panel shows the variation for cloudy days.

leaves. However, the variation of these variables may also correlate with the seasonal variation of photochemical yield, therefore the seasonal GPP variation also exbihited relatively high correlation with photochemical yield without considering the variation of PAR absorption by the photosynthetic tissues.

Although the PAM based ChlF estimation can be used for photochemistry yield calculation, the satellite retrieved SIF is different and cannot be directly used to derive this photochemistry yield. However, as we have pointed out in the method, SIF signal shared the APAR_{chl} term with GPP and the variation of SIF_{yield} also closely related to the variation of the LUE (Guanter et al., 2014; Guan et al., 2016). In addition, under unstressed condition, SIF_{yield} and LUE are reltively constant when radiation is moderate. However, many recent studies suggested the variation of the escaping coefficient (f_{esc}) is strongly wavelength dependent and are needed to provide better GPP estimation when radiation quality (direct or diffuse) is considered (Goulas et al., 2017; Liu et al., 2017b).

Our canopy level SIF measurements showed that a majority of the variation can be explained by the proxy of APAR_{chl}. Three vegetation indices did not exhibited a significant difference in explaining the variation. The addition of FWI does not significantly increase the predictive power, which may be caused by three reasons: (1) the uncertainty related to the observations, especially SIF. Since the QE-Pro spectrometer usually have long integration time (from seconds to maixmum of 30 seconds), changing the illumination condition will cause unstable or biased SIF retrievals. (2) the limitation of the soil water condition on photosynthesis is nonlinear. Soil water becomes a limiting factor unless a threshold is reached and the limitation may be also ralated to air temperature and/or VPD. (3) within a diurnal cycle, ϕ_F also changes with the change of irradiance. This process is related to the optimazation of energy partition for photosynthesis and will affect the SIF-APAR_{chl}

relationship (Porcar-Castell et al., 2014). However, for satellite observations, the overpass time mostly corresponds to higher radiation and the variation of ϕ_F is limited.

2.4.2 Solar induced chlorophyll fluorescence as an indicator of vegetation drought stress

Drought limits photosynthesis from both the physiological control, which is related to the stomatal closure (Flexas & Medrano, 2002), decrease enzyme activity and mesophyll conductance (Grassi & Magnani, 2005), as well as the canopy control, which is related to the decrease leaf area or the decreased pigments in the leaf (Zhang et al., 2016f). It is very important to separate these two controls so that both process can be modeled individually and precisely. The two drought events happened in year 2017 give a very good chance to investigate how different severity drought events can be detected by SIF, and what information is embeded in the SIF signal during the drought and recovery period.

The canopy control is related to the longer term changes either related to the leaf area or the pigments, while the physiological control is more instantly responsible to the environmental changes within a diurnal cycle. The first drought event triggered neither the canopy nor the physiological limitation. Although the root zone soil moisture also declined, plants still get enough water for transpiration. The follow-up recovery period (R1) also experienced higher SIF values and no drought lagecy effects. The second drought event (D2) sustained a much longer period with low soil water content. However, the limitation during drought were mostly physiological since the early morning still had a relatively high fPAR$\times SIF_{yield}$ while during the midday, SIF_{yield} dropped because of environmental stress and recovered in the late afternoon. Since the second drought is more severe, it also exhibited a lagecy

effect, which decreased the fraction of PAR being absorbed. And during the R2 period, the physiological control is limited and did not induced an obvious midday depression of fPAR$\times SIF_{yield}$.

Previous studies that focused on the canopy limitation during drought most uses LAI or NDVI as a indicator of canopy change (Ji & Peters, 2003; Ciais et al., 2005; Reichstein et al., 2007). However, the canopy change which controled the light absorption caused by drought can be separated to two category: (1) change of total leaf area and (2) change of pigments within each leaf. Both of which contribute to the light absorption by the photosynthetic pigments of the entire canopy and are more related to the canopy photosynthetic capacity. In our study, we found different responses of vegetation indices. The chlorophyll related vegetation indices (EVI, MTCI) showed higher sensitivity during the R2 period than the leaf area related VI (NDVI) (Zhang et al., 2016f; Dong et al., 2015; Wagle et al., 2014). When the leaves become brown after a drought, the leaf quantity does not change much while the chlorophyll concentration declines significantly. This is also supported by our *in situ* LAI and chlorophyll content measurements. However, the decrease is still not strong enough when compared with a 39% drop of fPAR$\times SIF_{yield}$. Some of which may be also attributed to the drop related to SIF_{yield}. These results are also consistent with previous studies which showed satellite retrieved SIF signal can be a good indicator for soil moisture during drought period (Sun et al., 2015).

2.5 Conclusion

Solar induced chlorophyll fluorescence have proved to have great potential to track the seasonal variation of the photosynthesis activities. In this study, using the observations from both the leaf level ChlF and canopy level SIF, we have shown that

the seasonal variation of leaf level assimilation can be imporved by incorporating the chlorophyll content in the leaf. The canopy level SIF can be well explained by the absorption of PAR by chlorophyll, and environmental stress including soil water content are responsible for lower SIF values.

Canopy level SIF also showed higher sensitivity to drought stress than optical vegetation indices. SIF signal contains the information of both physiological and canopy limitation on photosynthesis. The lagecy effect of drought stress also changed the photosynthetic pigments in the leaf and can be tracked by both SIF and vegetation indices. The results of this study demonstrated the advantage of SIF in monitoring the drought impact on vegetation photosynthesis than tradational optical vegetation indices and suggested that *in situ* and satellite retrieved SIF can be used as benchmarks to improve earth system models in tracking the seasonal variation of GPP and drought responses.

2.A Appendix

2.A.1 Data acquisition using SpecFluo system and processing

The FluoSpec system is a integrated canopy reflectance and solar-induced chlorophyll fluorescence measuerement system. It uses a Raspberry Pi 3 micro computer as the controller and which is customizable and energy efficient.

A program written in C language using the "seabreeze" library is used to control the two spectrometers. A detailed operation process is shown in Figure 2.A.1. The major difference between the two spectrometers is that the QE-PRO is equiped with a Thermoelectric cooler (TEC) and a internal shutter. The TEC can adjust the temperature to ±30°C from the ambient. The operating temperature for QE-PRO is set to -10°C to get higher accuracy. Since ice on the charge-coupled device (CCD) will greatly affect the spectrum measuerement, in every measuerement cycle, the TEC is first heated to 20°C to evaporate possible water on CCD. The internal shutter will also close to get two dark measurement using the optimum integrating time for both irradiance and radiance measurement.

The post-processing of the raw digit number (DN) value to irradiacne and radiance includes several steps. (1) Dark current correction. For HR2000+, we used the average of electrical dark values as the dark current, and were subtracted from all DN values. For QE-PRO, the dark current measurement are the corresponding dark measuerement with the internal shutter closed. (2) Non-linearity correction. Both HR2000+ and QE-PRO uses a 7 order polynomial to correct the non-linearity, the correction factors were obtain from each spectrometer. The final irradiance and irradiance values were calculated using the equation below:

$$I_P = C_P \times \left(\frac{S_P}{T \times A \times dL_P} \right) \tag{2.A.1}$$

where I_p is the spectral flux density at wavenumber P, C_P is the calibration file obtained using a light source during the radiometric calibration. S_P is the sample spectrum after dark and non-linearity correction. T is the integration time. A is the collection area and dL_P is the wavelength spread.

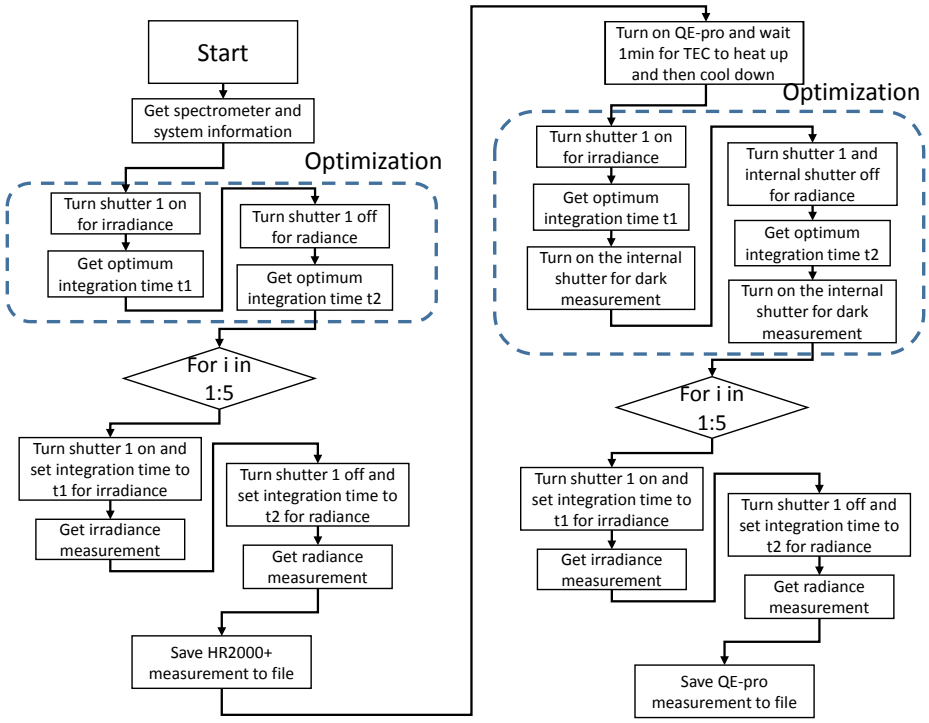


Figure 2.A.1: A work flow for FluoSpec system to obtain irradiance and radiance measurement of the canopy from HR2000+ and QE-PRO.

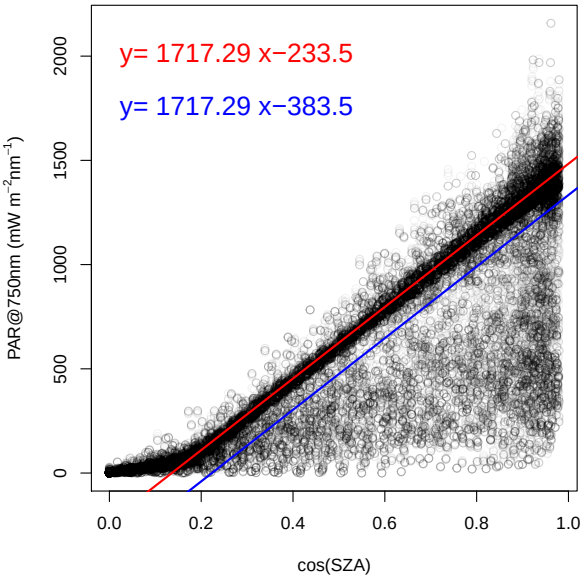


Figure 2.A.2: Comparison between spectral flux density of irradiance at 750 nm and the cosine of the sun zenith angle.

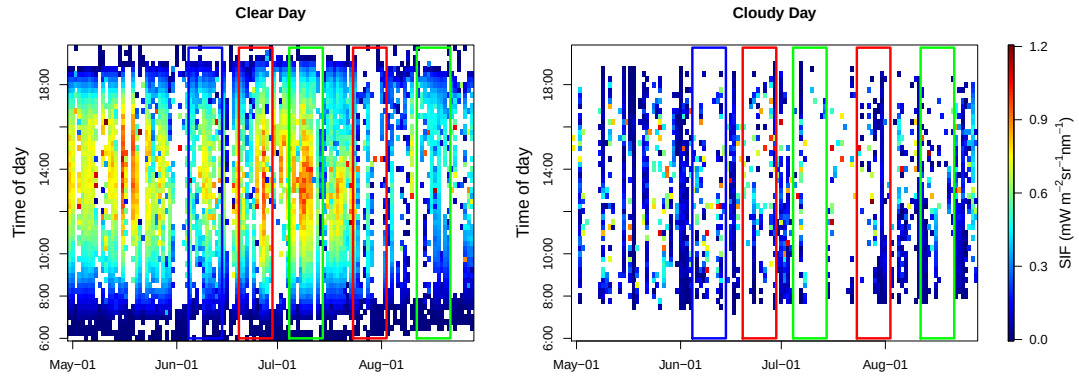


Figure 2.A.3: The seasonal and diurnal variation for SIF during the peak growing season. The SIF is separated for (a) clear day and (b) cloudy day since SIF is greatly affected by the solar radiation.

Chapter 3: On the relationship between sub-daily instantaneous and daily total gross primary production: implications for interpreting satellite-based SIF retrievals

Abstract

Spatially and temporally continuous estimation of plant photosynthetic carbon fixation (or gross primary production, GPP) is crucial to our understanding of the global carbon cycle and the impact of climate change. Besides spatial, seasonal and interannual variations, GPP also exhibits strong diurnal variations. Satellite retrieved solar-induced chlorophyll fluorescence (SIF) provides a spatially continuous, but temporally discrete measurement of plant photosynthesis, and has the potential to be used to estimate GPP at global scale. However, it remains unclear whether the seasonal time series of SIF snapshots taken at a fixed time of the day can be used to infer daily total GPP variation at spatial and seasonal scales. In this study, we first used GPP estimates from 135 eddy covariance flux sites, covering a wide range of geographic locations and biome types, to investigate the relationship between the instantaneous GPP (GPP_{inst}) and daily GPP (GPP_{daily}) on the seasonal course for different times of the day. Latitudinal and diurnal patterns were found to correspond to variations in photosynthetically active radiation (PAR) and light use efficiency (LUE), respectively. We then used the Soil-Canopy Observation Photosynthesis and Energy Balance (SCOPE) model and the FluxCom GPP product to investigate the instantaneous and daily SIF-GPP relationships at five flux tower sites along a latitudinal gradient and at a global scale for different biome types. The results showed that daily SIF had a stronger linear correlation with daily GPP than instantaneous SIF at the seasonal scale, with an instantaneous to daily SIF conversion factor following the latitudinal and seasonal pattern driven by PAR. Our study

highlights the necessity to take the latitudinal and diurnal factors into consideration for SIF-GPP relationship analyses or for physiological phenology analyses based on SIF.

3.1 Introduction

Photosynthetic carbon fixation by plants is the most influential CO_2 flux connecting the atmosphere and the biosphere. Every year, approximately 120 Pg carbon is fixed by the terrestrial ecosystems through photosynthesis, providing food and materials for human beings while also largely driving the global carbon cycle (Beer et al., 2010). The underlying ecophysiological mechanisms controlling this biochemical process have been long studied, mostly at the leaf or molecular scale (Farquhar et al., 1980; Krause & Weis, 1991). Actual estimation of the photosynthetic exchange flux at the ecosystem scale, also known as gross primary productivity (GPP), only became practical in the 1990s with the emergence of the eddy covariance (EC) technique (Baldocchi et al., 2001). EC flux towers measure the net ecosystems exchange (NEE) which can be further partitioned into GPP and ecosystem respiration (Lasslop et al., 2010; Reichstein et al., 2005; Wohlfahrt & Gu, 2015). These ground observations have been critical to the development and testing of models used to simulate GPP at a larger scale, but the performance of these models is still not satisfactory, with large discrepancies existing among different models (Anav et al., 2015). Using observations as a constraint can help to improve the model performance so that models may better predict the global carbon cycle under future climate scenarios (Luo et al., 2011; Peng et al., 2011b). However, different types of GPP variations need to be taken into consideration when conducting this model-data fusion.

Plant photosynthesis is powered by light and affected by numerous environ-

mental factors and plant phenological phases. Its variation is often characterized by four aspects: (1) Diurnal variation: as the solar radiation has a diurnal cycle, it directly affects the incoming energy and carbon assimilation of plants. Other environmental or physiological variables affecting stomatal conductance and CO_2 uptake, such as air temperature, vapor pressure deficit (VPD), or leaf water potential also show diurnal cycles. (2) Seasonal variation: driven by the climate (e.g., temperature, water availability, radiation) seasonality and plant phenology, it represents one of the most important components of GPP overall variability. Most in situ and remote observations are also conducted at this scale. (3) Spatial variation: due to the spatial distribution of plant species, latitudinal pattern of incoming solar radiation, topography, and spatial variations in climate and soil properties, GPP also exhibits strong spatial variations. (4) Interannual variation: usually driven by climate anomalies and land cover changes, it is one order of magnitude smaller than other types of variations and are therefore the most challenging level for models to simulate accurately (Verma et al., 2015).

For some methods, e.g., the eddy covariance (EC) technique, a single site can capture ecosystem to landscape-scale diurnal, seasonal, and interannual variations because the measurement is continuous at a high sampling frequency (Aubinet et al., 2012). However, EC sites are spatially dispersed and cannot provide spatially continuous measurements (Schimel et al., 2015). In contrast, remote sensing technologies usually have high spatial coverage with polar orbiting (low Earth orbiting, LEO) satellites, while the continuous temporal sampling is generally not possible. For LEO satellite platforms, we can only get from zero to possibly a few observations per day depending on the swath width of the instrument and latitude (multiple observations per day with a single instrument are only possible at high latitudes and with a wide swath instrument, e.g. (Guanter et al., 2015)). If observing

conditions are not favorable, e.g., owing to clouds or aerosols, a valid observation may not be present over several days (Sims et al., 2005). For optical remote sensing that uses vegetation indices (VIs) to quantify vegetation canopy and leaf properties that change relatively slowly, usually over the course of weeks to months, this low sampling frequency is adequate to quantify the spatial, seasonal and interannual variations (Guan et al., 2015; Huete et al., 2006; Zhang et al., 2016d). The diurnal variation of satellite observed VI (an indicator of vegetation greenness) or canopy coverage is mostly caused by leaf inclination or bidirectional reflectance (Los et al., 2005). As long as the satellite overpass time is stable, these effects are minor and a VI measurement at most time of the day (when the satellite and solar zenith angles are low) may be a good proxy of the VI for that day (Chen 1996). However, as the sun-sensor geometry also gradually changes at seasonal scales, seasonal dynamics of VIs should take this effect into consideration, especially in tropical regions where backscattering and forward scattering shift within a year (Bi et al., 2015; Morton et al., 2014).

Following the successful retrieval of solar-induced chlorophyll fluorescence (SIF) signals from satellite sensors (Frankenberg et al., 2011; Joiner et al., 2013, 2012; Guanter et al., 2012), we have access to a new type of vegetation observation, which is based on energy re-emitted by plants rather than reflected. SIF is a small amount of energy re-emitted during the light reaction of the photosynthesis process (Baker, 2008; Porcar-Castell et al., 2014). Studies have shown that it is highly correlated with the energy absorbed by chlorophyll pigments and the photosynthetic electron transport (Zhang et al., 2014b, 2016e). Like GPP, SIF is also driven by photosynthetically active radiation (PAR), and has a strong diurnal cycle embedded within the seasonal, spatial, and interannual variations. Previous studies attempted to use satellite-based SIF to estimate GPP, however, this relationship was only tested at

individual sites for cropland or broadleaf forest (Guanter et al., 2014; Wagle et al., 2016; Yang et al., 2015). Moreover, these studies mostly compared satellite derived instantaneous SIF with the daily GPP. The discrepancies between the underlying different temporal scales, i.e., instantaneous SIF observation at satellite overpass time vs. daily integrated GPP, so far have not been fully evaluated.

Previous studies have shown that SIF and GPP are linked through the photon partitioning after absorption by plant chlorophyll (Genty et al., 1989). Absorbed photons undergo three different pathways (i) forming the electron transport chain and chemical energy further used for the Calvin Cycle (ϕ_p), (ii) being dissipated as heat (ϕ_d), or (iii) being reemitted as fluorescence (ϕ_f). These mechanisms can be used to build up the link between instantaneous GPP and SIF (Damm et al., 2010; van der Tol et al., 2014, 2009). Many studies have investigated these relationships at the scale of sub-seconds to minutes, but the spatial and seasonal variation of this relationship remains unclear (Porcar-Castell et al., 2014). In addition, because SIF measurements from satellites are usually not continuous over time, we still need to understand the scale conversion from instantaneous to daily sums, i.e., whether a snapshot of photosynthetic activity at a specific time of the day can represent the daily total carbon fixation at both spatial and temporal (seasonal and interannual) scales. Sims et al. (2005) and Ryu et al. (2012) showed that the midday value of GPP or ET can be a representative of daily or 8-day value. But those studies only focused on a limited number of sites and the MODIS overpass time (10:00 11:00 and 13:00 14:00). As the satellites from which SIF retrievals can be made have different overpass times (Figure 3.1), it is unclear how that can affect the relationships between instantaneous SIF and daily GPP at different locations.

This study aims to fill those gaps with both observations and modeling approach: we used eddy flux data from 135 sites, covering a wide range of geographical regions

and biome types, the global GPP product from FluxCom, and SIF from Global Ozone Monitoring Experiment 2 (GOME-2) and Orbiting Carbon Observatory 2 (OCO-2), to explore the instantaneous-daily relationship among GPP, PAR, light use efficiency (LUE) and SIF. In particular, we focused on the following questions which have not yet been addressed: (1) What is the relationship between the daily total GPP and instantaneous GPP at different times of day (TOD) and different locations? (2) What is the cause of these spatial and temporal patterns? (3) Does SIF also exhibit these spatio-temporal patterns and how does this affect our interpretation of the SIF-GPP relationship?

3.2 Materials and Method

3.2.1 GPP from FLUXNET data base and preprocessing

We used eddy flux data from 135 sites covering a large variety of biome types. The flux dataset was acquired from the FLUXNET 2015 release (December 2015, http:

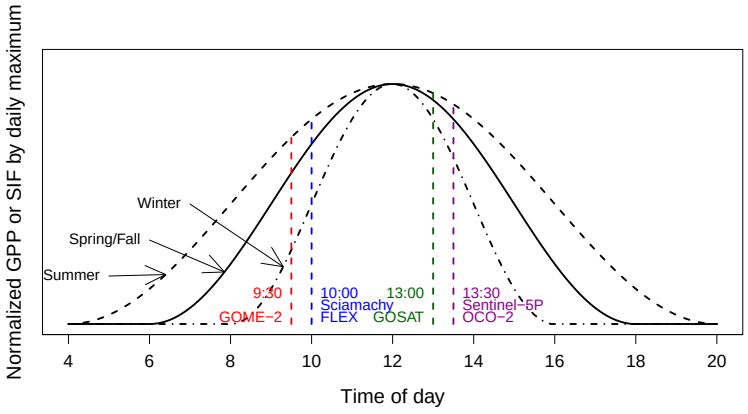


Figure 3.1: Schematic graph showing the diurnal course of GPP or SIF normalized by their daily maximum values. These schematic curves are shown for different seasons. Overpass time (solar time) of different satellites/sensors measuring SIF are also indicated.

//fluxnet.fluxdata.org/data/fluxnet2015-dataset/). The spatial distribution and the information about each site can be found in Appendix (Figure 3.A.1, Table 3.A.1). This dataset was processed using a standardized protocol, which enabled us to make a cross-site comparison (http://fluxnet.fluxdata.org/data/fluxnet2015-dataset/data-processing/). To answer the question whether the seasonal cycle of instantaneous GPP (GPP_{inst}) at a certain time of day can represent the seasonal cycle of the daily GPP (GPP_{daily}), we used both the original half-hourly data and the daily data. The half-hourly data were aggregated into 2-hour bins from 6:00 am to 6:00 pm to represent the GPP_{inst}. A rigorous data quality check was applied during this aggregation process: 1) Only the half-hourly and daily data in the weeks with more than 75% of valid (not gap-filled) radiation and net ecosystem exchange (NEE) observations were used. 2) To reduce the uncertainty related to the NEE partitioning, we compared the GPP estimates from both the daytime method (light response curve; Lasslop et al. (2010)) and the nighttime method (nighttime NEE as respiration; Reichstein et al. (2005)) at weekly scales. The GPP estimation was considered unbiased only if the GPP from both methods were within 20% of each other, in which case GPP was then calculated as the average of both methods. We did not use the original half-hourly data as it would generate too many $GPP_{inst} - GPP_{daily}$ comparisons; six two-hour bins were enough to get the diurnal change of their relationship.

3.2.2 Relationship between instantaneous and daily GPP at seasonal scale across sites

The relationship between daily GPP (GPP_{daily}) and instantaneous GPP (GPP_{inst}) can be built for each day using a conversion factor (γ_{GPP}):

$$\gamma_{GPP} = \frac{GPP_{daily}}{GPP_{inst}} \tag{3.1}$$

This conversion factor can be calculated for each site each day at seasonal scale. If γ_{GPP} at one site has little variation across time, it indicates that GPP_{inst} can represent GPP_{daily} at temporal scale. Similarly, if γ_{GPP} has little variation across sites, it indicates that GPP_{inst} can represent GPP_{daily} at spatial scale. For simplicity, we built linear regressions with zero intercept between GPP_{daily} and GPP_{inst} for each site at seasonal scale; a high R^2 indicates γ_{GPP} is seasonally stable for a given site and γ_{GPP} can be calculated as the regression slope (Figure 2.2). The variability of regression slopes (γ_{GPP}) across sites is indicative of the variability of the relationship across space.

3.2.3 Relationship between instantaneous and daily LUE at seasonal scale across sites

LUE is a very important parameter that connects light absorption by the ecosystem and the carbon fixation through photosynthesis (Monteith, 1972). The instantaneous and daily light use efficiency (LUE_{inst} and LUE_{daily}, respectively) are defined as follows:

$$LUE_{inst} = \frac{GPP_{inst}}{fPAR \times PAR_{inst}} \tag{3.2}$$

$$LUE_{daily} = \frac{GPP_{daily}}{fPAR \times PAR_{daily}} \tag{3.3}$$

The GPP_{inst} and $APAR_{inst}$ were also averaged over 2-hours from 6:00 am to 6:00 pm local time for each site. Within one day, the diurnal variation of the fraction of the PAR absorbed by the canopy (fPAR) is relatively small (Fensholt et al., 2004) and is neglected. Following the definition of γ_{GPP}, we can also define the γ_{LUE}, i.e., the

ratio of LUE_{daily} over LUE_{inst}.

$$\gamma_{LUE} = \frac{LUE_{daily}}{LUE_{inst}} = \frac{\frac{GPP_{daily}}{APARdaily}}{\frac{GPP_{inst}}{APAR_{inst}}} \approx \frac{\frac{GPP_{daily}}{PARdaily}}{\frac{GPP_{inst}}{PAR_{inst}}} = \frac{ELUE_{daily}}{ELUE_{inst}} \tag{3.4}$$

Similarly, we did not calculate γ_{LUE} for each day, but used the regression slope between daily and instantaneous ecosystem LUE (ELUE_{daily}=GPP_{daily}/PAR_{daily} and $ELUE_{inst} = GPP_{inst} = APAR_{inst}$, respectively) for each site. The use of ELUE rather than LUE avoided the uncertainties related to the calculation of fPAR.

3.2.4 Analytical conversion from instantaneous to daily APAR

Both SIF and GPP are driven by the incident solar irradiance and therefore both exhibit a diurnal cycle. Thus, the relationship between the daily APAR ($APAR_{daily}$) and instantaneous APAR ($APAR_{inst}$) is very important to determine the relationship between SIF_{daily} and SIF_{inst}, and GPP_{daily} and GPP_{inst}. As diurnal changes in incoming solar radiation are mostly determined by the solar zenith angle (SZA), we can calculate the conversion factor between $APAR_{inst}$ and $APAR_{daily}$ (γ_{APAR}) as below:

$$LUE_{inst} = \frac{GPP_{inst}}{fPAR \times PAR_{inst}} \tag{3.5}$$

This approach did not consider the minor diurnal variation of fPAR and the cloud and atmospheric scattering effect on PAR. The $cos(SZA)_{daily}$ can be calculated following the method documented in Frankenberg et al. (2014):

$$LUE_{inst} = \frac{GPP_{inst}}{fPAR \times PAR_{inst}} \tag{3.6}$$

The SZA for each site was calculated using the "RAtmosphere" package (https://cran.r-project.org/web/packages/RAtmosphere/index.html) in R language (https:

//www.r-project.org/). The "SZA" function can calculate the SZA of a specific location based on its latitude, date, and local time of day. The instantaneous SZA was calculated at a local time between 7:00 to 17:00 with a time-step of two hours corresponding to the mid-time of each GPP aggregation bin. The $cos(SZA)_{daily}$ was calculated numerically as the integral of cosâĄą$(SZA(t))dt$ at a 10-minute time-step. Similarly, we used a linear regression between $cos(SZA)_{daily}$ and $cos(SZA)_{inst}$ to estimate γ_{APAR} at different times of the day (TOD). The regression was forced to pass through the origin and the regression slope represented γ_{APAR} for a specific location. Because SZA is a function of local time and latitude, γ_{APAR} only varies with time and latitude.

3.2.5 SCOPE model simulation

To investigate the relationship between instantaneous and daily SIF (SIF_{inst} and SIF_{daily}, respectively), and the GPP and SIF relationship both at bi-hourly and daily scales, we used the SCOPE model (van der Tol et al., 2014, 2009) to simulate both SIF and GPP. To test whether γ_{SIF} (SIF_{daily}/SIF_{inst}) also has a latitudinal pattern similar to GPP, we selected five grassland or savannas sites (DK-ZaH, US-Ivo, DK-Eng, US-Var, CG-Tch) along the latitude where the cosines of latitudes of these sites are close to 0.2, 0.4, 0.6, 0.8, and 1 (Table 3.A.1, Figure 2.A.1). We chose the grassland/savannas biome types since they are broadly distributed at different latitudes and their canopy structure is relatively simple.

Chlorophyll a + b content (Cab) and maximum carboxylation rate (V_{cmax}) and the leaf area index (LAI) are the most influential parameters for simulating SIF and GPP with the SCOPE model (Verrelst et al., 2015; Zhang et al., 2016b). For Cab, we followed the method used in previous studies (Zhang et al., 2014b, 2016b). The Cab was inversely estimated from a lookup table generated by the forward simu-

lation of the PROSPECT model with a large number of parameter combinations. The 8-day Enhanced Vegetation Index (EVI) and MERIS Terrestrial Chlorophyll Index (MTCI (Dash & Curran, 2004)) for those five sites were used as inputs and Cab was inverted at 8-day intervals. All other climate inputs were obtained from the flux tower measurements, and the LAI was obtained from the MODIS LAI product using the Oak Ridge National Laboratory MODIS global subsets tool with a footprint of 5 km to match with that of MTCI (https://modis.ornl.gov/cgi-bin/MODIS/GLBVIZ_1_Glb/modis_subset_order_global_col5.pl). The maximum carboxylation rate at 25 °C(V_{cmax}) were set to constant for each site following previous studies (52 μmol m^{-2} s^{-1} for C3 grass and 30 μmol m^{-2} s^{-1} for C4 grass) (Kattge et al., 2009; Wullschleger, 1993; Zhang et al., 2016b). Other unspecified parameters were set to their default values in SCOPE v1.61 (https://github.com/Christiaanvandertol/SCOPE).

3.2.6 Comparison of satellite retrieved SIF and GPP at global scale

Since SIF can also be expressed as a function of APAR (SIF=APAR×FE, FE: fluorescence efficiency), we can approximate SIF_{daily} from SIF_{inst} by assuming that FE has little variation at a diurnal scale. This is a first-order approximation since two contributing factors of FE, namely quantum yield for fluorescence (ϕ_f) and escape coefficient for near-infrared SIF (f_{esc}, how much SIF emitted by individual leaf can escape the canopy without being re-absorbed by other leaves) have a much smaller variation compared to the diurnal variation of PAR (data not shown). The SIF_{daily} can be approximated as:

$$LUE_{inst} = \frac{GPP_{inst}}{fPAR \times PAR_{inst}} \tag{3.7}$$

where SIF_{inst} is the satellite retrieved SIF and PAR_{daily} is analytically estimated from SZA, PAR_{inst} can be estimated from the SZA when the observation was made, which is embedded in the GOME-2 and OCO-2 SIF product. We did not use the PAR_{inst} for the satellite overpass time (e.g., 9:30 am for GOME-2 and 1:30 pm for OCO-2) since that overpass time only applies for equator, higher latitudes may have some variation. In this study, we used both the GOME-2 SIF v26 product from the MetOp-A satellite (Joiner et al., 2013, 2016), and the OCO-2 SIF Lite product (B7101r) (Frankenberg et al., 2014). The MetOp-A satellite has an overpass time of 9:30 am and SIF was retrieved around the wavelength of 740 nm using a principle component analysis algorithm (Joiner et al., 2013). These retrievals had a footprint of 40 km × 80 km (40 km × 40 km after 15 July 2013) and were further aggregated to a 0.5°× 0.5° monthly gridded product. The OCO-2 SIF was retrieved around 757 nm using an iterative least squares fitting technique. Each day, around 100000 soundings were collected on land with a footprint of 2 km × 1.3 km. We aggregated the raw SIF retrievals to monthly 0.5°× 0.5° gridded product following the quality check instructions. Since this dataset only became available since September 2014, it cannot be directly compared with GPP dataset. We used 2 year of data (2015, 2016) to calculate the average SIF of each month. In this way, we ignored the interannual variation and just focused on the seasonal variation.

We used the monthly GPP product from FluxCom with a spatial resolution of 0.5°× 0.5°. The FluxCom GPP was generated using three machine learning algorithms, combined with GPP estimated from the daytime method (Lasslop et al., 2010) and nighttime method (Reichstein et al., 2005) from the EC flux towers, and the remote sensing VIs and meteorological variables (Jung et al., 2017; Tramontana et al., 2016). The averaged GPP from 6 methods (3 machine learning algorithm × 2 partitioning methods) between 2007 and 2013 were calculated to match the GOME-

2 SIF data availability. To compare with the OCO-2 SIF, GPP from 2007 to 2013 were used to calculated the average GPP for the 12 months since these two products do not have overlapping period. Because monthly gridded OCO-2 SIF do not cover the entire global land surface due to the satelliteâĂŹs orbit, we masked the GPP with OCO-2 SIF for the corresponding months before comparison.

To compare the SIF-GPP relationship within each biome type, we aggregated the MODIS MCD12C1 land cover product (https://lpdaac.usgs.gov/dataset_discovery/modis/modis_products_table/mcd12c1) to 0.5°× 0.5° spatial resolution to match with GPP and SIF. For each 0.5°× 0.5° gridcell, we calculated the percentage of each land cover type. Only the gridcells dominated by one land cover type (more than 80%) were considered as "pure" gridcells and used for further analysis (Zhang et al., 2016d). Since the northern hemisphere and southern hemisphere have different growing season, SIF and GPP were averaged within each biome type for each hemisphere.

3.3 Results

3.3.1 Comparison between instantaneous GPP and daily GPP at seasonal scale

Figure 3.2 shows a comparison between GPP_{daily} and GPP_{inst} at seasonal scale for the Tchizalamousite site in the Congo (CG-Tch) as an example. All GPP_{inst} values at different times of the day (TOD) generally followed the variation of GPP_{daily}, and the γ_{GPP} was also relatively stable across time for TODs between 8:00 16:00 (Figure 3.2(a, b)). The regression analysis between GPP_{daily} and GPP_{inst} also showed a similar pattern: TOD with less γ_{GPP} variation exhibited a higher R^2 and the regression slope between GPP_{daily} and GPP_{inst} corresponded to the value of γ_{GPP}. This confirms the feasibility of using regressions between GPP_{daily} and GPP_{inst} to in-

vestigate the seasonal and spatial variations of γ_{GPP}. Using the correlation analysis between GPP_{daily} and GPP_{inst} from all 135 sites at a seasonal scale, we gathered information of the coefficient of determination (R^2) and the regression slopes for each site. For most sites, GPP_{inst} showed a good correlation with GPP_{daily}, especially for GPP_{inst} between 8:00 to 16:00 (Figure 3.3a). The correlation was lower for very early morning and late afternoon, but the average R^2 values for these two periods were still higher than 0.8. The regression slopes between GPP_{daily} and GPP_{inst} also varied for different TODs. The averages of regression slopes slightly declined from early morning to midday and increased afterwards. For the period between 8:00 to 16:00 when GPP_{daily} and GPP_{inst} relationships were stronger, the regression slopes also showed less variation. We also explored the spatial patterns of the regression slopes between GPP_{daily} and GPP_{inst}, by comparing the regression slopes with the cosine of the latitude for each site (Figure 3.4). The regression slopes increased from tropical regions (cos(latitude) = 1) to polar regions (cos(latitude) = 0) for most TODs. Between 8:00 to 16:00, the regression slopes between GPP_{daily} and GPP_{inst} can be approximated as a function of cos(latitude), with relatively high R^2 during the midday period (0.81 and 0.87). Biome types did not show much effect on this relationship. Using the analytical approach based on the calculated SZA (Eq. 3.5), we obtained the γ_{APAR} at each latitude. The resultant black lines in Figure 3.4 generally well-predicted this latitudinal pattern, especially between 8:00 to 16:00. The R^2 between GPP_{daily} and GPP_{inst} also exhibited a latitudinal pattern that could be predicted by the analytical solution of APAR variation (Figure 3.A.2).

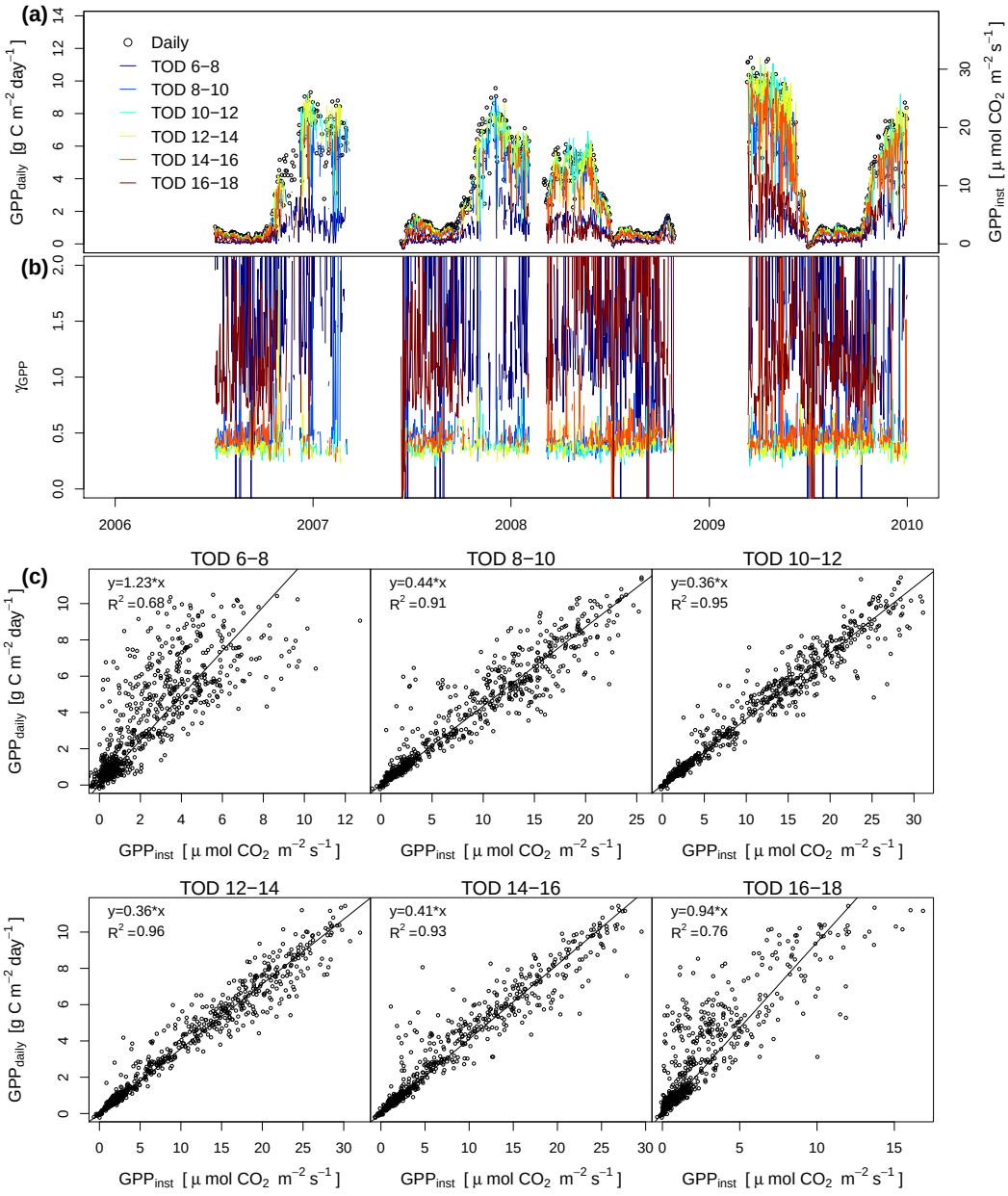


Figure 3.2: Seasonal variation of (a) GPP_{inst}, GPP_{daily}, and (b) γ_{GPP} of different time of day from a savanna flux tower site CG-Tch. (c) The regression between GPP_{daily} and GPP_{inst} from different times of the day (TOD). R^2 and the regression slope for each TOD are shown at the top left corner and will be used for cross-site statistics. Large gaps in 2007 and 2009 are observations that did not pass the quality checks. Note that the units for GPP_{daily} (g C m^{-2} day^{-1}) and GPP_{inst} (μmol CO$_2$ m^{-2} s^{-1}) are different.

3.3.2 Comparison between sub-daily instantaneous LUE and daily LUE at seasonal scale

Figure 3.5 shows the comparison between the instantaneous LUE and daily LUE for each site at the seasonal scale. Except for the early morning and late afternoon, LUE_{inst} values were generally highly correlated with LUE_{daily}, and this correlation was highest during the middle of the day (10:00 14:00). The regression slopes between LUE_{daily} and LUE_{inst} were also relatively stable for TODs when R^2 values were high. In addition, the slope showed an "U" shape along time with the lowest value being reached during the middle of the day (Figure 3.5b). The regression

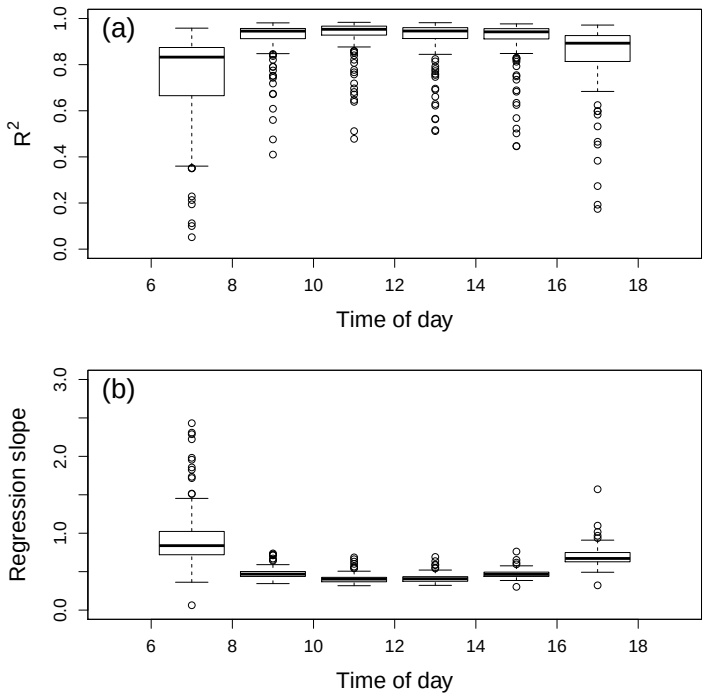


Figure 3.3: Boxplots of bi-hourly (a) coefficient of determination (R^2) and (b) linear regression slope between the daily and instantaneous GPP (γ_{GPP}) at seasonal scale across 135 flux tower sites. The linear regressions were forced to pass the origin. The unit of the instantaneous GPP was converted from μmol CO_2 m^{-2} s^{-1} to g C m^{-2} day^{-1} so that the regression slope is unitless.

slopes were close to 1 around 10:00 or 14:00, which indicated that the LUE_{inst} at those times can be an approximation of LUE_{daily}. The difference between the fitted γ_{GPP} curve (red) and simulated γ_{APAR} curve (black) at different TODs in Figure 3.4 can be explained by the diurnal change of the LUE_{daily} and LUE_{inst} relationship (γ_{LUE}). This diurnal change of γ_{LUE} is caused by light saturation of GPP as shown in Figure 3.6. GPP increases almost linearly with APAR until a light saturating period is reached, when GPP becomes less responsive to radiation (Figure 3.6b). This lead to lowest LUE values close to midday, when incident PAR and APAR are

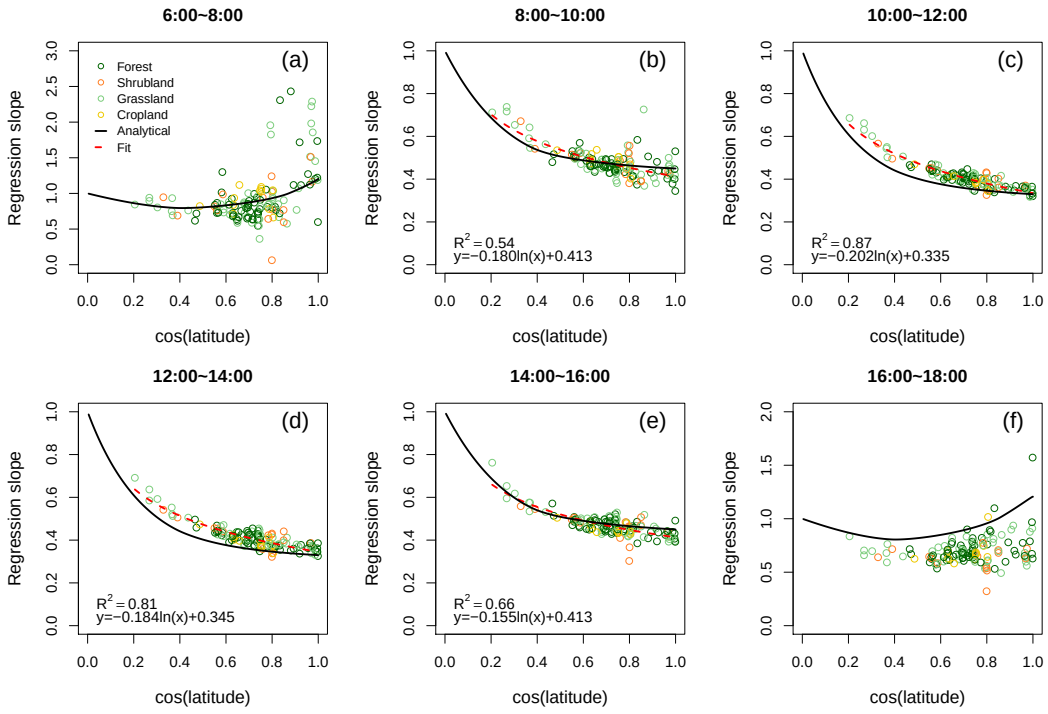


Figure 3.4: Latitudinal distribution of regression slopes between daily and instantaneous GPP (γ_{GPP}). All biome types (shown in different colors) are aggregated to forest (ENF, EBF, DNF, DBF, MF), shrubland (WSA, OSH, CSH), grassland (GRA, WET, SAV), and cropland (CRO), as shown in different colors. For the full names of the biome types, please refer to the Appendix Table 3.A.1. Black lines represent the relationship derived from the analytical approximation for γ_{APAR} and cos(latitude). The red dashed lines represent the fitted logarithmic regressions for all sites and not shown in (a) and (f) since the relationship was not significant.

the highest (Figure 3.6a). The light response curve also suggests that the LUE_{inst} around 9:00 and 15:00 solar time is close to the LUE_{daily}. This explains the overlap of the fitted γ_{GPP} and simulated γ_{APAR} curves during 8:00–10:00 and 14:00–16:00; and the higher γ_{GPP} between 10:00 14:00 over the latitudinal gradient (Figure 3.4).

3.3.3 Comparison between simulated instantaneous and daily SIF from the SCOPE model

To explore whether the instantaneous SIF (SIF_{inst}) and daily SIF (SIF_{daily}) also exhibit a similar latitudinal pattern, we used the SCOPE model and simulated both SIF and GPP for five grassland (or savannas) sites, which cover a wide latitudinal range. The model was run at 30-minute intervals for one year to be consistent with the EC

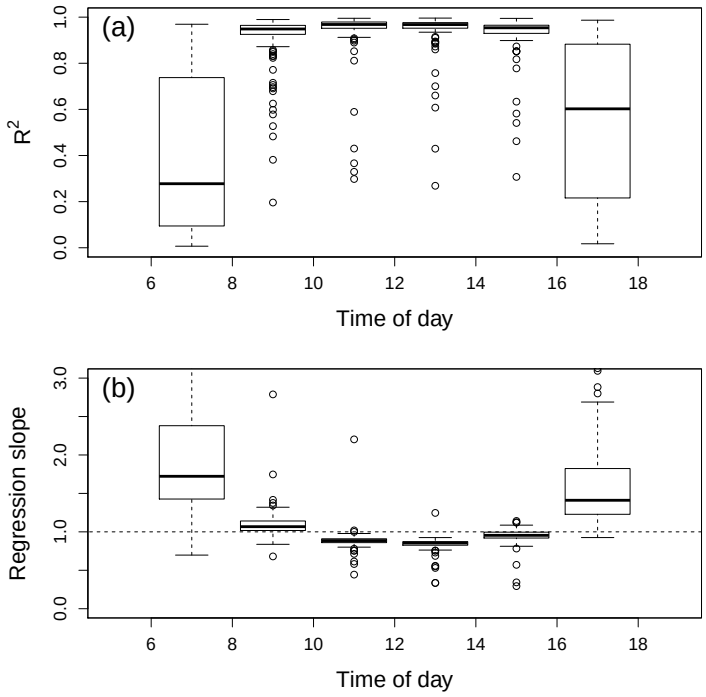


Figure 3.5: Comparison between bi-hourly LUE_{inst} and LUE_{daily} across flux tower sites at the seasonal scale. For each site, the correlation and regression slope between LUE_{daily} and LUE_{inst} (γ_{LUE}) at seasonal scale were calculated.

data. The simulated GPP and SIF data generally agreed well with the EC tower derived GPP and the SIF retrievals from the GOME-2 satellite instrument (Figure 3.A.3, 3.A.4).

Using the SCOPE model, we found that SIF also followed a similar latitudinal pattern driven by the seasonal variation of PAR. Since we only used one year of data, the γ_{GPP} values for the five sites were sometimes higher than the fitted relationship for some times of day. However, for 8:00 10:00 and 14:00 16:00 when the fitted γ_{GPP} was close to the analytical γ_{APAR}, the regression slopes for simulated SIF from the

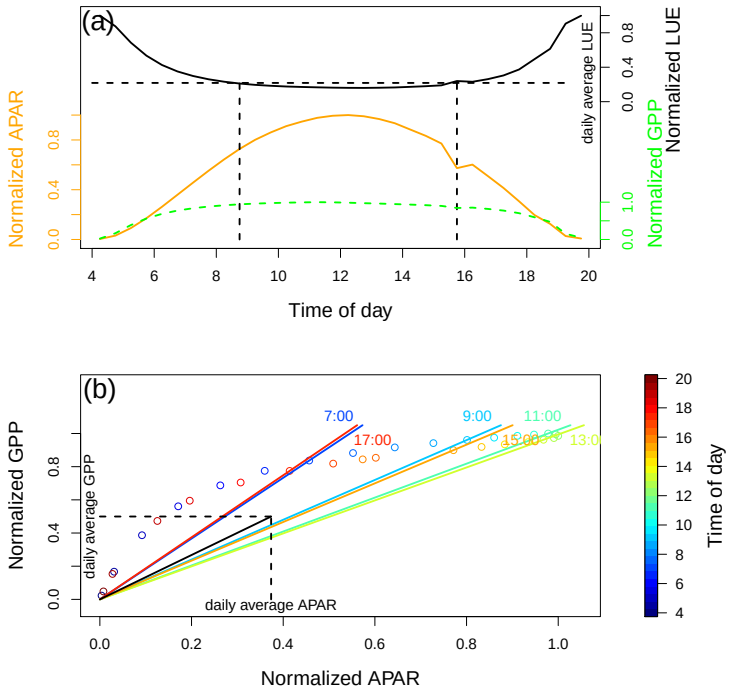


Figure 3.6: (a) Dynamic of sub-daily GPP, APAR, and LUE, and (b) the relationship between APAR and GPP at sub-daily scale. One clear day (June 13th, 2014) of data from the US-WCr site is used as an example. The GPP is estimated from the daytime (light response curve) method. All the indicators are normalized by their maximum values. The two vertical dashed lines in (a) indicate the time at which LUE_{inst} equals to LUE_{daily}. The slopes of the solid lines in (b) represent LUE_{inst} ($GPP_{inst}^{normalized} / APAR_{inst}^{normalized}$) at different times of the day and LUE_{daily}.

five sites were close to that of simulated GPP. For 10:00 14:00 when the fitted γ_{GPP} was higher than the analytical γ_{APAR}, the regression slopes for simulated GPP were also higher than those of simulated SIF. Unlike GPP, which has a light saturation period that makes the fitted γ_{GPP} deviate from the γ_{APAR} during the midday, SIF did not show much light saturation and directly followed the γ_{APAR} latitudinal pattern.

We further compared the relationship between the simulated instantaneous SIF and the daily total GPP at the seasonal scale for these five sites (Figure 3.5). The linear relationships between GPP and SIF were usually stronger at midday for low to mid- latitude sites, i.e., CG-Tch, US-Var, DK-Eng. But this advantage was not evident for higher latitude sites (DK-ZaH). The daily total SIF and daily total GPP

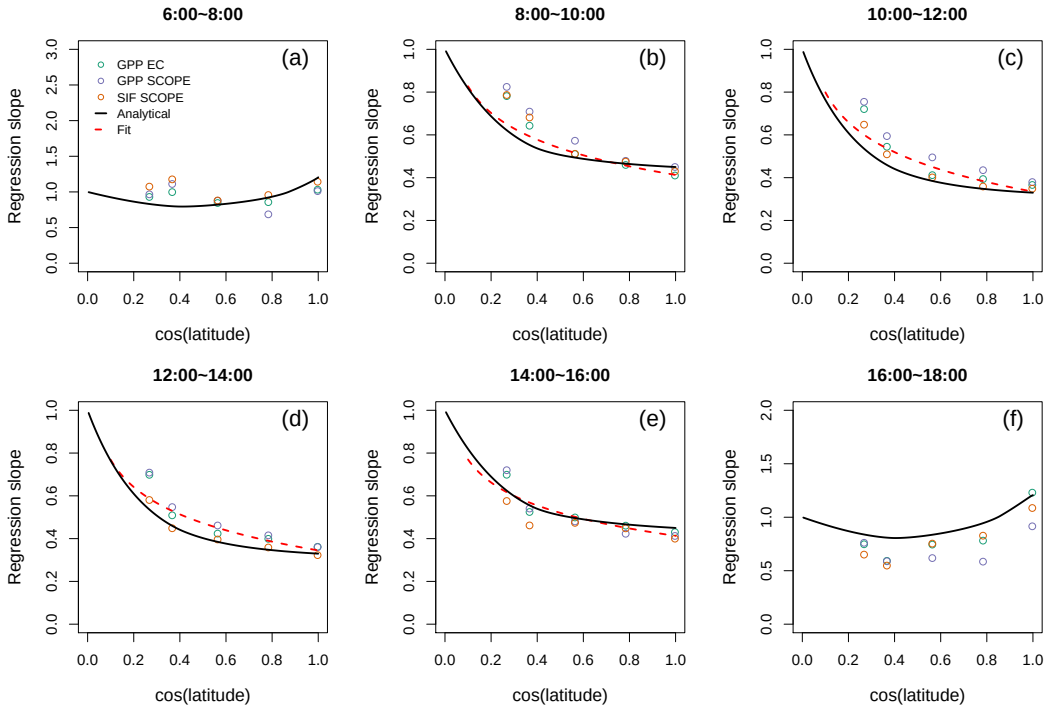


Figure 3.7: Latitudinal pattern of regression slopes between daily and instantaneous SCOPE simulated GPP, SIF, and GPP derived from EC tower (open circles). Only one year of data is used (Figure 3.A.3). The red dashed line is from the fitted relationship between daily and instantaneous GPP from EC towers as shown in Figure 3.4. The black lines represent the γ_{APAR} from the analytical estimation.

had the highest correlation. For C3 sites (except CG-Tch), the regression slopes for SIF and GPP exhibited a smaller variation for early morning and late afternoon (CV = 0.18 and 0.12 for 6:00 8:00 and 16:00 18:00, respectively). While during midday, the variation was larger (CV = 0.31 and 0.27 for 10:00 12:00 and 12:00 14:00, respectively). When comparing SIF_{daily} with GPP_{daily}, the regression slopes for all C3 vegetation sites tended to converge to a constant value (0.066, CV = 0.10).

3.3.4 GPP-SIF comparison at global scale

Figure 3.9 shows the comparison between SIF_{inst} from GOME-2 and OCO-2 and SIF_{daily} from analytical approximation with GPP from FluxCom. The SIF_{daily} showed a slightly higher linear correlation (R^2=0.94±0.08 for GOME-2 and R^2=0.94±0.11 for OCO-2) with GPP than SIF_{inst} (R^2=0.92±0.11 for GOME-2 and R^2=0.88±0.17 for OCO-2). Except savannas in the southern hemisphere for GOME-2 (0.963 vs. 0.961) and evergreen needleleaf forest in the northern hemisphere for OCO-2 (0.986 vs. 0.983), all other biome types' coefficient of determination are higher for SIF_{daily} than SIF_{inst}. In addition, the regression slopes among all the biome types for both hemispheres had smaller variation for SIF_{daily} than SIF_{inst}. The use of SIF_{daily} rather than SIF_{inst} showed better improvement of the GPP-SIF relationship for OCO-2 than for GOME-2.

3.4 Discussion

3.4.1 The relationship between daily GPP and instantaneous SIF across space and time

The spatial and seasonal relationship between GPP_{daily} and satellite observed SIF_{inst} is complicated because both SIF and GPP are driven by solar radiation and have di-

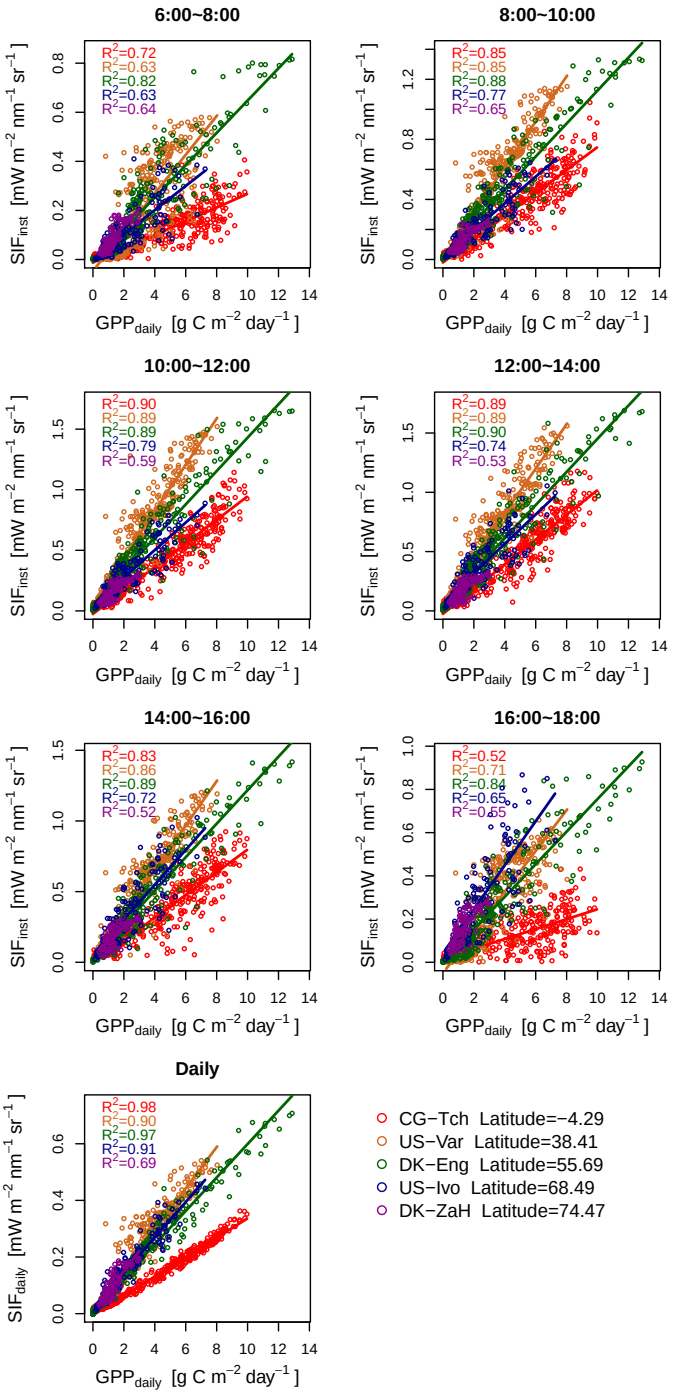


Figure 3.8: Scatter diagrams showing the relationship between the instantaneous (upper panels) and daily (bottommost panel) SIF with daily GPP as computed with the SCOPE model for the five sites (color coded) as indicated in the legend. The solid lines with different colors represent the linear regression between SIF and GPP.

urnal and seasonal cycles. In this study, using data from multiple flux tower sites, which cover a large spatial extent, we investigated the key issues for estimating spatial and seasonal GPP dynamics using satellite-retrieved SIF signals.

To link GPP_{daily} with SIF_{inst}, we use:

$$LUE_{inst} = \frac{GPP_{inst}}{fPAR \times PAR_{inst}} \tag{3.8}$$

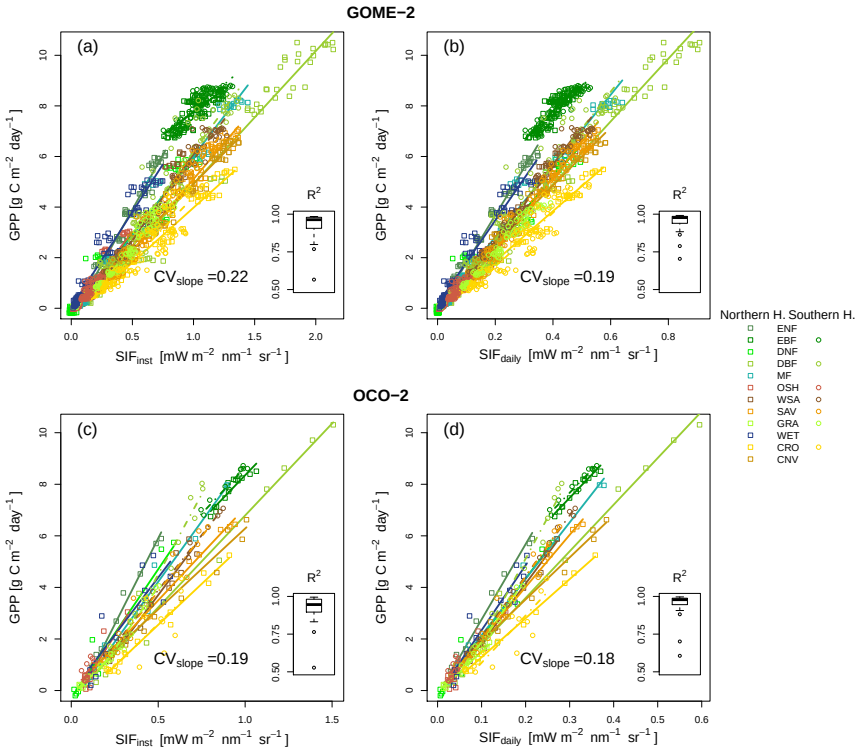


Figure 3.9: Comparison between SIF_{inst} and SIF_{daily} from GOME-2 (a, b) and OCO-2 (c,d) with GPP from FluxCom. Only the biome types with more than 100 gridcells were analyzed. Each point represents the average of SIF or GPP for all the gridcells within this biome type for each month for northern or southern hemisphere. For GOME-2, altogether 84 months are used; for OCO-2, 12 months are used (see methods). The solid lines represent the linear regression for northern hemisphere and the dashed lines represent that for southern hemisphere. The insets show the boxplot of the coefficients for all the regressions. For the full names of the biome type, please refer to the Appendix Table 3.A.1

In our study, we have demonstrated that the γ_{APAR} is related to the latitude, which is controlled by the seasonal change of day length. As the latitude increases from tropical to polar regions, the day length during the growing season also increases. The instantaneous PAR observation will be close to the average daily PAR during the polar daytime (during the peak growing season in summer), but will be much larger when sun only illuminates for half of the day. We also demonstrated that the variation of γ_{LUE} is related to the observation time mostly caused by the light saturation of photosynthesis. The combination of $\gamma_{APAR} \times \gamma_{LUE}$ can explain the latitudinal and diurnal pattern of the GPP_{daily}-GPP_{inst} relationship. For a specific satellite, we do not need to take γ_{LUE} into consideration as the observation time is often stable (except for the Polar Regions where multiple observations may be obtained within one day), but the latitudinal pattern of γ_{APAR} still needs to be considered. However, when comparing GPP with SIF data from different satellites, the observation time will affect the γ_{LUE} and needs to be taken into account. This means that the GPP-SIF relationship derived from one satellite cannot be directly applied to another if the overpass times of the satellites are different.

Simulations using the SCOPE model suggest that γ_{SIF} tends to follow γ_{APAR} during midday (Figure 3.7). This is consistent with the relatively stable fluorescence yield (ϕ_f) under high light intensity found in previous studies (Lee et al., 2015; van der Tol et al., 2014). But a larger variation of ϕ_f may occur during the shift from low to high irradiance, i.e., when the non-photochemical quenching begins to take effect and the negative correlation between ϕ_f and ϕ_p shifts to positive (Porcar-Castell et al., 2014). The relatively stable ϕ_f under high light intensity can also explain the higher GPP-SIF correlation during midday (10:00 14:00) than early morning or late afternoon for low latitude sites (Figure 3.8). However, this advantage is not evident for higher latitude sites, where the growing season in sum-

mer is characterized by a very long daytime length and the PAR is already/still high at 6:00 8:00 and 16:00 18:00. The regression slopes between GPP_{daily} and SIF_{inst} also had relatively larger variations for midday than early morning or late afternoon, which may be related to the light saturation: lower latitude sites are more likely to be light-saturated during the midday than higher latitude sites. It should also be noted that current version of the SCOPE model did not consider the relationship between nitrogen content (or chlorophyll a+b) and maximum carboxylation rate (V_{cmax}) (Ollinger et al., 2008; van der Tol et al., 2009), therefore the GPP-SIF relationship may be better evaluated with a variable V_{cmax} value.

The relationships between LUE_{inst} and fluorescence efficiency (FE_{inst}, includes the information of both ϕ_f and the escape coefficient) are still unclear at the seasonal and spatial scale (Porcar-Castell et al., 2014). Recent modeling studies suggested a nonlinear SIF GPP relationship at half-hour scale and a strong linear relationship at daily and 16-day scale (Damm et al., 2015b; Zhang et al., 2016b). Our comparison between the GOME-2 SIF and FluxCom GPP also showed higher correlation when using the SIF_{daily} value. The variations of the regression slopes across biome types may be related to the C3-C4 species composition (Guan et al., 2016; Liu et al., 2017a), average cloud cover during the growing season which affects the direct/diffuse radiation (Gu et al., 2002), canopy characteristics which affect the energy partitioning in different layers and SIF re-absorption, and environmental limitation of photosynthesis (temperature, water, etc.). These factors together with the latitudinal pattern need to be taken into account when interpreting the relationship between the satellite-based SIF_{inst} and GPP_{daily} at spatial and seasonal scales. In addition, since the midday SIF signal is stronger and the FE_{inst} is more stable and close to the daily average, satellites SIF_{inst} observations with a midday overpass time may have a more linear relationship with GPP_{daily} than those with a morning

or afternoon overpass (Figure 3.10).

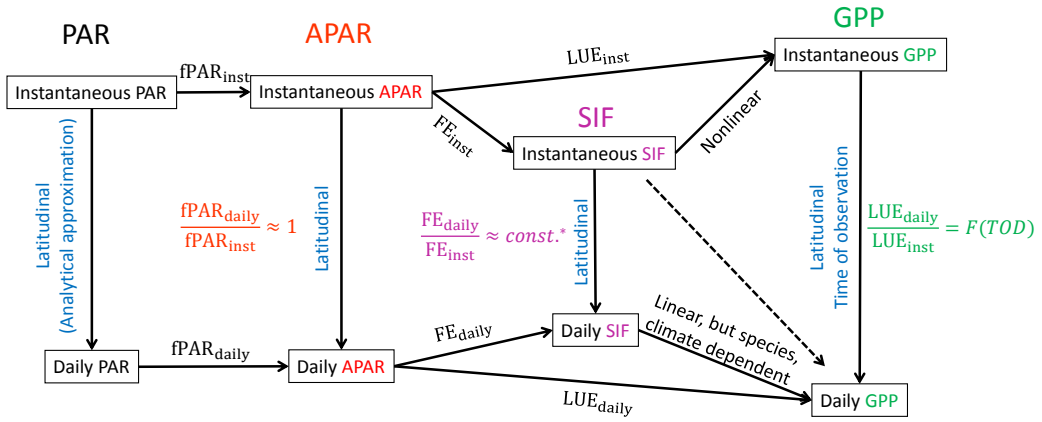


Figure 3.10: Schematic diagram showing the relationships between PAR, APAR, SIF and GPP at sub-daily and daily scales. The FE_{daily} and FE_{inst} relationship is close to a constant only under high light intensity, e.g., mid-noon. Abbreviations: PAR: photosynthetically active radiation; APAR: absorbed photosynthetically active radiation; fPAR: fraction of absorbed photosynthetically active radiation; FE: fluorescence efficiency; SIF: solar-induced chlorophyll fluorescence; LUE: light use efficiency; GPP: gross primary production; TOD: time of day.

3.4.2 Potential uncertainty for phenological analysis using GOME-2 SIF

As SIF is a measure of energy and has strong diurnal dynamics, the interpretation of SIF signals at seasonal scale should also be taken with caution. This is directly related to phenology studies, which used SIF as an indicator of vegetation activity (Jeong et al., 2017; Joiner et al., 2014; Walther et al., 2016). Previous phenology studies either used leaf/canopy development or seasonal change of plant physiological properties (e.g., GPP, APAR) (Migliavacca et al., 2015; Piao et al., 2006; Wu & Chen, 2013; Zhou et al., 2016). The leaf/canopy development measurement can either come from in situ observations (Fu et al., 2015) or satellite-based VIs (Zhang

et al., 2003). For the satellite-based VI studies, the start of the growing season is usually determined by detecting the maximum change of rate of VI (second order derivative equals to zero) (Wang et al., 2015; Wu & Liu, 2013; Zhang et al., 2013a), or using a threshold (Cong et al., 2013; Zhang et al., 2016c). Since VIs have little diurnal variation, the VIs obtained from different overpass times on a seasonal course can be regarded as the seasonal vegetation growth. In contrast, SIF is a measurement of the energy, and its seasonal variation is controlled by both the seasonal variation of incoming solar radiation, the leaf phenology (fraction of energy being absorbed) and the photosynthetic physiology (fraction of light being emitted as SIF). The contribution from solar radiation is higher at high latitude since PAR at a specific time of day also has large seasonal variations. Therefore, phenology derived from satellite-based SIF measurements cannot be directly compared with phenology derived from VI measurements.

Another question is whether SIF-based phenology can be comparable with GPP or net ecosystem exchange (NEE) based phenology (physiological phenology)? As concluded above, daily SIF has a strong linear relationship with daily GPP within each specific site and should have an advantage over VI at high latitude evergreen ecosystems. When doing phenology analysis, each pixel is analyzed in the temporal domain therefore the latitudinal pattern of instantaneous to daily conversion can be ignored. Then the question becomes whether the conversion from the SIF_{inst} to SIF_{daily} is stable across seasons? Figure 3.11(a) shows that the correction factor for GOME-2 and OCO-2 overpass time is not stable even during the growing season for the site US-Ivo. This correction factor has larger variations at higher latitudes, and differs for different satellite overpass times, which may explain the different phenology retrievals of using GOME-2 SIF and GOSAT SIF for boreal forest (Jeong et al., 2017). To reconcile the discrepancy between SIF and VI observations (Walther et al.,

2016), we can either calculate the SIF normalized by the incoming solar radiation at the satellite overpass, represented by the cosine of the solar zenith angle (cos(SZA)). SIF/cos(SZA) will be a measure of fPAR$\times FE_{inst}$ and can be used for leaf/greenness based phenology estimation. Alternatively, we can convert the satellite measured

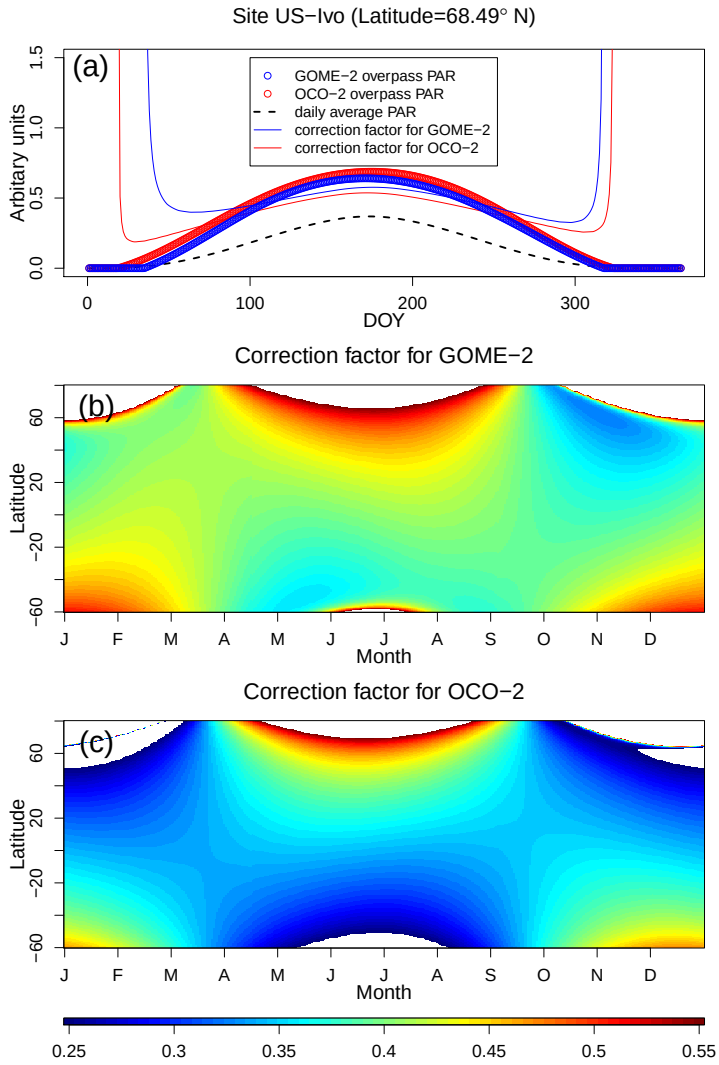


Figure 3.11: (a) Relationship between instantaneous PAR at GOME-2 and OCO-2 satellite overpass and the daily average PAR for site US-Ivo (latitude=68.49°N). Correction factor for (b) GOME-2 and (c) OCO-2 at different latitude throughout the year. These correction factors were calculated only considering the PAR_{inst}-PAR_{daily} relationship.

SIF_{inst} to SIF_{daily} using Eq. 3.7, which will be closely linked to the daily GPP. This will give another robust estimation of the photosynthetically active period that can be compared with site level gas exchange data. However, it should be noted that many studies show that fPAR also has a diurnal variation which is related to the SZA, diffused radiation, and LAI (Chen, 1996; Nouvellon et al., 2000), this may affect the SIF_{inst} to SIF_{daily} conversion using this SZA approximation method.

3.5 Conclusions

As satellite observations are often snapshots of the vegetation activity, the usage of satellite observations to infer vegetation activity at seasonal and spatial scales needs to be treated with caution, especially for energy-based measurements such as SIF that exhibit a large diurnal variation. Analyzing data from 135 flux tower sites, we found that both spatial and diurnal patterns exist between daily and instantaneous (bi-hourly) GPP. The latitudinal pattern is caused by the variation of PAR and the diurnal pattern is caused by the diurnal variation of LUE.

SIF has shown high potential to predict GPP across broad spatial and seasonal scales. However, the satellite instantaneous SIF retrieval and daily GPP relationships on spatial and seasonal courses are still affected by several factors such as C3/C4 composition, environmental stress. Using the SCOPE model simulation and the comparison between GOME-2 SIF and FluxCom GPP, we have shown that the relationship between daily average SIF and daily total GPP are more consistent across latitudinal gradients and biome types than those between instantaneous SIF and daily GPP, and the correction factor from instantaneous to daily SIF improved the linear relationship between satellite-based SIF retrievals and daily GPP. This factor should also be applied when using SIF to derive the physiological phenology. Since

this correction factor is based on the analytical approximation of solar zenith angle and does not consider the diurnal variation of other environmental factors (e.g., temperature, water stress), more in situ measurements of SIF are needed at sub-daily time scale for different ecosystems to better interpret the GPP-SIF relationship globally. The NASA Tropospheric Emissions: Monitoring of Pollution (TEMPO), Geostationary Carbon Cycle Observatory (GeoCARB), as well as European Sentinel 4 missions will also provide further valuable insights about the diurnal SIF variation at a regional and larger scales.

3.A Appendix

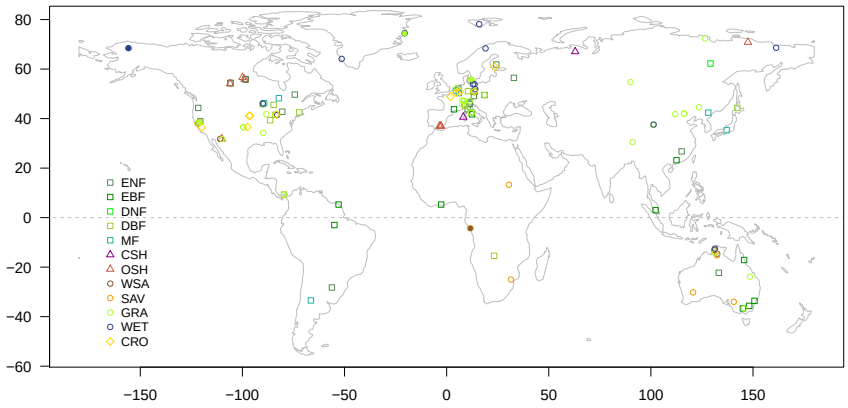


Figure 3.A.1: The spatial distribution of the 136 flux tower sites used in this study. The filled symbols indicate the five sites used for the SCOPE simulation.

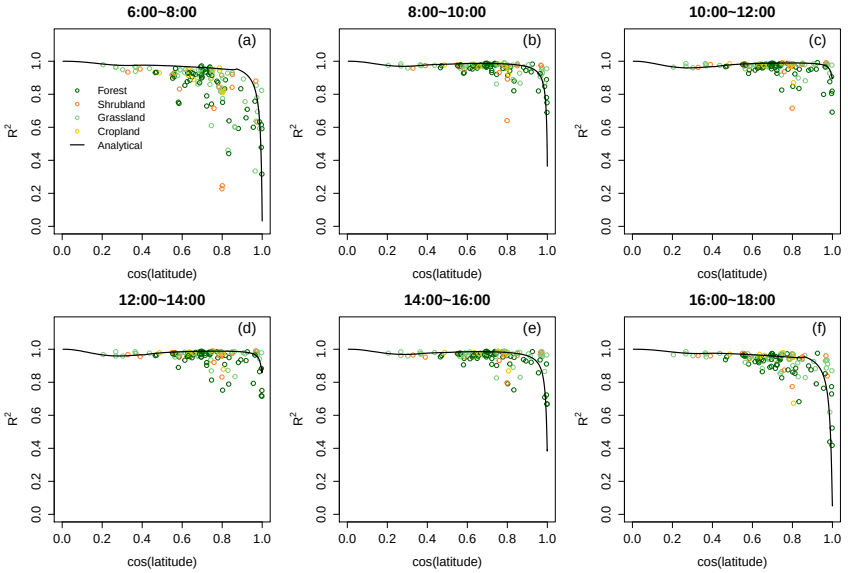


Figure 3.A.2: The coefficient of determination (R^2) for the correlation between instantaneous and daily GPP estimates from flux tower. The black line represents the predicted R^2 using the incoming solar radiation calculated from the analytical method.

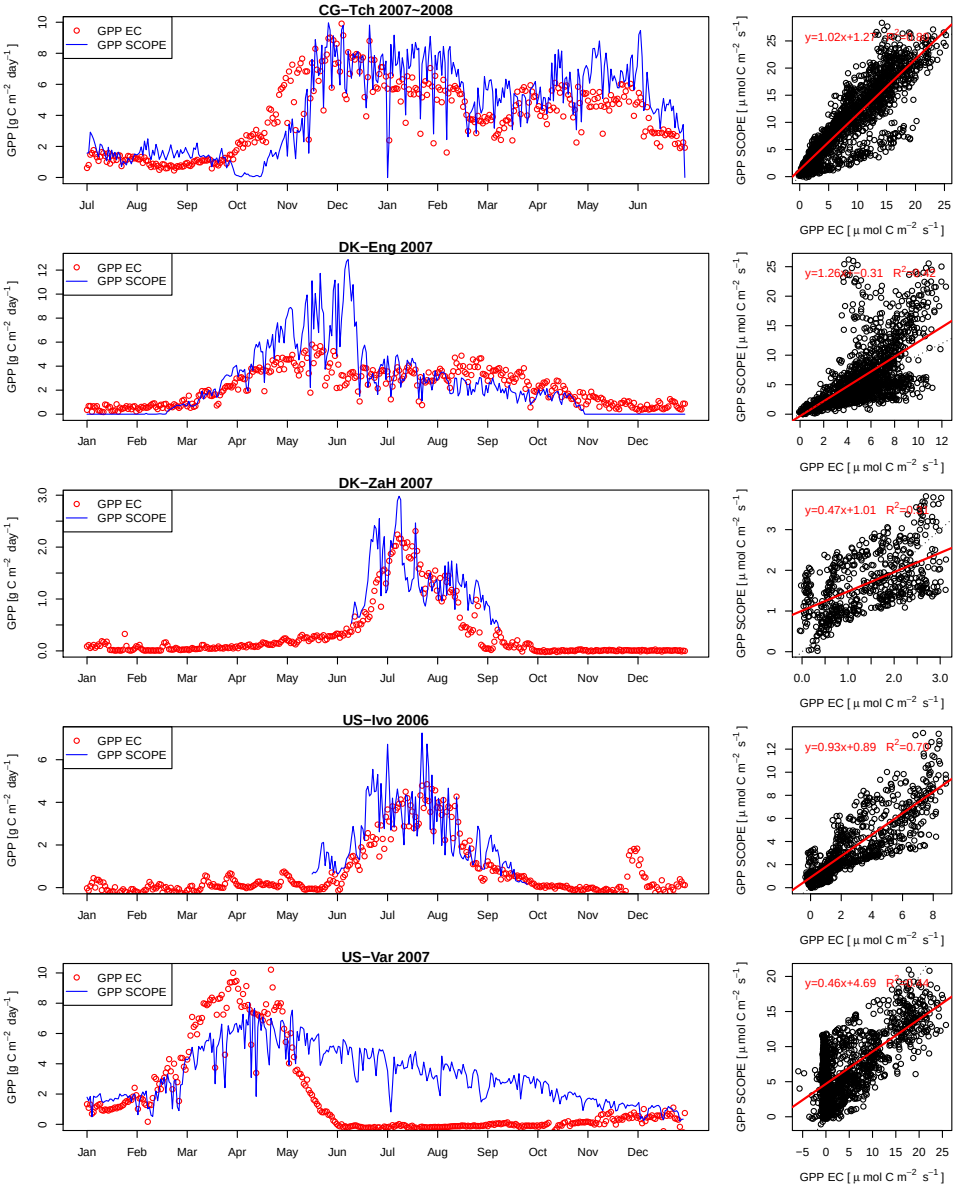


Figure 3.A.3: Comparison between the SCOPE simulated GPP and eddy covariance flux tower derived GPP. The left column shows the seasonal variations in the daily aggregated GPP value. The right column compares the raw GPP data at half-hour scale from EC and SCOPE. The big difference between GPP EC and GPP SCOPE for US-Var is caused by pixel mixture: within the MODIS LAI footprint (5 km), a lot of evergreen trees contributed to the satellite signal while the EC tower only measures the GPP of the temporary grassland.

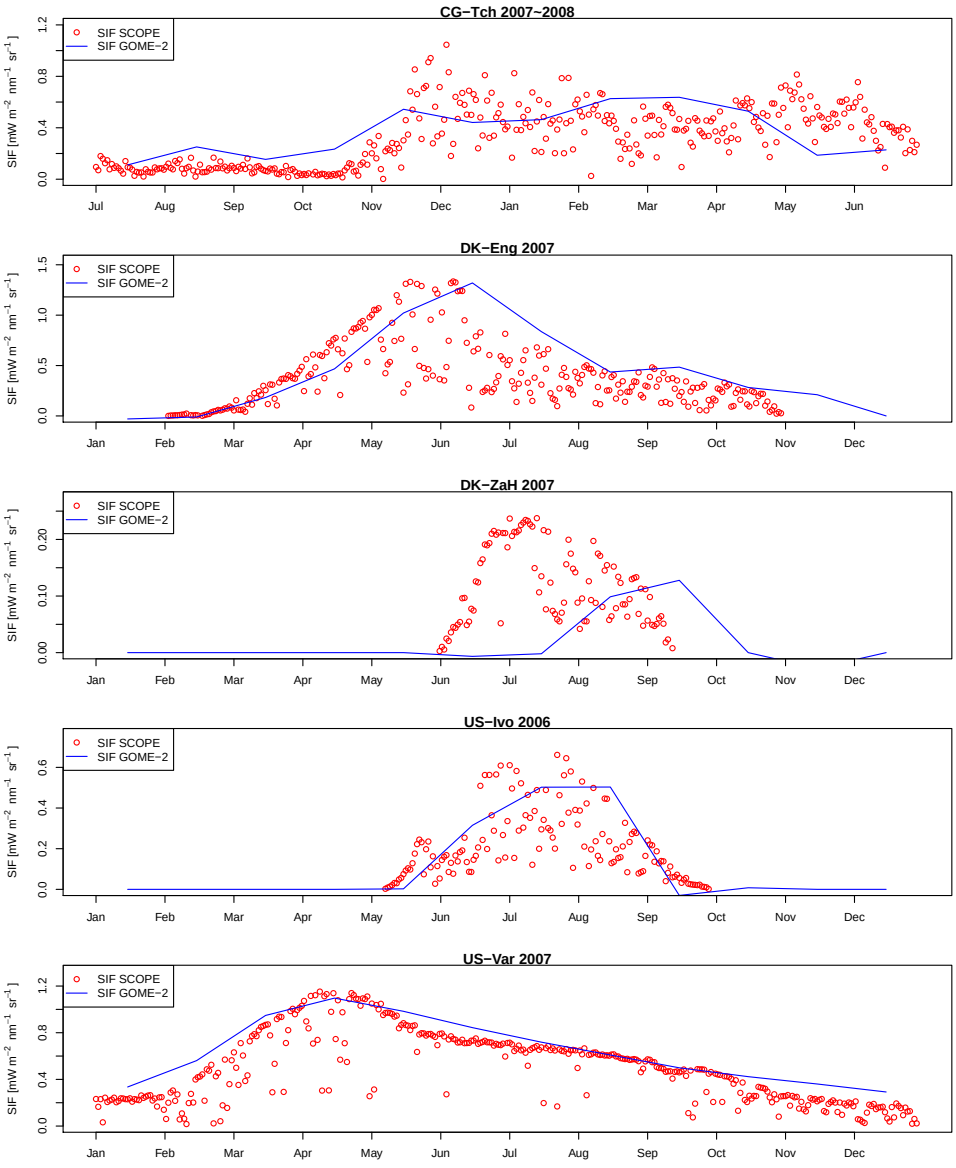


Figure 3.A.4: Comparison between the SIF simulated from the SCOPE model and from the GOME-2 satellite. SCOPE SIF simulation at 9:30 am solar time is used to compare with GOME-2 v26 SIF monthly data. The GOME-2 data are averaged over the period 2007-2015 to reduce uncertainty. The large discrepancy for DK-ZaH site is caused by the relative location of the EC flux tower footprint within the satellite gridcell: most of the area in this gridcell is either all-year snow covered mountain peaks or ocean. For other sites, the model simulation and satellite observation are similar.

Table 3.A.1: Flux tower sites used in this study. IGBP class represents the International Geosphere-Biosphere Programme land cover classification.

Site ID	Site name	Latitude	Longitude	IGBP type[1]	Reference
AR-SLu	San Luis	-33.4648	-66.4598	MF	-
AR-Vir	Virasoro	-28.2395	-56.1886	ENF	-
AT-Neu	Neustift/Stubai Valley	47.1167	11.3175	GRA	(Wohlfahrt et al., 2008)
AU-Ade	Adelaide River	-13.0769	131.1178	WSA	-
AU-ASM	Alice Springs	-22.283	133.249	ENF	-
AU-Cpr	Calperum	-34.0021	140.5891	SAV	-
AU-Cum	Cumberland Plains	-33.6133	150.7225	EBF	-
AU-DaP	Daly River Savanna	-14.0633	131.3181	GRA	-
AU-DaS	Daly River Cleared	-14.1593	131.3881	SAV	-
AU-Dry	Dry River	-15.2588	132.3706	SAV	-
AU-Emr	Emerald, Queensland, Australia	-23.8587	148.4746	GRA	-
AU-Fog	Fogg Dam	-12.5452	131.3072	WET	(Guerschman et al., 2009)
AU-GWW	Great Western Woodlands, Western Australia	-30.1913	120.6541	SAV	-
AU-RDF	Red Dirt Melon Farm, Northern Territory	-14.5636	132.4776	WSA	-
AU-Rig	Riggs Creek	-36.6499	145.5759	GRA	-
AU-Rob	Robson Creek, Queensland, Australia	-17.1175	145.6301	EBF	-
AU-Tum	Tumbarumba	-35.6566	148.1517	EBF	(Leuning et al., 2005)
AU-Whr	Whroo	-36.6732	145.0294	EBF	-
BE-Bra	Brasschaat (De Inslag Forest)	51.3092	4.5206	MF	(Janssens et al., 2001)
BE-Lon	Lonzee	50.5516	4.7461	CRO	(Moureaux et al., 2006)
BE-Vie	Vielsalm	50.3051	5.9981	MF	(Aubinet et al., 2001)
BR-Sa3	Santarem-Km83-Logged Forest	-3.018	-54.9714	EBF	(Steininger, 2004)
CA-Gro	Ontario - Groundhog River, Boreal Mixedwood Forest	48.2167	-82.1556	MF	(McCaughey et al., 2006)
CA-NS1	UCI-1850 burn site	55.8792	-98.4839	ENF	(Goulden et al., 2006)
CA-NS3	UCI-1964 burn site	55.9117	-98.3822	ENF	(Goulden et al., 2006)
CA-NS4	UCI-1964 burn site wet	55.9117	-98.3822	ENF	(Bond-Lamberty et al., 2004)
CA-NS5	UCI-1981 burn site	55.8631	-98.485	ENF	(Wang et al., 2002)
CA-NS6	UCI-1989 burn site	55.9167	-98.9644	OSH	(Bond-Lamberty et al., 2004)
CA-NS7	UCI-1998 burn site	56.6358	-99.9483	OSH	(Bond-Lamberty et al., 2004)
CA-Qfo	Quebec - Eastern Boreal, Mature Black Spruce	49.6925	-74.3421	ENF	(Bergeron et al., 2007)
CA-SF1	Saskatchewan-Western Boreal, forest burned in 1977	54.4850	-105.8180	ENF	(Amiro et al., 2006)
CA-SF2	Saskatchewan-Western Boreal, forest burned in 1989	54.2539	-105.8780	ENF	(Amiro et al., 2003)
CA-SF3	Saskatchewan-Western Boreal, forest burned in 1998	54.0916	-106.005	OSH	(Amiro et al., 2006)
CA-TP2	Ontario-Turkey Point 1989 Plantation White Pine	42.7744	-80.4588	ENF	(Arain & Restrepo-Coupe, 2005)
CG-Tch	Tchizalamou	-4.2892	11.6564	SAV	-

[1]ENF: evergreen needleleaf forest; EBF: evergreen broadleaf forest; DNF: deciduous needleleaf forest; DBF: deciduous broadleaf forest; MF: mixed forest; CSH: closed shrubland; OSH: open shrubland; WSA: woody savannas; GRA: grassland; SAV: savannas; WET: permanent wetland; CRO: cropland; CNV: cropland/natural vegetation mosaic.

CH-Cha	Chamau grassland	47.2102	8.4104	GRA	(Merbold et al., 2014)
CH-Fru	Fruebuel grassland	47.1158	8.5378	GRA	(Fritsche et al., 2008)
CH-Oe1	Oensingen1 grass	47.2858	7.7319	GRA	(Ammann et al., 2009)
CN-Cha	Changbaishan	42.4025	128.0958	MF	(Zhang et al., 2010)
CN-Cng	Changling	44.5934	123.5092	GRA	-
CN-Dan	Dangxiong	30.4978	91.0664	GRA	-
CN-Din	Dinghushan	23.1733	112.5361	EBF	(Zhang et al., 2010)
CN-Du2	Duolun_grassland (D01)	42.0467	116.2836	GRA	(Sun et al., 2011)
CN-Du3	Duolun Degraded Meadow	42.0551	116.2809	GRA	(Sun et al., 2011)
CN-Ha2	Haibei Shrubland	37.6086	101.3269	WET	-
CN-HaM	Haibei Alpine Tibet site	37.6167	101.3000	GRA	(Kato et al., 2006)
CN-Qia	Qianyanzhou	26.7414	115.0581	ENF	(Zhang et al., 2010)
CN-Sw2	Siziwang Grazed (SZWG)	41.7902	111.8971	GRA	(Shao et al., 2013)
CZ-BK1	Bily Kriz- Beskidy Mountains	49.5047	18.5411	ENF	(Marek et al., 2011)
CZ-BK2	Bily Kriz- grassland	49.4944	18.5429	GRA	(Marek et al., 2011)
DE-Akm	Anklam	53.8662	13.6834	WET	-
DE-Gri	Grillenburg- grass station	50.9495	13.5125	GRA	(Hussain et al., 2011)
DE-Hai	Hainich	51.0792	10.453	DBF	(Anthoni et al., 2004)
DE-Kli	Klingenberg - cropland	50.8929	13.5225	CRO	(Prescher et al., 2010)
DE-Lkb	Lackenberg	49.0996	13.3047	ENF	(Lindauer et al., 2014)
DE-Obe	Oberbarenburg	50.7836	13.7196	ENF	-
DE-RuS	Selhausen Juelich	50.8657	6.4472	CRO	(Eder et al., 2015)
DE-Spw	Spreewald	51.8923	14.0337	WET	-
DE-Tha	Anchor Station Tharandt - old spruce	50.9636	13.5669	ENF	(Grunwald & Bernhofer, 2007)
DE-Zrk	Zarnekow	53.8759	12.8890	WET	(Hahn-Schofl et al., 2011)
DK-Eng	Enghave	55.6905	12.1918	GRA	-
DK-NuF	Nuuk Fen	64.1308	-51.3861	WET	(Westergaard-Nielsen et al., 2013)
DK-Sor	Soroe- LilleBogeskov	55.4859	11.6446	DBF	(Pilegaard et al., 2001)
DK-ZaF	Zackenberg Fen	74.4791	-20.5557	WET	-
DK-ZaH	Zackenberg Heath	74.4732	-20.5503	GRA	(Lund et al., 2012)
ES-Amo	Amoladeras	36.8336	-2.2523	OSH	-
ES-LgS	Laguna Seca	37.0979	-2.9658	OSH	(Reverter et al., 2010)
ES-LJu	Llano de los Juanes	36.9266	-2.7521	OSH	(Serrano-Ortiz et al., 2007)
FI-Hyy	Hyytiala	61.8475	24.2950	ENF	((Suni et al., 2003)
FI-Jok	Jokionen agricultural field	60.8986	23.5135	CRO	(Lohila et al., 2004)
FR-Gri	Grignon (after 6/5/2005)	48.8442	1.9519	CRO	(Loubet et al., 2011)
FR-Pue	Puechabon	43.7414	3.5958	EBF	(Lhomme et al., 2001)
GF-Guy	Guyaflux	5.2788	-52.9249	EBF	(Epron et al., 2006)
GH-Ank	Ankasa	5.2685	-2.6942	EBF	-
IT-CA1	Castel d'Asso1	42.3804	12.0266	DBF	(Sabbatini et al., 2016)
IT-CA2	Castel d'Asso2	42.3772	12.0260	GRA	(Sabbatini et al., 2016)
IT-CA3	Castel d'Asso 3	42.3800	12.0222	DBF	(Sabbatini et al., 2016)
IT-Cp2	Castelporziano2	41.7043	12.3573	EBF	-
IT-Isp	Ispra ABC-IS	45.8126	8.6336	DBF	(Ferrea et al., 2012)
IT-La2	Lavarone2	45.9542	11.2853	ENF	-
IT-Lav	Lavarone (after 3/2002)	45.9562	11.2813	ENF	(Fiora & Cescatti, 2006)
IT-Noe	Sardinia/Arca di NoÃÍ	40.6061	8.1515	CSH	(Beier et al., 2009)
IT-PT1	Zerbolo-Parco Ticino- Canarazzo	45.2009	9.0610	DBF	(Migliavacca et al., 2009)
IT-Ren	Renon/Ritten (Bolzano)	46.5869	11.4337	ENF	(Marcolla et al., 2005)
IT-Ro1	Roccarespampani 1	42.4081	11.9300	DBF	(Rey et al., 2002)
IT-Ro2	Roccarespampani 2	42.3903	11.9209	DBF	(Tedeschi et al., 2006)
IT-SRo	San Rossore	43.7279	10.2844	ENF	(Chiesi et al., 2005)
IT-Tor	Torgnon	45.8444	7.5781	GRA	(Galvagno et al., 2013)
JP-MBF	Moshiri Birch Forest Site	44.3869	142.3186	DBF	-
JP-SMF	Seto Mixed Forest Site	35.2617	137.0788	MF	-
MY-PSO	Pasoh Forest Reserve (PSO)	2.973	102.3062	EBF	-
NL-Hor	Horstermeer	52.2404	5.0713	GRA	-
NL-Loo	Loobos	52.1666	5.7436	ENF	(Dolman et al., 2002)

NO-Adv	Adventdalen	78.186	15.923	WET	-
PA-SPn	Sardinilla Plantation	9.3181	-79.6346	DBF	(Wolf et al., 2011)
PA-SPs	Sardinilla Pasture	9.3138	-79.6314	GRA	(Wolf et al., 2011)
RU-Che	Cherskii	68.613	161.3414	WET	(Corradi et al., 2005)
RU-Cok	Chokurdakh	70.8291	147.4943	OSH	(van Huissteden et al., 2005)
RU-Fyo	Fyodorovskoye wet spruce stand	56.4615	32.9221	ENF	(Kurbatova et al., 2008)
RU-Ha1	Ubs Nur-Hakasija-grassland	54.7252	90.0022	GRA	-
RU-Sam	Samoylov Island-Lena Delta	72.3738	126.4958	GRA	(Kutzbach et al., 2007)
RU-SkP	Spasskaya Pad larch	62.255	129.168	DNF	-
RU-Vrk	Seida/Vorkuta	67.0547	62.9405	CSH	-
SD-Dem	Demokeya	13.2829	30.4783	SAV	(Ardö et al., 2008)
SE-St1	Stordalen Forest-Mountain Birch	68.3542	19.0503	WET	-
US-AR1	ARM USDA UNL OSU Woodward Switchgrass 1	36.4267	-99.42	GRA	-
US-AR2	ARM USDA UNL OSU Woodward Switchgrass 2	36.6358	-99.5975	GRA	-
US-ARM	ARM Southern Great Plains site- Lamont	36.6058	-97.4888	CRO	(Fischer et al., 2007a)
US-Blo	Blodgett Forest	38.8953	-120.633	ENF	(Misson et al., 2005)
US-CRT	Curtice Walter-Berger cropland	41.6285	-83.3471	(Chu et al., 2014)	
US-Goo	Goodwin Creek	34.2547	-89.8735	GRA	-
US-Ha1	Harvard Forest EMS Tower (HFR1)	42.5378	-72.1715	DBF	(Goulden et al., 1996)
US-IB2	Fermi National Accelerator Laboratory- Batavia (Prairie site)	41.8406	-88.241	GRA	(Matamala et al., 2008)
US-Ivo	Ivotuk	68.4865	-155.75	WET	(Epstein et al., 2004)
US-Lin	Lindcove Orange Orchard	36.3566	-119.842	CRO	-
US-Los	Lost Creek	46.0827	-89.9792	WET	(Sulman et al., 2009)
US-Me6	Metolius Young Pine Burn	44.3233	-121.608	ENF	(Ruehr et al., 2012)
US-MMS	Morgan Monroe State Forest	39.3232	-86.4131	DBF	(Schmid et al., 2000)
US-Myb	Mayberry Wetland	38.0498	-121.765	WET	-
US-Ne1	Mead-irrigated continuous maize site	41.1651	-96.4766	CRO	(Suyker et al., 2005)
US-Ne2	Mead - irrigated maize -soybean rotation site	41.1649	-96.4701	CRO	(Suyker et al., 2005)
US-Ne3	Mead - rainfed maize-soybean rotation site	41.1797	-96.4397	CRO	(Suyker et al., 2004)
US-Oho	Oak Openings	41.5545	-83.8438	DBF	(Noormets et al., 2008)
US-SRM	Santa Rita Mesquite	31.8214	-110.866	WSA	(Scott et al., 2009)
US-Syv	Sylvania Wilderness Area	46.242	-89.3477	MF	(Desai et al., 2005)
US-Ton	Tonzi Ranch	38.4316	-120.966	WSA	(Xu & Baldocchi, 2004)
US-Tw3	Twitchell Alfalfa	38.1159	-121.647	CRO	-
US-UMd	UMBS Disturbance	45.5625	-84.6975	DBF	(Nave et al., 2011)
US-Var	Vaira Ranch- Ione	38.4133	-120.951	GRA	(Ma et al., 2007)
US-WCr	Willow Creek	45.8059	-90.0799	DBF	(Cook et al., 2004)
US-Whs	Walnut Gulch Lucky Hills Shrub	31.7438	-110.052	OSH	(Scott et al., 2006)
US-Wkg	Walnut Gulch Kendall Grasslands	31.7365	-109.942	GRA	(Scott et al., 2010)
US-WPT	Winous Point North Marsh	41.4646	-82.9962	WET	(Chu et al., 2014)
ZA-Kru	Skukuza- Kruger National Park	-25.0197	31.4969	SAV	(Williams et al., 2009)
ZM-Mon	Mongu	-15.4378	23.2528	DBF	(Merbold et al., 2011)

Chapter 4: Spatio-temporal convergence of maximum daily light use efficiency based on radiation absorption by chlorophylls of the canopy

Abstract

Light use efficiency (LUE), which quantifies the efficiency of plants to utilize solar radiation for photosynthetic carbon fixation, has long been studied and used for estimation of gross primary production (GPP) from single sites to global scales. However, considerable uncertainties remain regarding how to parameterize these LUE-based photosynthesis models, as the maximum LUE (the LUE under optimum condition with little environmental stress) is often an empirical coefficient based on varying definitions of energy absorption. The energy can be absorbed by (1) the ecosystem, where all incident photosynthetically active radiation (PAR) is considered; (2) the canopy, where only PAR intercepted by the canopy is considered; or (3) the chlorophylls in the canopy, where only PAR absorbed by the total chlorophylls in all the leaves is considered. Here we use satellite-based solar-induced chlorophyll fluorescence (SIF) as a proxy for PAR absorbed by chlorophyll of the canopy ($APAR_{chl}$) and derive an estimation of the fraction of $APAR_{chl}$ ($fPAR_{chl}$) from four remote sensing based optical vegetation activity indicators (OVAIs). By comparing maximum LUE based on different radiation absorptions from 127 eddy flux sites (626 site-years), we found that the maximum daily LUE based on PAR absorption by chlorophyll of the canopy (LUE_{chl}), unlike other expressions of LUE, tends to converge to a common value independent of the biome types. The photosynthetic seasonality in tropical forests can also be tracked by the change of $fPAR_{chl}$, and the corresponding LUE_{chl} was also found to have less seasonal variation. This spatio-temporal convergence of LUE derived from $fPAR_{chl}$ can be used to build simple

but robust GPP models and to better constrain process-based models using satellite observations.

4.1 Introduction

Plants fix carbon through photosynthesis, sequestering carbon dioxide from the atmosphere and substantially mitigating the negative impact of anthropogenic emissions on climate. Ecological studies of photosynthesis often quantify carbon sinks at local, regional and global scales as ecosystem gross primary productivity (GPP), the quantity of carbon fixed prior to losses from respiration. Because of the driving role of photosynthesis in the global carbon cycle, accurate estimates of GPP are critical in carbon related research, e.g., global climate change, food production, and energy availability to consumers (Beer et al., 2010; Le Quéré et al., 2015). Many approaches are available to estimate GPP at different temporal and spatial scales, including in situ observations based on the eddy covariance technique (Baldocchi et al., 2001), chambers measurements of gas exchange (Field et al., 2000), and, at regional and global scales, earth observations and ecological models (Anav et al., 2015; Running et al., 2004).

The production efficiency model (PEM) or light use efficiency model offers a very simple and broadly applied conceptual framework to estimate GPP at different spatial scales (Monteith, 1972). This class of models calculates GPP using the product of the photosynthetically active radiation (PAR), the fraction of absorbed PAR, and a light use efficiency factor (LUE), which converts energy absorbed into the amount of carbon fixed:

$$GPP = PAR \times fPAR \times LUE \tag{4.1}$$

The LUE is often calculated as a function of the maximum daily light use efficiency (ε_{max}) regulated by environmental controls (temperature, soil water, vapor pressure deficit, etc.). The product of the first two terms on the right-hand side in Eq. 4.1 is absorbed PAR (APAR=PAR×fPAR), which can be expressed variously as incident PAR (fPAR = 1), PAR absorbed by the entire (non-photosynthetic and photosynthetic) canopy ($fPAR_{canopy}$) or by chlorophyll in all leaves of the canopy ($fPAR_{chl}$, photosynthetic-only) (Figure 4.1). Because of the different definitions of APAR (and fPAR), the LUE factor in Eq. 4.1, which corresponds to different maximum daily light use efficiency (ε_{max}) values, can differ substantially. In most studies, ε_{max} is an empirical parameter estimated from Eq. 4.1 that varies greatly because of the different LUE definitions (Song et al., 2013). Therefore, ε_{max} values cannot be used/compared when they were derived from different fPAR basis.

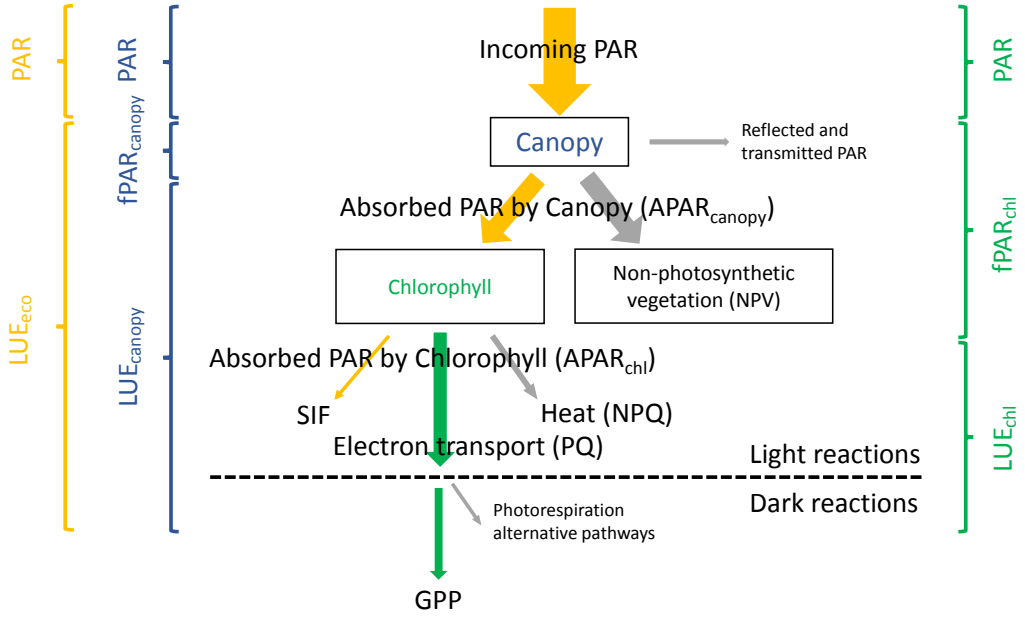


Figure 4.1: Idealized representation of the radiation partitioning in plant canopies for light use efficiency models. Left side is the LUE models based on the total PAR or PAR absorbed by canopy ($APAR_{canopy}$), right side is the LUE models based on PAR absorbed by chlorophyll of the entire canopy ($fPAR_{chl}$). This figure is modified from Figure 4.1 in Porcar-Castell et al. (2014).

Most PEMs employ the PAR absorbed by vegetation canopy ($APAR_{canopy}$) to estimate GPP (GPP=$LUE_{canopy} \times APAR_{canopy}$), e.g., the CASA model (Potter et al., 1993) and MODIS GPP (Running et al., 2004), where the fPAR is often calculated as a function of satellite-derived normalized difference vegetation indices (NDVI) or leaf area index (LAI). However, not all light absorbed by the canopy is used in the photosynthetic process (Figure 4.1). A substantial fraction of PAR will be absorbed by the non-photosynthetically vegetation (NPV, e.g. branch, stem, dry leaf, vein, etc.) and will be directly dissipated as heat (Xiao et al., 2004a). Importantly, the fraction of NPV is different for different biomes (Li et al., 2016), as a result, in those PEM models, ε_{max} may be biome-specific as $APAR_{canopy}$ is not corrected for the fraction of PAR absorbed by NPV (Choudhury, 2001; Gu et al., 2002; McCallum et al., 2009; Potter et al., 1993). However, the within-biome variation of NPV ratio is not considered in these models. In addition, the NPV composition not only varies across different biomes, but also with vegetation phenology and growth over seasons and years (Guerschman et al., 2009). Thus, there is a need to account for the temporal variability of biotic factors such as changes in the fraction of chlorophyll in the canopy/NPV with phenological cycles.

One fundamental theoretical assumption is that with more precise representation of fPAR absorbed by chlorophyll of the canopy, estimates of ecosystem GPP are significantly improved by reducing bias and variability associated with unaccounted differences among biomes or across time in the ratio of chlorophyll to NPV. If GPP is more tightly coupled with canopy chlorophyll absorption as hypothesized, ranges of ε_{max} variation across space and time will be smaller when estimated from the absorbed energy by chlorophyll, which is used to drive photosynthesis. Previous studies have shown that the LUE is more stable across the seasonal cycle in a cropland at using radiation absorption by chlorophyll than by leaf or canopy (Gitelson

& Gamon, 2015; Gitelson et al., 2006). However, these studies focused on a single vegetation type and used data from single site. Whether this phenomenon can be extrapolated to other biome types at seasonal scales, or across different biome types remains unclear.

Successful retrievals of solar-induced chlorophyll fluorescence (SIF) from satellites (Frankenberg et al., 2011; Joiner et al., 2013) provide a new probe of vegetation photosynthesis at regional to global scales (Porcar-Castell et al., 2014). SIF is a very small amount (1-2%) of energy reemitted during the light reactions of photosynthesis. Because SIF is only emitted from photosystems and can be interpreted as the photosynthetic electron transport rate (ETR) under unstressed condition (Guan et al., 2016; Liu et al., 2017a; Zhang et al., 2014b), it can be a good proxy of PAR absorbed by the chlorophyll ($APAR_{chl}$) that is more precisely focused on photosynthetic pigments than traditional measures of ecosystem or canopy APAR (Zhang et al., 2016e). However, current long-term SIF observations have relatively high uncertainties and low spatial resolution (Joiner et al., 2014) which makes them not suitable for direct comparisons with eddy covariance (EC) flux tower observations of LUE and GPP. Most PEMs still use satellite based optical vegetation activity indicators (OVAIs, we did not use the conventional vegetation index term because $fPAR_{mod15}$ is not a vegetation index) to serve as $fPAR_{canopy}$ or $fPAR_{chl}$, which allow GPP simulation at spatial resolutions similar to the footprint of EC flux tower sites.

In this study, we try to test our hypothesis whether the maximum daily light use efficiency based on radiation absorbed by chlorophyll of the canopy (ε^{chl}_{max}, corresponds to LUE_{chl}) are more stable across space and time. We divide this task into three steps:

(1) We would like to derive proxies of $fPAR_{chl}$ and $fPAR_{canopy}$ from OVAIs so

that they can be directly compared with GPP and PAR from flux tower. To do this, we explore the relationship between sun induced chlorophyll fluorescence (SIF) and OVAIs upscaled to SIF spatial resolution, and estimate $fPAR_{chl}$ from OVAIs (Figure 4.2). The OVAIs used in this study are satellite retrieved vegetation indicators such as normalized difference vegetation index (NDVI), enhanced vegetation index (EVI), and the fPAR product ($fPAR_{mod15}$) from the Moderate Resolution Imaging Spectroradiometer (MODIS) as well as the MERIS terrestrial chlorophyll index (MTCI) from the Medium Resolution Imaging Spectrometer (MERIS) (Dash & Curran, 2004). Through this comparison, we would like to a) identify which OVAI can serve as better proxies of $fPAR_{chl}$; b) test whether a linear relationship between OVAI and $fPAR_{chl}$ exist.

(2) After we obtain the proxies of $fPAR_{chl}$, $fPAR_{canopy}$, and GPP estimated from the FLUXNET dataset (Baldocchi et al., 2001), we then calculate ε_{max} values for different biome types based on different APAR definitions. A spatial convergence of ε_{max}^{chl} would be represented as a more stable value across different biome types over space.

(3) To test the temporal convergence, we obtained the photosynthetic capacity (PC) from two tropical forest sites where light use efficiency under a fixed environment can be derived for each month. In this way, we can compare the ecosystem LUE without considering the environmental limitations (Figure 4.2). A temporal convergence of ε_{max}^{chl} would be represented as $fPAR_{chl}$ fully tracked the biotic variation of ecosystem LUE.

4.2 Materials and Methods

4.2.1 Solar-induced chlorophyll fluorescence as a proxy of $APAR_{chl}$

The SIF product for the period from 2007 to 2015 is retrieved from the Global Ozone Monitoring Experiment 2 (GOME-2) instrument onboard the MetOp-A satellite (Joiner et al., 2013, 2016). GOME-2 SIF is retrieved at wavelengths around 740 nm, characterizing the photon trapping efficiency as mostly contributed by photosystem II (Lichtenthaler & Rinderle, 1988; Rossini et al., 2015). The GOME-2 V26 SIF product used in this study has a spatial resolution of 0.5°×0.5° and monthly temporal resolution. The uncertainty of this SIF product is 0.1–0.2 mW m^{-2} nm^{-1} sr^{-1}. SIF can be expressed using a similar form of LUE models (Guanter et al., 2014; Joiner et al., 2014):

$$SIF = PAR \times fPAR_{chl} \times FE \tag{4.2}$$

where FE is the fluorescence efficiency or quantum yield for fluorescence observed at top of canopy, which can be further decomposed into quantum yield for fluores-

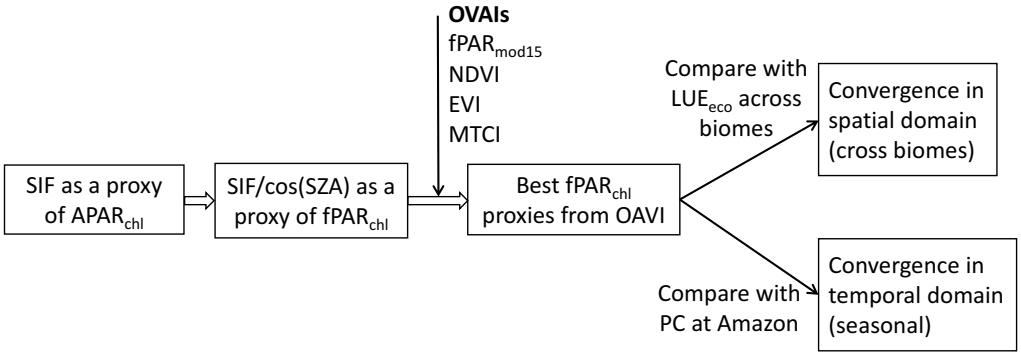


Figure 4.2: A flowchart showing the evaluation of spatio-temporal convergence of ε_{max} based on radiation absorption of chlorophyll of the canopy.

cence for individual leaf (ϕ_f), and the escaping factor (f_{esc}) that accounts for the absorption of fluorescence within the canopy by stem, branch, leaves or by the soil (Guanter et al., 2014). Because SIF retrieved from GOME-2 is a snapshot of vegetation activity in space and time, PAR in this equation is the instantaneous PAR (iPAR) during satellite overpass. Due to the different time of overpass and seasonal shift of the day length, we use the cosine of the sun zenith angle (SZA) to approximate the iPAR when the satellite observation is made (09:30 a.m. local time):

$$iPAR = \beta \times cos(SZA) \tag{4.3}$$

where β is the solar constant, representing sea-surface clear-sky solar radiation when the sun is at the zenith, i.e., cos(SZA) = 1, ignoring the atmospheric conditions. In fact, as solar radiation is affected by clouds and aerosols in the atmosphere during the satellite overpass, this approximation will cause an overestimation of iPAR when clouds and aerosols present. However, this effect is alleviated in our calculation as the SIF retrieval algorithm omits the retrievals that were significantly affected by clouds (Joiner et al., 2013). The uncertainty of this approximation is shown in Figure 4.A.3 and will be considered in further analysis. Thus, Eq. 4.2 can be written in a different form (Sun et al., 2015):

$$fPAR_{chl} = \frac{SIF}{\beta \times cos(SZA) \times FE} \tag{4.4}$$

Plant physiological studies have shown the radiation absorbed by chlorophyll ($APAR_{chl}$) undergoes three different pathways: photochemistry, heat dissipation, and fluorescence emission (Butler, 1978). Previous studies also showed that SIF is mostly driven by the amount of radiation absorbed by chlorophyll under unstressed con-

ditions (Liu et al., 2017a; Yang et al., 2015). The Soil Canopy Observation of Photochemistry and Energy fluxes (SCOPE) model incorporates such three-way energy partitioning of $APAR_{chl}$. Simulations using the SCOPE model suggest that ϕ_f is primarily affected by the maximum rate of carboxylation (V_{cmax}) and the incoming radiation Lee et al. (2015); van der Tol et al. (2014). Both alter energy partitioning into photochemical quenching (PQ, energy used for assimilation) or fluorescence and non-photochemical quenching (NPQ, heat dissipation). We found that the ϕ_f exhibited relatively small variation (FE=1.69±0.18 J nm^{-1} sr^{-1} mol^{-1}, CV=0.11) with a very wide range of V_{cmax} and incoming radiation using the SCOPE model (Figure 4.A.1). Another simulation using a wide range of three other parameters that are closely related to the SIF reabsorption also suggested that the f_{esc} has much smaller variation (FE=2.04±0.34 J nm^{-1} sr^{-1} mol^{-1}, CV=0.17) compare to $APAR_{chl}$ (Figure 4.A.2). This is also confirmed by previous studies because of the low canopy reabsorption of SIF at far-red band (Van Wittenberghe et al., 2015). Therefore, we regard FE as a constant in this study and the uncertainties are considered in the error propagation analysis (Section 4.2.5). With this approximation, we define $fPAR_{SIF}$ as SIF/cos(SZA), considering a constant β and FE in Eq. 4.4, $fPAR_{SIF}$ is proportionate to $fPAR_{chl}$:

$$fPAR_{chl} \propto fPAR_{SIF} = \frac{SIF}{cos(SZA)} \tag{4.5}$$

where $fPAR_{SIF}$ does not follow the conventional range of 0 to 1, but that of an empirical parameter that can be calculated from SIF data. We use this relationship to evaluate proxies for $fPAR_{chl}$ using OVAIs both temporally for each pixel and spatially for each month.

SIF, vegetation indices (VIs, MOD13C1 C6) and $fPAR_{mod15}$ (MOD15A2H C6) are all retrieved from satellite observations and therefore are affected by atmospheric

conditions. Current retrieval algorithms account for such effects, but are rather product specific. To reduce the uncertainty caused by the atmospheric conditions and weak vegetation seasonality for the inter-comparison of remote sensing products, we applied a rigorous data quality checks for three MODIS product, only the highest quality observations are used for analysis: for NDVI and EVI, we only used quality layer Pixel Reliability = 0, (Good Data); for $fPAR_{mod15}$, we used same quality check method as described below in the site level analysis in Section 4.2.3; for MTCI, we masked out those areas that were identified as bad quality by above two quality check methods. We also eliminated the regions where all four OVAIs did not show a significant correlation with $fPAR_{SIF}$ at monthly scale. These low correlation coefficients are mostly caused by poor atmospheric conditions and weak seasonality of vegetation (e.g. tropical forest in northern Amazon). Because of the linear form of PEMs (Eq. 4.1), we use a linear transformation of OVAIs to approximate $fPAR_{chl}$ as follows:

$$fPAR_{chl} = a \times (OVAIs - c) \propto fPAR_{SIF} \tag{4.6}$$

The coefficient a can be regarded as a part of LUE and ideally, should be a fixed number for all biome types. The intercept c can be estimated from the intercept of the regression. A relatively stable regression slope and intercept (c) between OVAIs and $fPAR_{SIF}$ both spatially and temporally indicates that the approximation in Eq. 4.6 is plausible. The values (OVAIs$-c$) are considered as a proxy of (or proportional to) $fPAR_{chl}$ and are denoted with a subscripts m (e.g., $NDVI_m$=NDVI$-c$). The true value of ε^{chl}_{max} is not the goal of our study, as long as we can show ε_{max} for OVAIs-c are spatio-temporal convergent, ε^{chl}_{max} will be spatio-temporal convergent.

4.2.2 FLUXNET data processing and light use efficiency calculation

The ecosystem carbon dioxide exchange across a range of biomes and timescales used in this study is derived from EC data available from the FLUXNET2015 Tier 2 dataset (http://fluxnet.fluxdata.org/data/fluxnet2015-dataset/; 2015 December Release, Table 4.A.2) processed according to standardized protocols. Out of the 136 available sites we chose 127 sites (or specific site-year for cropland) where C3 species are dominant. These flux sites cover a large variety of ecosystem types and give altogether 626 site-years (Table 4.A.2, Figure 4.A.5). The measured net ecosystem exchange (NEE) was first gap-filled using the marginal distribution sampling (MDS) with different friction velocity (u*) filters to compensate the biases caused by reduced vertical exchange during nighttime (Reichstein et al., 2005). The NEE was then partitioned into GPP and ecosystem respiration (ER) using two different methods, the nighttime data-based method and daytime data-based method (Reichstein et al., 2012). The nighttime data-based method assumes no GPP during night and therefore, the nighttime NEE is regarded as ER and used to estimate the temperature dependency of respiration, which is then extrapolated to daytime. The daytime GPP is then calculated as the difference between measured NEE and modeled ER. The daytime data-based method assumes that the GPP can be described as a hyperbolic or non-hyperbolic function of light (Gilmanov et al., 2003; Lasslop et al., 2010). The measured NEE during the daytime is a combination of the largely light-dependent GPP and the temperature-dependent respiration, omitting other effects such as soil moisture limitation. Using half-hourly observations, the parameters of the response model are estimated and the GPP and ER terms are calculated simultaneously.

In order to compare the light use efficiency derived from flux measurements

with satellite retrievals, we aggregated the daily FLUXNET2015 dataset into 8-day intervals (and 10-day intervals for 2008-2012 to compare with MTCI, see Section 4.2.3). We applied the following screening rules to increase confidence: (1) For each 8-day (10-day) interval, we filtered out all periods with less than 75% of good quality (based on daily quality check field) gap-filled data of shortwave radiation and NEE observation. (2) To reduce the uncertainties of the flux partitioning, we compared the GPP estimates from both daytime and nighttime partitioning methods on 8-day (10-day) periods and excluded those with more than 10% difference between methods.

Limitations of water, temperature and other climate factors will down-regulate the LUE from its maximum value (ε_{max}), and these limitations are complex and may be different among ecosystems (Zhang et al., 2016f). In this study, we simplify this issue by assuming: (1) that plants in all ecosystems reach their maximum LUE during the peak growing season because of their long term acclimation of the photosynthetic apparatus given that no severe disturbances occur; (2) for tropical forest ecosystems which photosynthesis happens all year round, we followed (Wu et al., 2016) and use the photosynthesis capacity (PC) as seasonal dynamic of ε_{max}. PC is calculated as ecosystem light use efficiency under a small range of climate conditions (e.g., cloudiness, PAR, air temperature, VPD) throughout the year to eliminate the climate effect on photosynthesis. In this way, we can use seasonal variation of PC as a proxy of maximum ecosystem light use efficiency under a fixed environmental limitation across the year. This enables us to compare PC with $fPAR_{canopy}$ and $fPAR_{chl}$ proxies in the temporal domain. Based on these two assumptions, we can explore the maximum light use efficiency across different ecosystems, and the seasonal dynamics of maximum light use efficiency using tropical forests as an example. For each site-year, we identified the five 8-day (four 10-day) period with the

highest GPP values as the peak growing season. Subsequently, the abovementioned quality check for flux data was applied and only the 8-day (10-day) periods with high confidence were retained. For each 8-day (10-day) periods during the peak growing season, the maximum daily LUE_{eco} were then calculated as the average of daily GPP from eddy covariance measurements (GPP_{EC}) divided by the average of daily PAR. However, as disturbances may occur in some years and climate may limit LUE during the peak growing season, we only retained the upper 50^{th} percentile of the maximum daily LUE_{eco} from all available years for each site for further analysis.

Because many studies have shown different ε_{max} for clear and cloudy days (Gu et al., 2002; Mercado et al., 2009), we separate the sunny and cloudy period for each 8-day (10-day) during the peak growing season using a clearness index (actual shortwave radiation/potential shortwave radiation) of 0.55 (which is 80% of its maximum actual value because of atmospheric scattering, and this threshold gives us enough points for clear day and cloudy day analysis). Corresponding to the different definitions of fPAR (Figure 4.1), LUE or ε_{max} can also be calculated at different levels, using incoming top of canopy PAR (LUE_{eco}=GPP_{EC}/PAR), canopy absorbed PAR (LUE_{canopy}=$GPP_{EC}/APAR_{canopy}$), and chlorophyll of the canopy (chlorophyll for short) absorbed PAR (LUE_{chl}=$GPP_{EC}/APAR_{chl}$) (Gitelson & Gamon, 2015; Zhang et al., 2016a, 2009). For LUE_{canopy} and LUE_{chl}, they can also be calculated from $LUE_{eco}/fPAR_{canopy}$ and $LUE_{eco}/fPAR_{chl}$, respectively. Therefore, a convergence of LUE from canopy to chlorophyll level across biome types will be represented as a convergence of regression slopes in the simple linear regression with 0 intercept between LUE_{eco} and $fPAR_{chl}$ than LUE_{eco} and $fPAR_{canopy}$.

The uncertainty of daily GPP derived from eddy covariance flux tower is 15–20% (Falge et al., 2002; Hagen et al., 2006). By summing up the daily GPP to annual scale, the relative uncertainty decrease as the random error cancel with each other. The

annual GPP uncertainty is estimated to be 5% (Desai et al., 2008; Verma et al., 2014). In our study, since we use daily GPP averaged over five 8-day, the uncertainty for this averaged GPP is estimated to be 10% (between daily and annual uncertainty). The uncertainty of PAR measurement from flux tower can be assumed to be negligible since it is much smaller than that of GPP.

4.2.3 Remote sensing observations at flux tower sites

We used two vegetation indices (NDVI and EVI), one fPAR product ($fPAR_{mod15}$) from MODIS and one chlorophyll index (MTCI) to represent the $fPAR_{canopy}$ and their transformations (OVAI$-c$) as proxies of $fPAR_{chl}$ (Table 4.1). The NDVI and $fPAR_{mod15}$ are often used as an indicator of canopy coverage (Carlson & Ripley, 1997; Myneni et al., 2002). The EVI is often considered to be a proxy of the green (photosynthetically active) vegetation (Gitelson & Gamon, 2015; Xiao et al., 2005a). MTCI is thought to be related to the leaf chlorophyll content integrated over the canopy as they use spectrum bands which are more sensitive to chlorophyll absorption (Dash et al., 2010; Dash & Curran, 2007; Rossini et al., 2012; Vuolo et al., 2012).

Due to the sensitivity of remote sensing retrievals to atmospheric contaminations, when comparing the remotely sensed OVAIs with eddy flux measurements, we used a similar procedure reported in Zhang et al. (2016f) to screen and gap-fill the remotely sensed OVAI observations of poor quality: (1) The robustness of MODIS VIs (i.e., NDVI, EVI) retrievals was checked using the quality control layer from MOD09A1 C6; observations affected by cloud ("internal cloud algorithm flag" equals to "1"), high or climatological aerosols ("aerosol quantity" equals to "00" or "11"), and snow ("internal snow mask" equals to "1") were eliminated (Vermote & Vermeulen, 1999). For the MOD15A2H C6 fPAR product ($fPAR_{mod15}$), the ad-

ditional five-level confidence score was evaluated ("SCF_QC" equals to "000" or "001"), and only observations using the main algorithms (radiative transfer model) were retained (Myneni et al., 2002). (2) The BISE algorithm (Viovy et al., 1992) was applied to remove values that were potentially biased by atmospheric conditions and that were not identified by previous quality checks. (3) The remaining high quality values were then linearly interpolated to fill the gaps created from the previous steps. For MTCI, we did not apply any quality check procedure and just replaced all zero values with NAs during the analysis as no quality control layer is provided by the data product.

The seasonal dynamics of vegetation indices in tropical forests have been investigated for years (Huete et al., 2006; Myneni et al., 2007; Saleska et al., 2007; Wu et al., 2016; Xiao et al., 2006), and some recent studies suggest that the dry season increase of EVI is related to the sun-sensor geometry or bi-directional reflectance distribution function (BRDF) (Morton et al., 2014). To reduce artifacts caused by this issue, instead of using the ordinary NDVI and EVI, we used the Multi-Angle Implementation of Atmospheric Correction (MAIAC) algorithm reflectance dataset (Lyapustin et al., 2012) to calculate NDVI and EVI for the Amazon K67 (2.85°S, 54.97°W) and K34 (2.61°S, 60.21°W) sites. The MAIAC algorithm implements rigorous BRDF and atmospheric corrections and is therefore more robust than the current MODIS EVI calculated from MOD09A1 C6 when detecting changes in tropical forests. The original MAIAC 1km×1km reflectance data were downloaded from ftp://ladsweb.nascom.nasa.gov/MAIAC/. We first retrieved the reflectance for the nine surrounding pixels (3km×3km) for sites K67 and K34 from 2000 to 2012 and then calculated the NDVI and EVI using the BRDF corrected reflectance. All high quality observations that passed the quality check were aggregated into monthly values.

Table 4.1: Optical vegetation activity indices (OVAIs) used in this study. ρ with a subscription number indicate the satellite retrieved band reflectance centered at this wavelength.

OVAIs	Product	Calculation	Original spatial resolution	Temporal resolution	Data quality check	Uncertainty (absolute value)	Spatial extent
$fPAR_{mod15}$	MOD15A2H C6	spectral information from MODIS surface reflectance at 648 nm and 858 nm and radiative transfer equation based Look-up-Table	500 m	8-day	both MOD09A1 QA and MOD15A2H QA	0.15[a]	global
NDVI	MOD09A1 C6 for site, MOD13C2 C6 for regional	$\frac{\rho_{858.5}-\rho_{645}}{\rho_{858.5}+\rho_{645}}$	500 m	8-day for site, monthly for regional	MOD09A1 QA for site, MOD13C2 Pixel Reliability for regional	0.025[b]	global
EVI	MOD09A1 C6 for site, MOD13C2 C6 for regional	$2.5 \times \frac{\rho_{858.5}-\rho_{645}}{\rho_{858.5}+(6\times\rho_{645}-7.5\times\rho_{469})+1}$	500 m	8-day for site, monthly for regional	MOD09A1 QA for site, MOD13C2 Pixel Reliability for regional	0.015[c]	global
MTCI	NEODC MTCI Level 3	$\frac{\rho_{753.75}-\rho_{708.75}}{\rho_{708.75}-\rho_{681.25}}$	~5000 m	8-day for 2002-2007, 10-day for 2008-2012	NA	0.1[d]	180°W–180°E, 80°S–80°N

[a] Yan et al. (2016)
[b] https://landval.gsfc.nasa.gov/ProductStatus.php?ProductID=MOD13
[c] https://landval.gsfc.nasa.gov/ProductStatus.php?ProductID=MOD13
[d] Elsobky (2015), this number is a rough estimate across different biomes

4.2.4 Land cover dataset for major biome types

The land cover classification is based on the IGBP classification scheme from the MCD12C1 C5 dataset for 2007 to 2013 (Friedl et al., 2010). The MCD12C1 data have a spatial resolution of 0.05°×0.05°, and for each gridcell, 16 numbers correspond to the areal percentages of 16 IGBP land cover types. We further aggregated this dataset to 0.5°×0.5° to match the spatial resolution of SIF and recalculated the areal percentages of 16 biome types for each 0.5°×0.5° gridcell. If one land cover type occupies more than 80% of the area of a 0.5°×0.5° gridcell, this gridcell is considered a "pure" pixel and further used for the biome-based statistical analysis (Figure 4.6). 13 vegetated land cover types for both MCD12C1 and flux tower sites were aggregated into four major biome types. Forests include DBF, EBF, ENF, DNF, and MF. Shrublands include OSH, CSH, and WSA. Grasslands include GRA, SAV, and WET. Croplands include CRO and NVM. A full list of these acronyms can be found in Table S2.

4.2.5 Error propagation

Since our study includes several comparisons and approximations, the uncertainties related to each dataset and approximations will propagate and affect the final result. Therefore, we analyzed the uncertainties using the error propagation law (Deming, 1943):

$$\sigma_f^2 = \mathbf{g}^T \mathbf{V} \mathbf{g} \tag{4.7}$$

Here σ_f^2 represents the variance of the function f with a set of parameters $\boldsymbol{\beta}$, whose variance-covariance matrix is $\boldsymbol{V}$. The ith element in the vector $\boldsymbol{g}$ is $\frac{\partial f}{\partial \beta_i}$. If the parameters in vector $\boldsymbol{\beta}$ are uncorrelated, the error propagation can be simplified to:

$$\sigma_f^2 = \sum \left(\frac{\partial f}{\partial \beta_i} \right)^2 \sigma_{\beta_i}^2 \tag{4.8}$$

This equation allows us to calculate the variance of a function (σ_f^2) from the variance of its individual input ($\sigma_{\beta_i}^2$). The uncertainties of a variable can be greatly reduced by averaging n measurements:

$$\sigma_{\overline{f}}^2 = \frac{\sigma_f^2}{n} \tag{4.9}$$

The error propagation for a linear regression can be quantified from two aspects: (1) the uncertainty of the regression, which can be quantified as an error term ϵ, and (2) the uncertainty from the independent variable. A detailed error propagation calculation can be found in the Appendix 4.A.2, and the uncertainties for each step are summarized in Table 4.2.

Table 4.2: The uncertainties of approximations used in our study.

Variables	Estimated from	Uncertainty (represented as s.d. or RMSE)
iPAR	cos(SZA)	85.6 W m^{-2}
$fPAR_{SIF}$[a]	SIF	0.34
$OVAI_m$[b] (approximation of $fPAR_{chl}$ using OVAI)	$fPAR_{mod15}$	0.17 (0.11)
	NDVI	0.09 (0.08)
	EVI	0.04 (0.03)
	MTCI	0.24 (0.22)

[a] $fPAR_{SIF}$ considered the uncertainty of FE.

[b] These uncertainties are estimated for the 8-day (10-day) temporal resolution, the values in the parentheses are adjusted for peak growing season period (five 8-day or four 10-day) to compare with LUE_{eco}.

4.3 Results

4.3.1 Relationship between $fPAR_{SIF}$ and OVAIs

We calculated the averages of OVAIs for all pixels within each vegetation type for each month and compared them with $fPAR_{SIF}$ for the period 2007 to 2015 (2007 to 2012 for MTCI). For $fPAR_{mod15}$ and NDVI, their relationships with $fPAR_{SIF}$ for different biome types were scattered, and the R^2 of the regression within each biome type was relatively lower compared to those for EVI and MTCI (Figure 4.3). EVI and MTCI also showed a stronger linear correlation with $fPAR_{SIF}$ when all the biome types were combined together. The relationship between $fPAR_{SIF}$ and MTCI was also consistent across biomes except for the forests in the southern hemisphere. The lower $fPAR_{SIF}$ values for the southern hemisphere forests may be caused by an overestimation of incoming radiation using SZA that ignores cloud effects.

The intercepts of these linear regressions (c in Eq. 4.6) are important to establish and assess variation in the relationship between OVAIs and $fPAR_{chl}$. We compared the intercept estimates from both the spatial averaged regressions (Figure 4.3) and the regressions of individual gridcells (Figure 4.A.7). MTCI and EVI showed less variable intercepts than $fPAR_{mod15}$ and NDVI across four biome types. The $fPAR_{mod15}$ exhibited the largest variation of intercepts independent of biome types, while variations for EVI and MTCI were comparatively smaller. The average intercepts on x-axis are ~0.2 for $fPAR_{mod15}$ and NDVI, ~0.1 for EVI and ~1.0 for MTCI. We used these intercepts to build up the relationship between OVAIs and the $fPAR_{chl}$. Based on these analyses, EVI and MTCI were considered stronger proxies of $fPAR_{chl}$ than either $fPAR_{mod15}$ or NDVI. The uncertainty of this approximation is shown in Figure 4.A.4.

We also used simple linear regression to determine the relationship between

monthly $fPAR_{SIF}$ and OVAIs for individual gridcells. Figure 4 shows the spatial pattern and the frequency statistics of the regression slopes between $fPAR_{SIF}$ and the four OVAIs with fixed intercepts from the previous steps. The regression slopes of MODIS $fPAR_{mod15}$, NDVI and EVI showed a similar spatial pattern. The spatial variations of the regression slopes using $fPAR_{mod15}$ and NDVI were relatively larger than those using EVI and MTCI, as represented by a larger coefficient of variance (c.v.). The frequency statistics of these regression slopes showed biome-specific characteristics for $fPAR_{mod15}$, NDVI and EVI, where the lowest values were found

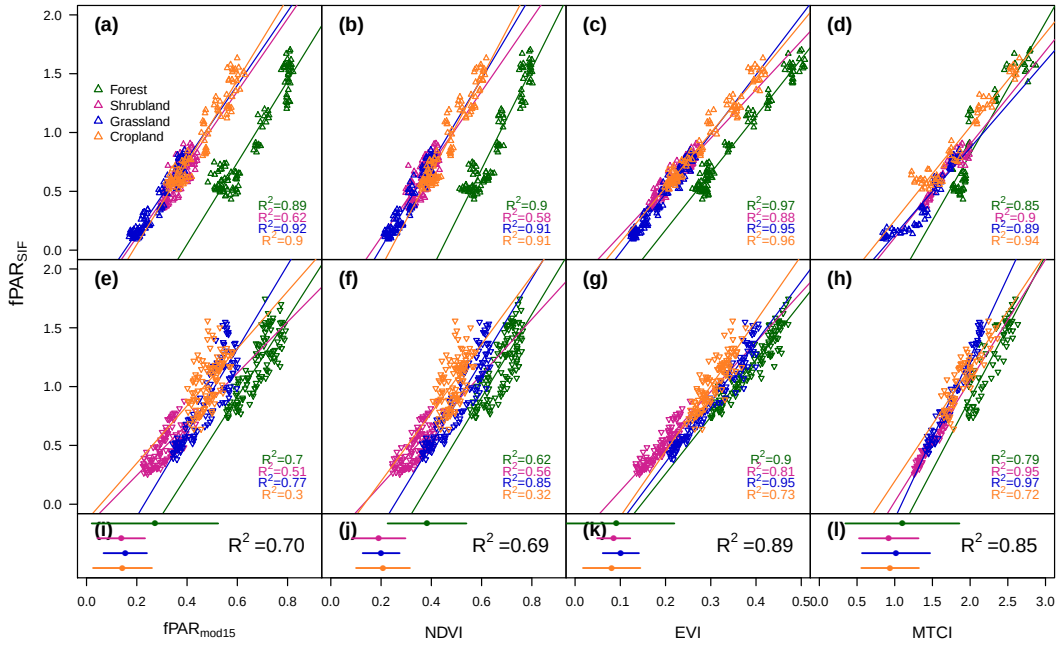


Figure 4.3: Relationships between $fPAR_{SIF}$ and four OVAIs for Northern (a-d) and Southern Hemisphere (e-h). Each point represents the average value of all the gridcells within a specific land cover type for either the Northern or Southern Hemisphere for each month. Two hemispheres were calculated separately because of different phenological cycles. The coefficients of determination for each regression are given in the lower-right corner. The four horizontal lines with dots in (i-l) represent the mean value and standard deviation of the regression intercepts between the $fPAR_{SIF}$ and OVAIs for individual pixel (Figure 4.A.7). Coefficients of determination for all data points (all land cover types and both hemispheres) are shown in black.

for forests, followed by shrublands, grasslands, and croplands. The MTCI, on the other hand, showed a relatively stable slope across the different biome types. In addition, EVI also showed slightly higher coefficients of determination (R^2) for the regression models (Figure 4.A.9).

4.3.2 LUE estimation at different scales across biomes based on flux tower GPP

To compare with the GPP estimated from flux towers (GPP_{EC}), we used the EVI_m (EVI_m=EVI−0.1), $MTCI_m$ ($MTCI_m$=MTCI−1), $NDVI_m$ ($NDVI_m$=NDVI−0.2) and $fPAR_m$ ($fPAR_m$=$fPAR_{mod15}$−0.2) as approximations of $fPAR_{chl}$, and the original $fPAR_{mod15}$ and NDVI as $fPAR_{canopy}$ (Figure 4.1), which are also commonly used in other studies (Prince & Goward, 1995; Running et al., 2004). With the assumption that long-term acclimation enables plants to reach maximum photosynthetic capacity during the peak growing season, we tested whether the maximum daily light use efficiency (ε_{max}) at chlorophyll scale (ε_{max}^{chl}) rather than canopy scale ($\varepsilon_{max}^{canopy}$) converges across different biome types, i.e., whether regression slopes between LUE_{eco} and $fPAR_{chl}$ (represented by $OVAI_m$) for each biome types show less variation than those between LUE_{eco} and $fPAR_{canopy}$ (represented by $fPAR_{mod15}$ and NDVI). For clear days, the regressions between LUE_{eco} and EVI_m or $MTCI_m$, which are considered better $fPAR_{chl}$ approximations, showed smaller variation of regression slopes within each biome types than those using the other two canopy indicators ($fPAR_{mod15}$ and NDVI) (Figure 4.5a-d). EVI_m and $MTCI_m$ were also characterized by a smaller root mean square errors (RMSE) and higher coefficients of determination (R^2) than fPARm and $NDVI_m$ when all biome types were combined together (Table 4.A.3, 4.A.4). Similar results were also found for cloudy days (Figure 4.5 e-h).

From the ecosystem (top of canopy) scale to canopy and chlorophyll scales,

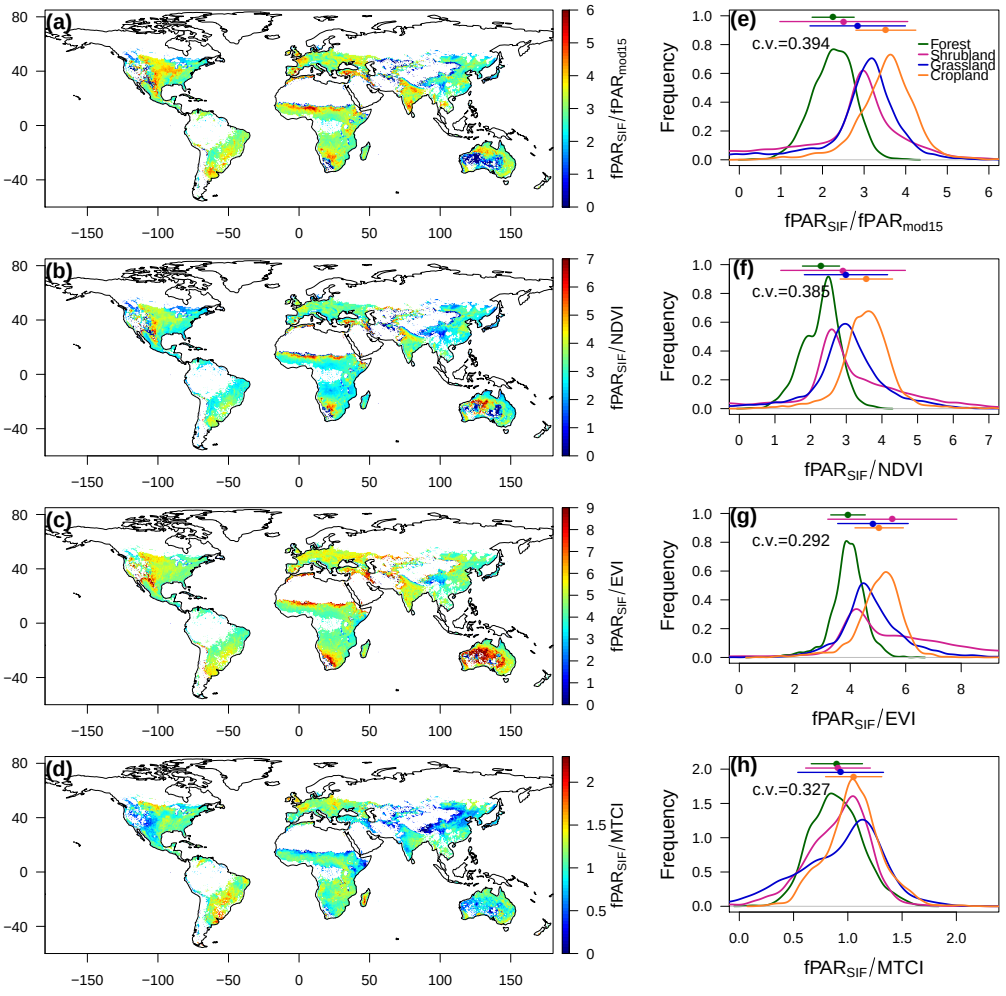


Figure 4.4: Spatial distribution and frequency distribution of the regression slopes between $fPAR_{SIF}$ and four optical vegetation activity indicators (OVAIs) with fixed intercepts (c in equation 4.6) for the period 2007 to 2015. The left column (a-d) shows the spatial distribution of regression slopes where the regression is significant at 0.05 level. The white areas in tropical and boreal region are caused by very limited valid observations after quality check. The right column (e-h) shows the frequency distribution for 4 major land cover types. Points with error bar at the top of each plot represent the mean $\pm$ 1 standard deviation (SD) of the slopes within each land cover type.

the maximum daily LUE converges as shown by smaller c.v. across biomes using fPAR=1, $fPAR_{canopy}$, and $fPAR_{chl}$ approximations (Figure 6). All $OVAI_m$ showed less variations than OVAI, for both clear and cloudy days, which indicates that the approximation method we used did improve the estimation of $fPAR_{chl}$.

GPP_{EC} from clear days (left panel) and cloudy days (right panel). Each open circle represents one week from a site year. Solid lines represent the regression between LUE_{eco} and modified OVAIs (with a subscript m, as proxies of $fPAR_{chl}$) which are forced to pass [c,0] (c for the fixed intercept in Eq. 4.6); dashed lines represent the regression between LUE_{eco} and OVAIs which are forced to pass [0,0]. Regressions lines and slope values (ε_{max}) in black represent all biome types combined together.

4.3.3 Using $fPAR_{chl}$ approximations to track seasonal dynamic of photosynthetic capacity

Across a broad array of 127 sites covering multiple biomes, we have shown that the biome differences of ε_{max} tend to diminish if we used fPAR of radiation absorption by chlorophyll of the canopy rather than at canopy or ecosystem scales, possibly owing to its emphasis on photosynthetic pigments (section 4.3.2.). We also tested whether this convergence can be found across time, i.e., whether the seasonal changes of PC can be explained by the change of the canopy chlorophyll. We chose two tropical forest sites in the Amazon forest where multi-year eddy flux observations were available (Wu et al., 2016). For both sites, $MTCI_m$ showed a similar seasonal pattern of PC, while NDVI was not sensitive to seasonal changes (Figure 4.7). The use of $fPAR_{chl}$ approximations ($OVAI_m$) did not show much advantage over their original values (OVAI) in terms of RMSE. However, EVI_m and $MTCI_m$ had higher dry-season increases which better represented the seasonal dynamic of

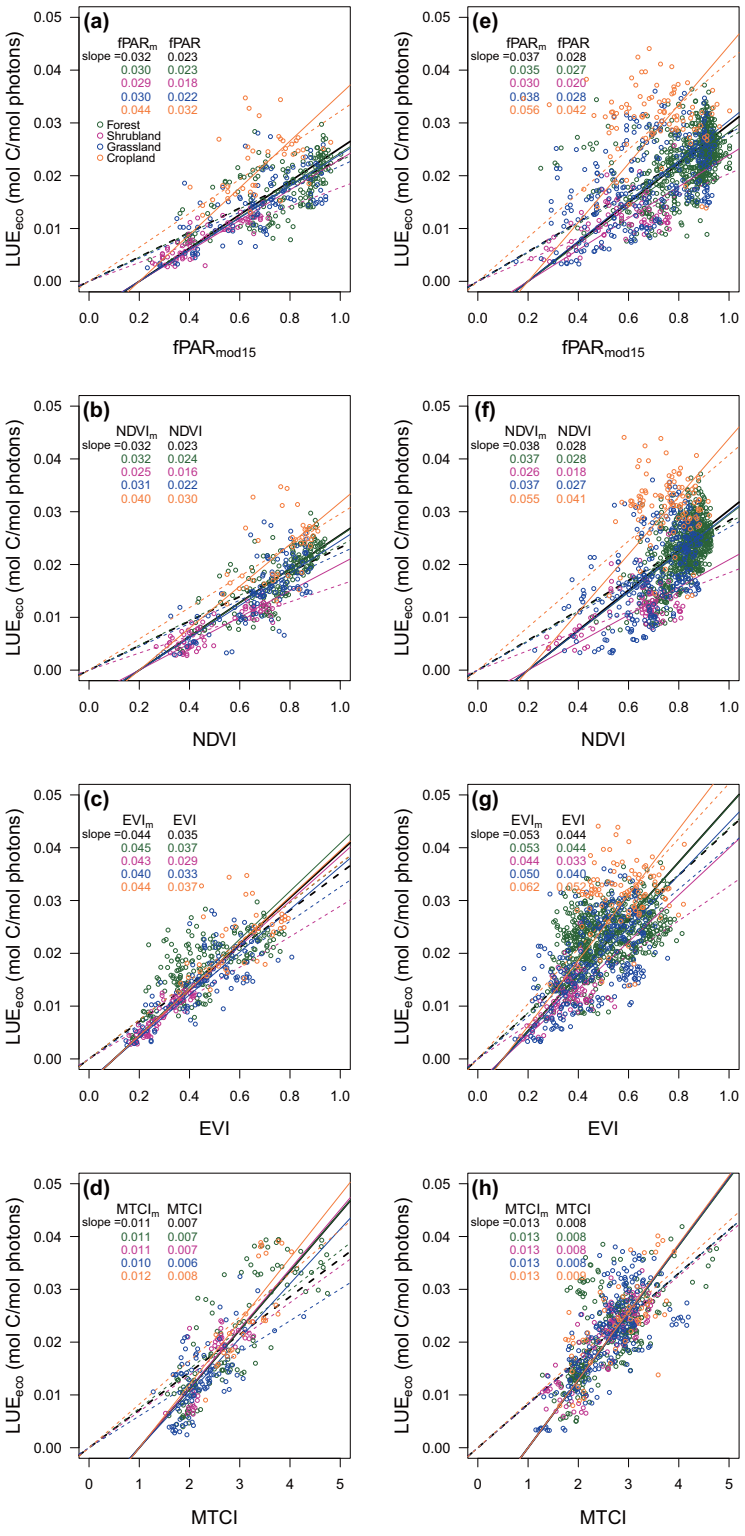


Figure 4.5: Relationship between different OVAIs and LUE_{eco} for peak growing season using GPP_{EC} from clear days (left panel) and cloudy days (right panel). Each open circle represents one week from a site year. Solid lines represent the regression between LUE_{eco} and modified OVAIs (with a subscript m, as proxies of $fPAR_{chl}$) which are forced to pass [c,0] (c for the fixed intercept in Eq. 4.6); dashed lines represent the regression between LUE_{eco} and OVAIs which are forced to pass [0,0]. Regressions lines and slope values (ε_{max}) in black represent all biome types combined together.

PC.

4.4 Discussion

4.4.1 Advantages and biophysical interpretation of $fPAR_{chl}$

In this study, we have shown that EVI and MTCI are robust proxies of $fPAR_{chl}$ with the possible uncertainties being taken into consideration, and a fixed ε_{max} can be used for C3 plants-dominated ecosystems across biomes and time to estimate GPP. Previous studies also find higher correlation between GPP and EVI (MTCI) than with NDVI or $fPAR_{mod15}$, and attribute this advantage to the exclusion of NPV or a better indicator of green leaf/chlorophyll content, which are more directly related to plant canopy photosynthesis (Gitelson et al., 2014; Ma et al., 2014; Rossini et al., 2012; Shi et al., 2017; Xiao et al., 2004a,b). However, these studies usually focused on a single site and did not separate the seasonal change of abiotic (environmental) limitation

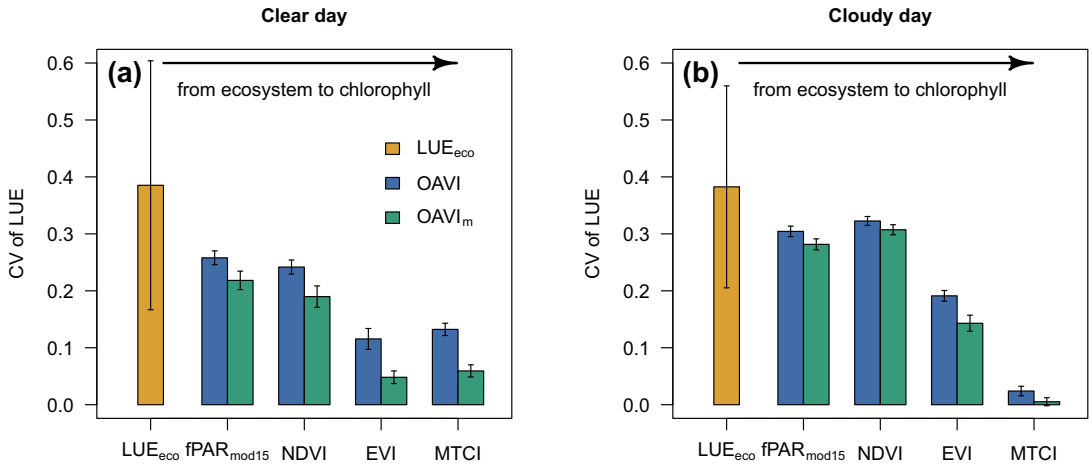


Figure 4.6: The variation of maximum daily LUE as represented by the coefficient of variation (c.v.). $fPAR_{mod15}$, NDVI are used to represent $fPAR_{canopy}$ and EVI_m and $MTCI_m$ are used as proxies of $fPAR_{chl}$. All c.v. are calculated based on the regression slopes in Figure 4.5 or the average of LUE_{eco} for each biome type. The error bar on each bar is calculated from error propagation considering all the uncertainties in both input datasets and each approximation step (Appendix 4.A.2).

on photosynthesis. Using the SIF retrieval from satellite and a flux sites across the globe, our study further demonstrated the advantage of this approach is caused by a more directed proxy of canopy chlorophyll content.

Chlorophyll content has been successfully retrieved at canopy scale as the interaction between these pigments and light will affect the canopy reflectance spec-

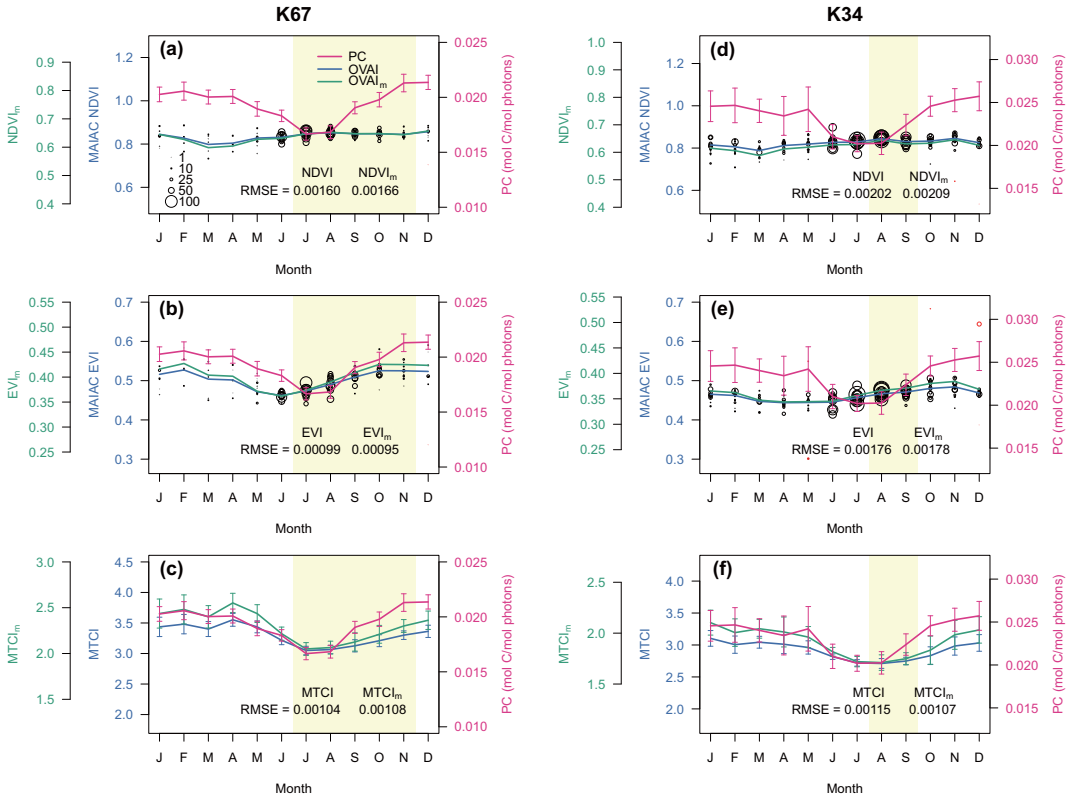


Figure 4.7: Comparing EVI, NDVI, MTCI and their approximation of $fPAR_{chl}$ (EVI_m, $NDVI_m$, $MTCI_m$) with PC at K67 and K34 sites in Amazon forest. EVI and NDVI data are calculated from MAIAC reflectance. Each circle represents average of all valid observations for each year each month. The size of the circles represents the numbers of valid observations used. Some obvious outliers were colored in red and eliminated from further analysis. The blue and green lines in (a, b, d, e) represent the observation numbers weighted averages of EVI or NDVI. The error bars for PC represent the standard error of mean (SEM). The error bars for MTCI and $MTCI_m$ in (c and f) represent the standard deviation for the period 2002 to 2012. Shades in light yellow represent dry season. RMSE are calculated based on regressions with zero intercept.

trum (Asner & Martin, 2008; Curran, 1989; Sims & Gamon, 2002). Compared with PEMs which only focus on the LAI or $fPAR_{canopy}$, the use of $fPAR_{chl}$ can better estimate both leaf quantity (LAI) and leaf physiological quality (chlorophyll concentration, nitrogen content), the latter is often regarded as the secondary factor that responsible for LUE_{canopy} (Wu et al., 2016). The possible explanation for this spatio-temporal convergence may be that all the C3 plants share the same electron transport mechanism and chemical reactions to fix carbon. And all plants under different environmental conditions tend to maximum their photosynthetical capacity during the peak growing season to increase their competitiveness. The variation of $fPAR_{chl}$ though space and time can be synergistic to the variation of maximum carboxylation rate (V_{cmax}), quantum efficiency (α_q) and leaf area index (LAI) (**?**), but still need future test.

4.4.2 Potential of using SIF and $fPAR_{chl}$ for GPP estimation and data assimilation

As SIF is closely related to the $APAR_{chl}$, both theoretically from model simulations and experimentally using in situ observations (Frankenberg et al., 2011; van der Tol et al., 2014), this relationship, conserved across biomes, can be used to build simple models to directly estimate GPP from SIF and to improve PEMs. Guanter et al. (2014) have explored the feasibility of estimating GPP using SIF for croplands. Many studies suggest SIF contains not only the information of light absorption, but also the light use efficiency information (Yang et al., 2015). However, these studies all used SIF_{yield} (SIF_{yield}=SIF/$APAR_{canopy}$) defined at the canopy scale. At present, we still do not know whether the good relationship between SIF_{yield} and LUE_{canopy} is caused by the variation of canopy chlorophyll content, which is embedded in both SIF_{yield} and LUE_{canopy} (Figure 4.1), or whether SIF_{yield} actually captures environmental stress. Understanding this underlying mechanism will

pave the way to better estimate GPP from SIF.

The estimates of $fPAR_{chl}$ using vegetation indices also provide an alternative opportunity to benchmark state-of-the-art land surface models. Currently, many dynamic global vegetation models (DGVMs) use data assimilation techniques, which employ remote sensing retrieved leaf area index or fPAR products to improve performance (Demarty et al., 2007; Rayner et al., 2005). Some other studies try to use SIF or MTCI to constrain models output or inversely estimate some key parameters of the photosynthesis processes (Alton, 2017; Koffi et al., 2015; Zhang et al., 2014b). As we have shown that EVI and MTCI can be used as a proxy of $fPAR_{chl}$ and that LUE tends to converge across different biome types, $fPAR_{chl}$ estimated from EVI and MTCI is more directly related to GPP and can be used for data assimilation to improve model performance.

4.4.3 Implications for PEMs

Due to its simple form, PEMs play an important role in simulating GPP at regional to global scale. However, the parameterization is a critical issue, especially for ε_{max}, which determines the efficiency of plants converting the daily solar energy to biochemical energy, thus directly affecting the magnitude of the GPP estimation. Previous studies have made efforts to correctly estimate the biome-based ε_{max} (Zhao et al., 2005; Zhou et al., 2015b). Some studies even suggest site level ε_{max} is necessary to improve model accuracy (Cheng et al., 2014; Kross et al., 2016). However, it is unlikely that, outside of flux towers footprints, we can obtain spatially continuous ε_{max} estimates from in situ measurement. On the other hand, other studies based on data from 168 flux sites and 7 PEMs suggest that vegetation-specific model parameters are not necessary for deriving accurate GPP estimates (Yuan et al., 2014a, 2016). The spatial convergence of ε_{max} across biomes at chlorophyll scale justi-

fies that a constant ε_{max} may be applied for simple but robust parameterization of PEMs. This approach could simplify the model parameterization by avoiding the need of vegetation maps (e.g., forest, shrub, grass) and vegetation specific parameters, ultimately reduce the uncertainty and improve the robustness of the GPP estimates (Zhang et al., 2016a). The seasonal dynamic of $fPAR_{chl}$ is closely related to that of PC, however, this biotic change is not simulated in $fPAR_{canopy}$ based PEMs (e.g. MOD17). Using $fPAR_{chl}$ could improve the prediction of biotic regulation of GPP at seasonal scale. However, in study, we did not give ε_{max}^{chl} value for C3 plants since we used EVI_m and $MTCI_m$ as proxies of $fPAR_{chl}$, while the true value of $fPAR_{chl}$ is unknown. This does not affect the use of EVI_m or $MTCI_m$ based LUE models since the corresponding ε_{max} can be empirically derived. Future studies using inversion of radiative transfer models can give an accurate estimate of $fPAR_{chl}$ and ε_{max}^{chl}.

Although the cross-biome variation in ε_{max} diminishes when using EVI_m and $MTCI_m$ as an approximation of $fPAR_{chl}$, we show that the within-biome ε_{max} variation does not decrease much compared to the $fPAR_{canopy}$ based indicators. This may be caused by several reasons: 1) ε_{max} is still constrained by environmental conditions and may change from one year to the other year for a given site, even during the peak growing season; 2) site-specific characteristics (soil type, fertilization, etc.) still affect the ε_{max} to some extent; 3) the direct and diffuse radiation composition affect ε_{max}; 4) flux and satellite measurements uncertainties still exist; and 5) the inconsistency of flux tower footprint and OVAI pixels may introduce noise in the relationship.

In this study, we find based on light absorption of chlorophyll of the canopy, which directly reflect light harvest of photosynthesis process, ε_{max} tends to converge across space and time, which can greatly simplify the structure and parame-

terization of PEMs. However, to improve model accuracy, more studies are needed to investigate the environmental limitations on ε_{max} and photosynthesis. Different forms of temperature and water limitations have been widely used, but recent studies also suggest the need to employ mixed forms of the limitations for forests and non-forested sites, especially during drought periods (Zhang et al., 2016d). With more data accumulated from global flux networks and remotely sensed images from different satellites, PEMs will provide more accurate estimates of GPP to support a better understanding of the global carbon cycle.

4.A Appendix

4.A.1 Relationship between SIF and $fPAR_{chl}$

We use the soil-canopy spectral radiances, photosynthesis, fluorescence, temperature and energy fluxes (SCOPE) model (van der Tol et al., 2009) to explore the robustness of using SIF to derive $fPAR_{chl}$. The SCOPE model simulates (1) the distribution of incident light over leaves as a fuction of leaf position in the canopy and leaf orientation, (2) the conversion of incident light on leaves into fluorescence emission spectra, and (3) the propagation of fluorescence through the canopy. At the leaf level, it also simulates photosynthesis as a function of irradiance, leaf temperature, humidity and CO2 concentration. For the first step, the 'Scattering of Arbitrary Inclined Leaves' (SAIL) model (Verhoef, 1984) concept is used, and for the second step, the Fluspect model (Verhoef & Bach, 2007), a model that simulates the probability of the light absorbed by chlorophyll to three sinks, i.e., photochemistry (ϕ_p), fluorescence (ϕ_f) and heat dissipation (ϕ_d), is used. For the third step, the FluorSAIL model simulates the reabsorption of fluorescence in the canopy that reduce the fluorescence to a value that is lower than the total emitted fluorescence by all leaves; this reabsorption can be characterized using a factor f_{esc}. In essence, the simulated photosynthesis summed over all leaves (A) and the simulated observation of SIF can be expressed as:

$$A = \phi_p \times fPAR_{chl} \times PAR \tag{4.A.1}$$

$$SIF = \phi_f \times fPAR_{chl} \times PAR \times f_{esc} \tag{4.A.2}$$

The integration of the $\phi_f \times f_{esc}$ of the canopy equals to fluorescence efficiency

(FE) in Eq. 2.2. To test whether FE can be approximated as a constant, we tested the variation of the two components of FE, i.e., ϕ_f and f_{esc}, comparing with the variation of $APAR_{chl}$ ($fPAR_{chl}\times$ PAR). Previous studies suggest the maximum carboxylation rate (V_{cmax}) is one of the most important factor which determines the probability of the partitioning of the absorbed photon by chlorophyll (ϕ_f) (van der Tol et al., 2009; Zhang et al., 2014b). We first ran the SCOPE model using different V_{cmax} values for one vegetation type (LAI = 3, Cab = 80 μ g cm^{-2}) over different values of irradiance (thus constant f_{esc} but variable PAR) and showed that the ϕ_f can be considered as a first approximation as a constant (Figure 4.A.1), because the variability of $APAR_{chl}$ is much larger than that of ϕ_f. As SIF is also sensitive to chlorophyll a+b content (Cab), dry matter content (Cdm) and leaf area index (LAI) (Verrelst et al., 2015), which may alter SIF through the change of f_{esc}. We then ran SCOPE for one value of irradiance but different value of Cab, Cdm and LAI (thus constant PAR but variable f_{esc}) (Table 4.A.1), we found that the FE has much less variation (2.04±0.34 J nm^{-1} sr^{-1} mol^{-1}) (Figure 4.A.2) compared to the $fPAR_{chl}$ (0.57±0.18). Considering the PAR variation during the satellite overpass, the total variation of $APAR_{chl}$ will be much higher than f_{esc}. Because both ϕ_f and f_{esc} have much smaller variation compared with $APAR_{chl}$, FE can be considered as a first approximation as a constant.

4.A.2 Error propogation in each approximation

There are two major approximations in our analyses: (1) using SIF as an approximation of $fPAR_{chl}$ ($fPAR_{SIF}$). (2) using OVAIs as approximations of $fPAR_{chl}$ ($fPAR_{SIF}$). In this error propagation analysis, the uncertainties of $fPAR_{chl}$ and $fPAR_{SIF}$ are same in terms of CV, since the uncertainties in ϕ_f and f_{esc} are also considered for

$fPAR_{SIF}$. For the first step of approximation, $fPAR_{chl}$ can be expressed as:

$$fPAR_{chl} = \frac{SIF}{iPAR \times \phi_f \times f_{esc}} \tag{4.A.3}$$

The uncertainty of $fPAR_{SIF}$ ($\sigma_{fPAR_{SIF}}$) can be calculated from the uncertainties from each independent variable using the error propagation law and assuming each independent variable is independent from each other:

$$\frac{\sigma_{fPAR_{SIF}}}{fPAR_{SIF}} = \frac{\sigma_{fPAR_{chl}}}{fPAR_{chl}} = \sqrt{\left(\frac{\sigma_{SIF}}{SIF}\right)^2 + \left(\frac{\sigma_{iPAR}}{iPAR}\right)^2 + \left(\frac{\sigma_{\phi_f}}{\phi_f}\right)^2 + \left(\frac{\sigma_{f_{esc}}}{f_{esc}}\right)^2} \tag{4.A.4}$$

where $\frac{\sigma_{iPAR}}{iPAR}$, can be calculated from the approximation of cos(SZA) (Figure 4.A.1), $\frac{\sigma_{\phi_f}}{\phi_f}$ and $\frac{\sigma_{f_{esc}}}{f_{esc}}$ can be obtained from the SCOPE simulation.

To evaluate the performance of the four OVAIs as proxies of $fPAR_{SIF}$, we first spatially averaged the both $fPAR_{SIF}$ and each OVAIs for each month. This average will greatly reduce the uncertainty in both $fPAR_{SIF}$ and OVAIs. Except for the cropland in Southern Hemisphere which only include 382 0.5°× 0.5° gridcells, all other biome types have at least 2000 gridcells. which will reduce the uncertainty of $fPAR_{SIF}$ to around or less than 0.01 CV ($0.45\sqrt{2000}$). The uncertainties of the OVAIs in this comparison is also less than 0.01 CV. Therefore, the uncertainties from the data sources of this comparison (Figure 4.3) are ignored.

The uncertainties of using OVAIs as a proxy of $fPAR_{SIF}$ come from two major aspects: (1) the uncertainty in the linear regression, which can be quantified as an error term ϵ, and (2) the uncertainty in the independent variables, i.e., OVAIs. The $fPAR_{SIF}$ can be expressed as:

$$fPAR_{SIF} = a \times (OVAI - c) + \epsilon \tag{4.A.5}$$

or using $OVAI_m$ as the proxy of $fPAR_{chl}$:

$$OVAI_m = OVAI - c + \frac{\epsilon}{a} \tag{4.A.6}$$

The error term ϵ for each OVAI can be estimated from the linear regression between $fPAR_{SIF}$ and OVAIs with fixed intercepts c (0.2 for $fPAR_{mod15}$ and NDVI, 0.1 for EVI and 1 for MTCI, Figure 4.A.4). The uncertainty of $fPAR_{SIF}$ ($fPAR_{chl}$) estimated from OVAIs ($OVAI_m$) can be calculated from below:

$$\sigma_{OVAI_m} = \sqrt{{\sigma_{OVAI}}^2 + \left(\frac{\sigma_\epsilon}{a}\right)^2} \tag{4.A.7}$$

Since we used five 8-day (four 10-day for MTCI) average of $OVAI_m$ to compare with LUE_{eco}, this average will reduce the uncertainty contributed from the OVAI (σ_{OVAI}). The adjusted uncertainty ($\sigma_{OVAI'_m}$) is calculated below:

$$\sigma_{OVAI'_m} = \sqrt{\frac{{\sigma_{OVAI}}^2}{n} + \left(\frac{\sigma_\epsilon}{a}\right)^2} \tag{4.A.8}$$

where n is 5 for $fPAR_{mod15}$, NDVI and EVI, and 4 for MTCI. The result for these uncertainties are shown in Table 4.2. The uncertainties of regression slopes in LUE_{canopy} and LUE_{chl} estimation comes from both the uncertainty in GPP from flux tower, and the uncertainty of $fPAR_{canopy}$ and $fPAR_{chl}$ ($OVAI_m$). For a linear regression equation which passes the origin (0, 0) y=ax, the regression slope a can be calculated as:

$$a = \frac{\sum x_i y_i}{\sum x_i^2} \tag{4.A.9}$$

Based on the error propagation law, the uncertainty of a caused by the uncertainty

of x (σ_x)and y (σ_y) will be estimated as:

$$\begin{aligned}\sigma_a^2 &= \sum_{j=1}^{n}\left(\frac{\partial a}{\partial x_j}\sigma_{x_j}\right)^2 + \sum_{j=1}^{n}\left(\frac{\partial a}{\partial y_j}\sigma_{y_j}\right)^2 \\ &= \sum_{j=1}^{n}\left(\frac{y_i}{\sum_{i=1}^{n} x_i^2} - \frac{2x_j}{\left(\sum_{i=1}^{n} x_i^2\right)^2}\right)^2 {\sigma_{x_j}}^2 + \sum_{j=1}^{n}\left(\frac{x_j}{\sum_{i=1}^{n} x_i^2}\right)^2 \sigma_{y_j}^2\end{aligned} \tag{4.A.10}$$

where the uncertainty of y_j (σ_{y_j}) is regarded as 10% of y (LUE_{eco}); the uncertainty of x_j (σ_{x_j}) is a fixed value from Table 4.2. The CV is used to evaluate how convergent of the different definition of LUE (LUE_{eco}, LUE_{canopy}, LUE_{chl}), and can be calculated as:

$$CV = \frac{\sqrt{\frac{\sum_{i=1}^{n}(l_i-\bar{l})^2}{n-1}}}{\bar{l}} \tag{4.A.11}$$

where $\bar{l}$is the mean of l which can be calculated from:

$$\bar{l} = \frac{\sum_{i=1}^{n} l_i}{n} \tag{4.A.12}$$

The uncertainty of $\bar{l}$ ($\sigma_{overline l^2}$) is calculated as:

$$\sigma_{\bar{l}^2} = \frac{1}{n}\sum_{i=1}^{n}\sigma_{l_i}^2 \tag{4.A.13}$$

where the σ_{l_i} denotes the uncertainty of LUE estimated for each biome type. The

error propagation law allows us to calculate the uncertainties in CV of l as:

$$\begin{aligned}
\sigma_{CV}^2 &= \sum_{i=1}^{n}\left(\frac{\partial CV}{\partial l_i}\sigma_{l_i}\right)^2 + \left(\frac{\partial CV}{\partial \bar{l}}\sigma_{\bar{l}}\right)^2 \\
&= \sum_{j=1}^{n}\left(\frac{l_j-\bar{l}}{\bar{l}\sqrt{n-1}}\frac{1}{\sqrt{\sum_{i=1}^{n}\left(l_i-\bar{l}\right)^2}}\sigma_{l_j}\right)^2 + \left(\frac{1}{\sqrt{n-1}}\frac{\frac{\sum_{j=1}^{n}\left(\bar{l}-l_j\right)}{\sqrt{\sum_{k=1}^{n}(l_k-\bar{l})^2}}\bar{l}-\sqrt{\sum_{k=1}^{n}\left(l_k-\bar{l}\right)^2}}{\bar{l}^2}\sigma_{\bar{l}}\right)^2 \\
&= \sum_{j=1}^{n}\left(\frac{1}{n-1}\left(\frac{l_j-\bar{l}}{\bar{l}}\right)^2\frac{1}{\sum_{i=1}^{n}\left(l_i-\bar{l}\right)^2}\sigma_{l_j}{}^2\right) + \frac{1}{n-1}\frac{\sum_{k=1}^{n}\left(l_k-\bar{l}\right)^2}{\bar{l}^4}\sigma_{\bar{l}}{}^2
\end{aligned} \tag{4.A.14}$$

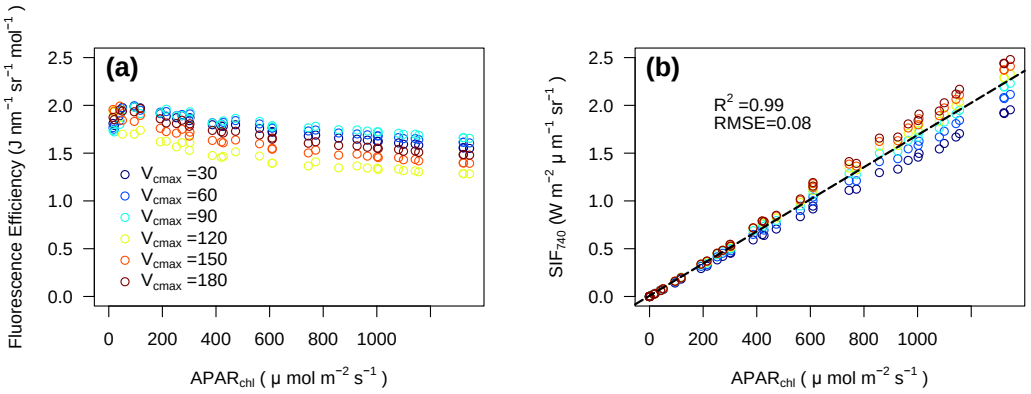


Figure 4.A.1: The relationship between (a) fluorescence efficiency and $APAR_{chl}$, and (b) SIF740 and $APAR_{chl}$ using the simulation from the SCOPE model.

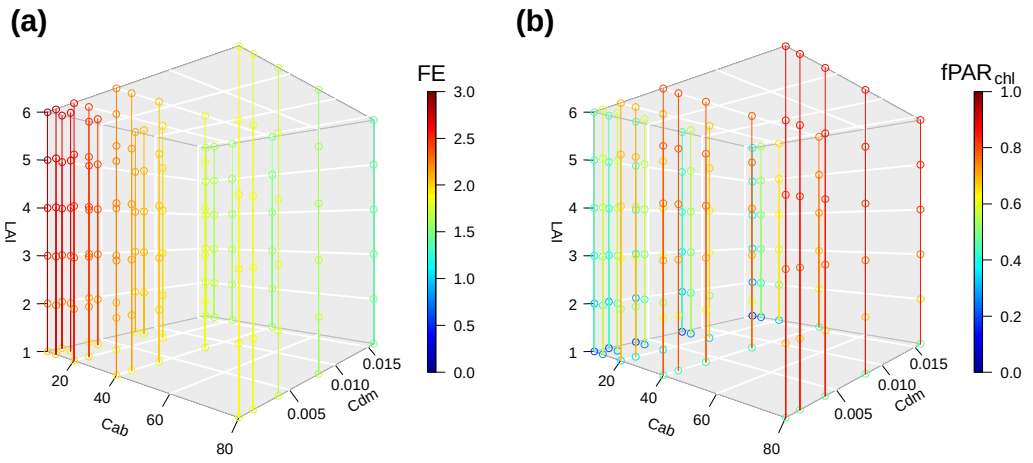


Figure 4.A.2: The variation of (a) fluorescence efficiency (in J nm^{-1} sr^{-1} mol^{-1}) and (b) $fPAR_{chl}$ under all possible combination of LAI, Cab and Cdm values in Table 4.A.1.

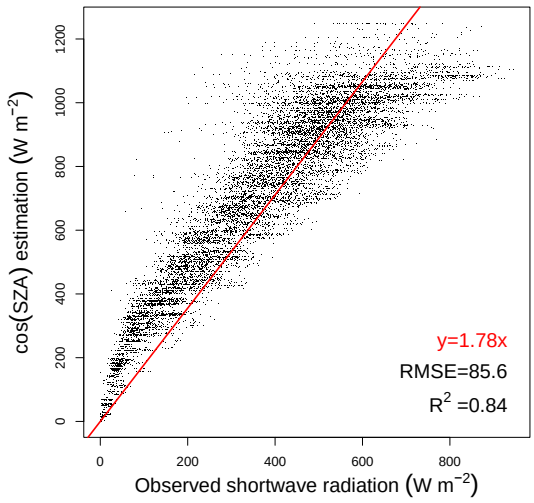


Figure 4.A.3: Comparison between the estimated iPAR at 9:30 am using cos(SZA) and observed iPAR from flux tower sites. This comparison used monthly averaged iPAR values to match the temporal resolution of GOME2 SIF product. Altogether 127 sites were used.

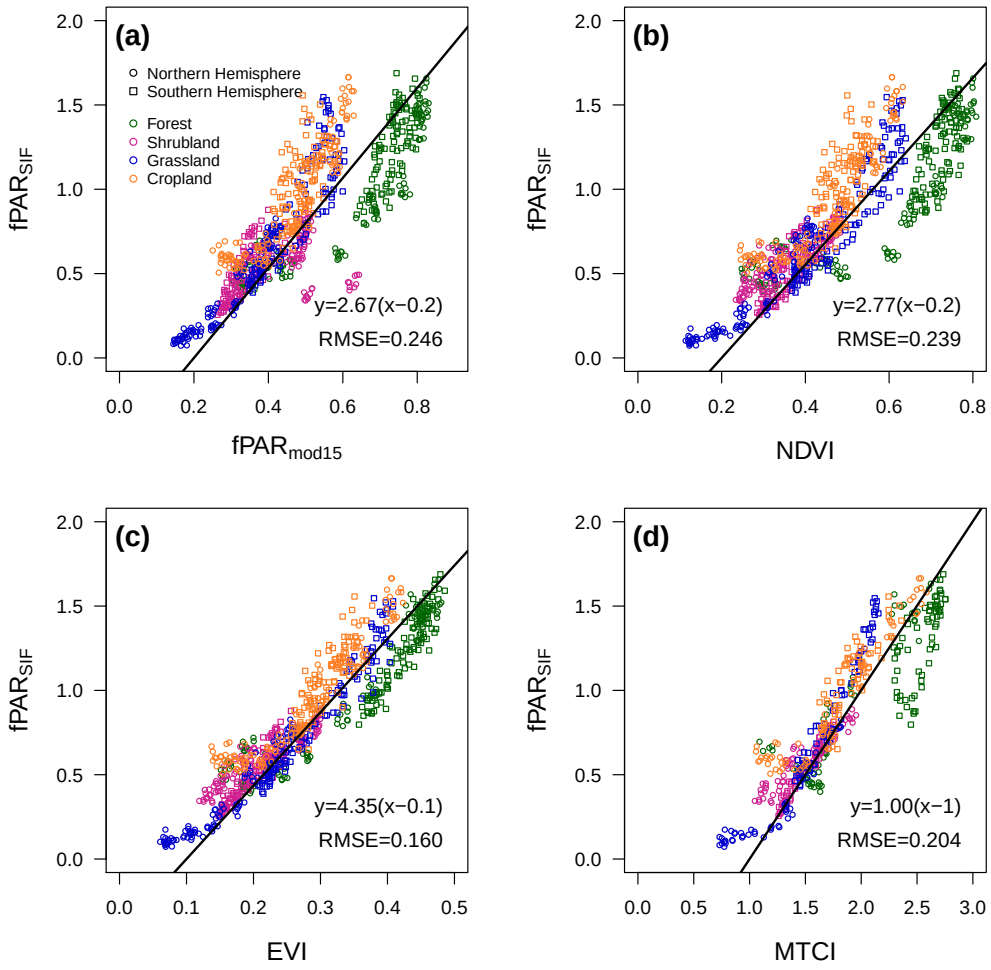


Figure 4.A.4: The linear regression with fixed OVAI intercept, same dataset from Figure 4.3 is used. The RMSE value were used as the uncertainty of regression for error propagation analysis.

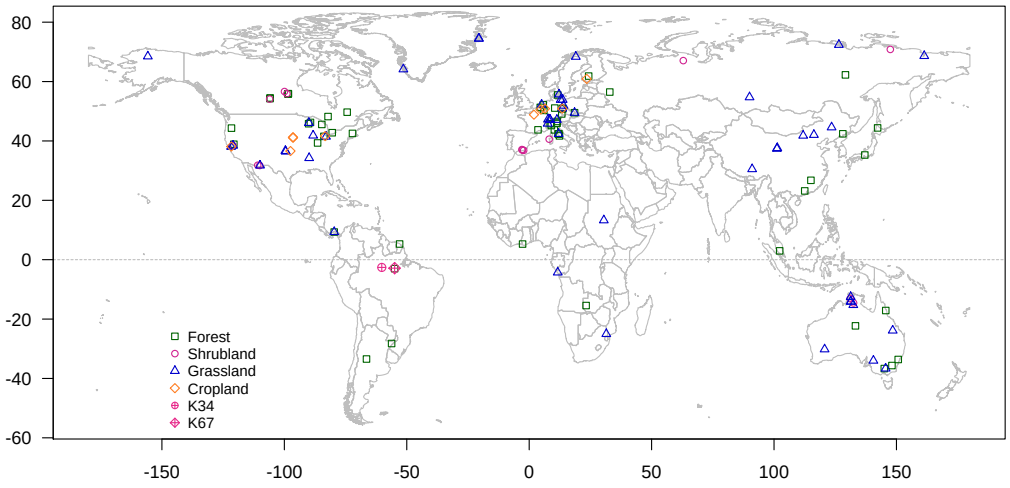


Figure 4.A.5: The spatial distribution of the flux tower sites used in this study. The biome types are regrouped into four types to correspond to the biome type in the SIF analysis. Forest includes ENF, EBF, DNF, DBF, and MF; shrubland includes CSH, OSH, and WSA; grassland includes SAV, GRA, WET; cropland includes CRO and CNV. For the full name of the vegetation types and the IGBP classification of land cover types, please refer to Table 4.A.2. K34 and K67 are two amazon sites used for seasonality analysis.

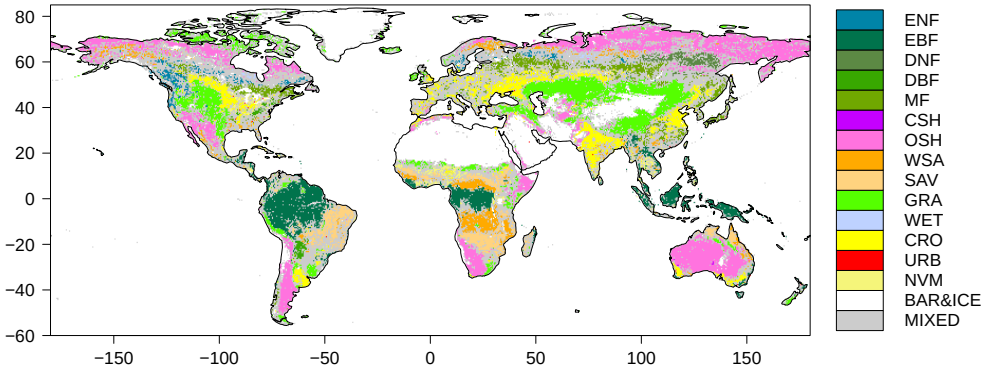


Figure 4.A.6: The land cover type at the resolution of 0.5°× 0.5° for year 2007. Only the "pure" pixels which are used for further analysis are shown. White areas are barren and ice covered; grey are mixed pixels. For a complete list of the legend acronyms, please refer to Table 4.A.2.

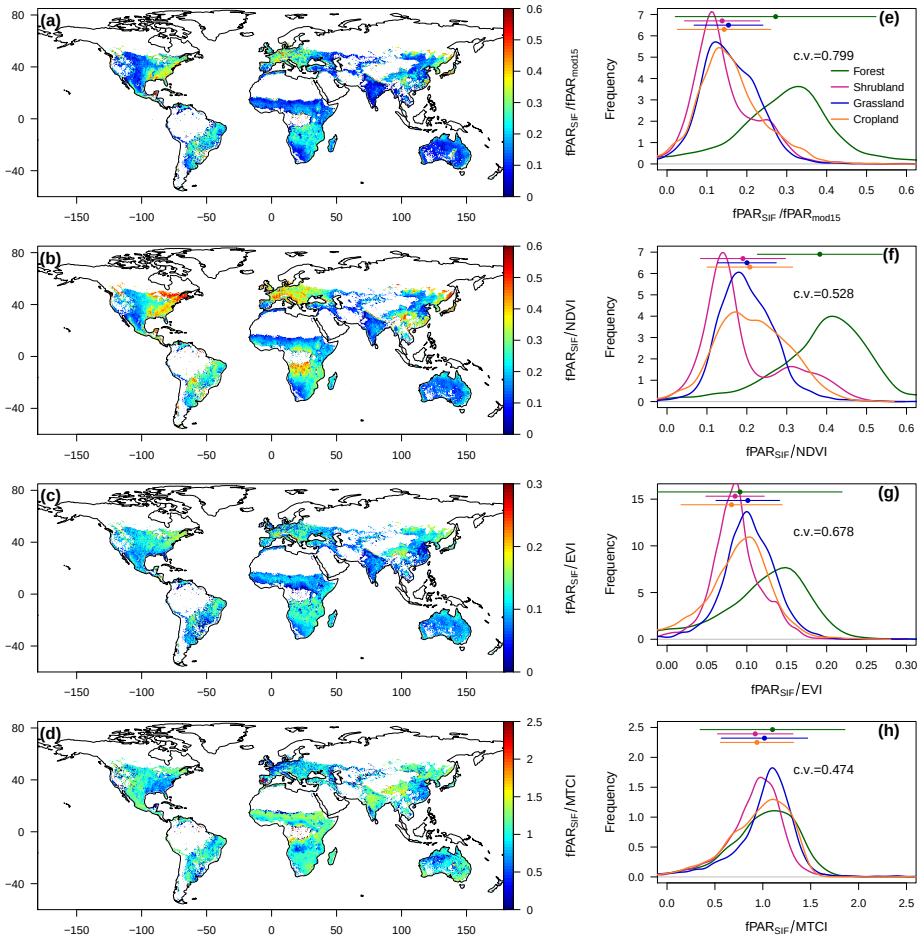


Figure 4.A.7: Spatial pattern (left column) and frequency distribution (right column) of the regression intercept (c in Eq. 4.6). (a, e) fPAR, (b, f) NDVI, (c, g) EVI, (d, h) MTCI. The dots with horizontal bars at the top of frequency distribution figures (e-h) represent the means and standard deviations within each biome type. The SIF and OVAIs data from 2007 to 2015 were used to build the relationship.

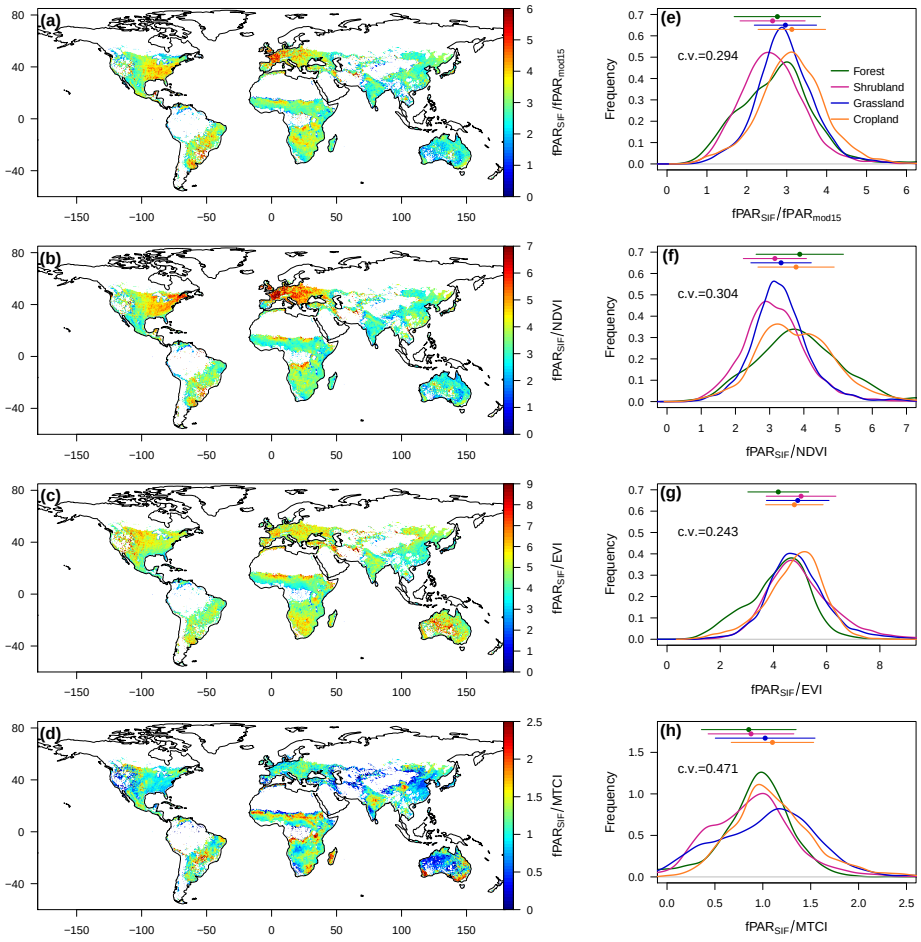


Figure 4.A.8: Spatial distribution (left column) and frequency distribution (right column) of regression slopes without fixing the intercept. The dots with horizontal bars at the top of frequency distribution figures (e-h) represent the means and standard deviations within each biome type. The SIF and OVAIs data from 2007 to 2015 were used to build the relationship.

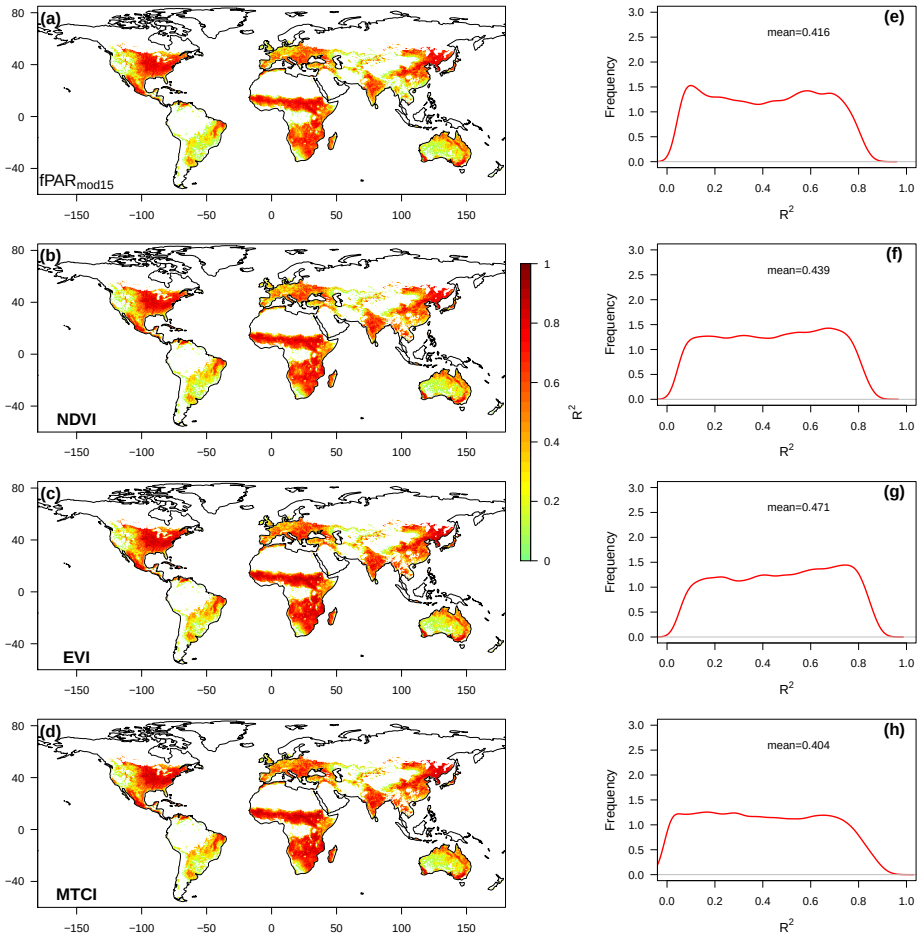


Figure 4.A.9: Spatial pattern (left column) and frequency distribution (right column) of the coefficient of determination (R^2) between $fPAR_{SIF}$ and three optical vegetation activity indicators (OVAIs). (a, d) fPAR, (b, e) NDVI, (c, f) EVI. The SIF and OVAIs data from 2007 to 2015 were used to build the relationship. The low correlation coefficients in tropical regions are caused by high cloud cover and weak seasonality of vegetation.

Table 4.A.1: Parameters settings used in the second run of the SCOPE model with fixed irradiance but variable parameters which result in different f_{esc} values.

Parameter	Symbol	Value	Range
Chlorophyll a+b content (μg cm^{-2})	Cab	0.001, 0.002, 0.004, 0.008, 0.016	0.001–0.02
Dry matter content (g cm^{-2})	Cdm	0.001, 0.002, 0.004, 0.008, 0.016, 0.032, 0.064	0.001–0.05
Leaf area index (m^2/m^{-2})	LAI	1, 2, 3, 4, 5, 6	1–6

Table 4.A.2: Flux tower sites used in this study. IGBP class represents the International Geosphere-Biosphere Programme land cover classification.

Site ID	Site name	Latitude	Longitude	Country	IGBP type[1]	Years used	Reference
AR-SLu	San Luis	-33.4648	-66.4598	Argentina	MF	2010	-
AR-Vir	Virasoro	-28.2395	-56.1886	Argentina	ENF	2012	-
AT-Neu	Neustift/Stubai Valley	47.1167	11.3175	Austria	GRA	2002-2005, 2007-2009, 2011	(Wohlfahrt et al., 2008)
AU-Ade	Adelaide River	-13.0769	131.1178	Australia	WSA	2007-2009	-
AU-ASM	Alice Springs	-22.283	133.249	Australia	ENF	2010-2012	-
AU-Cpr	Calperum	-34.0021	140.5891	Australia	SAV	2011-2013	-
AU-Cum	Cumberland Plains	-33.6133	150.7225	Australia	EBF	2013	-
AU-DaP	Daly River Savanna	-14.0633	131.3181	Australia	GRA	2008-2011, 2013	-
AU-DaS	Daly River Cleared	-14.1593	131.3881	Australia	SAV	2008, 2009, 2011-2013	-
AU-Dry	Dry River	-15.2588	132.3706	Australia	SAV	2010-2013	-
AU-Emr	Emerald, Queensland, Australia	-23.8587	148.4746	Australia	GRA	2011-2013	-
AU-Fog	Fogg Dam	-12.5452	131.3072	Australia	WET	2007, 2008	(Guerschman et al., 2009)
AU-GWW	Great Western Woodlands, Western Australia	-30.1913	120.6541	Australia	SAV	2013	-
AU-RDF	Red Dirt Melon Farm, Northern Territory	-14.5636	132.4776	Australia	WSA	2011, 2012	-
AU-Rig	Riggs Creek	-36.6499	145.5759	Australia	GRA	2012, 2013	-
AU-Rob	Robson Creek, Queensland, Australia	-17.1175	145.6301	Australia	EBF	2014	-
AU-Tum	Tumbarumba	-35.6566	148.1517	Australia	EBF	2004, 2006-2013	(Leuning et al., 2005)
AU-Whr	Whroo	-36.6732	145.0294	Australia	EBF	2012, 2013	-
BE-Bra	Brasschaat (De Inslag Forest)	51.3092	4.5206	Belgium	MF	2000, 2005-2009, 2011-2013	(Janssens et al., 2001)

[1]ENF: evergreen needleleaf forest; EBF: evergreen broadleaf forest; DNF: deciduous needleleaf forest; DBF: deciduous broadleaf forest; MF: mixed forest; CSH: closed shrubland; OSH: open shrubland; WSA: woody savannas; GRA: grassland; SAV: savannas; WET: permanent wetland; CRO: cropland; CNV: cropland/natural vegetation mosaic.

BE-Lon	Lonzee	50.5516	4.7461	Belgium	CRO	2004, 2005, 2007-2009, 2011-2013	(Moureaux et al., 2006)
BE-Vie	Vielsalm	50.3051	5.9981	Belgium	MF	2002, 2003, 2005-2010, 2012-2014	(Aubinet et al., 2001)
BR-Sa3	Santarem-Km83-Logged Forest	-3.018	-54.9714	Brazil	EBF	2001-2003	(Steininger, 2004)
CA-Gro	Ontario - Groundhog River, Boreal Mixedwood Forest	48.2167	-82.1556	Canada	MF	2004-2009, 2013	(McCaughey et al., 2006)
CA-NS1	UCI-1850 burn site	55.8792	-98.4839	Canada	ENF	2002-2005	(Goulden et al., 2006)
CA-NS3	UCI-1964 burn site	55.9117	-98.3822	Canada	ENF	2004, 2005	(Goulden et al., 2006)
CA-NS4	UCI-1964 burn site wet	55.9117	-98.3822	Canada	ENF	2003-2005	(Bond-Lamberty et al., 2004)
CA-NS5	UCI-1981 burn site	55.8631	-98.485	Canada	ENF	2002-2005	(Wang et al., 2002)
CA-NS6	UCI-1989 burn site	55.9167	-98.9644	Canada	OSH	2002, 2004, 2005	(Bond-Lamberty et al., 2004)
CA-NS7	UCI-1998 burn site	56.6358	-99.9483	Canada	OSH	2002, 2004, 2005	(Bond-Lamberty et al., 2004)
CA-Qfo	Quebec - Eastern Boreal, Mature Black Spruce	49.6925	-74.3421	Canada	ENF	2004-2006, 2008-2010	(Bergeron et al., 2007)
CA-SF1	Saskatchewan-Western Boreal, forest burned in 1977	54.4850	-105.8180	Canada	ENF	2003, 2005, 2006	(Amiro et al., 2006)
CA-SF2	Saskatchewan-Western Boreal, forest burned in 1989	54.2539	-105.8780	Canada	ENF	2002-2005	(Amiro et al., 2003)
CA-SF3	Saskatchewan-Western Boreal, forest burned in 1998	54.0916	-106.005	Canada	OSH	2001, 2003-2006	(Amiro et al., 2006)
CA-TP2	Ontario-Turkey Point 1989 Plantation White Pine	42.7744	-80.4588	Canada	ENF	2003-2005	(Arain & Restrepo-Coupe, 2005)
CG-Tch	Tchizalamou	-4.2892	11.6564	Republic of Congo	SAV	2006, 2007, 2009	-
CH-Cha	Chamau grassland	47.2102	8.4104	Switzerland	GRA	2007, 2008, 2010-2012	(Merbold et al., 2014)
CH-Fru	Fruebuel grassland	47.1158	8.5378	Switzerland	GRA	2007, 2008, 2010-2012	(Fritsche et al., 2008)
CH-Oe1	Oensingen1 grass	47.2858	7.7319	Switzerland	GRA	2002-2008	(Ammann et al., 2009)
CN-Cha	Changbaishan	42.4025	128.0958	China	MF	2003-2005	(Zhang et al., 2010)
CN-Cng	Changling	44.5934	123.5092	China	GRA	2008, 2010	-
CN-Dan	Dangxiong	30.4978	91.0664	China	GRA	2004, 2005	-
CN-Din	Dinghushan	23.1733	112.5361	China	EBF	2003, 2005	(Zhang et al., 2010)
CN-Du2	Duolun_grassland (D01)	42.0467	116.2836	China	GRA	2008	(Sun et al., 2011)
CN-Ha2	Haibei Shrubland	37.6086	101.3269	China	WET	2003-2005	-
CN-HaM	Haibei Alpine Tibet site	37.6167	101.3000	China	GRA	2002, 2003	(Kato et al., 2006)
CN-Qia	Qianyanzhou	26.7414	115.0581	China	ENF	2003-2005	(Zhang et al., 2010)
CN-Sw2	Siziwang Grazed (SZWG)	41.7902	111.8971	China	GRA	2011	(Shao et al., 2013)
CZ-BK1	Bily Kriz-Beskidy Mountains	49.5047	18.5411	Czech Republic	ENF	2003-2005, 2007-2012	(Marek et al., 2011)
CZ-BK2	Bily Kriz- grassland	49.4944	18.5429	Czech Republic	GRA	2006-2011	(Marek et al., 2011)
DE-Akm	Anklam	53.8662	13.6834	Germany	WET	2011-2013	-
DE-Gri	Grillenburg- grass station	50.9495	13.5125	Germany	GRA	2004-2006, 2008-2014	(Hussain et al., 2011)
DE-Hai	Hainich	51.0792	10.453	Germany	DBF	2000-2005, 2007-2009, 2012	(Anthoni et al., 2004)

DE-Kli	Klingenberg - cropland	50.8929	13.5225	Germany	CRO	2004-2006, 2009, 2010, 2014	(Prescher et al., 2010)
DE-Lkb	Lackenberg	49.0996	13.3047	Germany	ENF	2009, 2012, 2013	(Lindauer et al., 2014)
DE-Obe	Oberbarenburg	50.7836	13.7196	Germany	ENF	2008-2014	-
DE-RuS	Selhausen Juelich	50.8657	6.4472	Germany	CRO	2011-2014	(Eder et al., 2015)
DE-Spw	Spreewald	51.8923	14.0337	Germany	WET	2010-2012, 2014	-
DE-Tha	Anchor Station Tharandt - old spruce	50.9636	13.5669	Germany	ENF	2000, 2001, 2003-2005, 2007-2014	(Grunwald & Bernhofer, 2007)
DE-Zrk	Zarnekow	53.8759	12.8890	Germany	WET	2013, 2014	(Hahn-Schofl et al., 2011)
DK-Eng	Enghave	55.6905	12.1918	Denmark	GRA	2005	-
DK-NuF	Nuuk Fen	64.1308	-51.3861	Denmark	WET	2008, 2010, 2012-2014	(Westergaard-Nielsen et al., 2013)
DK-Sor	Soroe- LilleBogeskov	55.4859	11.6446	Denmark	DBF	2000, 2002-2012	(Pilegaard et al., 2001)
DK-ZaF	Zackenberg Fen	74.4791	-20.5557	Denmark	WET	2008, 2010, 2013, 2014	-
DK-ZaH	Zackenberg Heath	74.4732	-20.5503	Denmark	GRA	2002, 2003, 2005, 2006, 2008	(Lund et al., 2012)
ES-Amo	Amoladeras	36.8336	-2.2523	Spain	OSH	2010, 2011	-
ES-LgS	Laguna Seca	37.0979	-2.9658	Spain	OSH	2007-2009	(Reverter et al., 2010)
ES-LJu	Llano de los Juanes	36.9266	-2.7521	Spain	OSH	2004, 2006, 2008, 2010, 2011, 2013	(Serrano-Ortiz et al., 2007)
FI-Hyy	Hyytiala	61.8475	24.2950	Finland	ENF	2000, 2001, 2003-2005, 2008-2014	((Suni et al., 2003)
FI-Jok	Jokionen agricultural field	60.8986	23.5135	Finland	CRO	2001, 2003	(Lohila et al., 2004)
FR-Gri	Grignon (after 6/5/2005)	48.8442	1.9519	France	CRO	2005-2011, 2014	(Loubet et al., 2011)
FR-Pue	Puechabon	43.7414	3.5958	France	EBF	2001-2012	(Lhomme et al., 2001)
GF-Guy	Guyaflux	5.2788	-52.9249	French Guyana	EBF	2004-2006, 2008-2012	(Epron et al., 2006)
GH-Ank	Ankasa	5.2685	-2.6942	Ghana	EBF	2011, 2012, 2014	-
IT-CA1	Castel d'Asso1	42.3804	12.0266	Italy	DBF	2011, 2012	(Sabbatini et al., 2016)
IT-CA2	Castel d'Asso2	42.3772	12.0260	Italy	GRA	2011, 2013	(Sabbatini et al., 2016)
IT-CA3	Castel d'Asso 3	42.3800	12.0222	Italy	DBF	2013	(Sabbatini et al., 2016)
IT-Cp2	Castelporziano2	41.7043	12.3573	Italy	EBF	2013	-
IT-Isp	Ispra ABC-IS	45.8126	8.6336	Italy	DBF	2014	(Ferrea et al., 2012)
IT-La2	Lavarone2	45.9542	11.2853	Italy	ENF	2001	-
IT-Lav	Lavarone (after 3/2002)	45.9562	11.2813	Italy	ENF	2003-2011	(Fiora & Cescatti, 2006)
IT-Noe	Sardinia/Arca di NoÃÍ	40.6061	8.1515	Italy	CSH	2004-2008, 2010	(Beier et al., 2009)
IT-PT1	Zerbolo-Parco Ticino- Canarazzo	45.2009	9.0610	Italy	DBF	2002, 2004	(Migliavacca et al., 2009)
IT-Ren	Renon/Ritten (Bolzano)	46.5869	11.4337	Italy	ENF	2001, 2002, 2004-2010, 2012, 2013	(Marcolla et al., 2005)
IT-Ro1	Roccarespampani 1	42.4081	11.9300	Italy	DBF	2001-2004, 2006-2008	(Rey et al., 2002)
IT-Ro2	Roccarespampani 2	42.3903	11.9209	Italy	DBF	2002-2008, 2010, 2012	(Tedeschi et al., 2006)
IT-SRo	San Rossore	43.7279	10.2844	Italy	ENF	2002, 2003, 2006-2012	(Chiesi et al., 2005)
IT-Tor	Torgnon	45.8444	7.5781	Italy	GRA	2008-2010, 2012, 2013	(Galvagno et al., 2013)
JP-MBF	Moshiri Birch Forest Site	44.3869	142.3186	Japan	DBF	2004	-
JP-SMF	Seto Mixed Forest Site	35.2617	137.0788	Japan	MF	2003, 2005, 2006	-

MY-PSO	Pasoh Forest Reserve (PSO)	2.973	102.3062	Malaysia	EBF	2003-2009	-
NL-Hor	Horstermeer	52.2404	5.0713	Netherlands	GRA	2005, 2007, 2008, 2010	-
NL-Loo	Loobos	52.1666	5.7436	Netherlands	ENF	2000-2002, 2004-2014	(Dolman et al., 2002)
PA-SPn	Sardinilla Plantation	9.3181	-79.6346	Panama	DBF	2007, 2008	(Wolf et al., 2011)
RU-Che	Cherskii	68.613	161.3414	Russia	WET	2002-2004	(Corradi et al., 2005)
RU-Cok	Chokurdakh	70.8291	147.4943	Russia	OSH	2003, 2006, 2007, 2009, 2011, 2012	(van Huissteden et al., 2005)
RU-Fyo	Fyodorovskoye wet spruce stand	56.4615	32.9221	Russia	ENF	2000-2006, 2008, 2009, 2011-2013	(Kurbatova et al., 2008)
RU-Ha1	Ubs Nur-Hakasija-grassland	54.7252	90.0022	Russia	GRA	2003, 2004	-
RU-Sam	Samoylov Island-Lena Delta	72.3738	126.4958	Russia	GRA	2005, 2006, 2008	(Kutzbach et al., 2007)
RU-SkP	Spasskaya Pad larch	62.255	129.168	Russia	DNF	2012-2014	-
RU-Vrk	Seida/Vorkuta	67.0547	62.9405	Russia	CSH	2008	-
SD-Dem	Demokeya	13.2829	30.4783	Sudan	SAV	2007-2009	(Ardö et al., 2008)
SE-St1	Stordalen Forest-Mountain Birch	68.3542	19.0503	Sweden	WET	2012, 2014	-
US-ARM	ARM Southern Great Plains site- Lamont	36.6058	-97.4888	USA	CRO	2003, 2004, 2006-2010, 2012	(Fischer et al., 2007a)
US-Blo	Blodgett Forest	38.8953	-120.633	USA	ENF	2003, 2004, 2006, 2007	(Misson et al., 2005)
US-CRT	Curtice Walter-Berger cropland	41.6285	-83.3471	USA	CRO	2011-2013	(Chu et al., 2014)
US-Goo	Goodwin Creek	34.2547	-89.8735	USA	GRA	2002-2004, 2006	-
US-Ha1	Harvard Forest EMS Tower (HFR1)	42.5378	-72.1715	USA	DBF	2000, 2001, 2003-2012	(Goulden et al., 1996)
US-Ivo	Ivotuk	68.4865	-155.75	USA	WET	2004, 2006, 2007	(Epstein et al., 2004)
US-Los	Lost Creek	46.0827	-89.9792	USA	WET	2001-2008, 2010, 2014	(Sulman et al., 2009)
US-Me6	Metolius Young Pine Burn	44.3233	-121.608	USA	ENF	2010-2012	(Ruehr et al., 2012)
US-MMS	Morgan Monroe State Forest	39.3232	-86.4131	USA	DBF	2000-2006, 2009, 2010, 2013, 2014	(Schmid et al., 2000)
US-Myb	Mayberry Wetland	38.0498	-121.765	USA	WET	2011-2014	-
US-Ne2	Mead - irrigated maize -soybean rotation site	41.1649	-96.4701	USA	CRO	2002, 2004, 2006, 2008	(Suyker et al., 2005)
US-Ne3	Mead - rainfed maize-soybean rotation site	41.1797	-96.4397	USA	CRO	2002, 2004, 2006, 2008, 2010, 2012	(Suyker et al., 2004)
US-Oho	Oak Openings	41.5545	-83.8438	USA	DBF	2004-2011, 2013	(Noormets et al., 2008)
US-SRM	Santa Rita Mesquite	31.8214	-110.866	USA	WSA	2004-2008, 2010-2014	(Scott et al., 2009)
US-Syv	Sylvania Wilderness Area	46.242	-89.3477	USA	MF	2002, 2012-2014	(Desai et al., 2005)
US-Ton	Tonzi Ranch	38.4316	-120.966	USA	WSA	2002-2007, 2009, 2012-2014	(Xu & Baldocchi, 2004)
US-Tw3	Twitchell Alfalfa	38.1159	-121.647	USA	CRO	2013, 2014	-
US-UMd	UMBS Disturbance	45.5625	-84.6975	USA	DBF	2008-2014	(Nave et al., 2011)
US-Var	Vaira Ranch- Ione	38.4133	-120.951	USA	GRA	2000-2007, 2009, 2011-2014	(Ma et al., 2007)
US-WCr	Willow Creek	45.8059	-90.0799	USA	DBF	2000, 2001, 2003-2006, 2011, 2013, 2014	(Cook et al., 2004)

US-Whs	Walnut Gulch Lucky Hills Shrub	31.7438	-110.052	USA	OSH	2007, 2008, 2010, 2011, 2013, 2014	(Scott et al., 2006)
US-Wkg	Walnut Gulch Kendall Grasslands	31.7365	-109.942	USA	GRA	2006-2008, 2010-2014	(Scott et al., 2010)
US-WPT	Winous Point North Marsh	41.4646	-82.9962	USA	WET	2011-2013	(Chu et al., 2014)
ZA-Kru	Skukuza- Kruger National Park	-25.0197	31.4969	South Africa	SAV	2000, 2009-2012	(Williams et al., 2009)
ZM-Mon	Mongu	-15.4378	23.2528	Zambia	DBF	2007-2009	(Merbold et al., 2011)

Table 4.A.3: Root mean square error (RMSE) for the regressions between LUE_{PAR} and OVAI or $OVAI_m$, with all biome types combined together.

	$fPAR_m$	fPAR	$NDVI_m$	NDVI	EVI_m	EVI	$MTCI_m$	MTCI
clear	0.00726	0.00722	0.00614	0.00661	0.00551	0.00558	0.00541	0.00613
cloudy	0.00742	0.00692	0.00650	0.00653	0.00671	0.00629	0.00590	0.00534

Table 4.A.4: Coefficient of determination (R^2) for the regressions between LUE_{PAR} and OVAI or $OVAI_m$, with all biome types combined together.

	$fPAR_m$	fPAR	$NDVI_m$	NDVI	EVI_m	EVI	$MTCI_m$	MTCI
clear	0.39	0.40	0.56	0.49	0.64	0.63	0.69	0.60
cloudy	0.08	0.20	0.30	0.29	0.25	0.34	0.40	0.51

Chapter 5: Canopy and physiological controls of GPP during drought and heat wave

Abstract

Vegetation indices (VIs) derived from satellite reflectance measurements are often used as proxies of canopy activity to evaluate the impacts of drought and heatwave on gross primary production (GPP) through production efficiency models (PEMs). However, GPP is also regulated by physiological processes that cannot be directly detected using reflectance measurements. This study analyzes the co-limitation of canopy and plant physiology (represented by VIs and climate anomalies, respectively) on GPP during 2003 European summer drought and heatwave for 15 Euroflux sites. During the entire drought period, spatial pattern of GPP anomalies can be quantified by relative changes in VIs. We also find that GPP sensitivity to relative canopy changes is higher for non-forest ecosystems (1.81±0.32 %GPP/%EVI), while GPP sensitivity to physiological changes is higher for forest ecosystems (0.18±0.05 g C m^{-2} day^{-1}/hPa). A conceptual model is further built to better illustrate the canopy and physiological controls on GPP during drought periods.

5.1 Introduction

Both drought frequency and intensity are predicted to increase along with global warming (Dai, 2012; Easterling et al., 2000b), which can alter the carbon cycle through inhibiting photosynthesis (Flexas & Medrano, 2002), increasing mortality rate (Allen et al., 2010; Peng et al., 2011a), and affecting ecosystem structure (Saatchi et al., 2013)Ṫhe decrease of net primary production caused by drought was estimated to be 0.55 Pg C globally for the first decade in the 21st century (Zhao & Running, 2010). The most direct effect of drought came from the declined gross primary produc-

tion (GPP) (Ciais et al., 2005). Many approaches have been proposed to estimate GPP at regional or global scale: 1) process-based dynamic global vegetation models (DGVMs) (Arora et al., 2013; Sitch et al., 2008), 2) remote sensing based production efficiency models (PEMs) (Zhao & Running, 2010), 3) and eddy flux based data driven models (Beer et al., 2010; Jung et al., 2011). Vetter et al. (2008) compared the predictions of these models for GPP and NEE anomalies during the 2003 European drought and heatwave. But the results from seven models were divergent, with estimates of drought induced GPP decline ranging from -0.02 to -0.27 Pg C. A clear difference has also been found between the eddy flux based data driven models which show little interannual variability (IAV) and the process-based models which exhibit larger IAV (Anav et al., 2015). Since drought is one of the most important factors which causes the IAV of GPP (Zscheischler et al., 2014a), it is crucial to improve the accuracy of GPP estimation during drought and heatwave to better understand the ecosystem responses under future climate.

Drought and heatwave have two direct impacts on plant photosynthesis (van der Molen et al., 2011). The first impact is the physiological response to water deficit and high temperature, including the reduction in enzyme activity, and stomatal conductance to prevent water loss (Flexas & Medrano, 2002; Hetherington & Woodward, 2003; Reichstein et al., 2002). These effects have been often related to temperature, vapor pressure deficit (Farquhar et al., 1980), and soil moisture deficit (Baldocchi et al., 2004). The second impact is the changes of vegetation canopy in response to drought, which includes leaf withering and senescence. The canopy changes can be represented by the decrease of leaf area index (LAI), and observed by satellites (Zhang et al., 2013b). These two processes also take effects at different time scales: the physiological processes respond at the scale of minutes to days, while the vegetation canopy changes occur at a scale of days to weeks.

Satellite-based PEMs differ in their approaches to quantify physiological and canopy responses to drought and heat. Some PEMs use VPD related scalars, e.g., MODIS PSN (Moderate Resolution Imaging Spectroradiometer Photosynthesis) (Running et al., 2004), CFLUX (carbon flux model) (Turner et al., 2006). However, GPP responses to VPD and temperature are different among ecosystems, even species (Blackman et al., 2009). For example, both the stomata characteristics (size and density) and intrinsic water use efficiency (A/gs, carbon assimilation rate divided by stomatal conductance) differ among individual vegetation types (Hetherington & Woodward, 2003). Therefore, using universal parameters to qualify these limitations will introduce biases. Some PEMs use transformed vegetation indices (VIs) to account for water stress, including VPM (vegetation photosynthesis model) (Xiao et al., 2004a), VPRM (vegetation photosynthesis and respiration model) (Mahadevan et al., 2008) and modified TG (temperature and greeness) model (Sims et al., 2014). However, the vegetation canopy responds to prolonged drought and heat, and different ecosystems have different spectral sensitivities to water stress (SSWS), i.e., the changes in canopy characteristics which can be captured by satellite under water stress (Sims et al., 2014). Trees with deeper roots are more resistant to decreased soil water, and have low SWSS. By contrast, SWSS are generally higher for grassland and shrubland. In addition, there may be a time lag between leaf senescence and GPP decline for most plants, which makes simulating GPP under drought even more difficult (Frank et al., 2015). Dong et al. (2015) suggested that remote sensing data-driven models that do not include water limitation factors performed much worse during drought periods. However, even for the models discussed above which consider water stress, their performances are not satisfied (Liu et al., 2015; Schaefer et al., 2012). The major problem is the over-sensitivity of VPD related water stress and under-sensitivity of VIs related water stress. Recent studies also high-

light the complexity of water stress limitation on GPP and light use efficiency (Yuan et al., 2014b; Zhang et al., 2015b). Improving PEMs performance is critical to better diagnose the effects of droughts and heatwaves on GPP.

The 2003 summer climate anomaly in Europe is suitable to investigate physiological and canopy controls on regional GPP, because of the relatively high density of flux tower sites, different ecosystems affected, and the spatial extent of the drought (Schar et al., 2004). In this paper, we address two specific questions: (1) Are satellite retrieved VIs sufficient to quantify the spatial differences in GPP anomalies across different ecosystems? (2) Are satellite retrieved VIs able to track the temporal GPP anomalies at each flux tower site?

5.2 Materials and Methods

5.2.1 Data

The data used in this study includes remotely sensed vegetation indices (VIs) and land surface temperature (LST), as well as vapor pressure deficit (VPD) and GPP measurements from the in situ flux tower records. VIs and LST for each site are derived from MODIS (MOD09A1 and MOD11A2). Even during drought period, there exists atmospheric contamination on data quality (Zhang et al., 2015b). In order to eliminate these corrupted observations, a data quality check and gap-filling algorithm was applied to these variables (Figure 5.A.1). The eddy flux data are from 15 flux tower sites in Europe, all of which experienced a decline of GPP during the 2003 drought and heatwave period (Figure 5.1a-c, Table 5.A.1). For more information about the data usage and processing, please refer to the Appendix.

5.2.2 Method

GPP can be calculated based on a function of a maximum potential value, , reduced by both canopy control (CC) and physiological control (PC):

$$GPP = GPP_{max} \times f(CC, PC) \tag{5.1}$$

For each specific stable ecosystem, the for a specific period can be regarded as a constant. The canopy control is related to three different characteristics of vegetation canopy: 1) leaf area or canopy coverage, 2) canopy pigments such as chlorophyll content, and 3) canopy water content (Xiao et al., 2005b). The physiological control is the environmental stress on carbon fixation process through stomatal conductance, enzyme activity, etc. We hypothesize that canopy control and physiological control are independent because they respond at different time scales. Therefore, the differential form of GPP with respect to these two controls is as follows:

$$dGPP = GPP_{max} \times (\frac{\partial GPP}{\partial CC} dCC, \frac{\partial GPP}{\partial PC} dPC) \tag{5.2}$$

the relative change in GPP can be calculated as:

$$\frac{dGPP}{\overline{GPP}} = GPP_{max} \times (\frac{\partial GPP/\overline{GPP}}{\partial CC/\overline{CC}} \frac{dCC}{\overline{CC}} + \frac{\partial GPP/\overline{GPP}}{\partial PC/\overline{PC}} \frac{dPC}{\overline{PC}}) \tag{5.3}$$

If we change the form of equations (2) and (3) and replace $GPP_{max} \times \frac{\partial GPP}{\partial CC}$ and $GPP_{max} \times \frac{\partial GPP}{\partial CC}$ with Φ_{CC} and Φ_{PC} , $GPP_{max} \times \frac{\partial GPP/\overline{GPP}}{\partial CC/\overline{CC}}$ and $GPP_{max} \times \frac{\partial GPP/\overline{GPP}}{\partial PC/\overline{PC}}$ with ϕ_{CC} and ϕ_{PC}, Eq. (5.2) and (5.3) are rewritten as:

$$\Delta GPP = \Phi_{CC} \times \Delta CC + \Phi_{PC} \times \Delta PC \tag{5.4}$$

$$\delta GPP = \phi_{CC} \times \delta CC + \phi_{PC} \times \delta PC \tag{5.5}$$

Φ_{CC} and Φ_{PC} indicate the sensitivity of GPP to the absolute change (Δ) of canopy and physiological control, respectively. ϕ_{CC} and ϕ_{PC} represent the sensitivity of GPP to the relative change (δ) of canopy and physiological control, respectively. The absolute anomaly (Δ) and relative anomaly (δ) can be calculated as below:

$$\Delta_{\gamma}^{i} = \gamma_i - \overline{\gamma_i} \tag{5.6}$$

$$\delta_{\gamma}^{i} = \frac{\gamma_i - \overline{\gamma_i}}{\overline{\gamma_i}} \tag{5.7}$$

where γ stands for different variables (e.g., VIs, GPP, VPD). γ_i and $\overline{\gamma_i}$ represent the ith observation for each 8-day period (hereafter referred to as week) in 2003, and the average value of the variable γ for the corresponding week for normal years, respectively. For each site, the normal years are defined as the years with flux observations, excluding 2003. $\overline{\Delta_\gamma}$ and $\overline{\delta_\gamma}$ denote the anomalies calculated from the entire drought period in 2003 compared to normal years. The drought period is defined as week 20 to 39 (June 2^{nd} to November 8^{th}) in 2003, when the average δ_{GPP} of the 15 flux sites drops below 0 (Figure 5.1b, c)

The two limitations are represented by indicators that can be directly observed. The canopy control (CC) is represented by three VIs, namely the normalized difference vegetation index (NDVI), the enhanced vegetation index (EVI), and the land surface water index (LSWI). These three VIs are selected because they are related to different properties of the canopy. NDVI is related to the leaf area [Carlson and Ripley, 1997], EVI is related to the green leaf (Zhang et al., 2005), and LSWI is related to the water content in the canopy (Xiao et al., 2004b). The physiological control (PC) is represented by satellite-retrieved LST and VPD from flux tower measurements,

both of which are frequently used in PEMs.

Based on absolute and relative anomalies (Eq. (5.6) and (5.7)), we investigate the relationship between GPP anomalies and anomalies of VIs, LST, and VPD for the entire drought period across all flux sites ($\overline{\Delta_\gamma}$ and $\overline{\delta_\gamma}$ were used). To explore the respective effects of the physiological and canopy controls during the drought period for each site, we first use VPD as the physiological control and analyze the partial correlation between dependent variable Δ_{GPP} or δ_{GPP} and two corresponding independent variables (Δ_{VIs} or δ_{VIs}, and Δ_{VPD} or δ_{VPD}), represented by $\rho_\Delta^{GPP,\gamma}$ or $\rho_\delta^{GPP,\gamma}$ (γ represents VIs or VPD, with the other controlled), respectively. We also consider a lagged response of VIs to GPP change with lags of 0 to 5 weeks. Previous studies suggested that lags from weeks to months exist for satellite retrieved canopy signals and precipitation decline (Ji & Peters, 2003; Wan et al., 2004). LST and VPD, which directly affect enzyme activity and stomatal conductance, respectively, are not analyzed with lags (confirmed by Figure 5.A.3, 5.A.4). Based on the partial correlation analysis, we use multi-variate regression to fit the GPP data into Eq. (5.4) and (5.5) to get the GPP sensitivity to absolute change (Φ) and relative change (ϕ) of canopy and physiological control, respectively. We also take the lag effect on canopy control into consideration; regressions are conducted only for the lags with highest partial correlation in the previous analysis. All these procedures are also conducted using LST instead of VPD as the physiological control.

5.3 Results

5.3.1 Sensitivity of GPP anomalies to changes in vegetation indices and climate over the entire drought period

All the 15 sites have negative Δ_{GPP} and δ_{GPP} during the drought period (Table 5.A.1). In terms of absolute anomalies, Δ_{GPP} is largest for grassland (GRA, -377.8 to -207.3 g C m^{-2}) and deciduous broadleaf forest (DBF, -321.0 to -175.0 g C m^{-2}), followed by evergreen needleleaf forest (ENF, -272.3 to -93.5 g C m^{-2}), while three other vegetation types (EBF, MF, OSH) have a smaller Δ_{GPP}. In terms of relative anomalies, non-forest sites (GRA and OSH) show a much larger δ_{GPP} decline (-57.2% to -17.8%) compared to the forest sites (-28.6% to -2.8%) (Figure 5.1i, Table 5.A.1).

Figure 5.1 (d-h) shows the relationship between the averaged anomalies of GPP and three VIs, LST, and VPD during the entire drought period. The canopy responses during the drought period are divergent among sites, and show only slight differences when different VIs are used. $\overline{\delta_{VIs}}$ for non-forest are mostly negative, suggesting that the canopy properties are significantly affected during the drought. In contrast, $\overline{\delta_{VIs}}$ for all the forest sites are close to zero, indicating that the canopy optical characteristics merely change. The coefficients of determination between δ_{GPP} and δ_{VIs} are high ($R^2 > 0.73$). The slopes of the regressions are lowest for LSWI (0.79), suggesting that a small change in GPP corresponds to a larger change in LSWI. The intercepts for the three VIs are similar ($\sim$ 20%). When using absolute anomalies, the correlation between GPP and VIs are much lower (Figure 5.A.2).

We also investigated the relationship between the anomalies of GPP and physiological indicators (LST and VPD). During the drought period compared to normal years, LST and VPD increase by 0.49 to 3.71°C and 0.50 to 6.83 hPa, respectively (Table 5.A.1). Correlation between $\overline{\delta_{GPP}}$ and $\overline{\delta_{LST}}$ is stronger (R^2 = 0.25) than that

between $\overline{\delta_{GPP}}$ and $\overline{\delta_{VPD}}$ (R^2 = 0.01), or air temperature ($\overline{\delta_{T_{air}}}$, R^2 = 0.01) measured at flux tower sites (Figure 5.1g, h, Figure 5.A.5). Even though all VIs and climate variables respond to drought, only $\overline{\delta_{VIs}}$ show significant correlation with $\overline{\delta_{GPP}}$. This indicates that the spatial difference, i.e., from site to site, of the GPP decline due to drought and heatwave can be partially explained by the averaged relative changes in VIs. However, for the drought affected regions, even when the average VIs did not change, GPP can still decline ~ 20% (intercept in Figure 5.1d, e, f).

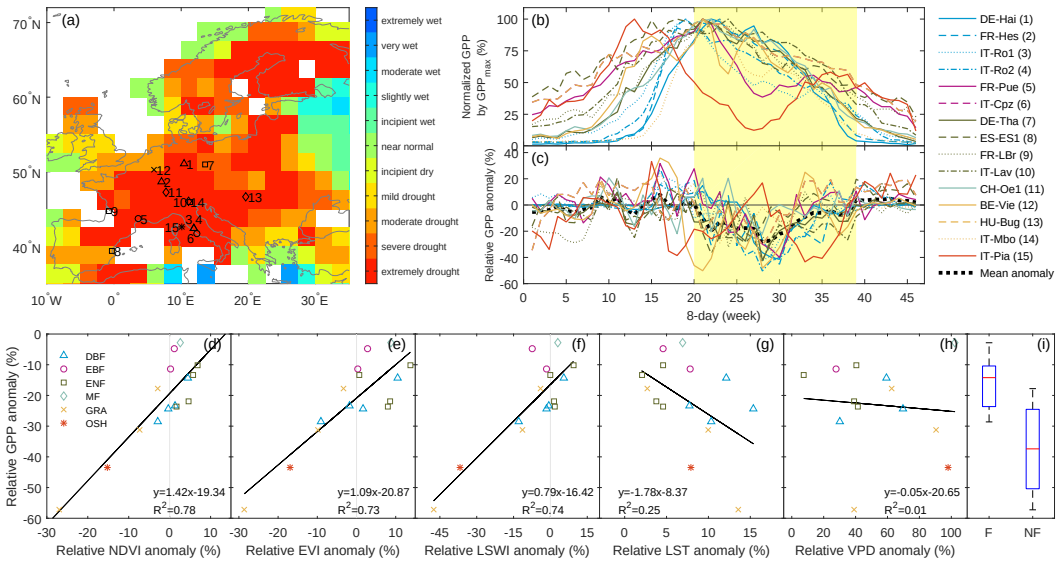


Figure 5.1: (a) Location of the flux tower sites used in this study, and the averaged drought intensity from June to October in 2003. The drought intensity was indicated by the Palmer Drought Severity Index (PDSI) averaged over the drought period. PDSI data was down loaded from the National Center for Atmospheric Research Climate & Global Dynamics (NCAR-CGD) website (http://www.cgd.ucar.edu/cas/catalog/climind/pdsi.html) [Dai, 2012]. Site ID in the map can be interpreted using the legend for (b). (b) Seasonal GPP normalized by maximum GPP for normal years. (c) GPP relative anomalies for 2003 for 15 flux tower sites. Different colors represent different vegetation types, using the same colors as (d). The black dashed line represents the average anomaly of all the 15 sites. (d-h) Relationship of averaged relative anomalies for the entire drought and heatwave period (δ_γ) between GPP and vegetation indices (EVI, NDVI, LSWI), land surface temperature (LST), and vapor pressure deficit (VPD). (i) GPP decrease for forest (F) and non-forest (NF) in relative anomaly.

5.3.2 *Sensitivity of GPP anomalies to changes in vegetation indices and climate at 8-day intervals during the drought period*

We calculated the partial correlations between GPP and VIs (with climate variables in control) or climate variables (with VIs in control) in both absolute and relative anomalies, and investigated GPP responses to canopy and physiological controls. We chose EVI with different time lags to represent the canopy control, and VPD with no lag for the physiological control because the anomalies of these predictors have higher correlations with GPP anomalies. There are clear differences between forest and non-forest ecosystems with respect to vegetation canopy versus physiological controls (Figure 5.2). All non-forest sites, while only about half of the forest sites show strong partial correlation ($\rho > 0.5$) in relative anomalies ($\rho_{\delta}^{GPP,EVI}$, Figure 5.2c). The lags where the highest correlation is reached are also shorter for non-forest than forest sites. Strong partial correlation ($\rho > 0.5$) between GPP and VPD in absolute anomalies ($\rho_{\Delta}^{GPP,VPD}$) is found for most (7 out of 9) forest sites (Figure 5.2b). In contrast, $\rho_{\Delta}^{GPP,VPD}$ is positive for most non-forest sites. The correlations calculated using relative anomalies ($\rho_{\delta}^{GPP,VPD}$) are weaker than that using absolute anomalies ($\rho_{\Delta}^{GPP,VPD}$, Figure 5.2d). These analyses were also conducted for the two other VIs (NDVI and LSWI) with VPD, and all three VIs with LST; the correlations become weaker when using LST instead of VPD (Figure 5.A.6–5.A.10).

We further use eq. (5.4) and (5.5) to decompose the canopy and physiological control, and the results are shown in Table 5.1. When using absolute anomalies (Δ), non-forest ecosystems usually have a higher level of significance for canopy sensitivity (Φ_{CC}) in the regression model, with an average value of 19.85±9.25 g C m^{-2}/(EVI); forest ecosystems have a higher level of significance for physiological sensitivity (Φ_{PC}), with an average value of -0.18±0.05 g C $m^{-2}day^{-1}$/hPa). When

using the relative anomalies (δ), canopy sensitivity (ϕ_{CC}) shows a higher control of GPP for non-forest sites (1.81±0.32 %GPP/%EVI), but the physiological sensitivity (ϕ_{PC}) has much lower p-values for forest ecosystems. We also found that all sensitivities (Φ_{CC}, Φ_{PC}, ϕ_{CC} and ϕ_{PC}) have a large range of variation for all ecosystems. Forest and non-forest ecosystems show a distinct difference ($p < 0.1$, student's t test) for three sensitivity factors except for Φ_{CC} (Figure 5.A.11). Canopy sensitivities (Φ_{CC}, ϕ_{CC}) are lower for forest than non-forest while physiological sensitivities (Φ_{PC}, ϕ_{PC}) are opposite in absolute values. This regression analysis confirms the finding of the partial correlation analysis and the results are similar when using different canopy indicators (NDVI, LSWI) and physiological indicator (LST) (Table 5.A.2-5.A.6).

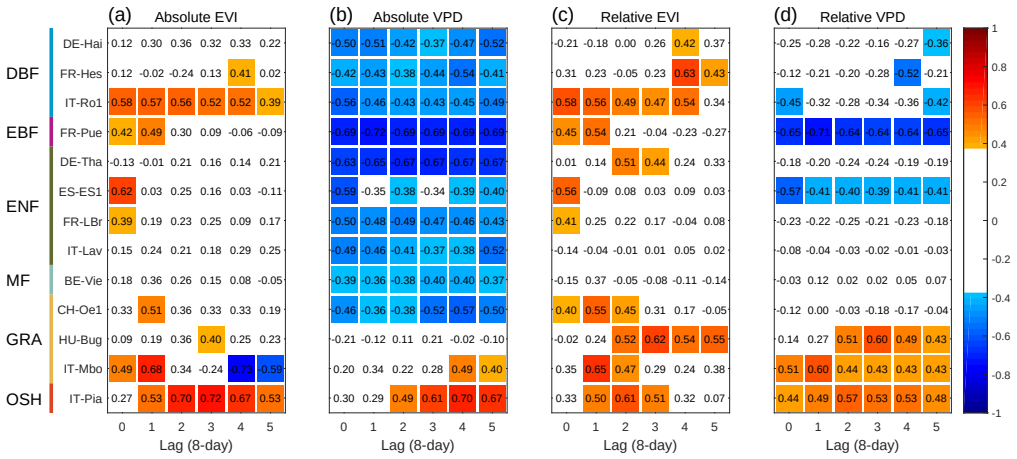


Figure 5.2: Partial correlation between anomalies in GPP and anomalies in EVI (a, c) and VPD (b, d). EVI with different lags were used. (a, b) are using absolute anomalies (Δ_γ), and (c, d) are using relative anomalies (δ_γ). Only partial correlations that are significant at 0.1 level ($p < 0.1$) are shown in reddish or bluish color. The numbers represent the partial correlation coefficients.

Table 5.1: Parameters of the regression models for both absolute anomalies (Δ) and relative anomalies (δ). Φ_{CC} and Φ_{PC} are the GPP sensitivity to absolute changes in canopy control and physiological control, respectively. ϕ_{CC} and Φ_{PC} are the sensitivity of relative changes in canopy and physiological control, respectively. p-values are the significance of independent variables in the regressions. The lags are determined based on the strongest partial correlation between GPP anomalies and corresponding VIs. In this table, EVI is used to represent the canopy control and VPD is used to represent the physiological control. Red asterisks indicate positive sensitivity factors (Φ or ϕ).

Site	IGBP class	absolute anomaly (Δ)						relative anomaly (δ)					
		Φ_{CC}	p-value	Φ_{PC}	p-value	R^2	lag	ϕ_{CC}	p-value	ϕ_{PC}	p-value	R^2	lag
DE-Hai	DBF	11.70	0.127	-0.18	0.070	0.34	2	0.39	0.076	-0.05	0.264	0.22	4
FR-Hes	DBF	20.90	0.084	-0.23	0.017*	0.32	4	1.72	0.004**	-0.12	0.021*	0.42	4
IT-Ro1	DBF	18.02	0.010**	-0.15	0.012*	0.55	0	2.00	0.009**	-0.23	0.054	0.51	0
FR-Pue	EBF	19.93	0.032*	-0.20	0.001***	0.60	1	2.89	0.017*	-0.72	0.001***	0.58	1
DE-Tha	ENF	2.60	0.384	-0.24	0.002**	0.47	2	0.37	0.025*	-0.05	0.323	0.29	2
ES-ES1	ENF	17.61	0.005**	-0.24	0.008**	0.48	0	0.80	0.013*	-0.32	0.011*	0.43	0
FR-LBr	ENF	8.05	0.095	-0.15	0.029*	0.35	0	0.52	0.083	-0.06	0.333	0.21	0
IT-Lav	ENF	6.30	0.222	-0.12	0.106	0.33	4	0.07	0.825	0.00	0.966	0.00	4
BE-Vie	MF	6.56	0.134	-0.10	0.125	0.26	1	0.52	0.118	0.02	0.626	0.14	1
CH-Oe1	GRA	31.88	0.025*	-0.21	0.130	0.44	1	2.08	0.014*	0.00	0.992	0.31	1
HU-Bug	GRA	15.98	0.090	0.13	0.393	0.21	3	1.82	0.004**	0.54	0.006**	0.40	3
IT-Mbo	GRA	21.39	0.001***	0.12	0.150	0.50	1	1.36	0.003**	0.08	0.007**	0.56	1
IT-Pia	OSH	10.13	0.000***	0.10	0.005**	0.64	3	1.99	0.006**	0.45	0.010**	0.51	2

*indicates significance at 0.05 level
**indicates significance at 0.01 level
***indicates significance at 0.001 level

5.4 Discussion

5.4.1 Differences between forest and non-forest ecosystems in response to drought and heatwave

Relative changes in GPP vary among biomes due to different resistance to drought. Forest ecosystems have deeper roots and higher regulatory capacity on transpiration during the early and middle phases of an extreme drought like 2003 (Teuling et al., 2010), therefore, they can better utilize soil water, and are more resistant to short-term drought. Non-forest ecosystems are more vulnerable to drought due to their lower capability to utilize soil water (Baldocchi et al., 2004). The difference between forests and grasslands is also supported by distinctive energy balance between forests and grasslands during the drought and heatwave period (Teuling et al., 2010; Wicke & Bernhofer, 1996; Zaitchik et al., 2006).

GPP anomaly is regulated by the combined effects of canopy and physiological changes. For forest ecosystems, the canopy changes are minor, and GPP anomalies primarily come from physiological limitation on photosynthesis. For non-forest ecosystems (GRA and OSH), both physiological and vegetation canopy changes contribute to the change in GPP during the drought and heatwave period. Canopy changes are dominant for these non-forest ecosystems, with previous studies showing that in situ measured LAI has a good correlation with GPP during the drought period (Aires et al., 2008). Although forest and non-forest ecosystems have different regulatory mechanisms, VIs can partially explain the observed relative changes in GPP during the drought across different biomes. By contrast, the physiological control (VPD or LST) on photosynthesis is a fast process and cannot be temporally averaged to evaluate the cross-site GPP differences during the entire drought period.

5.4.2 *A conceptual model for canopy and physiological limitation on forest and non-forest during drought and heatwave*

Indicators perform differently for temporally tracking the GPP anomalies at each site. In general, forest sites show weaker correlation between VI anomalies and GPP anomalies, and have longer lags (but with large differences across sites), which makes it difficult to predict drought impacts on GPP using only VIs. GRA and OSH have shorter lags and show stronger correlation with VIs because of the higher SSWS. For forest ecosystems, VPD is a superior predictor of GPP anomalies over VIs. However, GPP responses to VPD may vary for different forest types, and even for specific sites (Lin et al., 2015). Together with different VPD base values for the referential period, they contribute to the higher partial correlation when using absolute VPD anomalies rather than relative anomalies (Figure 5.2). Non-forest ecosystems have a lower sensitivity to VPD possibly because of less stomatal regulation and the relatively dominant role of vegetation canopy change in affecting GPP.

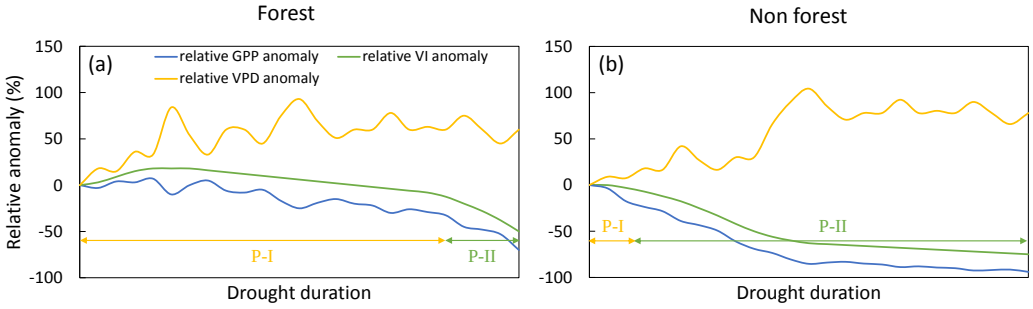


Figure 5.3: The conceptual model for vegetation canopy and physiological controls on (a) forest and (b) non-forest during the drought period. Relative anomalies (δ_γ) were used. For simplicity and readability, VI fluctuation was removed, and only the VI trend was plotted. As drought progresses over time, two different drought stages are annotated as P-I and P-II. For the first stage (P-I), physiological control dominates the GPP variation, and for the second stage (P-II), canopy control dominates the GPP variation.

Based on the above findings, we built a conceptual model to describe the relationship among the relative anomalies in VPD, VIs and GPP (Figure 5.3). The anomaly in GPP is the combined result of VPD and VI anomalies, with remarkable differences between forest and non-forest ecosystems. The drought can be divided into two periods: P-I is the initial period of drought, in which the VPD and radiation increases, but the canopy does not start to change due to the available soil water and ecosystem self-regulation. During this period, the primary regulation on GPP is through VPD and temperature. Forests have a much longer P-I, with higher sensitivity to VPD than non-forests. P-II starts when soil water is depleted and cannot sustain water supply to meet transpiration demand of plants, and the falling leaves result in the changes in vegetation canopy or VIs. During this period, the primary regulation on GPP is the vegetation canopy. Non-forest ecosystems have a longer P-II phase than forests, and the VIs may change enormously during this period due to the senescence of leaves.

5.4.3 Implication and limitation of the canopy and physiological control analysis

Different drought stages and regulation factors in forest and non-forest ecosystems suggest that we cannot use a single indicator to temporally track the GPP anomaly during the drought period for all ecosystems. For non-forest ecosystems, canopy control, which explains much of the GPP variation, has been partially embedded in the fraction of photosynthetic active radiation (FPAR) in PEMs (canopy sensitivity (ϕ_{CC}) is greater than 1 %GPP/%EVI). The physiological control on GPP still exists, but has much smaller variation. Because of the decoupling of atmospheric and soil water deficit from photosynthesis during extreme drought condition (Beringer et al., 2011; Yuan et al., 2014b), VPD and other climate factors may not well represent physiological control on GPP at daily or longer time scales. Rapid canopy responses

in non-forest ecosystems allow transformed VIs to be used to represent the physiological control on GPP, such as the LSWI based water scalar used in VPM (Xiao et al., 2004b). For forest sites, VPD can be used, but more site-specific parameters are required. Similar biome-based differences were also reported by Zhang et al. (2015c). Because the absolute anomaly of VPD (Δ_{GPP}) shows an advantage over the relative anomaly (δ_{VPD}) in both partial correlation analysis and the regression model (Figure 5.2, Table 5.1), it also suggests a non-linear response of VPD control on photosynthesis, rather than the piecewise function currently used in MODIS PSN model (Running et al., 2004).

The 2003 European drought and heatwave gives us a unique opportunity to study the drought impact on GPP and the feasibility of estimating the drought impacts on GPP using remote sensing based PEMs. This research benefits from high density of carbon flux towers, however, it also faces the following limitations: (1) the inconsistency of the flux tower footprint and MODIS pixel size; the land cover is relatively patchy and mixed pixels exist. The climate and GPP anomalies are also much larger in finer resolution images (Zaitchik et al., 2006). (2) The data quality of VIs may still be unreliable even after gap-filling and smoothing for some sites. This issue is more critical when doing interannual analysis at temporal scales, but can be alleviated when VIs values are averaged over the entire drought period. (3) GPP and satellite-retrieved data are at 8-day time scale, however, VPD/LST affects photosynthesis at the hourly scale, the inconsistency of operation time scales will also reduce the model predictability. (4) Several subsequent droughts and heatwaves also influenced parts of Europe in 2006 and 2011. However, these years were not eliminated when calculating the reference values because of the different spatial extents and severities of these drought events.

5.5 Conclusions

This study presents an analysis of how GPP from different ecosystems responds to drought through vegetation canopy change and physiological responses. Distinctive responses to drought are found between forest and non-forest ecosystems. During the entire drought period, forests do not show obvious changes in canopy optical characteristics, while non-forests tend to have a faster canopy response. Relative anomalies of VIs can still be used as indicators to evaluate the drought-induced GPP decline spatially. At the temporal scale for each site, because of different dominant factors in two drought stages (P-I/P-II) and the different stage lengths for forest and non-forest, forest GPP is more responsive to changes in VPD while non-forest GPP is more sensitive to changes in VIs. In the near future, soil moisture data from Soil Moisture Active Passive (SMAP) satellite and sun-induced chlorophyll fluorescence (SIF) observations from Orbiting Carbon Observatory-2 (OCO-2) or Sentinel-5 Precursor satellite may be used to provide a better estimation of GPP decline from canopy and physiological control during severe drought and heatwave period.

5.A Appendix

The L4 8-day eddy covariance data from 15 flux tower sites were used in our study (Figure 5.1). These sites were selected due to the significant decrease of GPP in summer (June to August) 2003 compared to the average of other years, and also for the data quality. These 15 sites covered 5 vegetation types: Deciduous Broadleaf Forest (DBF), Evergreen Broad Leaf Forest (EBF), Evergreen Needle Leaf Forest (ENF), Grassland (GRA), and Open Shrub land (OSH). To make eddy covariance data comparable with the Moderate Resolution Imaging Spectroradiometer (MODIS) products, we only used the flux data after 2000. We also find some sites with data missing

for a relatively long period. This directly affected our site selections. If 8-day GPP data is missing during the 2003 drought period (from week 20 to week 39), this site was discarded; if the GPP data is missing during the corresponding drought period in normal years, this site-year was excluded from analysis. This gave us 118 site-years of available data. The anomaly was calculated between the difference of 2003 and the long-term average (2003 excluded); the average reference period for each site is 6.9 years. GPP was estimated from the Marginal Distribution Sampling gap-filling method ('GPP_st_MDS'). Along with GPP, we also used 8-day vapor pressure deficit ('VPD'), precipitation ('Precip'), and air temperature ('Ta_f') to quantify the drought severity (Table 5.A.1).

The vegetation indices and land surface temperature (LST) were obtained from MODIS onboard the Terra satellite. To make the MODIS data comparable with the flux data, each site had the same period of observations, depending on the data availability from both MODIS and flux tower. Although the LST from Aqua satellite has a better bypass time (13:30) which is closer to the highest temperature of the day, it was not used because a lot of flux data would be discarded to match the same observation period of Aqua satellite (start from July, 2002). The MODIS-derived 8-day vegetation indices were calculated from MOD09A1 C5 product, with a spatial resolution of 500 meters. The day-time LST was obtained from MOD11A2 C5 product at 8-day temporal resolution. Data quality was checked for cloud and aerosol, and a temporal gap-filling method was used to remove bad observations.

The three vegetation indices were calculated from the MOD09A1 product using the following equations:

$$EVI = 2.5 \times \frac{\rho_{nir} - \rho_{red}}{\rho_{nir} + (6 \times \rho_{red} - 7.5 \times \rho_{blue}) + 1} \tag{5.A.1}$$

$$NDVI = 2.5 \times \frac{\rho_{nir} - \rho_{red}}{\rho_{nir} + \rho_{red}} \tag{5.A.2}$$

The three vegetation indices were then temporally gap-filled and smoothed using different procedures. Atmospheric corruption and measurement failure tend to decrease the value of EVI and NDVI. Therefore, we used a similar data quality check procedure as described by Reichstein et al. (2007): 1). The data quality for the vegetation indices were checked using the quality flag layer embedded in the MOD09A1 data. The quality flag is a 16-bit number for each observation and the data is only considered valid when the following requirements were met: MOD35 cloud = 'clear' (bit 0-1 equals '00'); aerosol quantity = 'low' or 'average' (bit 6-7 equals '01' or '10'). 2) the best index slope extraction (BISE) algorithm with a window size of two time steps was used to eliminate some low values which cannot be correctly identified by the MODIS quality control layer (Viovy et al., 1992). A larger window size of BISE algorithm can get a smoother curve, but it will also reduce the information about disturbance (drought and heatwave in our study). After the BISE algorithm finds the valid points which can be used for temporal interpolation, we further use a threshold to remove the sudden spikes which can be caused by other unforeseen problems: if a VI value is greater than 1.5 fold of the average of its two nearby values, it will also be removed. 3) The very last points were then linearly interpolated to generate the time series of EVI/NDVI. Through this procedure, we found that most abnormal values in the growing season were removed (Figure 5.A.1a, b). Because atmospheric corruption may increase LSWI and violate the hypothesis of BISE algorithm, we used a different procedure: 1) like EVI and NDVI, the data quality was checked for each observation. 2) The invalid observations were then masked and linearly interpolated with nearby good values. 3) A Savitzky-Golay filter was then

applied to the time series to eliminate the high frequency noises (Figure 5.1c).

The LST data from MOD11A2 C5 followed the same routine of gap-filling and smoothing procedure like LSWI while the quality flag is different; the quality flag is an 8-bit number and the valid data should have Mandatory QA Flags = 'LST produced' (bit 0-1 equals '00' or '01'), Data Quality Flag = 'good data quality' (bit 2-3 equals '00').

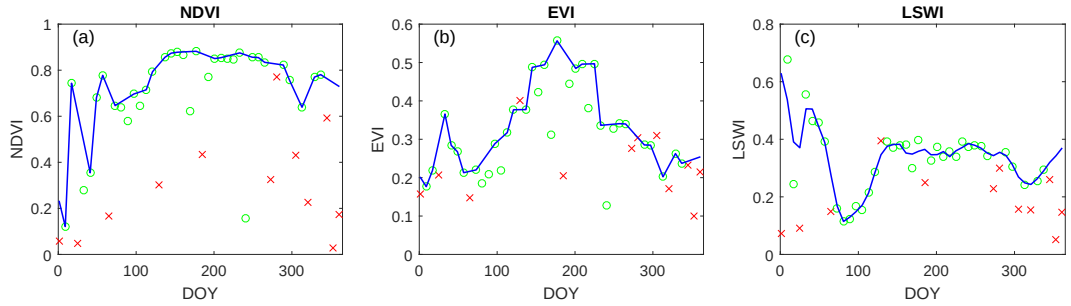


Figure 5.A.1: Gap-filled results of NDVI (a), EVI (b), and LSWI (c) for site DE-Tha for year 2003. Red crosses indicate the corrupted observations identified by the MODIS quality check layer. Green circles indicate observations that passed the quality check, and the blue lines are the final smoothed vegetation indices.

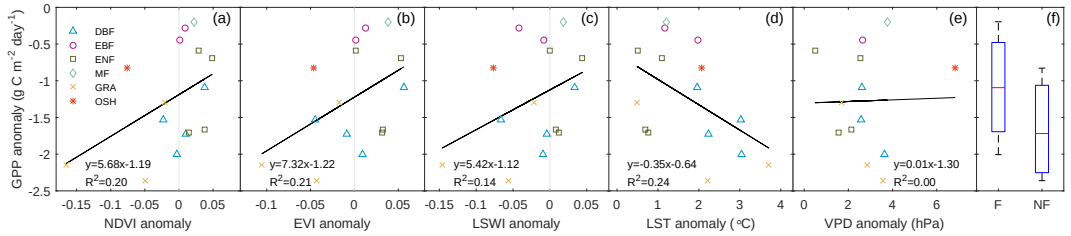


Figure 5.A.2: Relationship of averaged absolute anomalies ($\overline{\Delta_\gamma}$) between GPP and vegetation indices (EVI, NDVI, LSWI), land surface temperature (LST), and vapor pressure deficit (LST) for the entire drought and heatwave period (a-e). GPP decrease for forest (F) and non-forest (NF) in absolute anomaly (f).

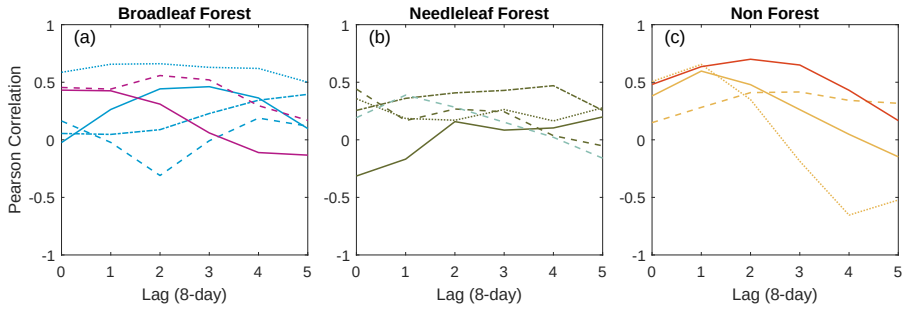


Figure 5.A.3: Pearson correlation between anomalies in absolute value for GPP (Δ_{GPP}) and EVI (Δ_{EVI}) with different lags applied.

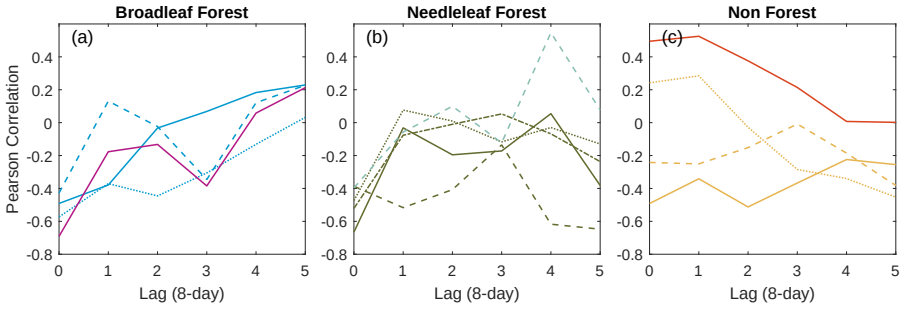


Figure 5.A.4: Pearson correlation between anomalies in absolute value for GPP (Δ_{GPP}) and VPD (Δ_{VPD}) with different lags applied.

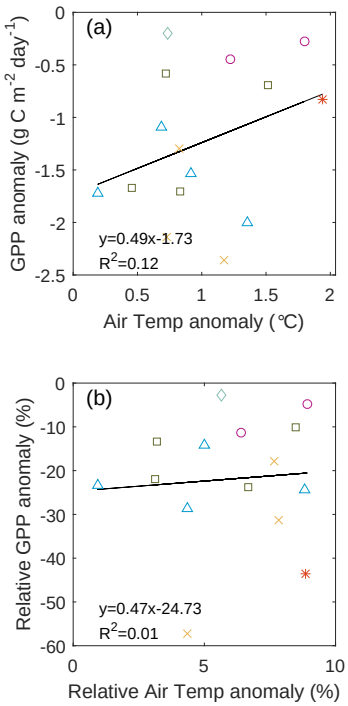


Figure 5.A.5: Relationship of average anomalies between GPP and air temperature for the entire drought and heatwave period. (a) is using averaged absolute anomalies ($\overline{\Delta_\gamma}$) and (b) is using averaged relative anomalies ($\overline{\delta_\gamma}$).

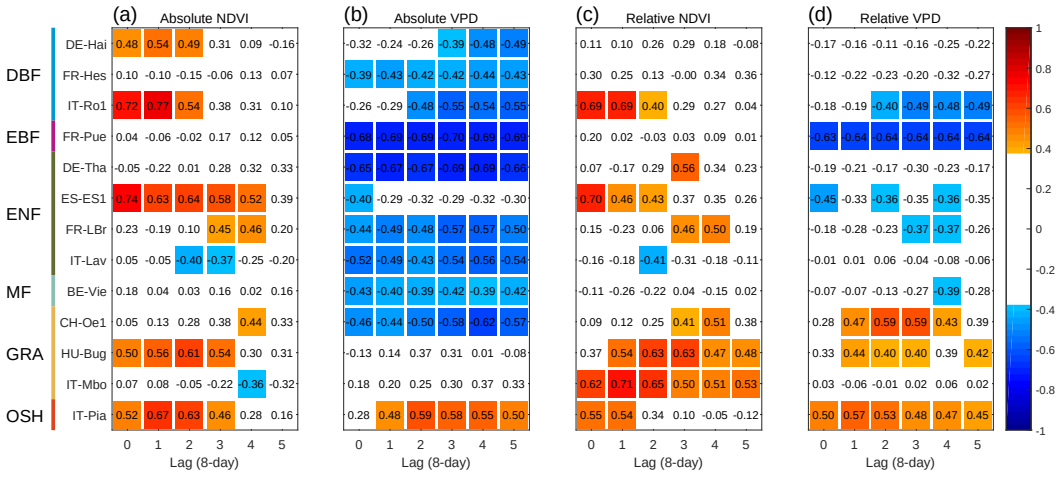


Figure 5.A.6: Same as Figure 5.2, but for NDVI instead of EVI.

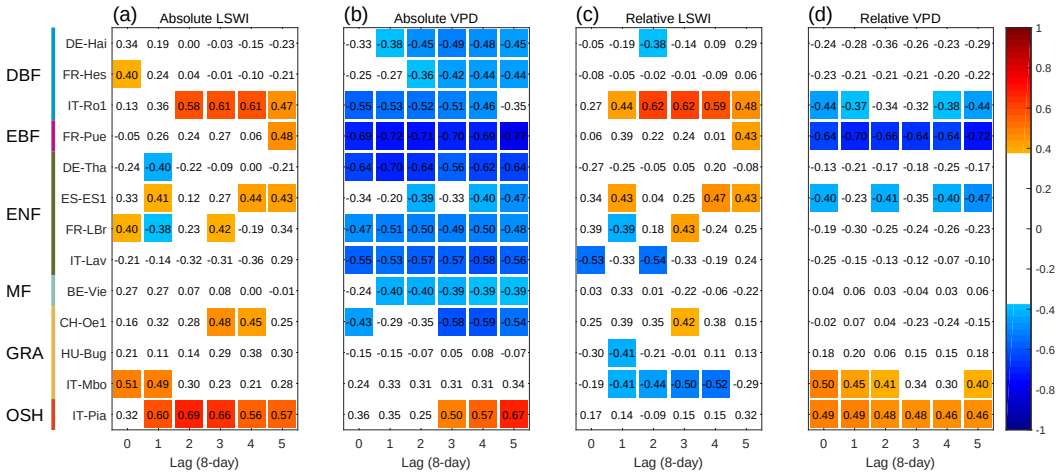


Figure 5.A.7: Same as Figure 5.2, but for LSWI instead of EVI.

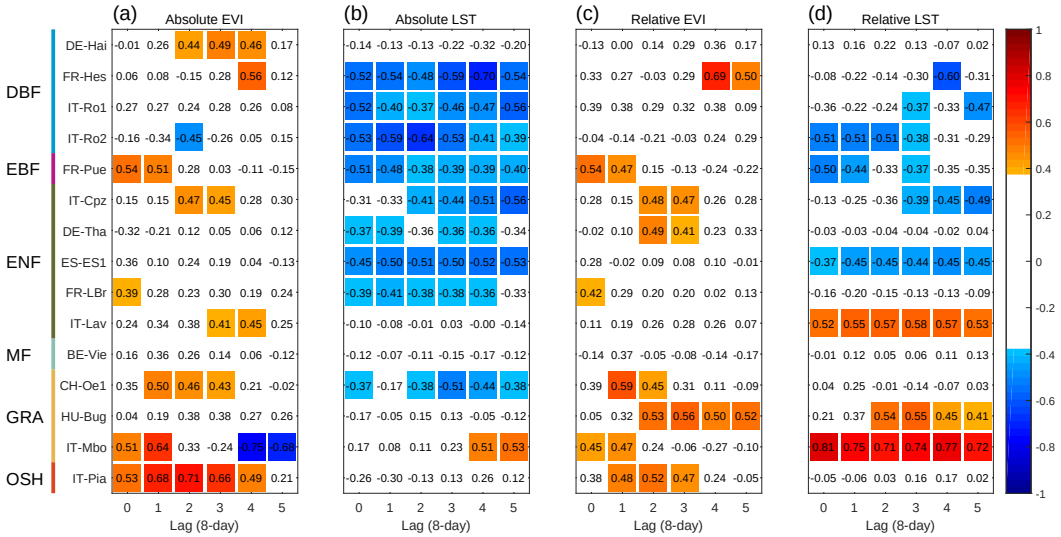


Figure 5.A.8: Same as Figure 5.2, but the climate indicator was replaced with land surface temperature instead of VPD.

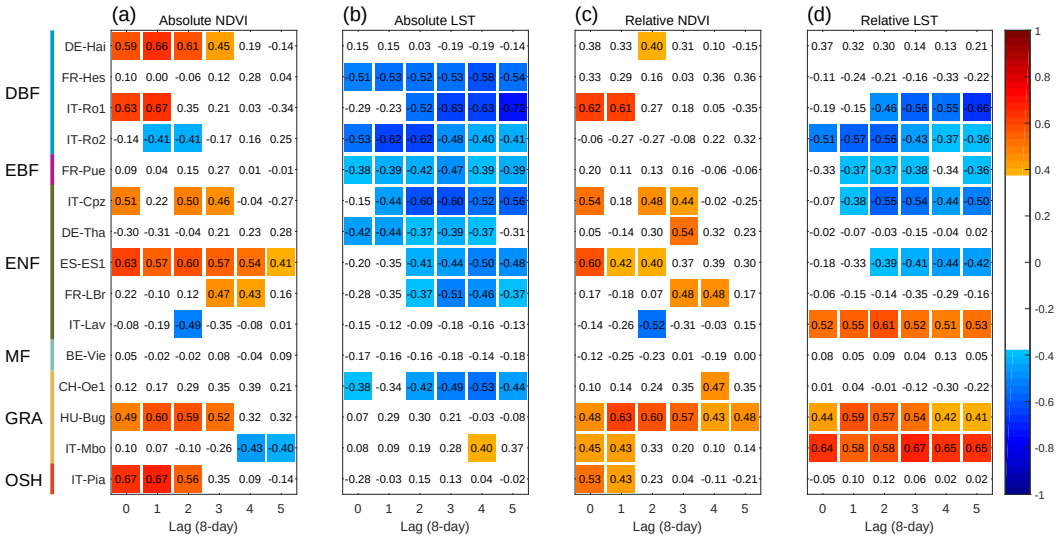


Figure 5.A.9: Same as Figure 5.A.8, but for NDVI instead of EVI.

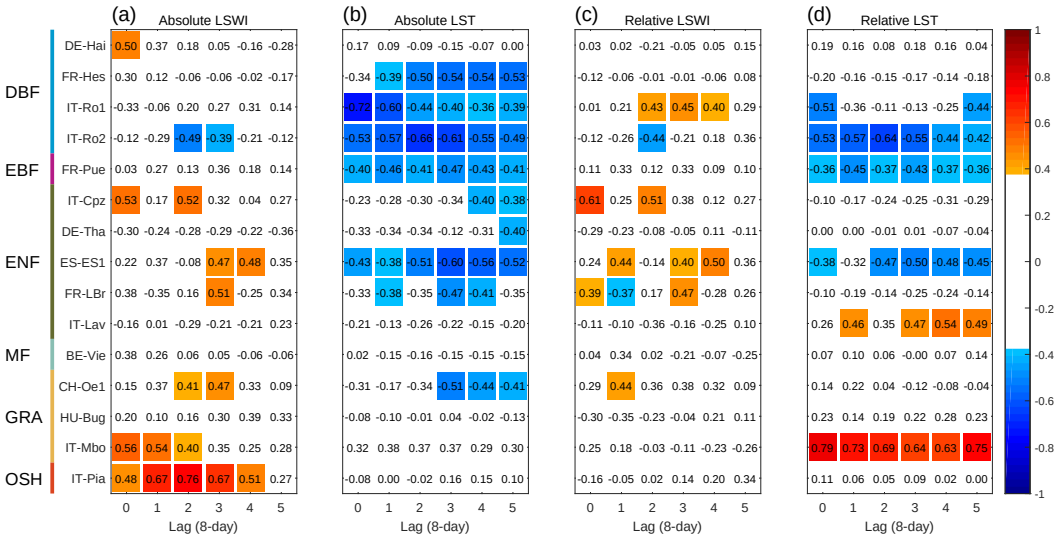


Figure 5.A.10: Same as Figure 5.A.8, but for LSWI instead of EVI.

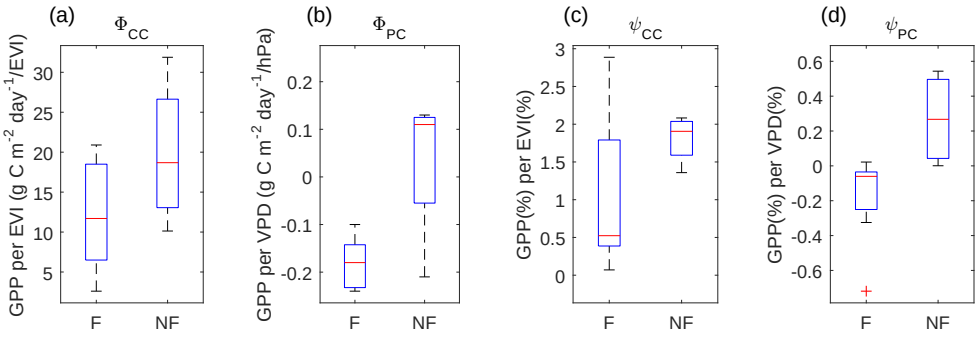


Figure 5.A.11: Box plot of the absolute and relative sensitivity of canopy control (CC) and physiological control (PC) for forest (F) and non-forest (NF).

Table 5.A.1: Flux tower sites used in our analysis. $\overline{\Delta_{GPP}}$ and $\overline{\delta_{GPP}}$ stand for the absolute and relative GPP anomaly for the drought period (June 2^{nd} to November 16^{th}) compared to the normal year average.

Site	Period of record	Country	Latitude	Longitude	IGBP class	$\overline{\Delta_{GPP}}$ ($g\,C\,m^{-2}$)	$\overline{\delta_{GPP}}$ (%)	Δ_{Precip} (mm)	$\overline{\Delta_{T_a}}$ °C	$\overline{\Delta_{LST}}$ °C	Reference
BE-Vie	2000-2008	Switzerland	50.3055	5.9968	MF	-31.3	-2.8	-159.3	0.74	1.20	(Aubinet et al., 2001)
CH-Oe1	2002-2007	Switzerland	47.2858	7.7319	GRA	-377.8	-31.3	-162.9	1.17	2.21	(Ammann et al., 2007)
DE-Hai	2000-2007	Germany	51.0792	10.4530	DBF	-175.0	-14.2	-125.0	0.68	1.96	(Mund et al., 2010)
DE-Tha	2000-2008	Germany	50.9636	13.5669	ENF	-267.2	-22.0	-197.9	0.46	0.68	(Grunwald & Bernhofer, 2007)
ES-ES1	2000-2006	Spain	39.3460	-0.3188	ENF	-93.5	-13.3	16.1	0.72	0.50	(Sanz et al., 2004)
FR-Hes	2000-2010	France	48.6742	7.0656	DBF	-321.0	-24.4	-208.0	1.35	3.04	(Granier et al., 2008)
FR-LBr	2000-2008	France	44.7171	-0.7693	ENF	-110.7	-10.1	81.6	1.52	1.09	(Berbigier et al., 2001)
FR-Pue	2001-2008/ 2010-2011	France	43.7414	3.5958	EBF	-70.9	-11.4	-55.1	1.22	1.98	(Allard et al., 2008)
HU-Bug	2003-2008	Hungary	46.6911	19.6013	GRA	-342.8	-57.2	-78.0	0.73	3.71	(Nagy et al., 2005)
IT-Cpz	2000-2008	Italy	41.7053	12.3761	EBF	-44.5	-4.7	3.8	1.80	1.16	(Garbulsky et al., 2008)
IT-Lav	2001-2012	Italy	45.9562	11.2813	ENF	-272.3	-23.7	âĹŠ	0.83	0.76	(Cescatti & Marcolla, 2004)
IT-Mbo	2003-2012	Italy	46.0147	11.0458	GRA	-207.3	-17.8	-96.2	0.82	0.49	(Marcolla et al., 2011)
IT-Pia	2002-2006	Italy	42.5839	10.0784	OSH	-132.5	-43.5	-76.3	1.94	2.06	(Vaccari et al., 2012)
IT-Ro1	2001-2006/2008	Italy	42.4081	11.9300	DBF	-245.7	-28.6	-102.7	0.92	3.02	(Rey et al., 2002)
IT-Ro2	2002-2008/ 2010-2012	Italy	42.3903	11.9209	DBF	-276.2	-23.3	-46.7	0.19	2.23	(Tedeschi et al., 2006)

Table 5.A.2: Same as Table 5.1, but using NDVI as the canopy control and VPD as the physiological control.

Site	IGBP class	absolute anomaly (Δ)						relative anomaly (δ)					
		Φ_{CC}	p-value	Φ_{PC}	p-value	R^2	lag	ϕ_{CC}	p-value	ϕ_{PC}	p-value	R^2	lag
DE-Hai	DBF	18.12	0.016*	-0.09	0.324	0.47	1	0.66	0.233	-0.03	0.516	0.13	3
FR-Hes	DBF	8.21	0.600	-0.18	0.058	0.20	4	1.96	0.126	-0.06	0.258	0.17	5
IT-Ro1	DBF	29.86	0.000***	-0.06	0.225	0.72	1	4.89	0.001***	-0.09	0.442	0.61	1
FR-Pue	EBF	7.88	0.480	-0.21	0.001***	0.49	3	2.49	0.403	-0.68	0.004**	0.43	0
DE-Tha	ENF	8.37	0.172	-0.22	0.002**	0.50	5	2.28	0.013	-0.06	0.213	0.34	3
ES-ES1	ENF	16.44	0.000***	-0.12	0.089	0.61	0	1.72	0.001***	-0.2	0.053	0.58	0
FR-LBr	ENF	16.23	0.049*	-0.18	0.011*	0.39	4	1.83	0.029	-0.1	0.117	0.29	4
IT-Lav	ENF	1.34	0.824	-0.17	0.023*	0.27	0	-0.50	0.652	-0.01	0.803	0.01	5
BE-Vie	MF	10.40	0.462	-0.13	0.067	0.18	0	0.06	0.885	0.000	0.928	0.00	3
CH-Oe1	GRA	14.72	0.062	-0.47	0.005**	0.39	4	1.56	0.025*	-0.14	0.103	0.27	4
HU-Bug	GRA	13.93	0.005**	0.19	0.123	0.41	2	1.78	0.004**	0.47	0.008**	0.41	2
IT-Mbo	GRA	2.23	0.737	0.10	0.408	0.07	1	1.30	0.001***	0.05	0.060	0.62	1
IT-Pia	OSH	6.30	0.002**	0.08	0.037*	0.58	1	1.73	0.016**	0.39	0.031*	0.46	0

*indicates significance at 0.05 level
**indicates significance at 0.01 level
***indicates significance at 0.001 level

Table 5.A.3: Same as Table 5.1, but using LSWI as the canopy control and VPD as the physiological control.

Site	IGBP class	absolute anomaly (Δ)						relative anomaly (δ)					
		Φ_{CC}	p-value	Φ_{PC}	p-value	R^2	lag	ϕ_{CC}	p-value	ϕ_{PC}	p-value	R^2	lag
DE-Hai	DBF	13.76	0.160	-0.15	0.164	0.33	0	-0.02	0.593	-0.06	0.270	0.07	5
FR-Hes	DBF	20.78	0.092	-0.10	0.298	0.31	0	0.04	0.819	-0.04	0.517	0.05	5
IT-Ro1	DBF	13.02	0.006**	-0.13	0.026*	0.58	3	0.38	0.013*	-0.24	0.048*	0.49	3
FR-Pue	EBF	13.07	0.038*	-0.25	0.000***	0.60	5	0.40	0.002**	-0.50	0.007**	0.67	5
DE-Tha	ENF	0.09	0.991	-0.24	0.004**	0.44	4	0.13	0.338	-0.02	0.765	0.09	4
ES-ES1	ENF	8.19	0.057	-0.15	0.092	0.32	4	-0.03	0.683	-0.25	0.075	0.18	4
FR-LBr	ENF	12.32	0.077	-0.15	0.035*	0.36	3	0.01	0.894	-0.06	0.349	0.05	3
IT-Lav	ENF	3.48	0.223	-0.18	0.013*	0.33	5	0.00	0.992	-0.01	0.914	0.00	5
BE-Vie	MF	13.26	0.256	-0.11	0.086	0.22	1	0.11	0.503	0.00	0.996	0.03	1
CH-Oe1	GRA	24.67	0.038*	-0.37	0.009**	0.41	3	-0.34	0.026*	-0.07	0.299	0.27	3
HU-Bug	GRA	10.32	0.109	0.04	0.752	0.19	4	0.00	0.560	0.11	0.442	0.04	5
IT-Mbo	GRA	12.74	0.026*	0.09	0.321	0.30	0	0.12	0.010**	0.05	0.147	0.50	0
IT-Pia	OSH	9.91	0.001**	0.04	0.310	0.61	2	0.04	0.220	0.40	0.050*	0.29	5

*indicates significance at 0.05 level
**indicates significance at 0.01 level
***indicates significance at 0.001 level

Table 5.A.4: Same as Table 5.1, but using EVI as the canopy control and LST as the physiological control.

Site	IGBP class	absolute anomaly (Δ)						relative anomaly (δ)					
		Φ_{CC}	p-value	Φ_{PC}	p-value	R^2	lag	ϕ_{CC}	p-value	ϕ_{PC}	p-value	R^2	lag
DE-Hai	DBF	15.94	0.035*	-0.08	0.369	0.25	3	0.44	0.127	-0.05	0.767	0.16	4
FR-Hes	DBF	28.00	0.012	-0.29	0.001***	0.51	4	2.13	0.001***	-0.55	0.006**	0.49	4
IT-Ro1	DBF	7.67	0.238	-0.19	0.045*	0.53	3	1.51	0.102	-0.81	0.132	0.46	0
IT-Ro2	DBF	5.10	0.554	-0.32	0.100	0.28	5	0.58	0.223	-0.94	0.228	0.34	5
FR-Pue	EBF	27.84	0.018*	-0.14	0.025*	0.40	0	3.69	0.016*	-0.98	0.030*	0.39	0
IT-Cpz	EBF	11.70	0.042*	-0.13	0.079	0.43	2	0.92	0.037*	-0.48	0.132	0.38	2
DE-Tha	ENF	2.28	0.622	-0.07	0.159	0.15	5	0.36	0.032*	-0.01	0.874	0.24	2
ES-ES1	ENF	9.40	0.134	-0.21	0.051	0.36	0	0.41	0.238	-0.86	0.114	0.27	0
FR-LBr	ENF	8.53	0.096	-0.11	0.101	0.26	0	0.54	0.077	-0.14	0.503	0.19	0
IT-Lav	ENF	10.35	0.052	0.00	0.998	0.22	4	0.32	0.245	0.29	0.010**	0.33	3
BE-Vie	MF	7.34	0.125	-0.02	0.761	0.16	1	0.51	0.120	0.07	0.618	0.14	1
CH-Oe1	GRA	34.74	0.028*	-0.08	0.485	0.37	1	2.39	0.007**	0.29	0.304	0.35	1
HU-Bug	GRA	13.98	0.107	0.06	0.541	0.19	2	1.34	0.013*	1.06	0.015*	0.34	3
IT-Mbo	GRA	20.84	0.003**	0.02	0.753	0.43	1	0.76	0.040*	0.35	0.000***	0.70	1
IT-Pia	OSH	12.53	0.001**	-0.04	0.597	0.50	2	1.93	0.023*	0.16	0.897	0.27	2

*indicates significance at 0.05 level
**indicates significance at 0.01 level
***indicates significance at 0.001 level

Table 5.A.5: Same as Table 5.1, but using NDVI as the canopy control and LST as the physiological control.

Site	IGBP class	absolute anomaly (Δ)						relative anomaly (δ)					
		Φ_{CC}	p-value	Φ_{PC}	p-value	R^2	lag	ϕ_{CC}	p-value	ϕ_{PC}	p-value	R^2	lag
DE-Hai	DBF	23.08	0.002**	0.05	0.550	0.45	1	0.93	0.094	0.16	0.217	0.19	2
FR-Hes	DBF	17.53	0.247	-0.24	0.009**	0.34	4	2.24	0.125	-0.29	0.174	0.16	4
IT-Ro1	DBF	28.35	0.002**	-0.07	0.341	0.71	1	5.22	0.005**	-0.37	0.432	0.61	0
IT-Ro2	DBF	11.56	0.300	-0.30	0.081	0.31	5	1.43	0.186	-1.08	0.126	0.35	5
FR-Pue	EBF	17.76	0.263	-0.16	0.044*	0.22	3	2.92	0.423	-0.69	0.171	0.16	0
IT-Cpz	EBF	49.83	0.027*	-0.05	0.551	0.45	0	8.12	0.017*	-0.10	0.779	0.43	0
DE-Tha	ENF	9.17	0.241	-0.07	0.191	0.20	5	2.23	0.018*	-0.05	0.538	0.29	3
ES-ES1	ENF	15.42	0.004**	-0.08	0.422	0.56	0	1.63	0.007**	-0.35	0.468	0.49	0
FR-LBr	ENF	16.48	0.043*	-0.16	0.026*	0.31	3	1.81	0.037*	-0.25	0.228	0.25	4
IT-Lav	ENF	0.37	0.965	-0.03	0.601	0.02	5	0.59	0.542	0.28	0.019*	0.29	5
BE-Vie	MF	1.37	0.711	-0.04	0.454	0.03	5	0.03	0.953	0.03	0.866	0.00	3
CH-Oe1	GRA	14.04	0.102	-0.33	0.019*	0.29	4	1.44	0.044*	-0.44	0.212	0.22	4
HU-Bug	GRA	13.64	0.006**	0.09	0.222	0.39	1	1.78	0.004**	1.03	0.008**	0.42	1
IT-Mbo	GRA	3.51	0.679	0.03	0.741	0.04	0	0.88	0.054	0.30	0.003**	0.70	0
IT-Pia	OSH	7.16	0.002**	-0.01	0.906	0.45	1	1.92	0.020*	-0.24	0.843	0.28	0

*indicates significance at 0.05 level
**indicates significance at 0.01 level
***indicates significance at 0.001 level

Table 5.A.6: Same as Table 5.1, but using LSWI as the canopy control and LST as the physiological control.

Site	IGBP class	absolute anomaly (Δ)						relative anomaly (δ)					
		Φ_{CC}	p-value	Φ_{PC}	p-value	R^2	lag	ϕ_{CC}	p-value	ϕ_{PC}	p-value	R^2	lag
DE-Hai	DBF	24.34	0.029*	0.07	0.475	0.27	0	0.02	0.686	0.15	0.388	0.04	5
FR-Hes	DBF	15.94	0.211	-0.14	0.151	0.35	0	0.05	0.772	-0.09	0.702	0.03	5
IT-Ro1	DBF	8.23	0.193	-0.16	0.128	0.53	4	0.36	0.012*	-1.09	0.009**	0.57	3
IT-Ro2	DBF	-3.67	0.639	-0.39	0.020*	0.28	0	0.24	0.000***	-0.63	0.172	0.69	5
FR-Pue	EBF	10.98	0.126	-0.14	0.041*	0.27	3	-0.01	0.947	-0.75	0.157	0.13	1
IT-Cpz	EBF	13.24	0.019*	-0.08	0.343	0.47	0	-0.42	0.010**	-0.14	0.675	0.46	0
DE-Tha	ENF	-8.63	0.372	-0.07	0.195	0.18	4	0.20	0.172	0.08	0.482	0.11	4
ES-ES1	ENF	8.29	0.035*	-0.24	0.014*	0.44	4	-0.04	0.635	-1.09	0.046*	0.22	4
FR-LBr	ENF	16.18	0.027*	-0.13	0.041*	0.35	3	0.01	0.932	-0.12	0.607	0.02	3
IT-Lav	ENF	3.30	0.334	-0.05	0.409	0.08	5	0.13	0.321	0.28	0.012*	0.32	5
BE-Vie	MF	22.27	0.105	0.00	0.950	0.17	0	0.11	0.520	-0.01	0.963	0.03	1
CH-Oe1	GRA	25.43	0.045*	-0.26	0.026*	0.34	3	-0.23	0.180	0.12	0.706	0.10	1
HU-Bug	GRA	8.79	0.103	-0.01	0.932	0.19	4	0.00	0.328	0.44	0.236	0.10	4
IT-Mbo	GRA	14.46	0.013*	0.07	0.187	0.33	0	0.05	0.280	0.33	0.005**	0.64	0
IT-Pia	OSH	11.13	0.000***	0.00	0.945	0.58	2	0.05	0.175	0.02	0.990	0.11	5

*indicates significance at 0.05 level
**indicates significance at 0.01 level
***indicates significance at 0.001 level

Chapter 6: Consistency between sun-induced chlorophyll fluorescence and gross primary production of vegetation in North America

Abstract

Accurate estimation of the gross primary production (GPP) of terrestrial ecosystems is vital for a better understanding of the spatial-temporal patterns of the global carbon cycle. In this study, we estimate GPP in North America (NA) using the satellite-based Vegetation Photosynthesis Model (VPM), MODIS images at 8-day temporal and 500 m spatial resolutions, and NCEP-NARR (National Center for Environmental Prediction-North America Regional Reanalysis) climate data. The simulated GPP (GPP_{VPM}) agrees well with the flux tower derived GPP (GPP_{EC}) at 39 AmeriFlux sites (155 site-years). The GPP_{VPM} in 2010 is spatially aggregated to 0.5 by 0.5 degree grid cells and then compared with solar-induced chlorophyll fluorescence (SIF) data from Global Ozone Monitoring Instrument 2 (GOME-2), which is directly related to vegetation photosynthesis. Spatial distribution and seasonal dynamics of GPP_{VPM} and GOME-2 SIF show good consistency. At the biome scale, the relationship between GPP_{VPM} and SIF shows strong linear relationships ($R^2 > 0.95$) and small variations in slopes (4.60–5.55 g C m^{-2} day^{-1} / mW m^{-2} nm^{-1} sr^{-1}). The total annual GPP_{VPM} in NA in 2010 is approximately 13.53 Pg C $year^{-1}$, which accounts for ~11.0% of the global terrestrial GPP and is within the range of annual GPP estimates from six other process-based and data-driven models (11.35–22.23 Pg C $year^{-1}$). Among the seven models, some models did not capture the spatial pattern of GOME-2 SIF data at annual scale, especially in Midwest cropland region. The results from this study demonstrate the reliable performance of VPM at the continental scale, and the potential of SIF data being used as a benchmark to compare

with GPP models.

6.1 Introduction

Carbon dioxide fixed through photosynthesis by terrestrial vegetation is known as gross primary production (GPP) at the ecosystem level. Increased carbon uptake during the past decades helped offset growing CO^2 emissions from fossil fuel burning and land cover change and mitigate the increase of atmospheric CO^2 concentration and global climate warming (Ballantyne et al., 2012). A variety of approaches have been used to estimate GPP of terrestrial ecosystems, and they can be grouped into four categories: 1) process-based GPP models; 2) satellite-based production efficiency models (PEM); 3) data-driven GPP models upscaled from eddy covariance data; and 4) models based on solar-induced chlorophyll fluorescence (SIF) (Figure 6.1). However, large uncertainty still remains regarding the spatial distribution and seasonal dynamics of GPP, which limits our capability to address scientific questions related to the increasing seasonal amplitude and interannual variation of atmospheric CO^2 (Graven et al., 2013; Poulter et al., 2014; Forkel et al., 2016). An accurate estimation of GPP at regional and global scales is essential for a better understanding of the underlying mechanisms of ecosystem-climate interactions and ecosystem response to extreme climate events, such as drought, heat wave, and flood, etc. (Beer et al., 2010; Yu et al., 2013).

Many process-based biogeochemical models employ the enzyme kinetics theory, most well-known as encapsulated by Farquhar et al. (1980) and its modification for C4 plants (Collatz et al., 1992). Some process-based models employ the light-use-efficiency (LUE) concept to estimate GPP (Zeng et al., 2005). These models also take multiple ecological processes into consideration so that they can be coupled

with general circulation models (GCMs) to predict feedbacks related to the global warming and CO^2 fertilization (Booth et al., 2012; Keenan et al., 2012; Piao et al., 2013; Xia et al., 2014). However, these models are often run at coarse spatial resolution and the simulation results vary enormously even with the same set of meteorological input datasets (Coops et al., 2009).

The remote sensing based PEMs estimate GPP as the product of the energy absorbed by plants (absorbed photosynthetically active radiation, APAR) and LUE that converts energy to carbon fixed during the photosynthesis process (Monteith 1972). These models can be further divided into two subcategories (Dong et al., 2015; Xiao et al., 2004b). The $FPAR_{canopy}$ based models, including the Carnegie Ames Stanford Approach (CASA) (Potter et al., 1993), the MODIS GPP algorithm (Photosynthesis, PSN) (Running et al., 2004; Zhao et al., 2005), and the EC-LUE model (Yuan et al., 2007), use the radiation absorbed by vegetation canopy. The $FPAR_{chl/green}$ based models use radiation absorbed by chlorophyll or green leaves and include the Vegetation Photosynthesis Model (VPM) (Xiao et al., 2004b,a), Greenness and Radiation (GR) model (Gitelson et al., 2006), and the vegetation index (VI) model (Wu et al., 2010b).

The eddy covariance (EC) technique provides estimates of GPP by partitioning measured net ecosystem CO^2 exchange (NEE) between land and the atmosphere into GPP and ecosystem respiration (Re) (Baldocchi et al., 2001). Over the past decades, the EC technique has been widely applied to measure NEE of various biome types throughout the world, and a large amount of GPP data (GPP_{EC}) has been accumulated (Baldocchi, 2014; Baldocchi et al., 2001). A number of statistical models have been developed to upscale GPP_{EC} from individual sites to the regional scales (Jung et al., 2009, 2011; Xiao et al., 2010, 2014; Yang et al., 2007). These algorithms, such as model tree ensembles (MTE) or regression tree approaches, build a series

of rules through data mining that relate *in situ* flux observations to satellite-based indices and climate data.

Solar-induced chlorophyll fluorescence (SIF), a byproduct of the vegetation photosynthesis process, has been recently retrieved using multiple satellite platforms/ instruments such as the Greenhouse gases Observing SATellite (GOSAT) (Frankenberg et al., 2011; Guanter et al., 2012; Joiner et al., 2012), the Global Ozone Monitoring Instrument 2 (GOME-2) (Joiner et al., 2013), and the Orbiting Carbon Observatory-2 (OCO-2) (Frankenberg et al., 2014). Recent field studies and theory suggest that SIF contains information from both APAR and LUE that is complementary to vegetation indices such as the normalized difference vegetation index (NDVI) (Guanter et al., 2013; Rossini et al., 2015; Yang et al., 2015). A simple regression model based on space-borne SIF has been developed to estimate cropland GPP (Guanter et al., 2014). Zhang et al. (2014b) have also shown the potential of SIF data to improve carbon cycle models and provide accurate projections of agricultural productivity (Guan et al., 2016).

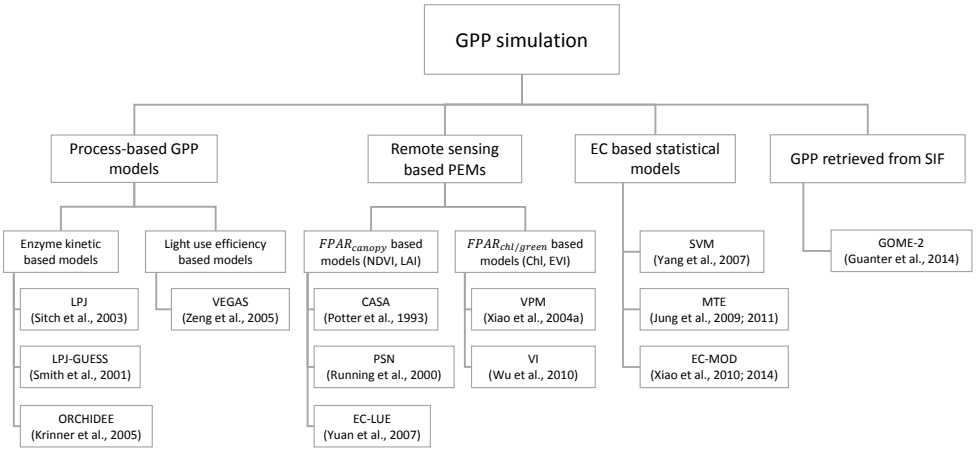


Figure 6.1: A list of different approaches and models (as examples) to estimate gross primary production (GPP) of vegetation.

Over the past several years, a number of studies have run the VPM model with

in situ climate data at various eddy flux tower sites. The resulting GPP_{VPM} was evaluated with GPP_{EC} at different ecosystem types, including forests (Xiao et al., 2004b,a, 2005a), croplands (Kalfas et al., 2011; Wagle et al., 2015), savannas (Jin et al., 2013), and grasslands (He et al., 2014; Wagle et al., 2014). Wu et al. (2010a) compared GPP from four models driven by remotely sensed data at the Harvard forest site and found that VPM performed best in terms of capturing the seasonal dynamics of GPP. (Yuan et al., 2014b) compared seven LUE based models at 157 eddy flux sites and showed that VPM had a moderate rank of performance. (Dong et al., 2015) used four EVI-based models to estimate GPP of grasslands and croplands under normal and severe drought conditions, and reported that VPM performed better than other models in capturing the impacts of drought on GPP. This was mostly because VPM uses Land Surface Water Index (LSWI) that is sensitive to water stress (Wagle et al., 2014, 2015), while the other three models lack a water stress scalar. Recently, simulations of VPM on the regional scale, driven by regional climate data, have been carried out in the Tibetan Plateau (He et al., 2014) and China (Chen et al., 2014), where only limited GPP_{EC} data are available. The sensitivity of VPM to *in situ* climate data from the flux tower sites and the regional data from NCEP-NARR was reported for croplands in conterminous U.S. (Jin et al., 2015)

In this study, we aim to assess the feasibility and performance of the VPM model in estimating GPP across North America (NA) and explore the relationship between SIF and GPP_{VPM} at regional scale. The selection of the NA study area is based on two facts: (1) large uncertainties exist in the GPP estimates from various models (ranging from 12.2 to 32.9 Pg C year^{-1}) (Huntzinger et al., 2012); and (2) a large number of eddy flux sites are available in NA, which provides an opportunity for a thorough validation. The specific objectives of this study are to: (1) implement the VPM simulation at the continental scale over NA; (2) evaluate the performance of VPM at

individual sites using GPP_{EC} data from 39 flux tower sites (155 site-years); (3) compare GPP_{VPM} with GOME-2 SIF data at 0.5° (latitude/longitude) resolution at the continental scale across NA; and (4) use of GOME-2 SIF as a reference to compare with GPP estimates from other six models. In this paper, we report (1) multi-year GPP_{VPM} and GPP_{EC} at individual flux tower sites, dependent upon availability of GPP_{EC} data, and (2) GPP_{VPM} in 2010 across NA.

6.2 Materials and Methods

6.2.1 Regional datasets for VPM simulations across North America

6.2.1.1 Climate data

The VPM model uses photosynthetically active radiation (PAR) and temperature data as climate input data. We use the National Center for Environmental Prediction-North America Regional Reanalysis (NCEP-NARR) datasets (Mesinger et al., 2006) for 2000-2014. The original three hourly data are first aggregated into 8-day averages to match the temporal resolution of MODIS vegetation indices. The day-time mean air temperature is obtained by averaging the temperature between 6 am to 6 pm local time. Zhao et al. (2006) reported that the NCEP-NARR product overestimates the surface shortwave radiation when comparing with the *in situ* observation at the flux tower sites. Jin et al. (2015) compared the NCEP-NARR radiation data with *in situ* radiation measurements at 37 AmeriFlux sites and reported a bias correction factor of 0.8. In this study, we applied this factor to adjust the radiation data. In order to run VPM at a 500 m spatial resolution, we use a non-linear spatial interpolation method (Zhao et al., 2005) to downscale the NCEP-NARR radiation and temperature dataset from the spatial resolution of 0.25°×0.25° to 500-m. It uses a fourth power of a cosine function and adopts the weighted distance from the near-

est four grid cells to calculate a value for each output pixel. The distance factor (D_i) for the four nearby grid cells can be calculated as follows:

$$D_i = \cos^4\left(\frac{\pi}{2} \times \left(\frac{d_i}{d_{max}}\right)\right) \qquad i = 1,2,3,4 \tag{6.1}$$

where d_i and d_max indicate the distance between the 500m MODIS pixel and each of the four vertex grid cells from NCEP-NARR data, and the maximum distance between the four vertex NCEP-NARR grid cells, respectively. For each MODIS pixel, the weight from the four surrounding NCEP-NARR grid cells can be calculated as:

$$W_i = \frac{D_i}{\sum_{n=1}^{4} D_i} \tag{6.2}$$

The final value for each interpolated MODIS pixel (V) can be expressed as a weighted average:

$$V = \sum_{n=1}^{4} (W_i \times V_i) \tag{6.3}$$

where V_i is the value for the four surrounding grid cell values of NCEP-NARR data.

6.2.1.2 MODIS data

MODIS surface reflectance and vegetation indices

The MODIS MOD09A1 surface reflectance product (500 m spatial resolution and 8-day temporal resolution) is used to calculate the enhanced vegetation index (EVI) (Huete et al., 2002) and LSWI as inputs to the VPM. LSWI is calculated as the normalized difference between NIR (0.78-0.89μ m) and SWIR (1.58-1.75μ m) and is sensitive to water content. Therefore, LSWI is a good indicator of water stress from the vegetation canopy and soil background (Xiao et al., 2002). These two indices are

calculated as follows:

$$EVI = 2.5 \times \frac{\rho_{nir} - \rho_{red}}{\rho_{nir} + (6 \times \rho_{red} - 7.5 \times \rho_{blue}) + 1} \tag{6.4}$$

$$LSWI = \frac{\rho_{nir} - \rho_{swir}}{\rho_{nir} + \rho_{swir}} \tag{6.5}$$

A temporal gap-fill algorithm is applied to the EVI time series data. The data quality is checked using the quality flag layer, and those observations not affected by cloud and climatological aerosols are considered 'GOOD' quality (MOD35 cloud = 'clear'; aerosol quantity = 'low' or 'average'). Each pixel is temporally linearly interpolated using only good-quality EVI observations within each year. A Savitzky-Golay filter is then applied to each pixel to eliminate high frequency noise (Chen et al., 2004). If a pixel has fewer than three out of 46 good observations for one year, the original data (no gap-filled) are used. Fortunately, this happens only for less than 0.5% of the total pixels and the majority of those are in less productive, boreal areas.

MODIS land cover data

The MODIS MCD12Q1 land cover product at 500-m spatial resolution (Friedl et al., 2010) includes annual land cover types from 2001 to 2013. We use MCD12Q1 data in 2001 to represent year 2000, and MDD12Q1 data in 2013 to represent year 2014, which allows us to have a full time series of land cover types for 2000-2014. The IGBP land cover classification scheme in the dataset is used to provide biome specific information for the VPM. A lookup-table (LUT) is used to get the essential parameters including maximum LUE as well as the maximum, minimum, and optimum temperatures for vegetation photosynthesis (see Appendix).

In order to investigate the relationship between GPP_{VPM} and SIF (0.5 degree latitude and longitude resolution) in different vegetation/biome types, we also aggregate the original 500 m land cover data to 0.5° grid cells using the following procedure. The original IGBP land cover data are first merged and reprojected onto the longitude-latitude projection with the original spatial resolution. We calculate the frequency (number of 500-m pixels) of individual vegetation types within a 0.5°×0.5° grid cell. Then, for each 0.5°×0.5° grid cell, if one vegetation type is dominant (more than 75% of the grid cell), this grid cell is assigned that vegetation type; if no land cover type is dominant, the grid cell is not assigned a type.

MODIS land surface temperature data

The MODIS MYD11A2 land surface temperature dataset is used to derive the thermal growing season and eliminate the snow cover period, which avoids the effect of snow cover in retrieving the yearly maximum LSWI. The MYD11A2 data set is chosen because it provides observations at 1:30 am, which is close to the daily minimum temperature. For each pixel each year, the thermal growing season is defined using the nighttime land surface temperature (Dong et al., 2015). Once three consecutive 8-day's in the spring have nighttime temperatures above 5°C, the thermal growing season begins; when three consecutive 8-day's in the fall have nighttime temperatures below 10°C, the thermal growing season ends. A detailed application of this temperature-based phenology was recently reported (Zhang et al., 2015a).

6.2.2 Datasets used to evaluate and compare VPM simulations across North America

6.2.2.1 CO_2 eddy flux data from AmeriFlux tower sites

CO_2 flux data from 39 AmeriFlux sites are downloaded from the AmeriFlux data portal (http://ameriflux.ornl.gov/). These flux sites cover most of the major biomes in NA (DBF, ENF, MF, GRA, CRO, CSH, OSH, WET and WSA) (Table 6.1). The 8-day level-4 gap-filled flux data with the Marginal Distribution Sampling (MDS) method is used (Reichstein et al., 2005). GPP_{EC} estimates from individual sites are used to evaluate GPP_{VPM}.

6.2.2.2 Solar-induced chlorophyll fluorescence (SIF) data from GOME-2

The latest version (v26) of monthly SIF data from the GOME-2 instrument onboard Eumetsat's MetOp-A satellite is available to the public (Joiner et al., 2013). GOME-2 captures earth radiation in the range from ~600 to 800 nm with a spectral resolution of ~0.5 nm at a nominal nadir footprint of 40×80 km^2 in the nominal observing configuration. Wavelengths around 740 nm at the far-red peak of the SIF emission are used for SIF retrievals with a principal component analysis approach to account for atmospheric absorption. The results are then quality-controlled (e.g., heavily cloud contaminated data removed) and aggregated to monthly means at 0.5°×0.5° spatial resolution (Joiner et al., 2013). In this study, we use GOME-2 SIF data for the period from January 2010 to February 2011.

6.2.2.3 GPP data from other six models

The GPP data from the four process-based models (LPJ, LPJ-GUESS, ORCHIDEE, and VEGAS) are part of the TRENDY projects, which intended to compare trends in net land-atmosphere carbon exchange over the period 1980–2010 (Table 6.3). These

four models, driven by the CRU+NCEP climate data and global annual atmospheric CO^2, are chosen because they have different algorithms to simulate GPP at 0.5°×0.5° spatial resolution.

Another two models involved in the comparison are the MPI-BGC and MODIS PSN. The MPI-BGC estimates GPP by upscaling global CO^2 flux observations using a Model Tree Ensemble approach (Jung et al., 2009). MODIS PSN employs a production-efficiency approach and uses the MODIS fraction of photosynthetically active radiation product (MOD15A2) and meteorological data (Running et al., 2004). The C55 version of MODIS PSN product (MOD17A2 C55) is used.

6.2.3 A brief description of the Vegetation Photosynthesis Model (VPM)

The satellite-based VPM (Xiao et al., 2004b,a) uses the product of light use efficiency (LUE, ε_g), and absorbed photosynthetically active radiation by chlorophyll ($FPAR_{chl}$) to estimate GPP as follows (Figure 6.2):

$$GPP = \varepsilon_g \times APAR_{chl} \tag{6.6}$$

VPM uses the fraction of absorbed photosynthetic active radiation by chlorophyll ($fAPAR_{chl}$) to estimate $APAR_{chl}$. The $fAPAR_{chl}$ is estimated from a linear function of EVI where the coefficient α is set to be 1.0 (Xiao et al., 2004b).

$$APAR_{chl} = fAPAR_{chl} \times PAR \tag{6.7}$$

$$fAPAR_{chl} = \alpha \times EVI \tag{6.8}$$

The light-use-efficiency (ε_g) in the VPM is a down-regulation of maximum LUE (ε_0) by temperature (T_{scalar}) and water stress limitation (W_{scalar}) on photosynthesis as

follows:

$$\varepsilon_g = \varepsilon_0 \times T_{scalar} \times W_{scalar} \tag{6.9}$$

ε_0 is a biome-specific parameter and differs for C3 and C4 plants. The ε_0 values are obtained from a lookup-table (LUT) using the MODIS land cover data. T_{scalar} is estimated from the equation used in the Terrestrial Ecosystem Model (TEM) (Raich et al., 1991).

$$T_{scalar} = \frac{(T - T_{max}) \times (T - T_{min})}{(T - T_{max}) \times (T - T_{min}) - (T - T_{opt})^2} \tag{6.10}$$

$LSWI_{max}$ is the maximum LSWI during the growing season over several years. We delineate the plant growing season from the following steps: (1) during the growing season period pre-defined by the LST, $LSWI_{max}$ is retrieved as the yearly maximum LSWI. If temperature-based identification of the growing season fails in the boreal region where nighttime temperature is always below 10°C, the growing season is set to be June to August. (2) LSWI will have an abnormally high value if snow exists and

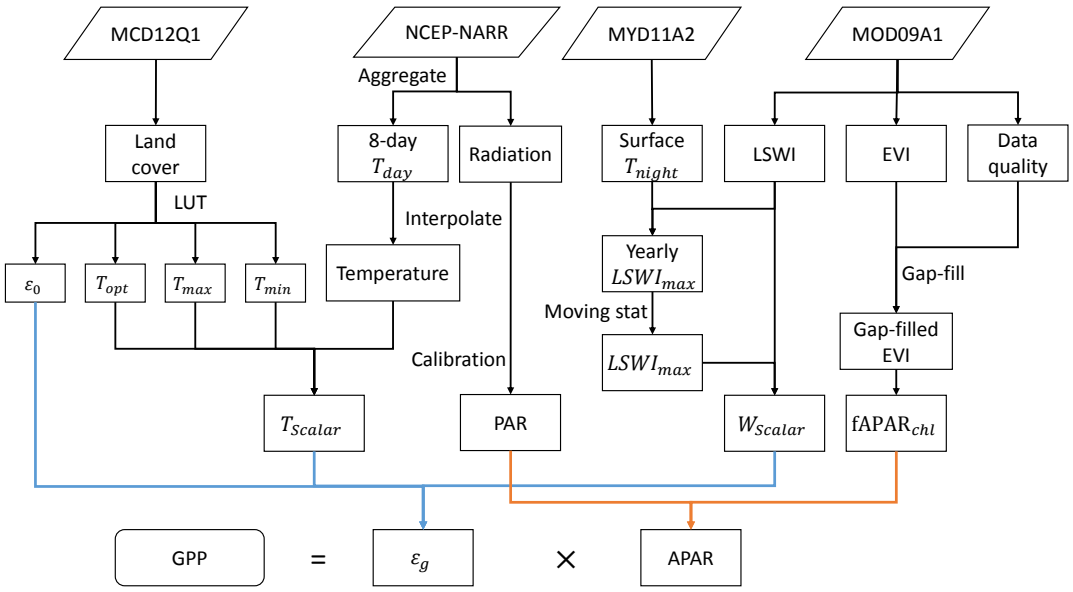


Figure 6.2: Flowchart of the data processing procedures for vegetation photosynthesis model (VPM).

a lower value during drought periods. To eliminate these abnormal values and take the land cover change into consideration, we further calculate the $LSWI_{max}$ using a moving-window statistical algorithm: we select a window of five years and pick the second largest maximum LSWI in this period.

6.3 Results

6.3.1 Seasonal dynamics of GPP at individual flux tower sites

Figure 6.3 shows the seasonal dynamics and interannual variations of GPP_{EC} and GPP_{VPM} across the 39 flux tower sites. The VPM accurately predicts the seasonality and magnitude of GPP for most natural vegetation (vegetation types other than cropland and cropland/natural vegetation mosaic in IGBP classification) (Figure 6.3). Table 6.1 summarizes the correlation between GPP_{EC} and GPP_{VPM} at individual sites over years. Nearly two thirds of the natural biomes sites have a RMSE less than 1.5 g C m^{-2} day^{-1}. Cropland sites have slightly larger RMSE values of 2.20–3.06 g C m^{-2} day^{-1}

Table 6.1: Descriptions of the 39 flux tower sites used in this study. IGBP class, R^2, and RMSE are the International Geosphere-Biosphere Programme land cover classification, coefficient of determination, and root mean square error of the regression analysis between tower-based gross primary production (GPP_{EC}) and simulated GPP (GPP_{VPM}) using vegetation photosynthesis model.

ID	NAME	LAT	LON	IGBP class[1]	Years used	R^2	RMSE	Reference
US-Bo1	Bondville	40.0062	-88.2904	CRO	2001-2006	0.83	2.20	Hollinger et al. (2005)
US-Ne1	Mead irrigated continuous	41.1651	-96.4766	CRO	2001-2005	0.91	3.06	Suyker et al. (2004)
US-Ne2	Mead irrigated rotation	41.1649	-96.4701	CRO	2001-2005	0.91	2.71	Suyker et al. (2005)
US-Ne3	Mead rainfed rotation	41.1797	-96.4397	CRO	2001-2005	0.85	2.76	Suyker et al. (2005)
US-Ro1	Rosemount-G21	44.7143	-93.0898	CRO	2004-2006	0.80	2.45	Griffis et al. (2005)
US-Ro3	Rosemount-G19	44.7217	-93.0893	CRO	2004-2006	0.81	2.22	Griffis et al. (2005)
US-KS2	Kennedy Space Center	28.6086	-80.6715	CSH	2004-2005	0.72	0.96	Dijkstra et al. (2002)
US-Los	Lost Creek	46.0827	-89.9792	CSH	2001-2002	0.90	1.59	Sulman et al. (2009)

US-Bar	Bartlett Experimental Forest	44.0646	-71.2881	DBF	2004-2006	0.93	1.33	Jenkins et al. (2007)
US-Ha1	Harvard Forest	42.5378	-72.1715	DBF	2000-2006	0.83	2.05	Urbanski et al. (2007)
US-LPH	Little Prospect Hill	42.5419	-72.1850	DBF	2001-2005	0.91	1.30	Vanderhoof et al. (2013)
US-MMS	Morgan Monroe State Forest	39.3232	-86.4131	DBF	2005-2007	0.91	1.59	Schmid et al. (2000)
US-MOz	Missouri Ozark Site	38.7441	-92.2000	DBF	2000-2006	0.89	1.37	Gu et al. (2006)
US-UMB	Univ. of Mich. Biological Station	45.5598	-84.7138	DBF	2000-2006	0.97	0.78	Gough et al. (2008)
US-WCr	Willow Creek	45.8059	-90.0799	DBF	2002-2005	0.96	1.05	Cook et al. (2004)
CA-NS1	UCI-1850 burn site	55.8792	-98.4839	ENF	2003-2005	0.65	1.00	Goulden et al. (2006)
CA-NS2	UCI-1930 burn site	55.9058	-98.5247	ENF	2002-2005	0.70	0.88	Goulden et al. (2006)
CA-NS3	UCI-1964 burn site	55.9117	-98.3822	ENF	2002-2005	0.92	1.49	Goulden et al. (2006)
CA-NS4	UCI-1964 burn site wet	55.9117	-98.3822	ENF	2003-2004	0.84	1.08	Goulden et al. (2006)
CA-NS5	UCI-1981 burn site	55.8631	-98.4850	ENF	2002-2005	0.89	1.13	Goulden et al. (2006)
US-Blo	Blodgett Forest	38.8953	-120.6328	ENF	2000-2006	0.74	1.58	Goldstein et al. (2000)
US-Fmf	Flagstaff Managed Forest	35.1426	-111.7273	ENF	2007	0.63	0.95	Dore et al. (2008)
US-Ho1	Howland Forest (main tower)	45.2041	-68.7402	ENF	2000-2004	0.88	0.84	Hollinger et al. (2004)
US-Ho2	Howland Forest (west tower)	45.2091	-68.7470	ENF	2000-2004	0.69	0.98	Hollinger et al. (2004)
US-Me2	Metolius-intermediate aged pine	44.4523	-121.5574	ENF	2002, 2004-2007	0.91	1.03	Law et al. (2004)
US-Me3	Metolius-second young aged pine	44.3154	-121.6078	ENF	2004-2005	0.69	1.26	Law et al. (2000)
US-Me5	Metolius-first young aged pine	44.4372	-121.5668	ENF	2000-2002	0.94	0.60	Law et al. (2000)
US-NC1	North Carolina Clearcut	35.8115	-76.7115	ENF	2005-2006	0.95	0.93	Noormets et al. (2010)
US-Wi0	Wisconsin young red pine	46.6188	-91.0814	ENF	2002	0.81	1.79	Sun et al. (2008)
US-Wi4	Wisconsin mature red pine	46.7393	-91.1663	ENF	2002-2005	0.92	0.81	Sun et al. (2008)
US-ARb	ARM SGP burn	35.5497	-98.0402	GRA	2005-2006	0.91	1.99	Fischer et al. (2007b)
US-ARc	ARM SGP control	35.5465	-98.0400	GRA	2005-2006	0.91	2.07	Fischer et al. (2007b)
US-Goo	Goodwin Creek	34.2547	-89.8735	GRA	2004-2006	0.68	1.93	Wilson & Meyers (2007)
US-Wlr	Walnut River Watershed	37.5208	-96.8550	GRA	2002-2004	0.94	0.81	Coulter et al. (2006)
US-Syv	Sylvania Wilderness Area	46.2420	-89.3477	MF	2001-2006	0.92	1.12	Desai et al. (2005)
CA-NS6	UCI-1989 burn site	55.9167	-98.9644	OSH	2002-2005	0.87	0.69	Goulden et al. (2006)
CA-NS7	UCI-1998 burn site	56.6358	-99.9483	OSH	2002-2005	0.86	0.63	Goulden et al. (2006)
US-Ivo	Ivotuk	68.4865	-155.7503	WET	2004, 2006	0.67	0.80	Epstein et al. (2004)
US-FR2	Freeman Ranch-Mesquite Juniper	29.9495	-97.9962	WSA	2004-2006	0.73	1.13	Heinsch et al. (2004)

Figure 6.4 shows the comparison between GPP_{EC} and GPP_{VPM} at biome levels. When compared to GPP_{EC}, GPP_{VPM} underestimate by 4% (according to regression slope and hereafter) for deciduous broadleaf forests (DBF), 8% for mixed

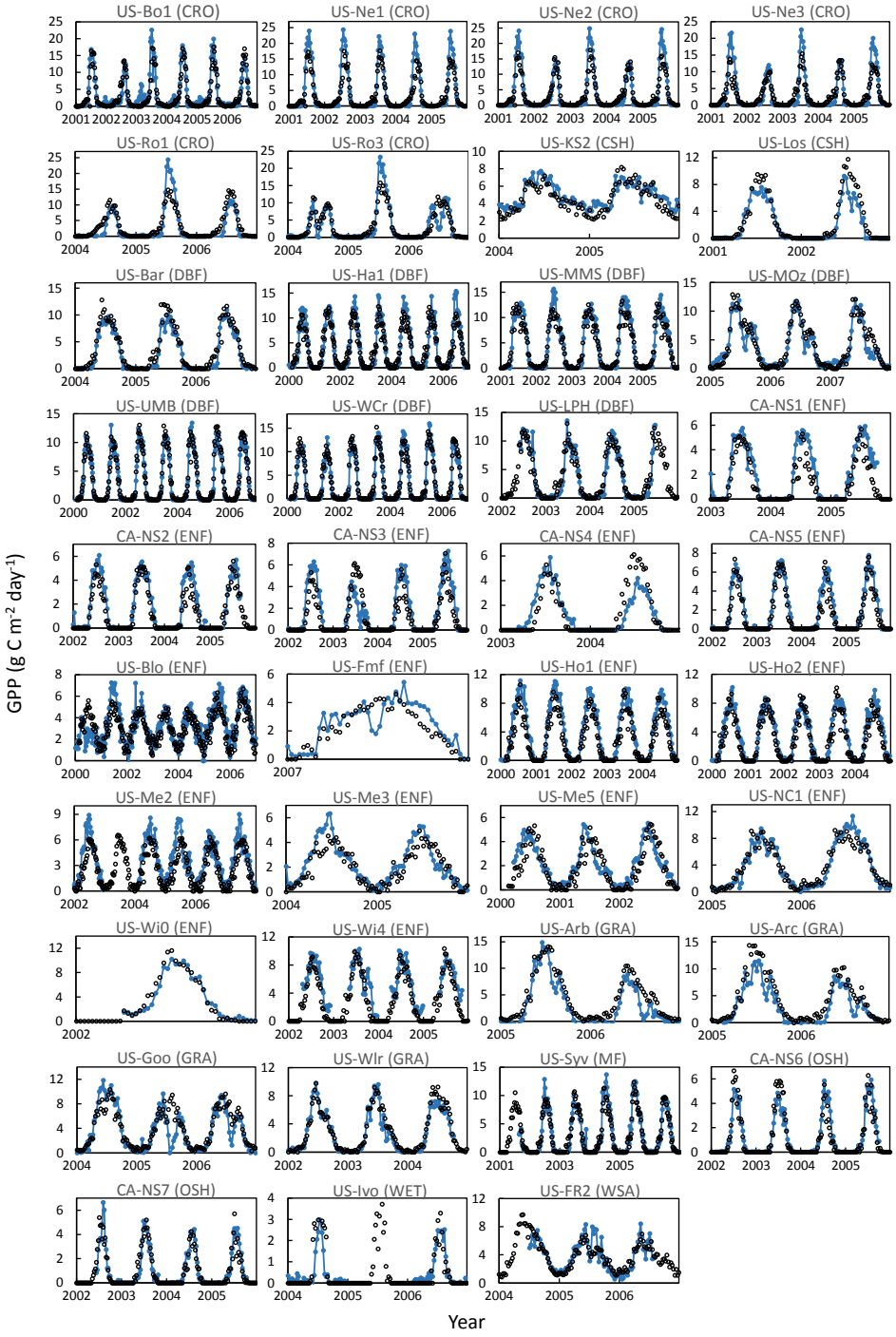


Figure 6.3: Seasonal dynamics and interannual variations of the tower-based (GPP_{EC}) and the modeled (GPP_{VPM}) gross primary production at 39 flux sites at 8-day intervals. The blue lines represent the GPP_{EC} and the black circles represent the GPP_{VPM}. The ticks on the x-axis represent the first date of the corresponding year.

forests (MF), and 16% for evergreen needleleaf forests (ENF). GPP_{VPM} and GPP_{EC} agree well for closed shrubland (2%) and open shrubland (4%). For grassland and woody savannas (WSA), the biases are less than 8%. When all natural biome sites are combined, GPP_{VPM} is slightly lower than GPP_{EC}, approximately 8% (y = 0.92x, R^2 = 0.85) (Figure 6.4). For cropland sites (cropland and cropland/natural vegetation mosaic in IGBP classification), GPP_{VPM} is lower than GPP_{EC} by 23% (y = 0.77x, R^2 = 0.82). When all 39 sites are lumped together, the difference between GPP_{VPM} and GPP_{EC} is approximately 13% (y = 0.87x, R^2 = 0.82). The LUE parameter in VPM improves the predictability of GPP, as represented by the decreased coefficient of determination (R^2) in the VPM model sensitivity analysis for both natural biomes and all biomes sites when LUE parameter is removed (Figure 6.A.1).

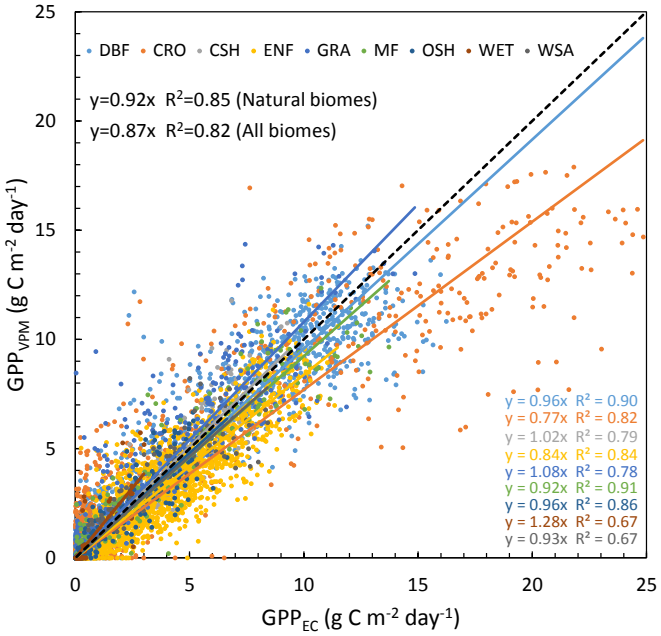


Figure 6.4: A comparison of the tower-based (GPP_{EC}) and the modeled (GPP_{VPM}) gross primary production by biome types. Data are pooled across the study period for each biome. The dash line is 1:1 line and solid lines are linear regression lines forced to pass the origin.

6.3.2 *Spatial patterns of GPP_{VPM} across North America in 2010 at 500-m spatial resolution*

Figure 6.5A shows the spatial distribution of annual GPP_{VPM} for 2010 across NA. The highest GPP_{VPM} (> 2,000 g C m^{-2} $year^{-1}$) occurs in the southernmost tropical regions. GPP_{VPM} decreases along a latitudinal gradient in the eastern region, owing to the decreasing temperature and growing season length. GPP_{VPM} also decreases along a longitudinal gradient from east (dominated by forest) to west (dominated by grasslands and desert). Figure 6.5B shows the spatial distribution of the maximum daily GPP_{VPM} in 2010. The highest value is ~20 g C m^{-2} day^{-1} for the Midwest Corn Belt. The southeastern U.S. has a relatively low value as compared with the mid-latitude region (35°N– 45°N). The biggest contrast between annual GPP_{VPM} and maximum daily GPP_{VPM} is found in the tropical and western coastal regions, where annual GPP_{VPM} is highest while the maximum daily GPP_{VPM} is moderate.

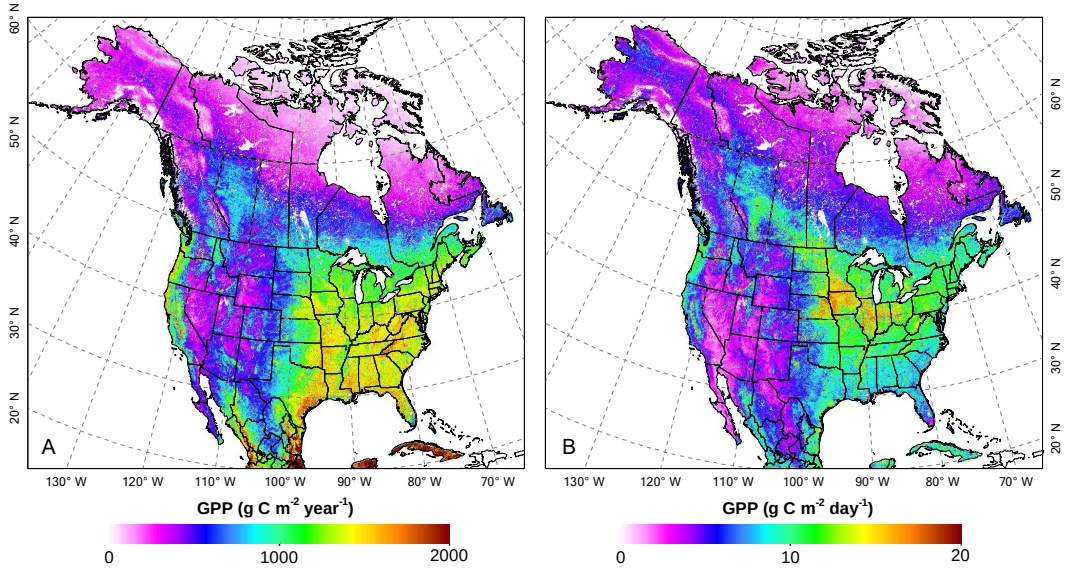


Figure 6.5: Spatial distribution of modeled (A) annual GPP_{VPM} and (B) maximum daily GPP_{VPM} for year 2010.

GPP_{VPM} varies significantly across biomes (Table 6.2). The most productive

ecosystem is the evergreen broadleaf forest with an annual GPP_{VPM} of more than 2,000 g C m^{-2} $year^{-1}$. Open shrubland and savannas are the least productive with an annual GPP_{VPM} less than 375 g C m^{-2} $year^{-1}$. Grassland, savannas, and shrublands have relatively high spatial variance because of the extensive distribution and high sensitivity to soil water. All natural vegetation contribute about 70% of the total GPP_{VPM}, with an average of 600.88 g C m^{-2} $year^{-1}$. Croplands accounts for about 27% of the total GPP but with a nearly doubled photosynthetic capacity (1,194.27 g C m^{-2} $year^{-1}$) compared with the mean of natural vegetation. The maximum daily GPP_{VPM} for different biomes varies from 3.59 to 12.00 g C m^{-2} day^{-1}. Croplands have the largest GPP_{VPM} magnitudes (9.94 to 12.00 g C m^{-2} day^{-1}). Forest ecosystems have a relatively higher maximum photosynthetic rate (8.79 g C m^{-2} day^{-1}) compared with other natural vegetation types (4.65 g C m^{-2} day^{-1}). The inconsistency between annual GPP_{VPM} sums and maximum daily GPP_{VPM} may be mainly attributed to different growing season lengths that are affected by temperatures and rainfall.

Table 6.2: The magnitudes and annual sums of simulated gross primary production (GPP_{VPM}) of different biomes in North America (170°–50°W, 20°–80°N) for year 2010.

IGBP class	Average annual GPP (g C m^{-2} $year^{-1}$)	Standard deviation of annual GPP (g C m^{-2} $year^{-1}$)	Average maximum daily GPP (g C m^{-2} day^{-1})	Standard deviation of maximum daily GPP(g C m^{-2} day^{-1})	Total (Pg C $year^{-1}$)
ENF	638.45	255.53	5.90	1.55	1.32
EBF	2038.76	448.32	9.63	1.71	0.16
DBF	1443.95	188.49	11.09	1.47	0.75
MF	1030.24	330.46	8.53	1.78	1.94
OSH	349.30	224.44	3.59	1.31	1.48
WSA	815.81	543.79	6.27	2.29	1.50
SAV	377.65	267.02	4.17	1.27	0.20
GRA	457.50	380.74	4.24	2.59	2.00
WET	539.26	253.98	5.00	1.41	0.21
CRO	1157.99	390.54	12.00	3.09	2.15
CNV	1248.95	317.55	9.94	1.67	1.54

Figure 6.6 shows the frequency distribution of annual GPP_{VPM} and maximum daily GPP_{VPM} for all pixels in NA and their distribution in the climate space. More than 70% of pixels have relatively low productivity, i.e., annual GPP_{VPM} less than 1,000 g C m^{-2} $year^{-1}$ or maximum daily GPP_{VPM} less than 10 g C m^{-2} day^{-1}. We also plot the distribution of the 39 flux tower sites in NA based on the annual and maximum daily GPP_{EC} (Figure 6.6). The distribution of the flux tower sites cover the broad range of maximum daily GPP_{VPM}, and most of them are located in regions with moderate annual GPP (1,000–1,800 g C m^{-2} $year^{-1}$). In the two-dimensional climate space described by mean annual temperature (MAT) and mean annual precipitation (MAP) (Figure 6.6C, D), the flux tower sites distribution covers most of the climate space. The annual GPP_{VPM} generally increases with MAT mad MAP, while the daily maximum GPP_{VPM} is highest in moderate MAT and MAP regions.

6.3.3 Spatial-temporal comparison between GPP_{VPM} and SIF across NA in 2010 at 0.5° spatial resolution

We aggregate the 8-day 500-m GPP_{VPM} estimates to the seasonal (3-month interval) and 0.5° latitude/longitude grid to compare with the seasonal SIF data. Both GPP_{VPM} and GOME-2 SIF data have strong seasonal dynamics and spatial variation across NA (Figure 6.7, 6.8).

During spring (March to May), both GPP_{VPM} and GOME-2 SIF are relatively high in the southeastern part of the United States (Figure 6.7), where forests dominate and plants grow through the spring. Both GPP_{VPM} and GOME-2 SIF are also high in California, where the Mediterranean climate (warm and wet spring and dry summer) occurs (Ma et al., 2007; Baldocchi et al., 2004). In comparison, the rest of lands with low temperature and/or rainfall in NA have low GPP_{VPM} and GOME-2 SIF values.

In summer months (June to August), the Corn Belt in mid-west U.S. and south-western Canada has the highest GPP_{VPM} and SIF. This is supported by the eddy flux data: GPP_{EC} for maize is > 25 g C m^{-2} day^{-1} during summer, much higher than that of the forest ecosystems. Overall, summer months contribute more than 62% of the annual GPP in NA, 42% of which come from Canada and 45% from the conterminous U.S. SIF data also show the highest values in the Corn Belt and lowest in the western and northern regions, consistent with the GPP_{VPM}.

In the fall (September to November), both GPP and SIF drop substantially in the mid-west region due to crop harvesting. Similar to spring, the high photosynthesis

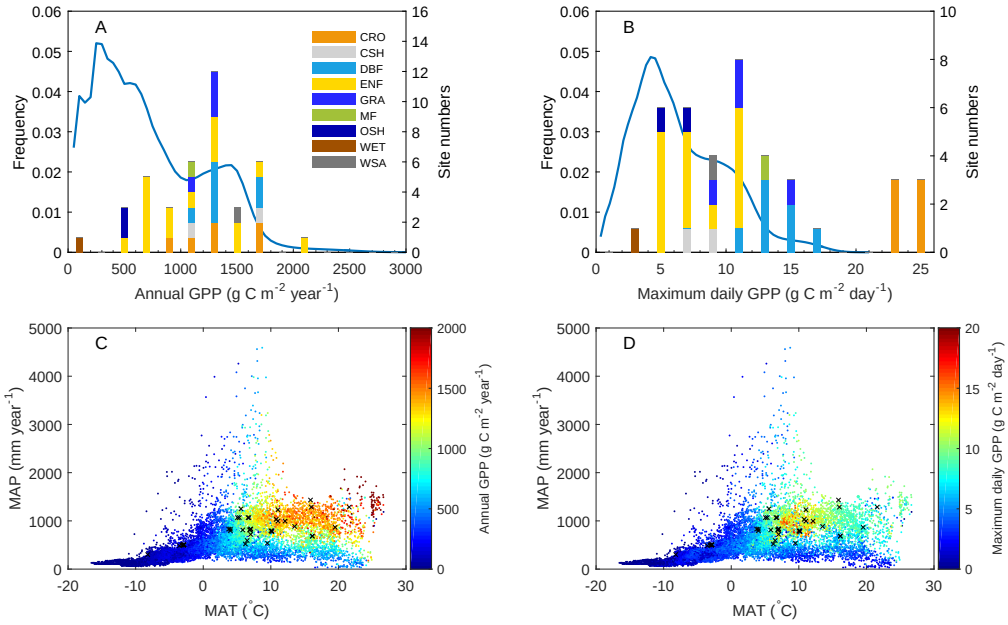


Figure 6.6: The frequency distribution of GPP_{VPM} of the (A) annual GPP and (B) maximum daily GPP compared to the flux site distribution and their distribution in the climate space defined by mean annual temperature (MAT) mean annual precipitation (MAP) (C, D). The blue curves in (A and B) indicate the frequency distribution calculated from Figure 6.5. The annual and maximum daily GPP for the flux tower sites are from the 39 sites used in our study. Black crosses in (C and D) represent the location of 39 flux tower sites in the climate space. Precipitation data from GPCC (Global Precipitation Climatology Centre) and temperature data from NCEP-NARR are used to generate the climate space.

rate also corresponds to a long growing season in the southeastern U.S., but the value is smaller than spring. The eastern and western coasts of Mexico as well as Cuba still fix carbon at a rate of more than 5 g C m^{-2} day^{-1}. In Alaska and northern Canada, all vegetation goes to dormancy, and both GPP and SIF values are close to 0. These spatial patterns are also evident in the SIF data.

During the winter (December through February), only the very southern part of the U.S., California, and coastal regions of Mexico and Cuba have moderate GPP_{VPM} and SIF values. All the other regions do not show any sign of photosynthesis activi-

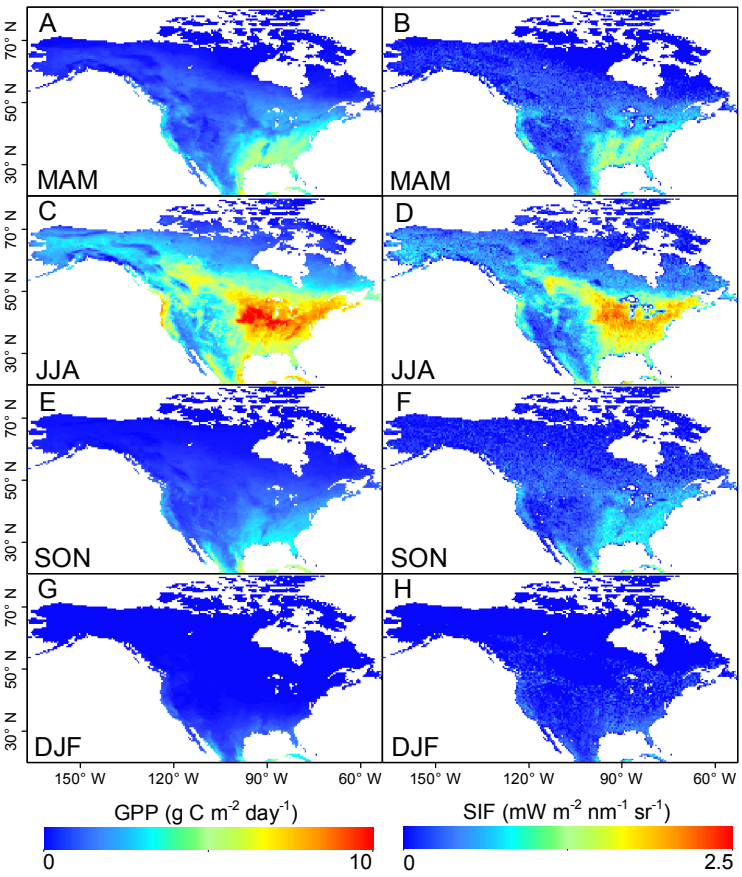


Figure 6.7: A comparison of seasonal average solar-induced fluorescence (SIF) from the GOME-2 satellite instrument and simulated gross primary production (GPP_{VPM}) during the period of March 2010 through February 2011. MAM, JJA, SON, and DJF correspond to spring, summer, fall, and winter, respectively.

ties, and both GPP_{VPM} and SIF values are close to zero.

6.4 Discussion

6.4.1 The relationship between SIF and GPP

SIF is emitted during the vegetation photosynthetic process. Absorbed energy by chlorophyll is partitioned into SIF, photochemical quenching (PQ, energy used for photosynthesis), non-photochemical quenching (NPQ, energy partitioned to heating), and efficiency loss (Baker, 2008). Previous studies have shown that SIF is positively correlated with PQ when light is moderate or high or environmental stress exists (Flexas et al., 2000; Lee et al., 2015; Porcar-Castell et al., 2006; Soukupová et al., 2008). However, the relationship between GPP and SIF emission at far-red peak (SIF740 used in our study) is also affected by the SIF contribution from photosystem II and photosystem I, alternative sinks of energy, photorespiration, internal CO^2 concentration of leaves and enzyme activities, etc. (Porcar-Castell et al., 2014). Nevertheless, SIF measurements from satellite provide a direct and independent estimations of photosynthetic activity which is different from reflectance based vegetation indices. The GPP-SIF relationship still needs intensive investigation.

Several studies (Joiner et al., 2014; Zhang et al., 2014b; Wagle et al., 2016) have reported on the direct comparison between satellite-derived SIF data (0.5°grid cell) and in situ GPP_{EC} from flux sites that often have footprint sizes of a few hundreds of meters, but such comparisons is problematic owing to spatial mismatches and heterogeneity due to mixed land cover types within a given 0.5° grid cell (Zhang et al., 2014b). In this study, the VPM simulations are aggregated to the same spatial resolution as the GOME-2 SIF data. Figure 6.8 shows the correlation between GPP_{VPM} and the SIF data for the four seasons. In spring, summer, and fall, GPP_{VPM} shows

a very high correlation with SIF. The coefficient of determination ranges from 0.74 to 0.86, and the GPP_{VPM}-SIF correlation increases with the increase in daily GPP or SIF value (from early to peak growing season). This high spatial correlation confirms our comparison in section 3.3 and can be further explained by the $APAR_{chl}$ used in the VPM. Both $APAR_{NDVI}$ (NDVI×PAR) and $APAR_{fPAR}$ (fPAR×PAR) have lower correlation with SIF compared with $APAR_{chl}$; an obvious saturation can be found in summer where SIF continues to increase while $APAR_{NDVI}$ and $APAR_{fPAR}$ tend to saturate. The regression slope between $APAR_{chl}$ and SIF are also more stable during the growing season (2.82±0.13). As SIF is reemitted from the photosystem II, the higher correlation between SIF and $APAR_{chl}$ also suggests that EVI can be a good proxy of light absorbed by chlorophyll. In the winter, however, the correlations between SIF and GPP_{VPM} and APAR are much weaker mostly due to the very low SIF signal and relatively lower signal-to-noise ratio. We also calculate the regression between GPP_{VPM} and SIF for points with $GPP_{VPM} > 1$ g C m^{-2} day^{-1} (to eliminate some low values with relatively higher bias during the non-growing season). The range of the regression slopes are narrower when only data for the period of $GPP_{VPM} > 1$g C m^{-2} day^{-1} are used as compared to all data points (SD_{slope}=0.42 vs. 0.74).

6.4.2 Comparison of SIF and GPP estimates in North America from several models

A number of models have reported annual total GPP in NA (Huntzinger et al., 2012; Xiao et al., 2014). The annual GPP_{VPM} is 13.53 Pg C in 2010. We further compared GPP_{VPM} with GPP from six other models (MODIS PSN, MPI-BGC, LPJ, LPJ-GUESS, ORCHIDEE, and VEGAS) (Figure 6.9). The VPM-based GPP estimates are close to the average of these six models (15.75 Pg C year^{-1}) (Table 6.3). Three process-based models (LPJ, LPJ-GUESS, and ORCHIDEE) predict very high GPP for the southeast-

ern U.S., which may be caused by different approaches they employed (enzyme kinetic vs. LUE).

Because SIF is directly retrieved from satellite and has a very good correlation with data driven model-based GPP (Frankenberg et al., 2011; Wagle et al., 2016), we use SIF as a reference to compare the spatial variations in GPP of all models. ORCHIDEE, PSN, MPI-BGC, and VPM show high consistency with SIF data. The ma-

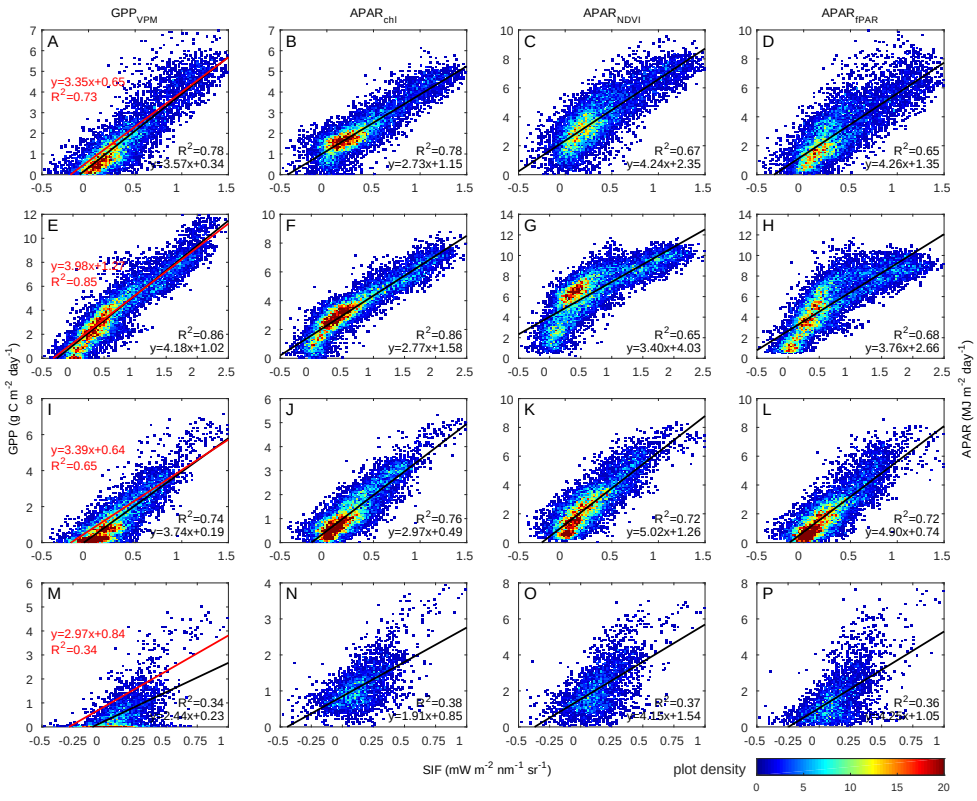


Figure 6.8: Relationship between SIF and GPP_{VPM} (A, E, I, M), $APAR_{chl}$ (EVI×PAR) (B, F, J, N), APARNDVI (NDVI×PAR) (C, G, K, O) and APARfPAR (fPAR×PAR) (D, H, L, P) for four seasons (by row from first to fourth: spring, summer, autumn, winter) in North America in 2010. EVI and NDVI are from monthly 0.05° MOD13C1 C5, fPAR is from 8-day 1km MOD15A2 C5, all of which are aggregated to seasonal and 0.5-degree spatial resolution. Black lines are regression for all the points, and the red lines are the regressions between GPP_{VPM} and SIF with $GPP_{VPM} > 1$ g C m^{-2} day^{-1}.

jor difference is the relative underestimation at the Corn-Belt and overestimation in the western coast along the U.S./Canada border in ORCHIDEE, PSN, and MPI-BGC. Recent studies reveal that cropland, especially maize in the U.S., makes a large contribution to the seasonal swing of atmospheric CO^2 concentration (Gray et al., 2014; Zeng et al., 2014). The high GPP values in this region are often underestimated by models (Guanter et al., 2014). Beer et al. (2010) also suggest that given the limited C4 vegetation flux data availability, great uncertainty remains in estimating the contribution of C4 plants while upscaling eddy flux observations. A similar issue is also found in a study focused on the conterminous U.S. (Xiao et al., 2010), which may explain the underestimation of the regional GPP sums. GPP_{VPM} and SIF data show similar spatial patterns for the mid-western Corn Belt (r = 0.87, p < 0.001) where a previous study showed SIF at a monthly scale has a high correlation with GPP (Guanter et al., 2014); this also supports that the spatial variation of GPP_{VPM} for croplands is to some degree an improvement over the other six models.

Table 6.3: Annual gross primary production (GPP) of North America (170°–50°W, 20°–80°N) estimated from different models for year 2010.

Models	Annual GPP ($Pg\,C\,year^{-1}$)	Reference
LPJ	22.23	(Sitch et al., 2003)
LPJ-GUESS	19.84	(Smith et al., 2001)
ORCHIDEE	17.52	(Krinner et al., 2005)
VEGAS	11.35	(Zeng et al., 2005)
MODIS GPP	13.13	(Zhao et al., 2005)
MPI-BGC	12.70	(Jung et al., 2011)
VPM	13.53	This study

Several previous studies indicate that the relationships between GPP and SIF should be different across biomes (Damm et al., 2015a; Guanter et al., 2012, 2014; Parazoo et al., 2014; Verrelst et al., 2015). This ecosystem-dependent GPP-SIF rela-

tionship is determined by different SIF contribution from both photosystem I and photosystem II, uncertainty in NPQ, and structural interference of SIF leaving the canopy (Damm et al., 2015a; Verrelst et al., 2015). Here we compare SIF with GPP estimates from three diagnostic models (VPM, MPI-BGC, and MODIS PSN) and APAR, as well as the relationship between SIF_{yield} (SIF/$APAR_{chl}$) and LUE (Figure 6.10). Being consistent with a previous study at site level (Yang et al., 2015), we also find that SIF contains the information of LUE, represented by a high correlation between SIF_{yield} ($SIF/APAR_{chl}$) and LUE_{VPM} (Figure 6.10E). This also partially supports

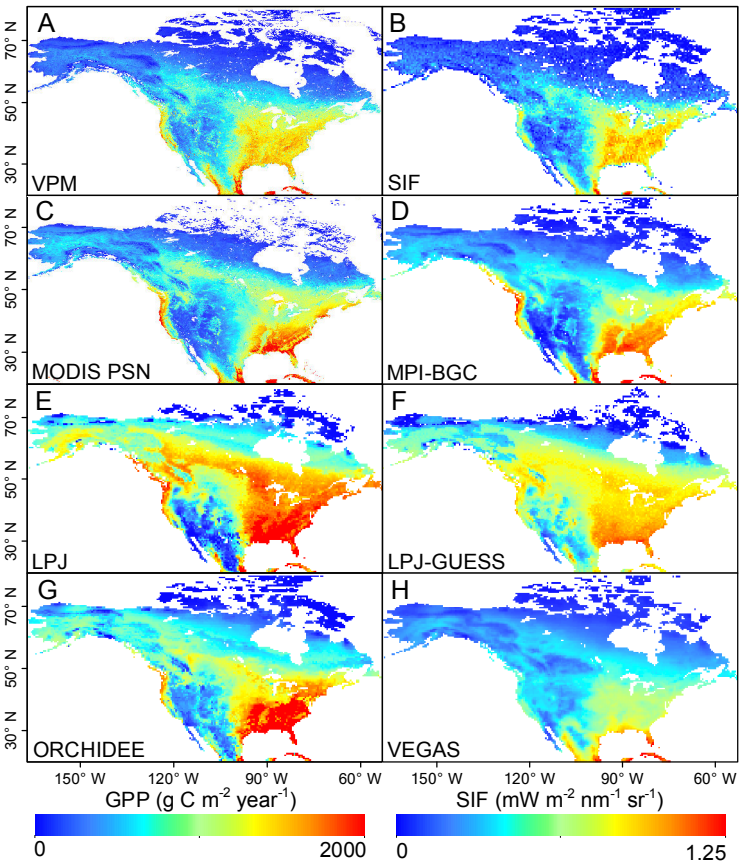


Figure 6.9: Comparison of annual gross primary production (GPP) from different LUE-based models (A, C), data-driven model (D), process-based models (E, F, G, H), and with solar-induced fluorescence (SIF) (B). Data are shown for the year 2010.

the GPP-SIF relationship. However, due to the spatial inconsistency, we did not directly compare GOME-2 SIFyield with LUEEC, more canopy or ecosystem level SIF measurement from in situ or airborne spectrometers will enable this kind of comparison in the near future. In terms of inter-model comparison, VPM and MPI-BGC show higher average R2 (0.86 and 0.89, respectively) for individual biomes than does MODIS PSN (0.83). The data points are also more scattered in the MODIS PSN than in other two models. Different biome types also show distinct differences in slopes (4.03–8.9 for VPM, 3.73–7.83 for MPI-BGC, and 2.76–11.12 for MODIS PSN). For the most highly productive biomes (average SIF > 1 mW m^{-2} nm^{-1} sr^{-1}), the correlations between predicted GPP and SIF are very high (R2 > 0.95) except for EBF; this may be caused by cloud and/or aerosol contamination of the satellite data. The range of slopes for these biomes also shows less variation (4.60–5.55 for VPM, 4.02–5.72 for MPI-BGC, and 3.60–6.02 for MODIS PSN). In contrast, the less productive regions usually have lower regression coefficents and more variable slopes. This may be partially due to the higher relative error for the GOME-2 SIF data (Joiner et al., 2013) and GPP models. SIF retrievals from later satellites (OCO-2, FLEX - Fluorescence Explorer, Sentinel-5 Precursor) will have better accuracy (Frankenberg et al., 2014; Guanter et al., 2015; Kraft et al., 2013) and can be used to improve and benchmark GPP for land models (Lee et al., 2015; Luo et al., 2011; Zhang et al., 2014b).

6.4.3 Sources of uncertainty for VPM simulations in North America

Maps of land cover types affect GPP estimates as the LUE parameter used in the model varies with biomes. In this study, the MOD12 land cover dataset lists croplands as one category and does not distinguish between C3 and C4 crops. Both C3 and C4 crops have different photosynthetic pathways and light use efficiency

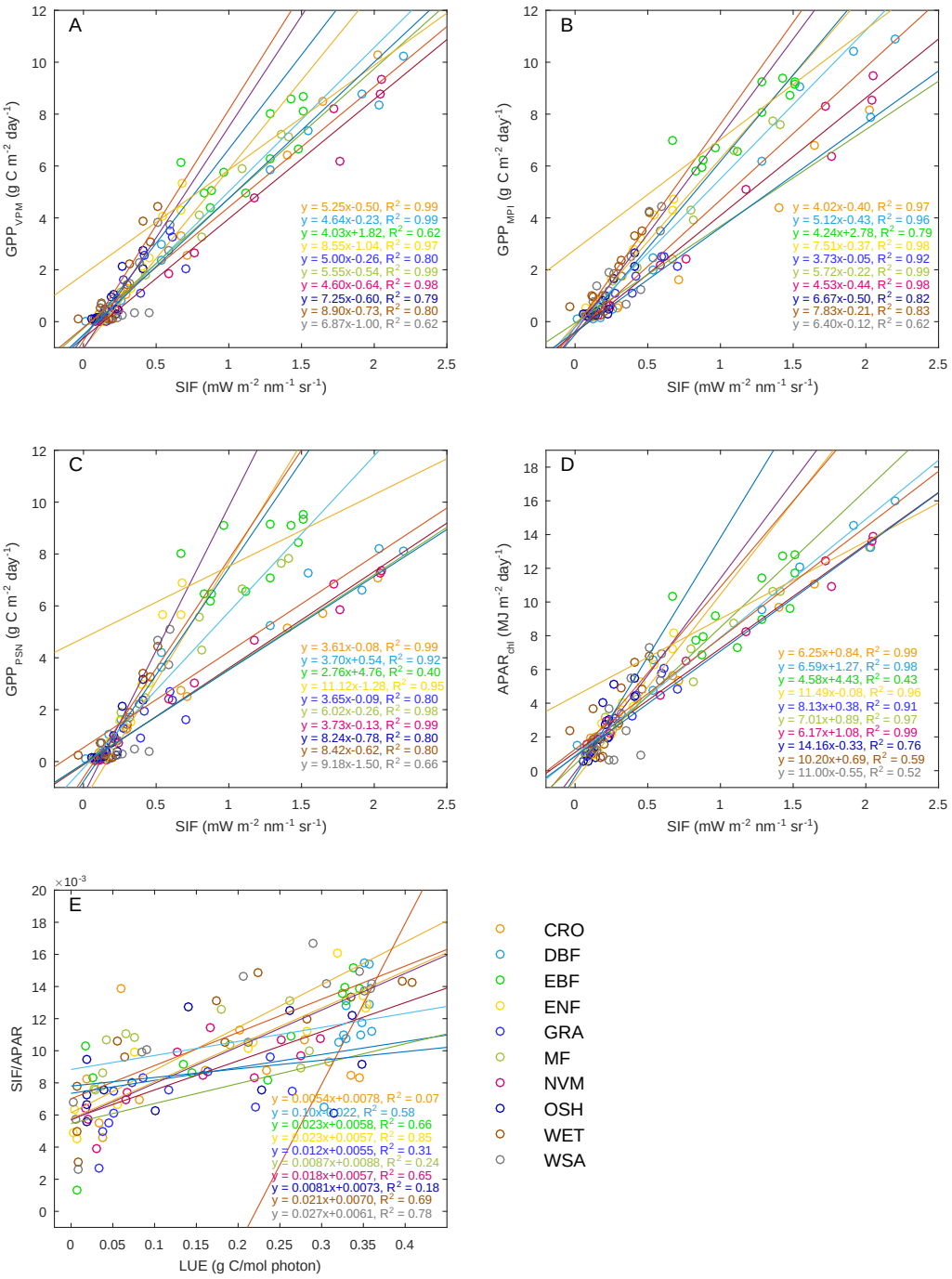


Figure 6.10: A comparison for relationship between GPP_{VPM} and SIF (A), GPP_{MPI} and SIF (B), GPP_{PSN} and SIF (C), $APAR_{chl}$ (EVI×PAR) and SIF (D), SIF_{yield} (SIF/APAR) and LUE_{VPM} (E) for different biome types in North America in 2010. For each month each biome type, a value is given by averaging all the grid cells with in this biome type.

(Kalfas et al., 2011; Yuan et al., 2015): C4 croplands (e.g., maize) have a higher GPP_{EC} that do C3 croplands (Figure 6.3). Thus, the LUE parameterization of croplands for each year depends upon our knowledge of crop rotation. For VPM simulations at the continental scale, there are four options to address this problem in a MODIS cropland pixel: (1) assume 100% C3 plants, (2) assume 100% C4 plants, (3) assume C3+C4 mixing ratio as 50% each, and (4) use known C3+C4 mixing ratio from other data sources (in situ data, or other maps). Because there is no yearly map of C3/C4 mixing ratio across NA, we simply chose the third option in this study. Therefore, GPP_{VPM} would either overestimate GPP for C3 plants (soybean, wheat, etc.) or underestimate for C4 plants (corn, sugar cane, etc.) in those pure pixels. In those C3/C4 mixed pixels, however, these artifacts (under- or over-estimation) can be partially alleviated. For example, both maize and soybean are grown in rotation at the US-Bo1 site within a 50 m radius, but within a 500 m radius of the flux tower site, corn and soybean areas have a mixing ratio of 50% each over the years. The GPP_{VPM}, driven by averaged LUE for C3 and C4 crops, captures both the seasonality and the magnitude at this site (Figure 6.11A). For pure pixels, VPM would provide better results if a specific crop type is given and an appropriate LUE value is used. We use the LUE value for C4 plants at the US-Ne1 site where maize is grown throughout the period (Figure 6.11B). This modification greatly improves the estimation of GPP, with an RMSE reduces from 3.06 to 2.32 g C m^{-2} day^{-1} and a slope increases from 0.65 to 0.86.

In our study, all cropland flux tower sites are located in the mid-west Corn Belt and altogether we have 16 corn years and 11 soybean years. As we use an average LUE of C3 and C4 for croplands, the model may underestimate GPP at the site scale owing to more corn years (Figure 6.4). At a regional scale, the bias mainly depends on the C3 and C4 crop mixing ratios within individual pixels. In the U.S. Midwest

where C4 crops (e.g., corn) are dominant, the VPM simulation may underestimate cropland production while in California or the Mississippi River Basin, where C3 crops are dominant, the VPM simulation may overestimate. Therefore, the lack of crop plant functional type (C3 and C4) is likely the largest source of uncertainty in the GPP_{VPM}. This clearly highlights the need to generate annual maps of plant functional types (C3 and C4) in NA in the near future. In addition, the mismatch between the flux tower footprint and the MODIS pixel, and the land cover fragmentation within each MODIS pixel are also critical issues when using EC data for model validation. All flux towers should be evaluated using footprint models and high resolution satellite images to provide the representativeness for the MODIS pixel (Chen et al., 2012).

Image data quality is always an important issue for the application of remote sensing. In this study, we use the vegetation indices calculated directly from the MODIS surface reflectance product. These indices are subject to atmospheric contamination (i.e., clouds, aerosols) and often result in a lower-than-normal value for

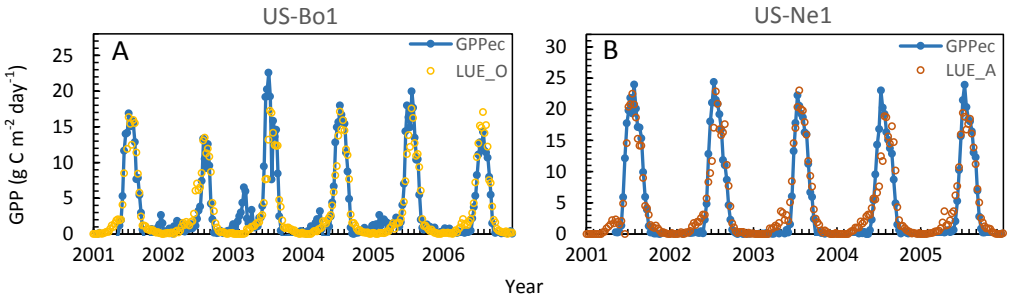


Figure 6.11: Seasonal dynamics and interannual variations of the tower-based (GPP_{EC}) and the modeled (GPP_{VPM}) gross primary production at two flux tower sites at 8-day intervals at a maize/soybean rotation site (US-Bo1) (A) and a continuous maize site (US-Ne1) (B). Blue lines represent estimated GPP from flux tower, yellow circles represent the present simulation result using the original LUE (LUE_O) and brown circles represent improved simulation result using an alternative LUE (LUE_A) for C4 plant.

EVI, especially in those regions where cloud and aerosol are persistent (boreal and tropical regions in our study). The effect of the atmospheric contamination can be partially eliminated through a gap-fill method. Figure 6.12 shows the comparison between the gap-filled and no gap-filled results. Obvious cloud contamination is marked in the black ellipse in Figure 6.12A, C. The gap-fill method used in our study not only temporally interpolates the low values that are marked as cloud or aerosol contaminated in the quality control layer, but also removes the noises caused by other factors. Some extremely high value data (dark green dots) in Figure 6.12A are also temporally smoothed, as shown in Figure 6.12B. The use of this gap-fill method also results in different regional GPP estimates. The GPP estimate without the gap-fill method shows a total GPP of NA in 2010 as 13.23 Pg C, while the gap-filled method leads to an annual GPP estimation of 13.53 Pg C. In addition, the GPP simulations with the gap-filled processing are more stable when conducting interannual comparisons or trend analyses.

Climate data input is another potential uncertainty source for VPM simulation. Previous studies show that VPM accurately simulates GPP at flux tower sites, when driven by in situ (site-specific) meteorological data and parameters (Jin et al., 2013; Kalfas et al., 2011; Wagle et al., 2014; Xiao et al., 2004b,a). As radiation is one of the direct inputs to model GPP, the accuracy of radiation directly influences GPP simulation. Recent studies which employ different models (MODIS PSN, EC-LUE) to investigate the performance of multiple meteorological datasets in estimating regional GPP report that the NCEP product overestimates radiation as compared with meteorological stations in U.S. and China (Cai et al., 2014; Zhao et al., 2006). Jin et al. (2015) assesses the feasibility of using large scale reanalysis meteorological data (NCEP-NARR) to drive VPM at cropland flux tower sites, and the resultant GPP_{VPM} agrees well with GPP_{EC} at those sites. Our validataion at the site level

shows that VPM accurately simulates GPP across different natural biome types in NA using the regional reanalysis meteorological data and biome specific parameters, suggesting that the recalibrated NCEP-NARR radiation product can be used to estimate regional GPP effectively in NA.

6.5 Conclusions

In this study, we use VPM, climate reanalysis data, and MODIS products (vegetation indices, land cover, and LST) to simulate GPP of North America. GPP_{VPM} agrees well with GPP_{EC} at individual flux tower sites and the GOME-2 SIF data across North America. The comparison between SIF and GPP_{VPM} showed very high spatial-temporal consistency during the growing season, mostly due to the

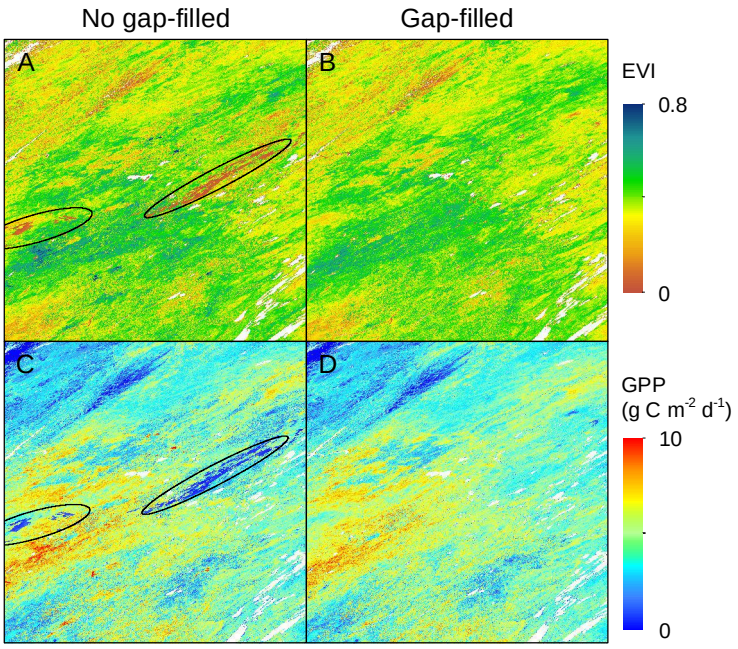


Figure 6.12: Comparison between no gap-filled and gap-filled enhanced vegetation index (EVI) and the corresponding modeled gross primary production (GPP_{VPM}). The low value in (A) and (C) are marked out using ellipses. The scene is from the tile h11v03 during the mid-growing season on August 13th, 2010.

close relationship between SIF and $APAR_{chl}$. The quality of GOME-2 SIF data may limit its application for evaluating the seasonal variation of GPP for very low productive biome types. The results from this study clearly demonstrate the potential of VPM for estimating GPP at the continental scale, and highlights the value of GOME-2 SIF data for evaluation of various LUE-based and process-based GPP models. The resultant high spatial and temporal resolution GPP_{VPM} dataset in North America will be provided to the public, which can be further used in a wide variety of applications, especially in those studies related to trend analysis, regional disturbance evaluation, model comparison, and the carbon cycle under global climate change.

6.A Appendix

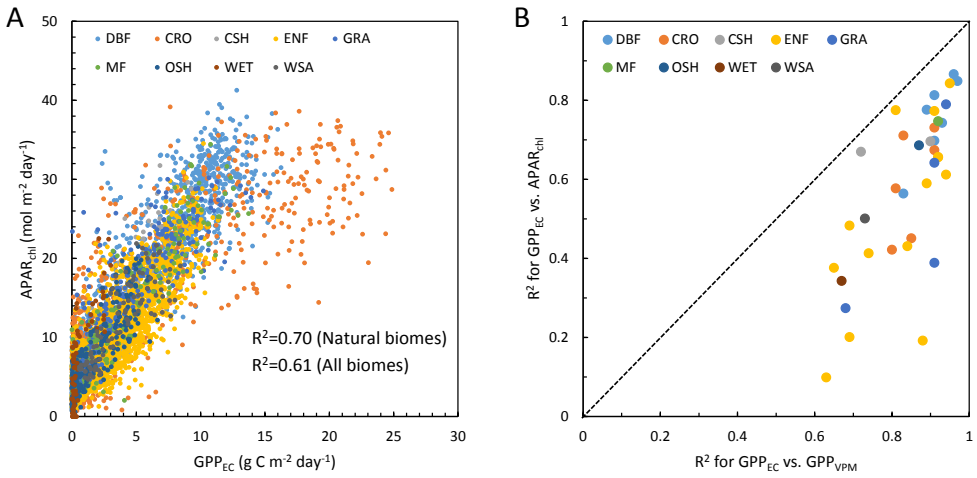


Figure 6.A.1: (A) A comparison between GPP_{EC} and $APAR_{chl}$ for all 39 sites using 8-day data. (B) comparison between the coefficient of determination (R2) between GPP_{EC} vs. GPP_{VPM}, and GPP_{EC} vs. $APAR_{chl}$ for individual sites.

Table 6.A.1: Biome specific lookup-table (LUT) used in the VPM model.

IGBP class	ENF[1]	EBF[2]	DNF	DBF[1]	MF[2]	CSH[2]	OSH[2]	WSA[2]	SAV[2]	GRA[2]	WET	CRO[3]	NVM
T_{min} (°C)	-1	2	-1	-1	-1	-1	1	-1	1	0	-1	-1	0
T_{opt} (°C)	20	28	20	20	19	25	31	24	30	27	20	30	27
T_{max} (°C)	40	48	40	40	48	48	48	48	48	48	40	48	48
ε_0 (g C m^{-2} day^{-1}/W m^{-2})	0.078	0.078	0.078	0.078	0.078	0.078	0.078	0.078	0.078	0.078	0.078	0.108	0.078

We use a similar temperature limitation from the Terrestrial Ecosystem Model and the T_{min}, T_{opt}, T_{max} used in this table are given by [1]Aber et al. (1996) [2]McGuire et al. (1992) and [3]Wagle et al. (2015) and Kalfas et al. (2011). For some biome types (DNF, WET, NVM) which we did not find reference for temperature parameters, we use parameters from similar ecosystems (e.g. ENF for DNF and WET, GRA for NVM). ε_0 for C3 plants are estimated from the Wagle et al. (2014), ε_0 for C4 crops is from Kalfas et al. (2011). Cropland is regarded as the half-half C3/C4 therefore uses an average value.

Chapter 7: Precipitation and carbon-water coupling jointly control the interannual variability of global land primary production

Abstract

Carbon uptake by terrestrial ecosystems is increasing along with the rising of atmospheric CO_2 concentration. Embedded in this trend, recent studies suggested that the interannual variability (IAV) of global carbon fluxes may be dominated by semi-arid ecosystems, but the underlying mechanisms of this high variability in these specific regions are not well known. Here we derive an ensemble of gross primary production (GPP) estimates using the average of three data-driven models and eleven process-based models. These models are weighted by their spatial representativeness of the satellite-based solar-induced chlorophyll fluorescence (SIF). We then use this weighted GPP ensemble to investigate the GPP variability for different aridity regimes. We show that semi-arid regions contribute to 57% of the detrended IAV of global GPP. Moreover, in regions with higher GPP variability, GPP fluctuations are mostly controlled by precipitation and strongly coupled with evapotranspiration (ET). This higher GPP IAV in semi-arid regions is co-limited by supply (precipitation)-induced ET variability and GPP-ET coupling strength. Our results demonstrate the importance of semi-arid regions to the global terrestrial carbon cycle and posit that there will be larger GPP and ET variations in the future with changes in precipitation patterns and dryland expansion.

7.1 Introduction

Carbon uptake through photosynthesis by terrestrial ecosystems is the largest flux in the global carbon cycle Beer et al. (2010). This flux, also known as gross primary production (GPP), drives not only ecosystem functioning, but also terrestrial carbon

sequestration, which currently offsets more than one third of anthropogenic CO_2 emissions (Le Quéré et al., 2015). Over the past 50 years, an enhanced seasonal exchange of CO_2 has been observed in the Northern Hemisphere (Graven et al., 2013), which was interpreted as increasing GPP in northern ecosystems induced by CO_2 fertilization, extended growing seasons, and nitrogen deposition (Baldocchi et al., 2016; Forkel et al., 2016; Graven et al., 2013). However, the GPP fluctuations superimposed on this increasing trend are less studied. With the increasing frequency of extreme climate events (Easterling et al., 2000a), the interannual variability (IAV) of GPP is also projected to increase (Zscheischler et al., 2014b), and will cause significant impacts on the global terrestrial carbon cycle (Reichstein et al., 2013). The IAV of carbon uptake was shown to have distinctive spatial patterns, with hotspots on semi-arid or grassland ecosystems (Ahlstrom et al., 2015; Knapp & Smith, 2001; Poulter et al., 2014). Although these spatial patterns are often explained by the interannual variation of water availability in semi-arid ecosystems, specifically, the precipitation variability, biotic meristem growth potential and their interactions (Knapp & Smith, 2001), the underlying mechanism is not well established. A key limitation to understanding this phenomenon and its potential feedbacks is that no accurate or direct GPP measurements are available at the global scale: diagnostic models and prognostic models show large differences in the spatio-temporal mean and variability patterns of GPP (Anav et al., 2015). Previous studies often use median or average values as model ensembles to reduce the uncertainties (Anav et al., 2013). However, un-weighted ensembles are not suitable to characterize spatial patterns for each individual year for two reasons: median values only keep limited information and unweighted averages may lead to biases from outliers.

In recent years, significant progress was made to develop satellite-retrieved solar-induced chlorophyll fluorescence (SIF) datasets (Frankenberg et al., 2011; Joiner

et al., 2016) that offer a new proxy for direct quantification of plant photosynthesis at a global scale. SIF is a very small amount of energy emitted by vegetation during photosynthesis, and it is sensitive to the electron transport rate and the absorbed radiation by chrolophyll (van der Tol et al., 2014). Empirical studies have shown that SIF is highly correlated with GPP in space and time (Frankenberg et al., 2011; Guanter et al., 2012, 2014; Joiner et al., 2014; Zhang et al., 2016e). Recent modelling studies also exhibited high correlation between SIF and GPP at daily or 8-day scales (Verrelst et al., 2016; Zhang et al., 2016e). Therefore, SIF can be used as a benchmark to evaluate GPP model performance (Luo et al., 2012).

In this study, our first objective is to improve the spatial patterns of global estimates of GPP. We developed a method to calculate a weighted ensemble of GPP from multiple models that best approximate spatial and temporal variations in SIF derived from GOME-2 instrument (Joiner et al., 2013, 2016). To improve global estimates of GPP as compared with a straight average of an ensemble of models, we provided a weighted ensemble estimate using three data-driven models (VPM (Zhang et al., 2016e), MTE (Jung et al., 2011), and MOD17 (Running et al., 2004)) and eleven process-oriented models from the TRENDY-v4 project (Sitch et al., 2008) (CLM4.5, ISAM, JSBACH, JULES, LPJ, LPJ-GUESS, LPX, OCN, ORCHIDEE, VEGAS, and VISIT, see Materials and Methods). The weight of each model was determined by how well its GPP matches the spatial patterns of its proxy, SIF, within each biome type, i.e., higher weights were given to more realistic models and vice versa (see Methods). Our second objective is to better understand what factors control the spatial patterns of GPP IAV using the resultant SIF-constrained grid-based GPP dataset. The IAV of GPP and Evapotranspiration (ET) were analyzed together since they are closely coupled. We also adopted the Budyko framework (Budyko, 1974) to explain the IAV pattern along the aridity index (hotspot in semi-arid regions).

7.2 Materials and Methods

7.2.1 GPP from 14 models

GPP dataset from 14 models for the period 2000 to 2011 can be grouped into two categories, i.e., three data driven models (VPM, MTE, and MOD17) and 11 process based models from TRENDY-v4 project. The VPM model and MOD17 are both light use efficiency models while using different driving data and parameters (Running et al., 2004; Xiao et al., 2004b). MTE uses machine learning algorithms which combine the observation from flux tower, satellite imagery, and gridded climate datasets (Jung et al., 2011, 2009). The TRENDY-v4 datasets are the latest release for the TRENDY project which compared the simulation results from dynamic global vegetation models (DGVMs) (Sitch et al., 2015). All these models are driven by the same climate forcing data and monthly GPP estimates are used. (see Appendix, Text 7.A.1).

7.2.2 Solar-induced chlorophyll fluorescence from GOME-2

The solar-induced chlorophyll fluorescence (SIF) measurements are retrieved from GOME-2 onboard the MetOp-A satellite. The GOME-2 instrument captures the Earth radiation from ~240 to 790 nm at a nominal nadir footprint of 40×80 km^2 (and 40×40 km^2 since 15 July 2013) with a spectral resolution of ~0.5 nm. Compared with SIF measurements from other satellites (GOSAT, OCO-2, etc.), GOME-2 data has the longest observation history (2007-2015). We used the version 26 SIF from Joiner et al. (2013) available at http://avdc.gsfc.nasa.gov. This product is retrieved at wavelengths surrounding 740 nm, where the far-red peak of SIF emission is located, based on a principal component analysis approach to account for atmospheric absorption. The initial results are quality controlled and aggregated to

produce a level 3 monthly mean product at 0.5°×0.5° spatial resolution (Joiner et al., 2013).

7.2.3 The ensemble of GPP using SIF

Sun-induced chlorophyll fluorescence (SIF) is a small amount of energy released during the photosynthesis process (Porcar-Castell et al., 2014). When sunlight is absorbed by vegetation, a large proportion of energy goes to photosynthesis (known as photochemical quenching, PQ), and most of the remaining energy is dissipated as heat (known as non-photochemical quenching, NPQ); a small amount of energy (~1–2%) is reemitted as chlorophyll fluorescence. In cases of environmental stress, both PQ and SIF decrease while NPQ increases. Therefore, SIF can serve as a good proxy for plant photosynthesis.

The SIF product from the Global Ozone Monitoring Experiment 2 (GOME-2) that we used in this study has a satellite overpass time near 9:30 am local time. Therefore, for most areas, GPP should be correlated with SIF for each biome type, and the ratio between GPP and SIF should converge on a monthly scale. Hence, we can use SIF as a proxy for GPP within each biome type both spatially and temporally. To get the ensemble of all GPP estimates, the weight of each GPP product should reflect how well the GPP product matches its respective SIF spatial or temporal pattern within each biome type. Considering that SIF has relatively low values (0–4.0 mW m^{-2} sr^{-1} nm^{-1}) compared to its uncertainties (0.1–0.4 mW m^{-2} sr^{-1} nm^{-1}) at monthly scales, to reduce uncertainty SIF can be averaged temporally (from monthly to yearly) or spatially (within-biome for each month) to reduce those uncertainties and compare with GPP. The land cover data used to identify different biome types came from MCD12C1 (Friedl et al., 2010). This dataset has a spatial resolution of 0.05 degree with a proportion of each biome type for each grid cell.

We aggregated it to 0.5 degree spatial resolution and recalculated the proportion of area for each biome type. For the GPP ensemble using SIF as a proxy for spatial (temporal) variations, both SIF and GPP were temporally (spatially) averaged to get an annual map (a value for each biome type for each month). For each model i, the correlation between SIF and GPP for all pixels within each biome type j (for all 12 months for biome type j) is calculated as $r^s_{i,j}$ ($r^t_{i,j}$).

The overall score of a model i ($score_i$) is the weighted average of $r_{i,j}$ by the area of each biome:

$$score_i = \sum_{j=1}^{n} (a_j \times r_{i,j}) \tag{7.1}$$

where a_j represents the biome type j as a fraction of the total area ($\sum_{j=1} na_j = 1$)). For each group (data-driven or process based or all-ensemble), the weight of ith model is calculated as:

$$W_i = \frac{score_i^\gamma}{\sum_i^n score_i^\gamma} \tag{7.2}$$

where γ is the order coefficient; in this study, we used $1^s t$ order, $2^n d$ order and $4^t h$ order to calculate W_i. The ensemble GPP for each year is calculated as:

$$GPP_ens = \sum_{i}^{n} (W_i \times GPP_i) \tag{7.3}$$

We chose the years 2007-2011 as the training period, due to the overlay of all process-based models, data-driven models, and availability of SIF from GOME-2. We applied the model contribution to the period 2000 to 2011 to get a GPP product at an annual scale for both spatial and temporal ensembles. Because we focused on the IAV of GPP, which is a spatial pattern, we only used the GPP ensemble with SIF

as a spatial representative.

7.2.4 The Budyko framework

The Budyko framework describes how energy availability (represented by potential evapotranspiration, PET or E_0) and water availability (represented by precipitation, P) determine evapotranspiration (ET). It hypothesizes that the ratio of ET over P is a function of the ratio of PET over P, as follows:

$$\frac{ET}{P} = f\left(\frac{PET}{P}\right) \tag{7.4}$$

One analytical solution (Yang et al., 2008) to this equation is:

$$ET = \frac{P \times PET}{(p^n + E_0^n)^{\frac{1}{n}}} \tag{7.5}$$

where the parameter n is used to define different Budyko curves for landscape and vegetation characteristics. This analytical solution is similar to FuâĂŹs solution (Zhang et al., 2001) and enables us to easily calculate the partial derivative of ET with respect to P. n ranges from 0.5 to 2, which covers most global landscape characteristics, and is used as a constraint to explain the ET and P IAV relationship. The IAV of ET (σ_E) can be derived from this Budyko framework (Koster & Suarez, 1999):

$$\frac{\sigma_{ET}}{\sigma_P} \approx \frac{\partial ET}{\partial} = f\left(\frac{PET}{P}\right) - \frac{PET}{P} f'\left(\frac{PET}{P}\right) = (AI^n + 1)^{-\frac{n+1}{n}} \tag{7.6}$$

We use different n to get the possible distributions of the relationship between $\frac{\partial ET}{\partial P}$ and $\frac{P}{PET}$ (aridity index).

7.3 Results and Discussion

The annual mean and IAV of the weighted ensemble of GPP (GPP_{ens}) show very good spatial consistency with the average of means and IAVs from individual models (GPP_i) and GOME-2 SIF retrievals (Joiner et al., 2013) (Figure 7.1). The weighted global mean GPP is 123.8±1.6 Pg C year^{-1} for data-driven models, 133.6±1.9 Pg C year^{-1} for process-based models, and 130.4±1.7 Pg C year^{-1} for all models (with ± being used for 1-sigma standard deviation). The weighted ensemble mean from data-driven models is very close to the previous estimates from multiple diagnostic models (Beer et al., 2010) (~123 Pg C year^{-1}), the seasonal cycle of oxygen isotope measurements of atmospheric CO_2 (Ciais et al., 1997) (~120 Pg C year^{-1}), and a recent synthesis study (Anav et al., 2015). The ensemble mean for all 14 models is slightly higher due to the relatively higher GPP estimates from the process-based models, possibly because these process models do not all represent nutrient limitation. The spatial patterns of mean annual GPP and IAV of GPP are similar for different weight orders and model groups (Appendix, Figures 7.A.7–7.A.9).

With this weighted ensemble of GPP from 14 models, we explore the linkage between the spatial patterns of GPP IAV and aridity index (Table S1), i.e., the ratio of long-term annual precipitation to potential evapotranspirative demand. Unlike previous studies defining semi-arid regions by vegetation types (Ahlstrom et al., 2015), we use the climatological definition from the Food and Agriculture Organization (FAO)(Middleton and Thomas 1997), where semi-arid regions are areas with the aridity index ranges from 0.2–0.5. Comparison with the aridity index shows that most of the areas with high GPP_{ens} IAV are located in semi-arid regions (Figure 7.2b). The average of GPP variability from individual models (GPP_i) and SIF versus aridity index confirms this relationship, with the average GPP variability reaching its

peak at aridity index values of around 0.3, corresponding to semi-arid regions. SIF IAV from GOME-2 also shows high variability in semi-arid regions, but another peak in humid regions, the latter being a possible artifact of higher SIF errors under the influence of the South Atlantic Anomaly (SAA) in South America (Köhler et al., 2015) (Appendix, Figure 7.A.10). Although humid regions defined by aridity index occupy a larger proportion of the global land surface (35%) and contribute a larger fraction

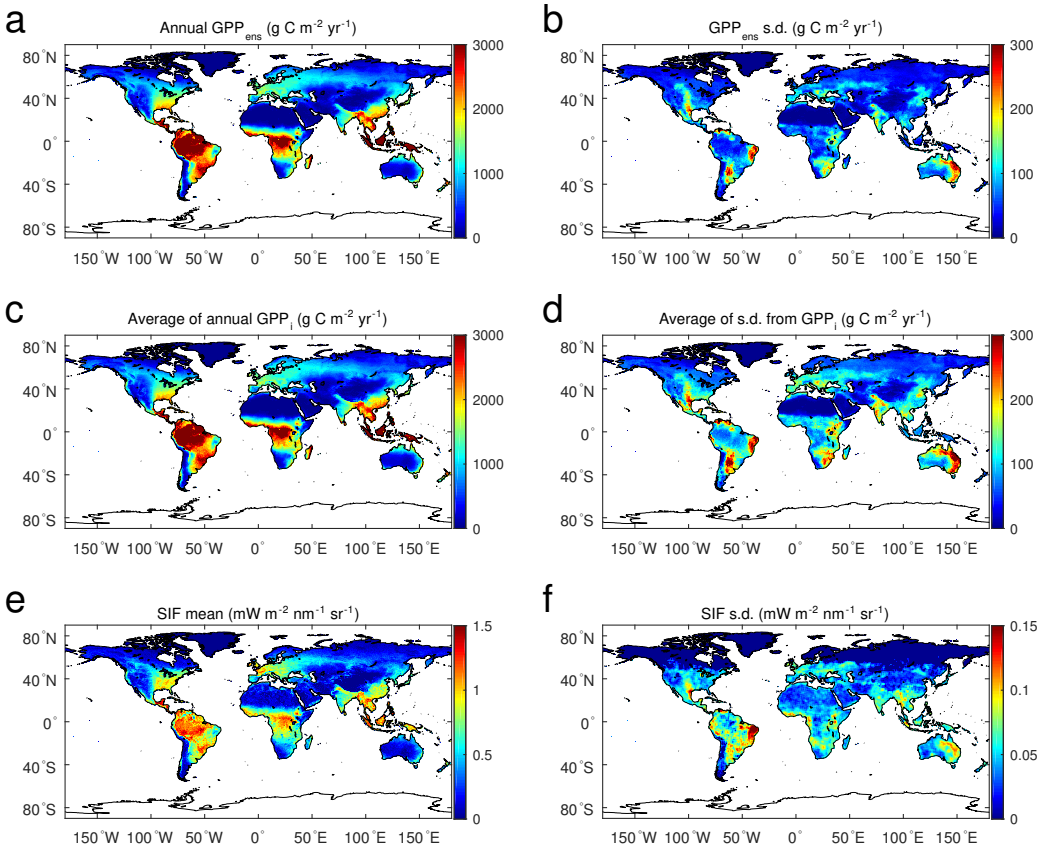


Figure 7.1: Mean and variability of GPP and SIF (2000-2011). (a, b) Mean and standard deviation (s.d., as a representative of variability) of annual GPP from ensemble of all models with the 2nd order weight (GPP_{ens}) for 2000-2011. (c, d) unweighted average of annual GPP and GPP s.d. calculated from each individual model (GPP_i) for 2000-2011. (e, f) Annual mean SIF and SIF s.d. from GOME-2 for 2007 to 2015. The SIF variances were smoothed with a 3×3 pixel smoothing window after removing the error (see Appendix, Text 7.A.7).

of global GPP (~57%), the total variability of GPP of humid regions is smaller than that in semi-arid regions (Figure 7.2c). In addition, the southern hemisphere contributes nearly 40% of the total GPP variability with only 25.8% of the global land area.

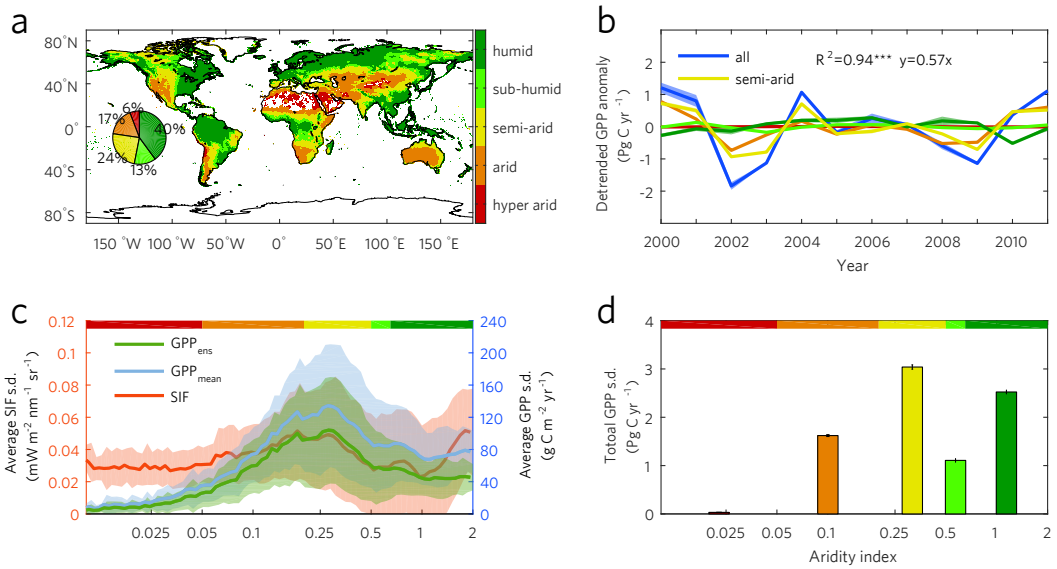


Figure 7.2: (a) The aridity map calculated as a ratio between precipitation from GPCC (Schneider et al., 2011) and potential evapotranspiration from MOD16 product (Mu et al., 2011)). Long-term averages from 2000 to 2013 for both products were used; the classification of aridity regions is based on UNEP (Appendix, Table 7.A.1). The small pie chart indicates the proportion of each class in the global land area. (b) IAV of GPP ensemble (GPP_{ens}), average of GPP IAV from individual models (GPP_i) and SIF IAV at different aridity indices, with the shaded area indicating one s.d. of variation. (c) The contribution of total GPP variability from different aridity classes. Error bars stand for one s.d. using different orders of ensemble. (d) Detrended GPP anomaly for global and 5 individual aridity regions, from 2000 to 2011. GPP ensemble comes from all models, and the shaded area indicates the range of s.d. from different orders of weight (1st, 2nd, 4th, see Methods).

When decomposing the variability of annual GPP during 2000-2011 into a long-term trend and detrended anomalies, semi-arid regions contribute 57% of the total detrended GPP variance (Figure 7.2d). This is in line with the results of Ahlstrom

et al. (2015) who used the model tree ensemble (MTE) data-driven GPP and TRENDY v3 process-based models. Similar results are also found if we use the ensembles from either only data-driven models or only process-based models (Appendix, Figure 7.A.11). Our results also show an increasing trend in the GPP ensembles with large geographic differences. The humid regions contribute the largest proportion to the increase (42.4%), followed by semi-arid regions (29.0%). The GPP in humid regions is less sensitive to the climate anomalies, but may benefit from nitrogen deposition in mid-latitudes that makes CO_2 fertilization more effective (Yu et al., 2014) and from longer growing seasons in high latitudes (Piao et al., 2007), therefore yielding a higher contribution to the trend than to IAV.

We further attribute the IAV of GPP to different climatic factors by calculating the partial correlation coefficients between GPP and precipitation, temperature, and shortwave downward radiation. Similar to the results from a previous analysis using the MTE approach (Beer et al., 2010), we find that for most land surfaces, annual GPP is controlled by precipitation, except for some tropical and boreal regions. Contributions from temperature and radiation are less significant (Figure 7.3a–c). In addition, for most drylands (aridity index < 0.65), GPP and ET are closely coupled, as represented by a high Pearson correlation coefficient (significant at the 0.05 level for 65.4% of areas in Figure 7.3d). This tight coupling between GPP and ET in dry regions is robust to the choice of a particular ET dataset, as it is present for 12 different ET datasets (Appendix, Text 7.A.2). When plotting the correlation coefficients between ET and GPP against the GPP variability, the strength of the GPP-ET relationship increases with GPP variability (Figure 7.3e), indicating that the changes in GPP in these high variability regions is closely linked to changes in ET. Precipitation is still the dominant climate factor for the large GPP variability, as represented by its highest partial correlation coefficient among the three major climate factors

(Figure 7.3e). Partial correlation between GPP and radiation is mostly negative due to the negative correlation with cloud cover and precipitation.

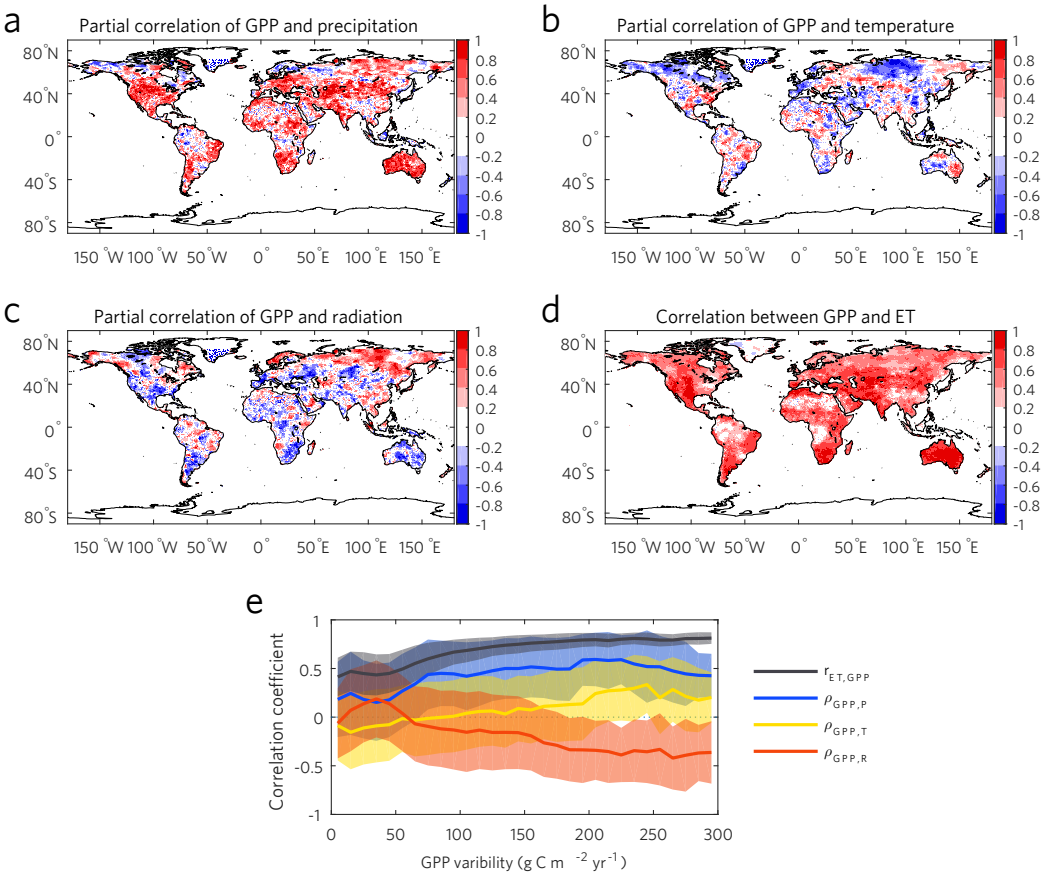


Figure 7.3: Relationship among GPP and GPP IAV, climate variables, and ET. Partial correlation (ρ) between annual GPP and (a) annual total GPCC precipitation, (b) annual mean CRU TS temperature and (c) annual sum CRUNCEP downward shortwave radiation with other two climate variable fixed. (d) averaged Pearson correlation (r) between GPP and all ET products (see Appendix, Text A.7.2). (e) The relationship between 4 types of correlation versus GPP variability, with a bin size of 10 g C m^{-2} year^{-1}. Shaded areas represent the s.d. range within each bin. GPP is from the 2-order ensemble of all models and GPP ET correlation is from (d).

As GPP and ET are highly coupled in high GPP variability (semi-arid) regions, and both fluxes are closely linked to the precipitation anomalies, we use this empirical relationship to diagnostically investigate the factors related to high GPP IAV in

semi-arid regions. One of the key factors that contributes to the GPP variability is the coupling strength or regression slope between GPP and ET (β). The contribution of this factor to the IAV of GPP is given by:

$$IAV_{GPP} = \beta \times IAV_{ET} \tag{7.7}$$

This equation only applies for regions where ET and GPP are strongly coupled on a temporal scale, i.e., high GPP variability areas as shown in the previous analysis (Figure 7.3e). We calculate this β factor by using the linear regression slopes for each pixel between the weighted GPP anomalies and ET anomalies from 12 different ET products (Appendix, Figure 7.A.12), and related it with the aridity index (Figure 7.4a). These regression slopes generally increase with aridity index and can also be regarded as an approximation of the ecosystem water use efficiency (WUE) as long as the ecosystem is water limited (Huxman et al., 2004). The increasing trend of β with aridity index (i.e., from hyper arid to humid) is consistent with the fact that WUE increasing with precipitation across spatial gradients as suggested by a recent study using an inter-comparison of multiple models (Sun et al., 2016). β starts to decrease when the aridity index approaches 1, where GPP and ET become decoupled from each other (Appendix, Figure 7.A.13), i.e., when ecosystems are no longer water limited, decreases of GPP will not necessarily be linked to decreases of ET. When aridity index > 1, some regions show relatively low β value; however, most of these regions are located in tropical forests where the ET-GPP correlation is low (Figure 7.3d). Therefore, β is highest in arid to sub-humid regions and Eq. 7.7 is valid in these regions due to the close relationship between ET and GPP.

Given that the carbon and water fluxes are highly coupled in high GPP variability areas, we try to identify the climate regulation of ET variability and also GPP

variability. Evapotranspiration is often thought to be physically constrained by the energy demand (potential evapotranspiration, PET) and water supply (precipitation, P) as described by the Budyko framework (Budyko, 1974; Zhou et al., 2015a) (see Methods). Based on this framework, the IAV of ET can be diagnosed from IAV

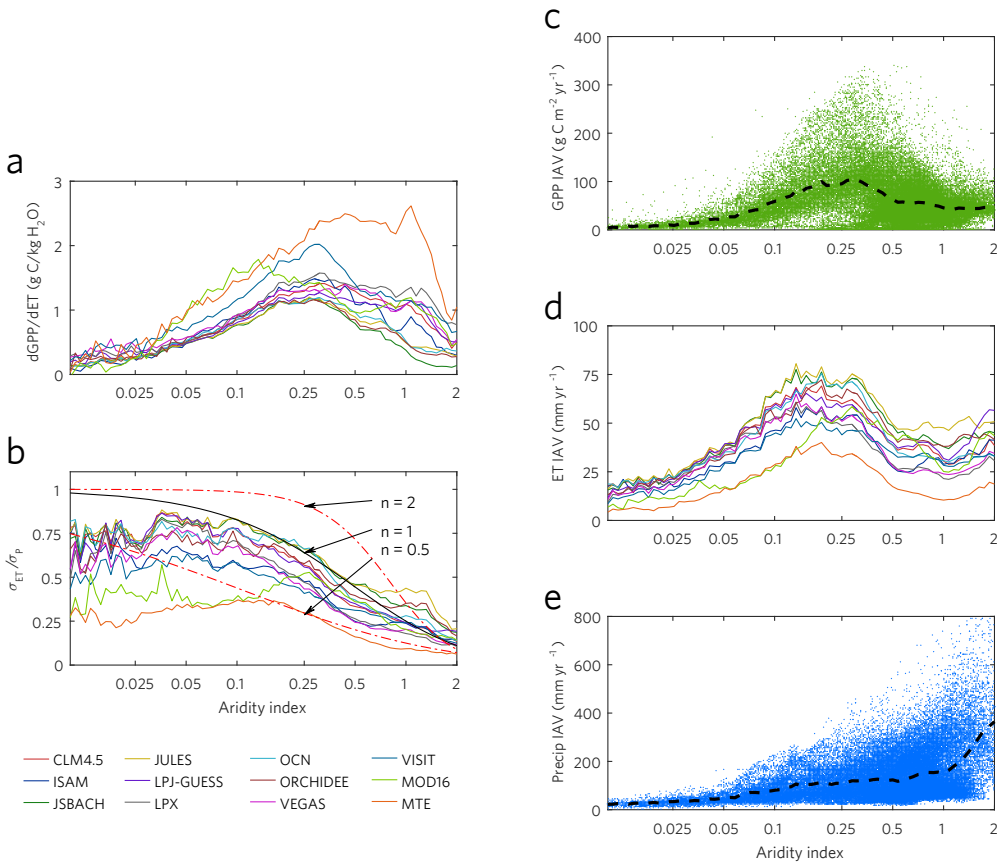


Figure 7.4: Decomposition of GPP IAV into ET IAV and precipitation IAV, and their relationship with aridity index. (a) Ratios of interannual anomalies of GPP to anomalies of ET (β) as a function of aridity index. Each line represents the mean value at each AI value. (b) Change in ET induced by change in precipitation, two dashed red line and the solid black line represent the prediction from Budyko framework with different n values. (c) GPP IAV from 2nd order ensemble (γ=2) of all models versus AI, the black dashed line represents mean value at each AI value. (d) ET IAV from all 12 ET products versus AI. (e) Precipitation IAV and its relationship with aridity index, the black dashed line represents the mean value at each AI value.

of precipitation, given that the contribution from IAV of PET is negligible(Koster & Suarez, 1999), which is also confirmed by our analysis (Appendix, Figure 7.A.14). Neglecting the contribution of PET is possible because precipitation variability in supply-(water) dominated regions is much larger than potential evapotranspiration (PET) variability in demand-(energy) dominated regions, and this difference amplifies when we calculate the contributions from precipitation or PET exclusively using the derivatives of a Budyko function (Yang et al., 2008) (Appendix, Figure 7.A.15).

As ET variability is mostly dominated by P variability in high GPP IAV regions, we can investigate the precipitation contribution to the variability of ET. We get the spatial pattern of this sensitivity factor ($\frac{\sigma_{ET}}{\sigma_P}$) by calculating the ratio of ET variation to the precipitation variation (Appendix, Figure 7.A.16). This sensitivity factor should, according to the Budyko framework (see Methods), decrease from 1 in hyper arid regions where all changes in precipitation leads to an equal magnitude change of ET, to 0 in extreme humid regions, where changes in precipitation do not affect ET (Figure 7.4b). The relationship is also regulated by landscape and vegetation characteristics and by vegetation-precipitation feedbacks, as represented by the value of the exponent n in the Budyko equation (see Methods). Our data also show that $\frac{\sigma_{ET}}{\sigma_P}$ decreases with increasing aridity index, and absolute $\frac{\sigma_{ET}}{\sigma_P}$ values are relatively lower for the two data-driven ET products than for the process-based models. This is caused by the relative lower interannual variation of ET in data-driven products. Since the precipitation variability (σ_P) increases with mean annual precipitation as well as with the aridity index, while the $\frac{\sigma_{ET}}{\sigma_P}$ decreases with aridity index, ET variability (σ_{ET}) reaches its highest values in arid to semi-arid regions (Figure 7.4d). In addition, regression slopes between GPP and ET (β) are also highest in arid to sub-humid regions, both of which explain the highest GPP variability in semi-arid regions.

Many studies have shown the importance of precipitation to the global carbon cycle (Beer et al., 2010; Fu et al., 2014). Previous studies hypothesize that the highest IAV of aboveground net primary production occurs in grasslands as a balance between the ecosystem potential productivity and the ecosystem stability (Knapp & Smith, 2001). Our study further documents a higher ET-GPP coupling (β) combined with a high precipitation-induced changes in water fluxes which is also predicted by Budyko framework in semi-arid regions. Using ET as an intermediate variable to connect the precipitation and stomata behavior which links both the carbon and water fluxes, we revealed how precipitation affects the IAV of GPP and ET. Because the highest ET variation in semi-arid regions is not only physically constrained by the precipitation and evapotranspiration ratio (fraction of precipitation that goes to evaporation, usually in the range from 0 to 1), but also affected by the vegetation coverage (Li et al., 2013). It is likely that the recent greening trend of vegetation, especially in northern hemisphere (Mao et al., 2016; Zhu et al., 2016), will also affect the peak of ET through the change of n in the Budyko equations. In addition, the elevated CO_2 concentration in the atmosphere will affect the stomata behavior and water use efficiency (Keenan et al., 2013), which may further affect the peak of GPP variability in the space of aridity index. These issues still need further investigation by future studies.

GPP and ET variability are projected to increase in the future with changes in precipitation regimes and increases in evapotranspirative demand: the aridity map has changed over the past 60 years (Spinoni et al., 2015), and drylands are projected to further expand in the future (Huang et al., 2015). In addition, as the precipitation variability increases with global climate change, larger GPP and ET variability is expected in the future. On the other hand, with increased CO_2 concentrations in the atmosphere, water will be more efficiently used and this tends to dampen the GPP

ET relationship (Keenan et al., 2013). Grazing and frequent fire occurrence in semi-arid regions may also alter the value of GPP ET ratios, which makes this issue more complicated. Whether GPP IAV will continue to increase in the future still needs to be further assessed by state-of-the-art Earth system models and manipulated experiments.

In this study, we presented a weighted ensemble method to provide a better estimate of the GPP IAV from multiple models. By giving better performing models a higher weight, we expect to see an improved prediction of the GPP spatial patterns. Due to the spatial inconsistency between model gridcell and *in situ* measurements footprints (Zhang et al., 2014b), we cannot directly verify the effectiveness of this method. However, this method is supposed to be more stable and robust to model selections, i.e., the variability of the GPP_{ens} IAV generated from different models will be smaller than that using a traditional unweighted averaging method. Figure 7.5 shows the difference of variability between the unweighted average and the weighted ensemble method using 13 out of 14 models as inputs (see Appendix, Text 7.A.9). For annual GPP, the weighted ensemble method shows a relatively larger difference in tropical rainforest, south eastern U.S. and China. This may be caused by the relative large GPP discrepancy between data-driven models and process-based models in these regions, and the relatively higher weight factors given to the data-driven models. In terms of GPP s.d., we can see that the weighted ensemble method has smaller variation for almost all regions. This indicates the weighted ensemble method will give a more stable prediction of GPP s.d., which is also the focus of this study.

Global carbon cycle studies often rely on models to predict the spatial pattern of carbon fluxes (Ciais et al., 2005; Forkel et al., 2016; Zhao & Running, 2010). However, large uncertainties still exist in different model groups (process-based or data-

driven), or even within the same group. The uncertainties becomes more evident when analyzing the interannual variability patterns (Anav et al., 2015). Our study presents a new framework to incorporate model simulations with global satellite observations to reduce these uncertainties of model outputs. Although GPP variability patterns produced by either process-based ensemble and data-driven ensembles are similar, we note that not all models captured these IAV patterns accurately, even models with similar distributions of annual GPP. With this precipitation-ET-GPP relationship being explained and the new ensemble framework developed, it provides a means to benchmark ecosystem models for water and carbon fluxes and their coupling.

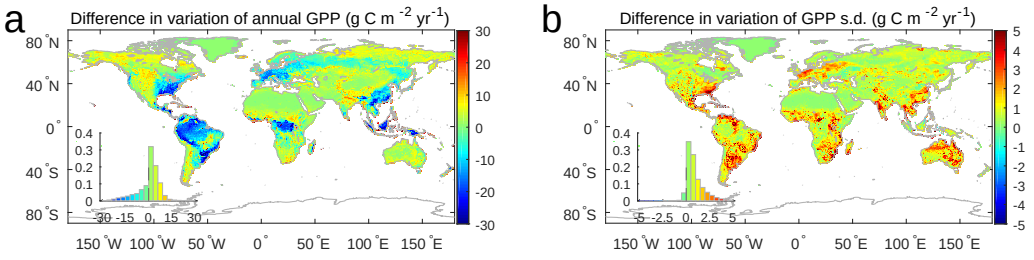


Figure 7.5: Difference in variation between the unweighted average and the weighted ensemble methods in terms of (a) annual GPP and (b) GPP s.d. Ensemble method with the order of two was used (γ=2). The insets in the lower left corner show the histogram of the frequency distribution. All the units are in g C m^{-2} year^{-1}.

7.A Appendix

7.A.1 GPP product

VPM

The Vegetation Photosynthesis Model (VPM) is a light use efficiency (LUE) model which has been tested over a variety of land cover types at CO_2 eddy flux tower sites (Jin et al., 2015, 2013; Kross et al., 2016; Wagle et al., 2014; Xiao et al., 2004b,a). The GPP product we used in this paper is driven by the MODIS 8-day 500 m surface reflectance product (MOD09A1 C6), the MODIS 8-day 1 km Land surface temperature product (MOD11A2 C5), the MODIS land cover product (MCD12A2 C5), and the shortwave radiation and air temperature from the NCEP-DOE Reanalysis 2 dataset. The VPM (version 2.0) estimates GPP by using the product of absorbed photosynthetic active radiation by the chlorophyll ($APAR_{chl}$, calculated by $fPAR_{chl} \times PAR$) and the light use efficiency (LUE, ε_g):

$$GPP = \varepsilon_g \times APAR_{chl} \tag{7.A.1}$$

$$fPAR_{chl} = a \times (EVI - 0.1) \tag{7.A.2}$$

where the factor a = 1.25, and 0.1 in Eq. A2 is used to adjust EVI baseline (Sims et al., 2008, 2006). The EVI is calculated from the MOD09A1 product and passed a rigorous quality check and gap-filling procedure (Zhang et al., 2016f). The LUE (ε_g) is reduced from a maximum light use efficiency (ε_0) by the temperature scalar (T_{scalar}) and a water scalar (W_{scalar}):

$$\varepsilon_g = \varepsilon_0 \times T_{scalar} \times W_{scalar} \tag{7.A.3}$$

Detailed information about the model parameter estimation were documented in previous publications (Jin et al., 2015; Xiao et al., 2004b; Zhang et al., 2016e).

The GPP product at 8-day temporal resolution and 500 m spatial resolution was reprojected and aggregated into 0.5 degree (latitude and longitude). The annual GPP is calculated as the sum of each 8-day GPP over a Julian year, and the interannual variation of GPP is calculated below:

$$IAV = \sqrt{\frac{\sum_{n=1}^{n}\left(GPP_i - \overline{GPP}\right)^2}{n}} \tag{7.A.4}$$

where GPP_i and $\overline{GPP}$ represent the annual GPP for year i and average annual GPP for year 2000 to 2011, respectively. n is the total number of years.

MPI-BGC (MTE)

The MPI-BGC estimates GPP by upscaling global in situ CO_2 eddy flux observations with climate data and remote sensing fraction of absorbed photosynthetic active radiation (fAPAR) using a Model Tree Ensemble approach (Jung et al., 2009, 2011). This dataset has a spatial resolution of 0.5°× 0.5°. This monthly dataset was first aggregated into annual sum and then the IAV over the period of 2000 to 2011 was calculated to match with other GPP products.

MOD17

The MODIS GPP product (MOD17) employs a light use efficiency (LUE) approach to calculate GPP. The PSN model used in the MOD17 GPP product uses MODIS fPAR product as the fraction of PAR absorbed by vegetation for photosynthesis. MOD17 also uses vapor pressure deficit (VPD) as the water limitation of LUE and uses variable maximum LUE for individual biome types, which are determined by MODIS

land cover map (MCD12). The MOD17 product (MOD17A2 C55) during 2000-2011 was downloaded from Numerical Terradynamic Simulation Group (http://www.ntsg.umt.edu/project/mod17#data-product) at the University of Montana. MOD17 GPP at 1-km spatial resolution and 8-day temporal resolution and was aggregated into 0.5 degree (latitude/longitude) to calculate annual GPP.

TRENDY-V4

The TRENDY project compared simulation results from dynamic global vegetation models (DGVMs) under the same climate forcing data, with an objective to investigate the trend in net biome production (NBP) over the period 1980 to 2010 (Sitch et al., 2015). The GPP simulation from 2000 to 2011 from the latest version TRENDY-V4 were used in our study. The model simulation is based on two experiments: S2, CO_2 and climate, S3, CO_2, climate and land use. In our study, the S2 simulation with variable CO_2 and climate forcing are used because not all models provide S3 simulations. Eleven models (CLM4.5 (Oleson et al., 2013), ISAM (Kato et al., 2013), JSBACH (Raddatz et al., 2007), JULES (Clark et al., 2011), LPJ (Sitch et al., 2003), LPJ-GUESS (Smith et al., 2001), LPX (Prentice et al., 2011), OCN (Zaehle & Friend, 2010), ORCHIDEE (Krinner et al., 2005), VEGAS (Zeng et al., 2005), and VISIT (Ito, 2008)) from the TRNEDY project were used to calculate the inter-annual variability (IAV) of GPP for the period 2000 to 2011 (Figure 7.A.1–7.A.3). The spatial resolution of CLIM4.5 is 2.5°×1.875°, JSBACH is ~1.875°×1.875°, JULES is 1.875°×1.25°, OCN and LPX are 1°×1°. These annual GPP means and IAVs are calculated at the original resolution and spatially interpolated to 0.5°×0.5° using cubic interpolation method.

7.A.2 Evapotranspiration and potential evapotranspiration dataset

Evapotranspiration datasets from the model tree ensemble (MTE) (Jung et al. (2011)), MODIS ET (Mu et al. (2011)) (MOD16A3 C5), and 10 TREDNY models are used in our study (ET from LPJ is not used due to a data problem—abnormally low ET in tropical reigons). The MTE method integrates the eddy flux tower measured ET with remote sensing satellite images and meteorological data using a machine-learning algorithm (Jung et al., 2009). The MOD16A3 product calculates ET based on the Penman-Monteith algorithm (Mu et al., 2007) and was recently improved (Mu et al., 2011). We downloaded the potential evapotranspiration (PET) and evapotranspiration (ET) from Numerical Terradynamic Simulation Group website at the University of Montana (http://www.ntsg.umt.edu/project/mod16). The PET and ET datasets were annual sums at 1 km×1 km spatial resolution and we aggregated to 0.5°×0.5°. ET from TRENDY-V4 were also interpolated into 0.5°×0.5° spatial resolution. All ET datasets from 2000 to 2011 were used.

7.A.3 Climate dataset

The GPCC V7 global precipitation at 0.5°×0.5° is used in our analysis (Schneider et al., 2011). This dataset has a monthly precipitation value from 1901 to 2013. The downward shortwave radiation was obtained from CRUNCEP V4 (http://dods.extra.cea.fr/data/p529viov/cruncep/) with a monthly sum and a spatial resolution of 0.5°×0.5°. The monthly mean temperature was from CRU TS 3.23 (Harris et al., 2014) (https://crudata.uea.ac.uk/cru/data/hrg/cru_ts_3.23/) and also has a 0.5°×0.5° spatial resolution. All the monthly climate datasets are aggregated to annual sums. The aridity index is calculated using GPCC precipitation over PET from MOD16 for the period 2000 to 2011. The classification scheme of the aridity regions based on

aridity index is from UNEP (Middleton & Thomas, 1997) and can be found in Table 7.A.1. Because CRUNCEP V4 does not provide radiation after 2010, the climate correlation is calculated using data from 2000 to 2010.

7.A.4 Aggregation of MODIS land cover map

In order to get the annual land cover map at 0.5°×0.5° spatial resolution, we aggregate the MCD12C1 C5 product spatially. The aggregation is based on the average of area percentage of each biome type, therefore the output also includes percentage of each biome type for each grid cell. To make sure we can compare the SIF and GPP within each land cover type, we set a threshold to extract the grid cells with 'pure' land cover types. We set the threshold from 50% to 100%. With the increase of this threshold, the number of mixed pixels also increased and the available pixels decreased (Figure 7.A.4). In this study, we used the 80% threshold, and only two biome types have less than 100 gridcells.

7.A.5 Rationale of GPP ensemble using SIF as a reference

Recent studies have successfully retrieved SIF from satellites, and these SIF retrievals showed very good correlation with GPP from flux tower upscaled models and light use efficiency models (Frankenberg et al., 2011). This close relationship between GPP and SIF is found to be higher within each biome type at monthly scale using data from both global simulation and in situ observations (Damm et al., 2015a; Guanter et al., 2012). The Soil Canopy Observation of Photochemistry and Energy fluxes (SCOPE) model is a process-based model which can also simulate energy exchange within photosynthesis process, including SIF (van der Tol et al., 2009). Using this SCOPE model, recent studies investigated the relationship between GPP and SIF (Lee et al., 2015; van der Tol et al., 2014). SIF_{yield} (defined as SIF/APAR,

absorbed photosynthetically active radiation) shows a good linear correlation with photochemical yield (defined as GPP/APAR) when APAR is higher than 400 to 600 μ mol $m^{-2}s^{-1}$. However, this linear relationship varies with Vcmax. If we assume the similar Vcmax within each biome type, SIF should have a good correlation with GPP at moderate or high light conditions relevant to satellite observations.

7.A.6 Comparing GPP ensemble using SIF as a temporal proxy and spatial proxy

Because of the close relationship between SIF and GPP within each biome type, SIF can be used as a reference to evaluate the performance of various models in GPP estimation. To reduce uncertainties of SIF from GOME-2, we proposed two strategies to reduce uncertainties: monthly SIF is averaged either temporally to yearly average, or spatially within each biome types; and we then use temporally averaged SIF as spatial representative or the spatially averaged SIF as temporal representative of photosynthetic activity. The weights for each model from these two approaches are given in Figures 7.A.5, 7.A.6. When using SIF as a temporal reference for each biome, the difference between each individual model is rather small (Table 7.A.2), and most models have relatively high correlation. This implies most models can simulate the seasonal variation of GPP relatively well. However, when using SIF as a spatial reference within each biome, the difference between each individual model is relatively large (Table 7.A.2), and many models have relatively low correlation coefficients. In addition, the interannual difference of the weight is very small (short error bar in Figure 7.A.5), proving the method is relatively stable.

7.A.7 Interannual variation of SIF

SIF data from the satellite have relative high noise because of the high spectral requirement for the sensor. For the GOME-2 dataset, the reported error for monthly

mean gridded data are ~0.1–0.4 mW $m^{-2}nm^{-1}sr^{-1}$ (Joiner et al., 2013). This reported error is contributed from several sources: (1) the error for each individual SIF measurement, which is affected by the radiance noise, atmospheric conditions; (2) different observing conditions (view angle), sampling locations and time; (3) cloud contaminations; (4) various systematic errors. When calculating the interannual variation, the contribution from 2-4 is limited and is ignored in our analysis.

We use the following scheme to calculate the interannual variation of SIF:

(1) For each gridcell each month, not only the aggregated SIF value (average of all valid SIF retrieval) is given, the GOME-2 SIF product also gives the number of individual SIF measurements used to aggregate the gridcell and the standard deviation of all retrievals. The uncertainty of this gridcell for month i (σ_i) will be the standard deviation of all retrievals (regarded as the uncertainty of each individual measurement) divided by $\sqrt{n}$, where n is the number of measurements used for aggregation. Therefore, we can get the uncertainty of SIF for each gridcell for each month.

(2) From the SIF value and uncertainty for each month, we will further calculate the SIF mean and uncertainties for each year. Assuming for each gridcell, the uncertainty of SIF for month i (ϵ_i) follows a normal distribution ($\epsilon_i \in N(0, \sigma_i)$), where σ_i is the uncertainty which we calculated in the previous step, the uncertainty of annual average SIF for year j (ϵ_j) will also follow a normal distribution:

$$\epsilon_j = \in N\left(0, \frac{\sqrt{\sum_{i=1}^{12} \sigma_i^2}}{12}\right) \tag{7.A.5}$$

(3) To calculate the actual IAV of SIF, we need to eliminate the uncertainty induced variability for each year ($\epsilon_j \in N(0, \sigma_j)$) from the calculated variability (σ_{cal}) for each gridcell. We found a very similar pattern of ϵ_j across different years. Because of the additivity of variance, the calculated IAV of SIF (σ_{cal}) can be explained by the real IAV of SIF (σ_{IAV}) and error of observation (σ_{ann}):

$$\sigma_{cal}^2 = \sigma_{IAV}^2 + \sigma_{ann}^2 \tag{7.A.6}$$

where the error of observation (σ_{ann}) is calculated as follows:

$$\sigma_{ann} = \sqrt{\frac{\sum_{j=2007}^{2015} \sigma_j^2}{9}} \tag{7.A.7}$$

The spatial patterns of σ_{cal} and σ_{ann} are shown in Figure 7.A.10.

7.A.8 Decompose ET variation from precipitation variation and potential evapotranspiration variation

Using the Budyko framework, similar with Eq. 7.6 in the methods, we can also get the ET sensitivity to PET (E_0) change:

$$\frac{\partial ET}{\partial P} = \frac{1}{\left(1 + \left(\frac{E_0}{P}\right)^{-n}\right)^{\frac{n+1}{n}}} = (AI^n + 1)^{-\frac{n+1}{n}} \tag{7.A.8}$$

$$\frac{\partial ET}{\partial E_0} = \frac{1}{\left(1 + \left(\frac{E_0}{P}\right)^{n}\right)^{\frac{n+1}{n}}} = (AI^{-n} + 1)^{-\frac{n+1}{n}} \tag{7.A.9}$$

Therefore, ET variability can be decomposed into ET variability caused by precipitation variability (ET_P), and ET variability caused by PET variability (ET_{E_0}).

$$ET_P = \frac{\partial ET}{\partial P} \times IAV_P \tag{7.A.10}$$

$$ET_{E_0} = \frac{\partial ET}{\partial E_0} \times IAV_{E_0} \tag{7.A.11}$$

We calculate the ET_P and ET_{E_0} using different n values (0.5, 1, 2) to infer the ET change from change in precipitation and change in E_0. Results are shown in Figure 7.A.15.

7.A.9 Verification of the stability and robustness of the weighted ensemble method

To verify the stability and robustness of the weighted ensemble method to model inputs, we use 13 out of 14 models as input and test the variation of the annual GPP and GPP s.d. for both unweighted average method and the weighted ensemble method. Each time, we drop one model from the 14 models and use the rest 13 models as input. The GPP for each year is calculated as the average of the 13 model estimates for this year or using the ensemble method described in the method section. The annual GPP and GPP s.d. is then calculated from the output of each year by both methods. By repeating this process for 14 times, we can get all the possible combination of using 13 models as inputs. The variations of the annual GPP and GPP s.d. from 14 times run for both methods are regarded as the methods stability (Figures 7.A.17).

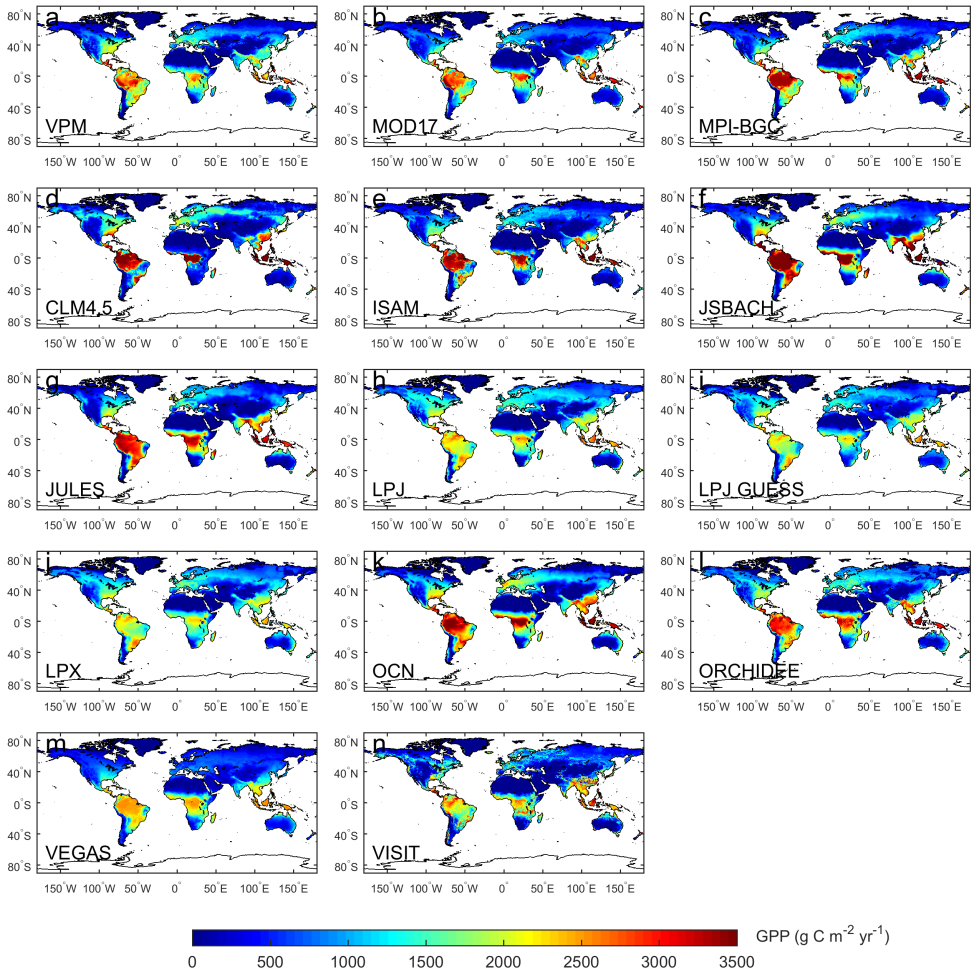


Figure 7.A.1: Spatial patterns of annual mean GPP from 3 data-driven models, and 11 DGVMs from the Trendy-V4 project.

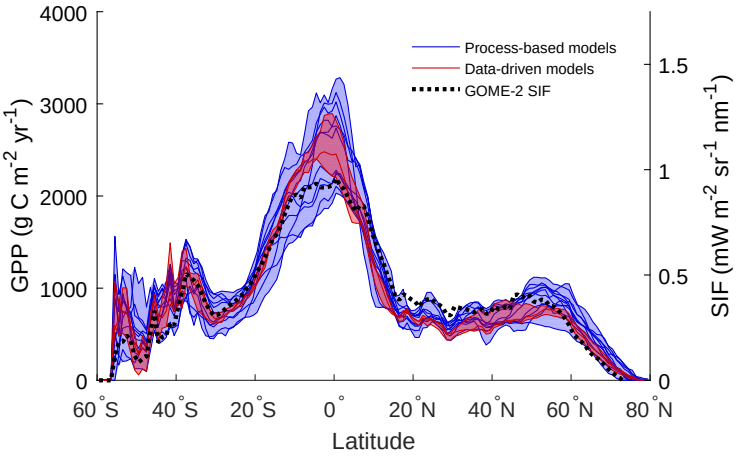


Figure 7.A.2: Latitudinal pattern (1° bands) of annual GPP. The blue area represents the range of the DGVMs from the Trendy-V4 project (CLM4.5, ISAM, JSBACH, JULES, LPJ, LPJ-GUESS, OCN, ORCHIDEE, TRIFFID, VEGAS, VISIT), the red area represents the range of the data-driven models (VPM, MTE, and MOD17).

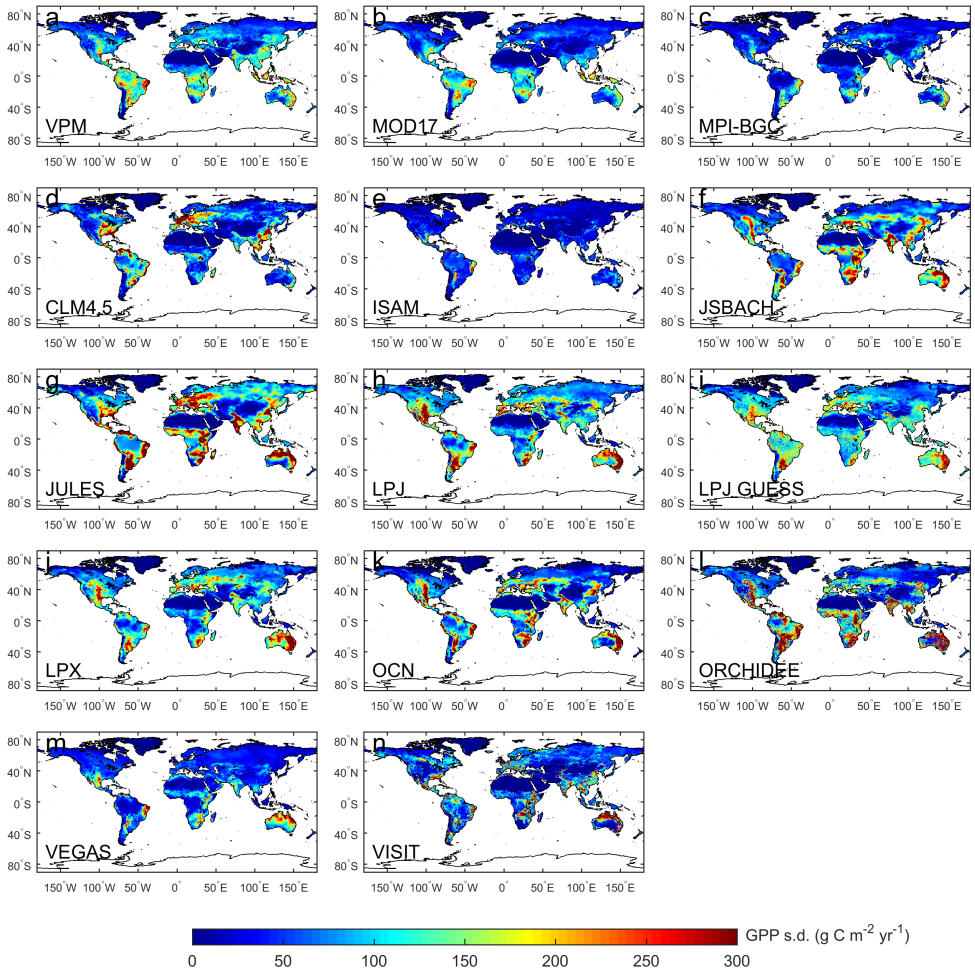


Figure 7.A.3: Spatial patterns of inter-annual variability (standard deviation, s.d.) of GPP from the 3 data-driven models and the 11 DGVMs from the Trendy-V4 project.

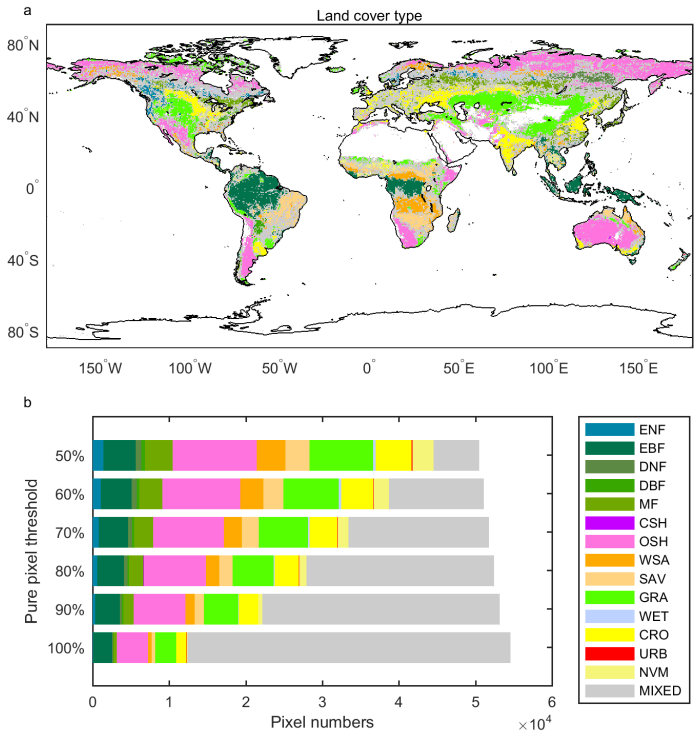


Figure 7.A.4: Land cover map (80% threshold value) from MODIS MCD12Q1 for 2007 (a) and the 'pure' pixel numbers for each land cover type at different threshold values(b). For statistic purpose, only vegetated land (no snow, barren, water) were shown.

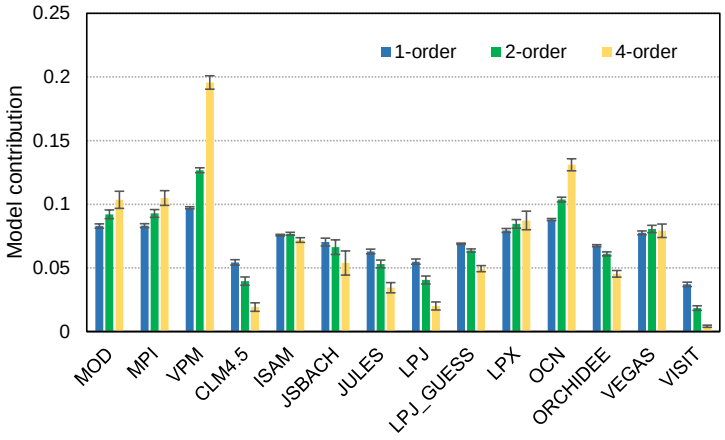


Figure 7.A.5: Average model contribution of spatial GPP ensemble (see Methods) with different orders. The error bars represent the standardized deviation (s.d.) across 5 years (2007–2011).

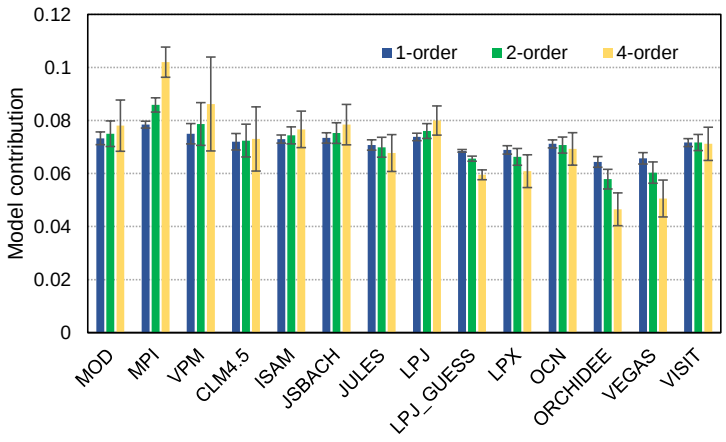


Figure 7.A.6: Average model contribution of temporal GPP ensemble (see Methods) with different orders. The error bars represent the standardized deviation (s.d.) across 5 years (2007–2011).

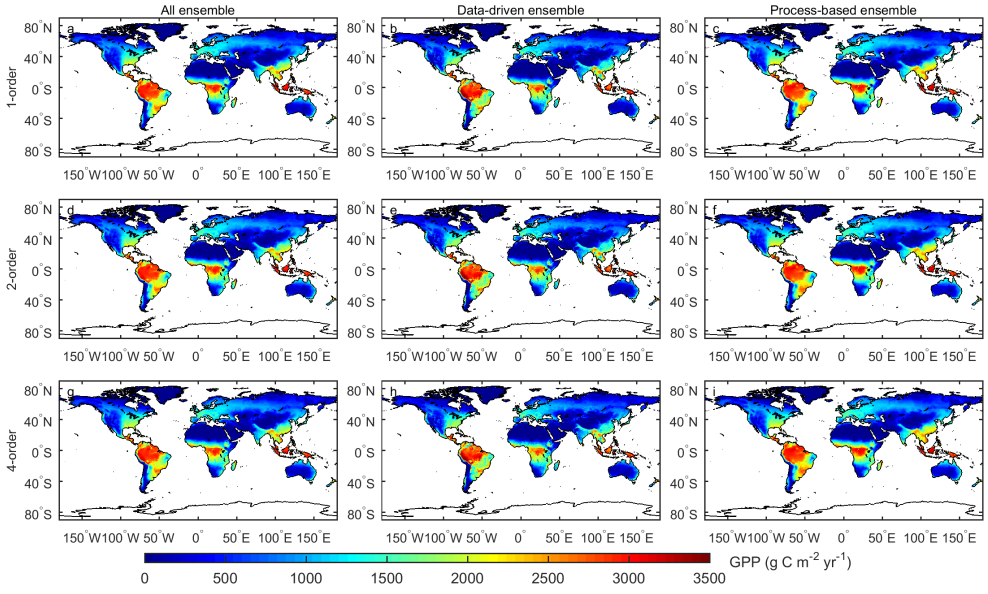


Figure 7.A.7: Spatial pattern of annual GPP ensemble from all models (first column), data-driven models (second column), and DGVMs (third column). Different rows represent different orders of weight applied.

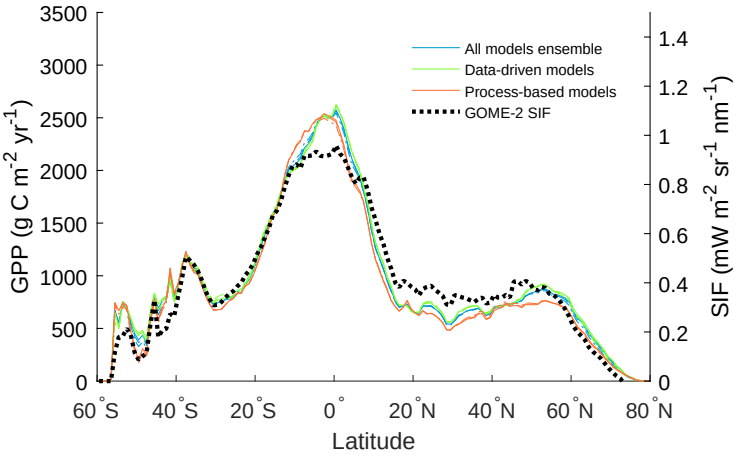


Figure 7.A.8: Latitudinal pattern (1° bands) of annual GPP. The solid line, dashed line and dash-dotted line represent 1-order, 2-order and 4-order weighted ensemble.

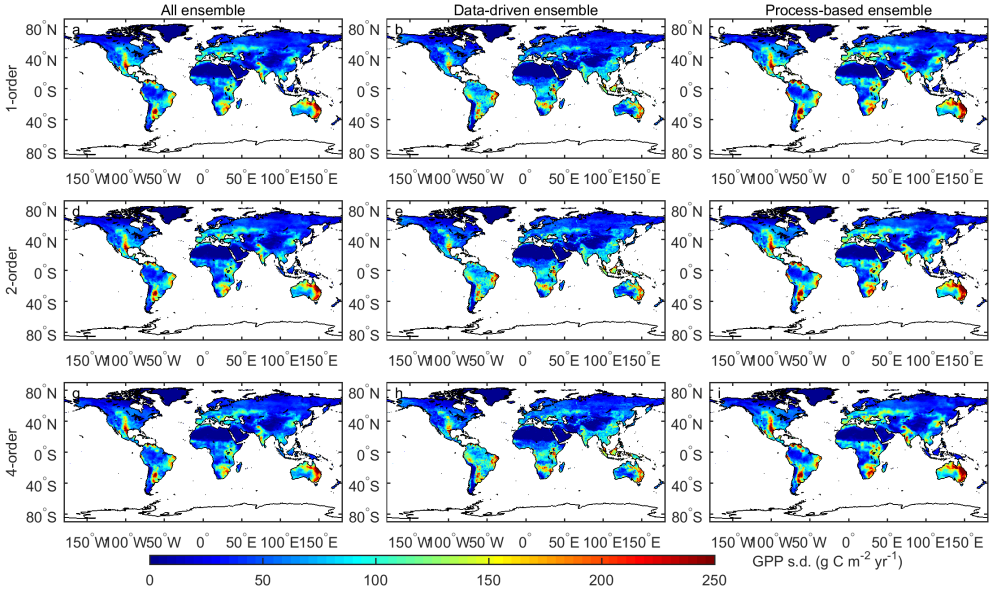


Figure 7.A.9: Spatial pattern of GPP IAV from all models ensemble (first column), data-driven models (second column), DGVMs (third column). Different rows represent different orders of weight applied.

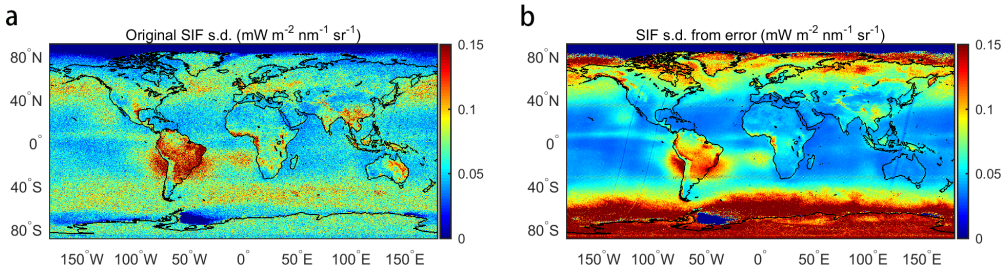


Figure 7.A.10: The calculated SIF variability from 2007 to 2015 using annual mean SIF value (a) and the average SIF error from each year (b).

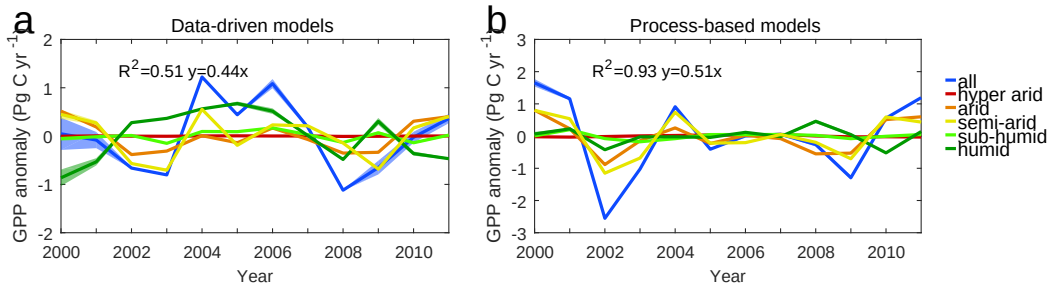


Figure 7.A.11: Detrended GPP anomaly from the ensembles of data-driven models (a) and process-based models (b).

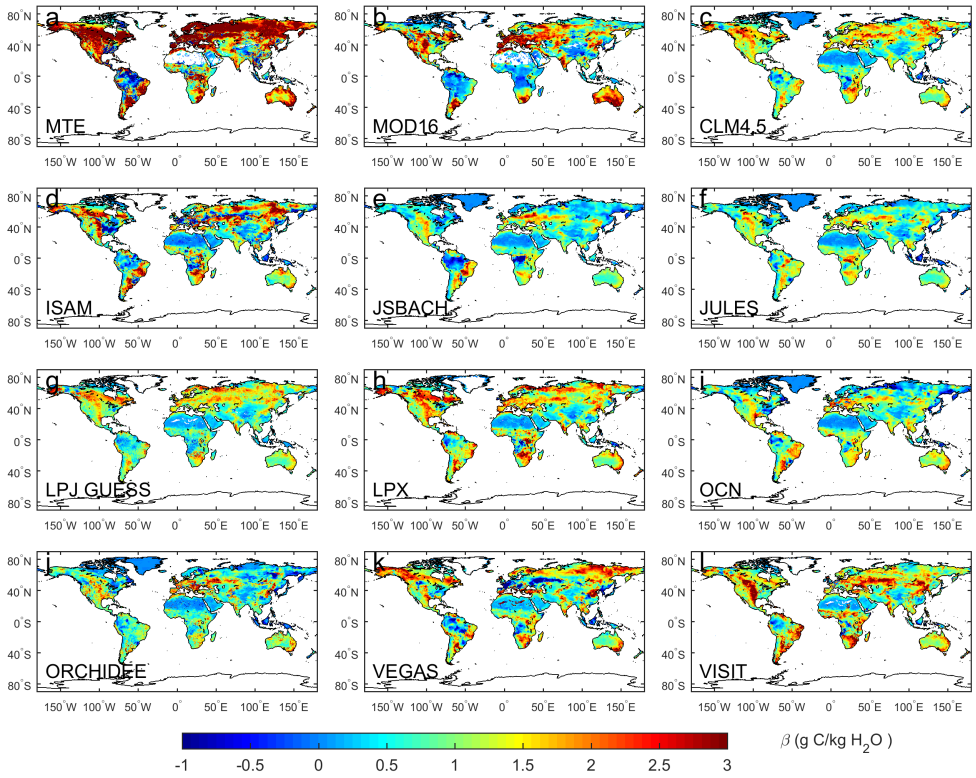


Figure 7.A.12: Regression slope between GPP and ET. GPP is from 2nd order of the GPP ensemble with all models and ET is from 12 models.

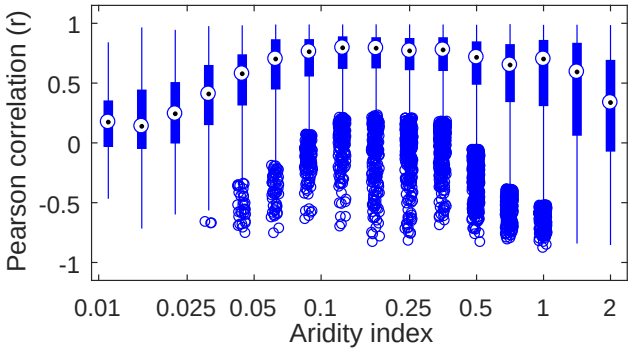


Figure 7.A.13: Correlation distribution between 2^{nd} order GPP ensemble and MTE ET across different aridity index. The water-carbon cycle is closely coupled in arid and semi-arid regions, but decreases after aridity index is greater than 0.5.

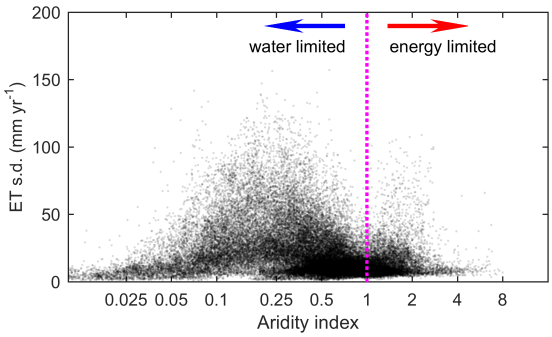


Figure 7.A.14: Relationship between ET variability and aridity index. ET variation are calculated from MTE ET dataset and aggregated to annual sum. Aridity equals to 1 indicate precipitation equals to evapotranspirative demand. With the aridity index decreasing from 1 to 0, ET variability becomes dominated by the precipitation variability; with the aridity index increasing from 1 to ∞, ET variability becomes dominated by the PET variability.

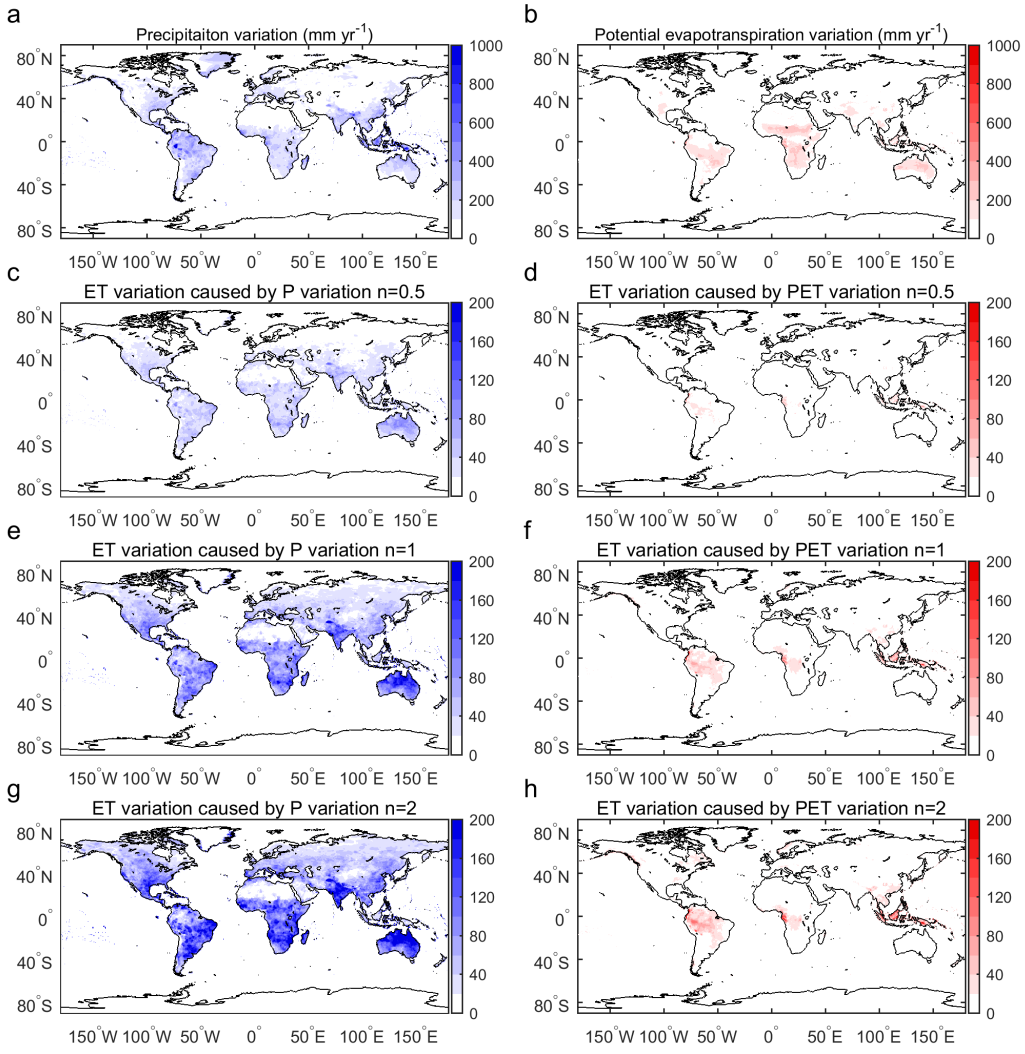


Figure 7.A.15: The spatial pattern of precipitation variation from GPCC and PET variation from MODIS MOD16, both datasets are annual sums from 2000-2013 (a, b). ET variation caused by precipitation variation and by PET variation with different n values (c - h).

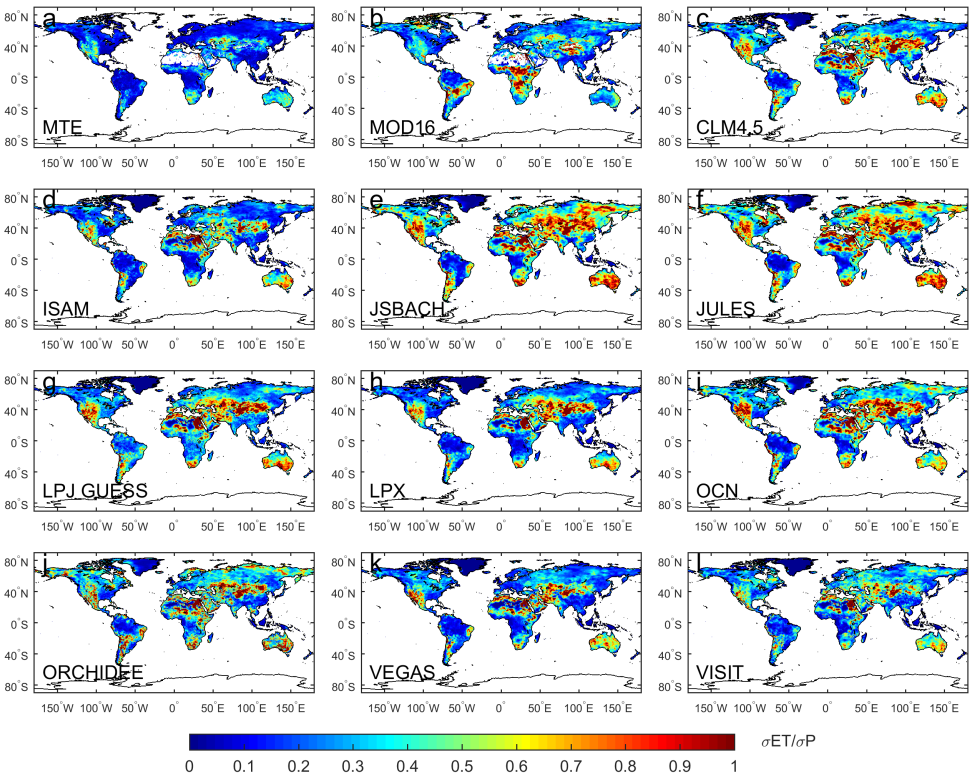


Figure 7.A.16: σ_{ET}/σ_P estimated from 12 ET models and the GPCC precipitation for 2000-2011.

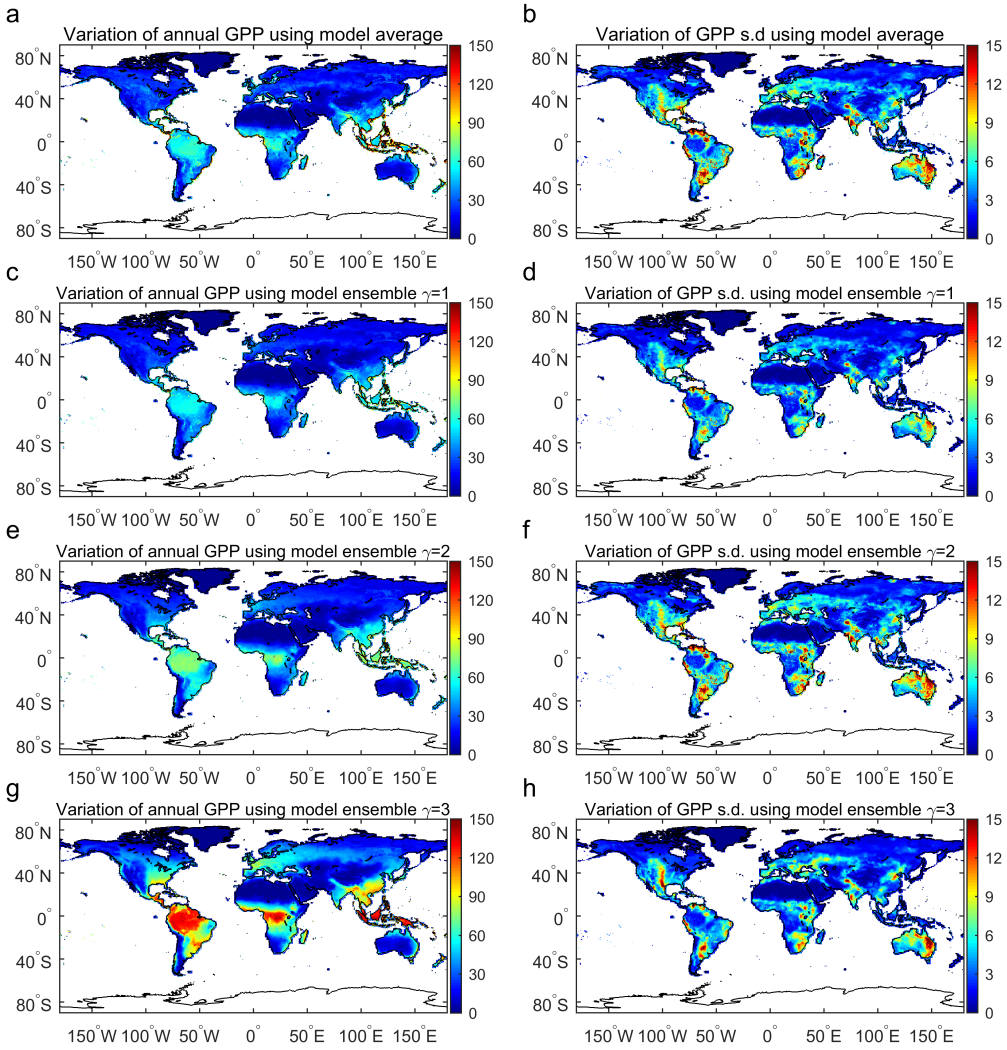


Figure 7.A.17: The variation of (a, c, e, g) annual GPP and (b, d, f, h) GPP s.d. using unweighted average (a, b) and weighted ensemble (c, d, e, f, g, h) with different order factor (γ in Eq. 7.2). All the units are g C m^{-2} $year^{-1}$.

Table 7.A.1: Classification scheme of aridity regions based on aridity index (AI). Aridity index is defined by FAO and the classification is inherited from UNEP Drylands are defined as AI < 0.65.

Aridity index	Aridity class
<0.05	Hyper arid
0.05–0.2	Arid
0.2–0.5	Semi-arid
0.5–0.65	Sub-humid
>0.65	Humid

Table 7.A.2: The biome area weighted correlation between GPP and SIF ($score_i$) using SIF as a temporal reference.

Models	2007	2008	2009	2010	2011
VPM	0.91	0.90	0.94	0.87	0.88
MOD	0.87	0.90	0.88	0.90	0.85
MPI	0.94	0.96	0.93	0.94	0.95
CLM4.5	0.87	0.91	0.77	0.89	0.89
ISAM	0.87	0.92	0.82	0.88	0.90
JSBACH	0.86	0.89	0.88	0.87	0.91
JULES	0.82	0.89	0.83	0.84	0.88
LPJ	0.87	0.92	0.87	0.87	0.91
LPJG	0.83	0.86	0.79	0.82	0.82
LPX	0.84	0.85	0.78	0.85	0.82
OCN	0.84	0.89	0.81	0.85	0.89
ORCHIDEE	0.78	0.81	0.71	0.81	0.77
VEGAS	0.81	0.84	0.73	0.80	0.77
VISIT	0.89	0.87	0.82	0.86	0.87

Table 7.A.3: The biome area weighted correlation between GPP and SIF ($score_i$) using SIF as a spatial reference.

Models	2007	2008	2009	2010	2011
VPM	0.71	0.74	0.74	0.76	0.74
MOD	0.59	0.63	0.63	0.66	0.63
MPI	0.60	0.63	0.62	0.66	0.64
CLM4.5	0.42	0.41	0.41	0.42	0.39
ISAM	0.55	0.57	0.57	0.59	0.58
JSBACH	0.51	0.51	0.51	0.59	0.53
JULES	0.47	0.45	0.47	0.51	0.48
LPJ	0.41	0.43	0.43	0.41	0.40
LPJG	0.51	0.52	0.52	0.54	0.51
LPX	0.59	0.62	0.59	0.62	0.59
OCN	0.65	0.67	0.66	0.68	0.67
ORCHIDEE	0.50	0.51	0.51	0.52	0.51
VEGAS	0.56	0.57	0.58	0.62	0.59
VISIT	0.28	0.28	0.30	0.28	0.27

Chapter 8: Conclusions and perspectives

Observation and simulation of GPP at regional and global scale is critical to understand vegetation responses to disturbances and global climate change. They also provide information of the spatial temporal variation of the global carbon cycle. Increasing observations, both *in situ* and remotely sensed, enable us to investigate plant photosynthesis from different scales and perspectives. This dissertation uses an integration of photosynthesis measurements at leaf, canopy, and ecosystem, and global scales, either by gas exchanges (CO_2 fluxes) or energy partitioning after plant absorption. The use of these datasets not only enhanced our understanding of plant photosynthesis in response to drought, but also improved a light use efficiency model — the vegetation photosynthesis model (VPM). Based on the improved model simulation, I developed a global GPP datasets and explored the relationship between GPP and solar induced chlorophyll fluorescence, and the spatial variability and climate regulation.

The results from Chapter 2 demonstrated the feasibility of using SIF and remote sensing spectroscopy to track the seasonal variation of vegetation photosynthesis capacity and drought limitation on energy partitioning after absorption by chlorophylls. Both leaf level and canopy level measurements suggest that the chlorophyll concentration is an important factor affecting the seasonal dynamic of photosynthesis other than leaf area. The drought can have impacts on both leaf level energy absorption and partitioning that can be tracked by SIF. Future studies can further test the relative contribution of chlorophyll and leaf area in determining the ecosystem photosynthetic capacity for different ecosystems and responses of different plant species to drought.

Chapter 3 used an integration of modeling and eddy covariance data and demon-

strated the important gap between instantaneous satellite SIF measurements and the daily integral of vegetation carbon fixation. Many previous studies ignored this temporal mismatch and the resultant relationship derived may be biased. Future studies should test how much difference are caused by this temporal mismatch using SIF from different satellite retrievals and at different latitude, and to what extent the vegetation specific GPP-SIF relationship are caused by this temporal mismatch. Since the use of instantaneous SIF also showed great advantage over other vegetation indices in tracking plant phenology, especially in boreal high latitude ecosystems. Future studies can also test whether the use of daily SIF will improve the phenology retrieval using SIF.

Chapter 4 demonstrated that the plants' ability to utilize light for photosynthesis is similar across species and times if only the light absorption by chlorophyll of the canopy is considered. Previous studies used canopy or ecosystem total radiation absorption fail to consider the variation of chlorophyll concentration in different leaves, therefore produced less satisfactory GPP estimations. However, the variation of maximum light use efficiency still exist within each biome types, which may be related to the canopy structure and fraction of diffused radiation. Future studies should test how much variation can be explain by the variation of plant canopy structure and how to simulate this effect using remote sensing datasets. The combination of plant structure and leaf pigments concentration will be beneficial to build new models to simulate GPP at a global scale.

Chapter 5 explained how two types of limitations worked in coordination during the drought period. Different biome types (forest or non-forest) also showed very different responses to drought in terms of their canopy stability and stomatal sensitivity. The sensitivity and stability are related to both the root depth and the plant iso/anisohydricty, which are indicators of plant water use strategy to drought.

Isohydric species tend to maintain a relative stable water potential in their leaves so that they will have more control on stomatal; Anisohydric species' leaf water potential will vary with the soil water potential and have less regulation on evapotranspiration. How do the plant spectral sensitivity to drought related to different root depth and plant iso/anisohydricity should be further investigated by future studies so that these traits can be incorporated in the earth system modeling and give better prediction of drought effect on global carbon cycle.

Chapter 6 uses the vegetation photosynthesis model (VPM) and simulate the GPP for North America for year 2010. The results showed that GPP and SIF showed very high consistency in terms of the spatial and temporal patterns. The implementation of the VPM at regional scale also showed very good performance when validated against flux tower site in NA. However, uncertainties still exist between the GPP-SIF relationship, one key question remained unanswered is whether GPP-SIF relationship is biome dependent or the variations across biomes are just caused by artifacts. Future studies should focus more on site level analysis using both SIF and EC measurement to explain the GPP-SIF relationship across space and time.

Chapter 7 focused on the hotspots on the GPP interannual variation. By combining multiple GPP products together using satellite SIF observations, we generated a new global GPP datasets and found high GPP interannual variability in the semi arid regions. We also explained this high variation using the Budyko framework and the carbon water coupling. Recent studies suggested although at regional scale, GPP interannual variability is caused by precipitation, the global total GPP anomalies are strongly coupled with temperature anomalies. This scale dependency are important to predict the future carbon cycle under climate change. Future studies should integrate both site level experiment and satellite observations to explore the sensitivity of carbon cycle to temperature and precipitation at different

ecosystems and how they work in coordination to control the regional and global carbon cycle.

Bibliography

Aber, J. D., Reich, P. B., & Goulden, M. L. (1996). Extrapolating leaf co2 exchange to the canopy: a generalized model of forest photosynthesis compared with measurements by eddy correlation. *Oecologia*, *106*(2), 257–265.

Ahlstrom, A., Raupach, M. R., Schurgers, G., Smith, B., Arneth, A., Jung, M., Reichstein, M., Canadell, J. G., Friedlingstein, P., Jain, A. K., Kato, E., Poulter, B., Sitch, S., Stocker, B. D., Viovy, N., Wang, Y. P., Wiltshire, A., Zaehle, S., & Zeng, N. (2015). The dominant role of semi-arid ecosystems in the trend and variability of the land co2 sink. *Science*, *348*(6237), 895–899.

Aires, L. M. I., Pio, C. A., & Pereira, J. S. (2008). Carbon dioxide exchange above a mediterranean c3/c4 grassland during two climatologically contrasting years. *Global Change Biology*, *14*(3), 539–555.

Allard, V., Ourcival, J. M., Rambal, S., Joffre, R., & Rocheteau, A. (2008). Seasonal and annual variation of carbon exchange in an evergreen mediterranean forest in southern france. *Global Change Biology*, *14*(4), 714–725.

Allen, C. D., Macalady, A. K., Chenchouni, H., Bachelet, D., McDowell, N., Vennetier, M., Kitzberger, T., Rigling, A., Breshears, D. D., & Hogg, E. (2010). A global overview of drought and heat-induced tree mortality reveals emerging climate change risks for forests. *Forest Ecology and Management*, *259*(4), 660–684.

Alton, P. B. (2017). Retrieval of seasonal rubisco-limited photosynthetic capacity at global fluxnet sites from hyperspectral satellite remote sensing: Impact on carbon modelling. *Agricultural and Forest Meteorology*, *232*, 74–88.

Amiro, B. D., MacPherson, J. I., Desjardins, R. L., Chen, J. M., & Liu, J. (2003). Post-fire carbon dioxide fluxes in the western canadian boreal forest: evidence from towers, aircraft and remote sensing. *Agricultural and Forest Meteorology*, *115*(1-2), 91–107.

Amiro, B. D., Orchansky, A. L., Barr, A. G., Black, T. A., Chambers, S. D., Chapin, F. S., Gouldenf, M. L., Litvakg, M., Liu, H. P., McCaughey, J. H., McMillan, A., & Randerson, J. T. (2006). The effect of post-fire stand age on the boreal forest energy balance. *Agricultural and Forest Meteorology*, *140*(1-4), 41–50.

Ammann, C., Flechard, C. R., Leifeld, J., Neftel, A., & Fuhrer, J. (2007). The carbon budget of newly established temperate grassland depends on management intensity. *Agriculture Ecosystems Environment*, *121*(1-2), 5–20.

Ammann, C., Spirig, C., Leifeld, J., & Neftel, A. (2009). Assessment of the nitrogen and carbon budget of two managed temperate grassland fields. *Agriculture Ecosystems Environment*, *133*(3-4), 150–162.

Anav, A., Friedlingstein, P., Beer, C., Ciais, P., Harper, A., Jones, C., Murray-Tortarolo, G., Papale, D., Parazoo, N. C., Peylin, P., Piao, S., Sitch, S., Viovy, N., Wiltshire, A., & Zhao, M. (2015). Spatiotemporal patterns of terrestrial gross primary production: A review. *Reviews of Geophysics*, *53*(3), 785–818.

Anav, A., Friedlingstein, P., Kidston, M., Bopp, L., Ciais, P., Cox, P., Jones, C., Jung, M., Myneni, R., & Zhu, Z. (2013). Evaluating the land and ocean components of the global carbon cycle in the cmip5 earth system models. *Journal of Climate*, *26*(18), 6801–6843.

Anderegg, W. R., Hicke, J. A., Fisher, R. A., Allen, C. D., Aukema, J., Bentz, B., Hood, S., Lichstein, J. W., Macalady, A. K., McDowell, N., Pan, Y., Raffa, K., Sala, A., Shaw, J. D., Stephenson, N. L., Tague, C., & Zeppel, M. (2015). Tree mortality from drought, insects, and their interactions in a changing climate. *New Phytol*, *208*(3), 674–83.

Anthoni, P. M., Knohl, A., Rebmann, C., Freibauer, A., Mund, M., Ziegler, W., Kolle, O., & Schulze, E. D. (2004). Forest and agricultural land-use-dependent co2 exchange in thuringia, germany. *Global Change Biology*, *10*(12), 2005–2019.

Arain, A. A., & Restrepo-Coupe, N. (2005). Net ecosystem production in a temperate pine plantation in southeastern canada. *Agricultural and Forest Meteorology*, *128*(3-4), 223–241.

Ardö, J., Mölder, M., El-Tahir, B. A., & Elkhidir, H. A. (2008). Seasonal variation of carbon fluxes in a sparse savanna in semi arid sudan. *Carbon Balance and Management*, *3*(7).

Arora, V. K., Boer, G. J., Friedlingstein, P., Eby, M., Jones, C. D., Christian, J. R., Bonan, G., Bopp, L., Brovkin, V., Cadule, P., et al. (2013). Carbon–concentration and carbon–climate feedbacks in cmip5 earth system models. *Journal of Climate*, *26*(15), 5289–5314.

Asner, G. P., & Martin, R. E. (2008). Spectral and chemical analysis of tropical forests: Scaling from leaf to canopy levels. *Remote Sensing of Environment*, *112*(10), 3958–3970.

Aubinet, M., Chermanne, B., Vandenhaute, M., Longdoz, B., Yernaux, M., & Laitat, E. (2001). Long term carbon dioxide exchange above a mixed forest in the belgian ardennes. *Agricultural and Forest Meteorology*, *108*(4), 293–315.

Aubinet, M., Vesala, T., & Papale, D. (2012). *Eddy covariance: a practical guide to measurement and data analysis*. Springer Science Business Media.

Baker, N. R. (2008). Chlorophyll fluorescence: A probe of photosynthesis in vivo. *Annual Review of Plant Biology*, *59*, 89–113.

Baldocchi, D. (2014). Measuring fluxes of trace gases and energy between ecosystems and the atmosphere - the state and future of the eddy covariance method. *Globe Change Biology*, *20*(12), 3600–9.

Baldocchi, D., Falge, E., Gu, L. H., Olson, R., Hollinger, D., Running, S., Anthoni, P., Bernhofer, C., Davis, K., Evans, R., Fuentes, J., Goldstein, A., Katul, G., Law, B., Lee, X. H., Malhi, Y., Meyers, T., Munger, W., Oechel, W., U, K. T. P., Pilegaard, K., Schmid, H. P., Valentini, R., Verma, S., Vesala, T., Wilson, K., & Wofsy, S. (2001). Fluxnet: A new tool to study the temporal and spatial variability of ecosystem-scale carbon dioxide, water vapor, and energy flux densities. *Bulletin of the American Meteorological Society*, *82*(11), 2415–2434.

Baldocchi, D., Ryu, Y., & Keenan, T. (2016). Terrestrial carbon cycle variability. *F1000Research*, *5*, 2371.

Baldocchi, D. D., Xu, L., & Kiang, N. (2004). How plant functional-type, weather, seasonal drought, and soil physical properties alter water and energy fluxes of an oak–grass savanna and an annual grassland. *Agricultural and Forest Meteorology*, *123*(1), 13–39.

Ballantyne, A. P., Alden, C. B., Miller, J. B., Tans, P. P., & White, J. W. (2012). Increase in observed net carbon dioxide uptake by land and oceans during the past 50 years. *Nature*, *488*(7409), 70–2.

Beer, C., Reichstein, M., Tomelleri, E., Ciais, P., Jung, M., Carvalhais, N., Rödenbeck, C., Arain, M. A., Baldocchi, D., & Bonan, G. B. (2010). Terrestrial gross carbon dioxide uptake: global distribution and covariation with climate. *Science*, *329*(5993), 834–838.

Beier, C., Emmett, B. A., Tietema, A., Schmidt, I. K., Penuelas, J., Lang, E. K., Duce, P., De Angelis, P., Gorissen, A., Estiarte, M., de Dato, G. D., Sowerby, A., Kroel-Dulay, G., Lellei-Kovacs, E., Kull, O., Mand, P., Petersen, H., Gjelstrup, P., & Spano, D. (2009). Carbon and nitrogen balances for six shrublands across europe. *Global Biogeochemical Cycles*, *23*.

Berbigier, P., Bonnefond, J. M., & Mellmann, P. (2001). Co2 and water vapour fluxes for 2 years above euroflux forest site. *Agricultural and Forest Meteorology*, *108*(3), 183–197.

Bergeron, O., Margolis, H. A., Black, T. A., Coursolle, C., Dunn, A. L., Barr, A. G., & Wofsy, S. C. (2007). Comparison of carbon dioxide fluxes over three boreal black spruce forests in canada. *Global Change Biology*, *13*(1), 89–107.

Beringer, J., Hacker, J., Hutley, L. B., Leuning, R., Arndt, S. K., Amiri, R., Bannehr, L., Cernusak, L. A., Grover, S., Hensley, C., Hocking, D., Isaac, P., Jamali, H., Kanniah,

K., Livesley, S., Neininger, B., U, K. T. P., Sea, W., Straten, D., Tapper, N., Weinmann, R., Wood, S., & Zegelin, S. (2011). Special-savanna patterns of energy and carbon integrated across the landscape. *Bulletin of the American Meteorological Society*, *92*(11), 1467–1485.

Bi, J., Knyazikhin, Y., Choi, S., Park, T., Barichivich, J., Ciais, P., Fu, R., Ganguly, S., Hall, F., Hilker, T., Huete, A., Jones, M., Kimball, J., Lyapustin, A. I., Mõttus, M., Nemani, R. R., Piao, S., Poulter, B., Saleska, S. R., Saatchi, S. S., Xu, L., Zhou, L., & Myneni, R. B. (2015). Sunlight mediated seasonality in canopy structure and photosynthetic activity of amazonian rainforests. *Environmental Research Letters*, *10*(6), 064014.

Blackman, C. J., Brodribb, T. J., & Jordan, G. J. (2009). Leaf hydraulics and drought stress: response, recovery and survivorship in four woody temperate plant species. *Plant, Cell Environment*, *32*(11), 1584–1595.

Bond-Lamberty, B., Wang, C. K., & Gower, S. T. (2004). Net primary production and net ecosystem production of a boreal black spruce wildfire chronosequence. *Global Change Biology*, *10*(4), 473–487.

Booth, B. B. B., Jones, C. D., Collins, M., Totterdell, I. J., Cox, P. M., Sitch, S., Huntingford, C., Betts, R. A., Harris, G. R., & Lloyd, J. (2012). High sensitivity of future global warming to land carbon cycle processes. *Environmental Research Letters*, *7*(2), 024002.

Budyko, M. (1974). Climate and life. *Academic, San Diego, Calif*, (pp. 72–191).

Butler, W. L. (1978). Energy distribution in the photochemical apparatus of photosynthesis. *Annual Review of Plant Physiology*, *29*(1), 345–378.

Butz, A., Guerlet, S., Hasekamp, O., Schepers, D., Galli, A., Aben, I., Frankenberg, C., Hartmann, J., Tran, H., & Kuze, A. (2011). Toward accurate co2 and ch4 observations from gosat. *Geophysical Research Letters*, *38*(14).

Cai, W., Yuan, W., Liang, S., Zhang, X., Dong, W., Xia, J., Fu, Y., Chen, Y., Liu, D., & Zhang, Q. (2014). Improved estimations of gross primary production using satellite-derived photosynthetically active radiation. *Journal of Geophysical Research: Biogeosciences*, *119*(1), 110–123.

Carlson, T. N., & Ripley, D. A. (1997). On the relation between ndvi, fractional vegetation cover, and leaf area index. *Remote sensing of Environment*, *62*(3), 241–252.

Cescatti, A., & Marcolla, B. (2004). Drag coefficient and turbulence intensity in conifer canopies. *Agricultural and Forest Meteorology*, *121*(3-4), 197–206.

Chen, B. Z., Coops, N. C., Fu, D., Margolis, H. A., Amiro, B. D., Black, T. A., Arain, M. A., Barr, A. G., Bourque, C. P. A., Flanagan, L. B., Lafleur, P. M., McCaughey, J. H., & Wofsy, S. C. (2012). Characterizing spatial representativeness of flux tower eddy-covariance measurements across the canadian carbon program network using remote sensing and footprint analysis. *Remote Sensing of Environment*, *124*, 742–755.

Chen, J., Jönsson, P., Tamura, M., Gu, Z., Matsushita, B., & Eklundh, L. (2004). A simple method for reconstructing a high-quality ndvi time-series data set based on the savitzky–golay filter. *Remote sensing of Environment*, *91*(3), 332–344.

Chen, J. M. (1996). Canopy architecture and remote sensing of the fraction of photosynthetically active radiation absorbed by boreal conifer forests. *Ieee Transactions on Geoscience and Remote Sensing*, *34*(6), 1353–1368.

Chen, Y., Xia, J., Liang, S., Feng, J., Fisher, J. B., Li, X., Li, X., Liu, S., Ma, Z., Miyata, A., Mu, Q., Sun, L., Tang, J., Wang, K., Wen, J., Xue, Y., Yu, G., Zha, T., Zhang, L., Zhang, Q., Zhao, T., Zhao, L., & Yuan, W. (2014). Comparison of satellite-based evapotranspiration models over terrestrial ecosystems in china. *Remote Sensing of Environment*, *140*, 279–293.

Cheng, Y.-B., Zhang, Q., Lyapustin, A. I., Wang, Y., & Middleton, E. M. (2014). Impacts of light use efficiency and fpar parameterization on gross primary production modeling. *Agricultural and Forest Meteorology*, *189-190*, 187–197.

Chiesi, M., Maselli, F., Bindi, M., Fibbi, L., Cherubini, P., Arlotta, E., Tirone, G., Matteucci, G., & Seufert, G. (2005). Modelling carbon budget of mediterranean forests using ground and remote sensing measurements. *Agricultural and Forest Meteorology*, *135*(1-4), 22–34.

Choudhury, B. J. (2001). Estimating gross photosynthesis using satellite and ancillary data: approach and preliminary results. *Remote Sensing of Environment*, *75*(1), 1–21.

Christen, D., Schönmann, S., Jermini, M., Strasser, R. J., & Défago, G. (2007). Characterization and early detection of grapevine (vitis vinifera) stress responses to esca disease by in situ chlorophyll fluorescence and comparison with drought stress. *Environmental and Experimental Botany*, *60*(3), 504–514.

Christidis, N., Jones, G. S., & Stott, P. A. (2014). Dramatically increasing chance of extremely hot summers since the 2003 european heatwave. *Nature Climate Change*, *5*(1), 46–50.

Chu, H. S., Chen, J. Q., Gottgens, J. F., Ouyang, Z. T., John, R., Czajkowski, K., & Becker, R. (2014). Net ecosystem methane and carbon dioxide exchanges in a

lake erie coastal marsh and a nearby cropland. *Journal of Geophysical Research-Biogeosciences*, *119*(5), 722–740.

Ciais, P., Denning, A. S., Tans, P. P., Berry, J. A., Randall, D. A., Collatz, G. J., Sellers, P. J., White, J. W. C., Trolier, M., Meijer, H. A. J., Francey, R. J., Monfray, P., & Heimann, M. (1997). A three-dimensional synthesis study of Îť18o in atmospheric co2: 1. surface fluxes. *Journal of Geophysical Research: Atmospheres*, *102*(D5), 5857–5872.

Ciais, P., Reichstein, M., Viovy, N., Granier, A., Ogée, J., Allard, V., Aubinet, M., Buchmann, N., Bernhofer, C., & Carrara, A. (2005). Europe-wide reduction in primary productivity caused by the heat and drought in 2003. *Nature*, *437*(7058), 529–533.

Clark, D. B., Mercado, L. M., Sitch, S., Jones, C. D., Gedney, N., Best, M. J., Pryor, M., Rooney, G. G., Essery, R. L. H., Blyth, E., Boucher, O., Harding, R. J., Huntingford, C., & Cox, P. M. (2011). The joint uk land environment simulator (jules), model description – part 2: Carbon fluxes and vegetation dynamics. *Geoscientific Model Development*, *4*(3), 701–722.

Collatz, G. J., Ribas-Carbo, M., & Berry, J. A. (1992). Coupled photosynthesis-stomatal conductance model for leaves of c4 plants. *Australian Journal of Plant Physiology*, *19*(5), 519–538.

Cong, N., Wang, T., Nan, H., Ma, Y., Wang, X., Myneni, R. B., & Piao, S. (2013). Changes in satellite-derived spring vegetation green-up date and its linkage to climate in china from 1982 to 2010: a multimethod analysis. *Globe Change Biology*, *19*(3), 881–91.

Cook, B. D., Davis, K. J., Wang, W. G., Desai, A., Berger, B. W., Teclaw, R. M., Martin, J. G., Bolstad, P. V., Bakwin, P. S., Yi, C. X., & Heilman, W. (2004). Carbon exchange and venting anomalies in an upland deciduous forest in northern wisconsin, usa. *Agricultural and Forest Meteorology*, *126*(3-4), 271–295.

Coops, N. C., Ferster, C. J., Waring, R. H., & Nightingale, J. (2009). Comparison of three models for predicting gross primary production across and within forested ecoregions in the contiguous united states. *Remote Sensing of Environment*, *113*(3), 680–690.

Corradi, C., Kolle, O., Walter, K., Zimov, S. A., & Schulze, E. D. (2005). Carbon dioxide and methane exchange of a north-east siberian tussock tundra. *Global Change Biology*, *11*(11), 1910–1925.

Coulter, R. L., Pekour, M. S., Cook, D. R., Klazura, G. E., Martin, T. J., & Lucas, J. D. (2006). Surface energy and carbon dioxide fluxes above different vegetation types within able. *Agricultural and Forest Meteorology*, *136*(3-4), 147–158.

Croft, H., Chen, J. M., Luo, X., Bartlett, P., Chen, B., & Staebler, R. M. (2017). Leaf chlorophyll content as a proxy for leaf photosynthetic capacity. *Globe Change Biology*, *23*, 3513–3524.

Curran, P. J. (1989). Remote sensing of foliar chemistry. *Remote Sensing of Environment*, *30*(3), 271–278.

Dai, A. (2012). Increasing drought under global warming in observations and models. *Nature Climate Change*, *3*(1), 52–58.

Damm, A., Elbers, J., Erler, A., Gioli, B., Hamdi, K., Hutjes, R., Kosvancova, M., Meroni, M., Miglietta, F., Moersch, A., Moreno, J., Schickling, A., Sonnenschein, R., Udelhoven, T., van der Linden, S., Hostert, P., & Rascher, U. (2010). Remote sensing of sun-induced fluorescence to improve modeling of diurnal courses of gross primary production (gpp). *Global Change Biology*, *16*(1), 171–186.

Damm, A., Guanter, L., Paul-Limoges, E., van der Tol, C., Hueni, A., Buchmann, N., Eugster, W., Ammann, C., & Schaepman, M. E. (2015a). Far-red sun-induced chlorophyll fluorescence shows ecosystem-specific relationships to gross primary production: An assessment based on observational and modeling approaches. *Remote Sensing of Environment*, *166*, 91–105.

Damm, A., Guanter, L., Verhoef, W., Schläpfer, D., Garbari, S., & Schaepman, M. E. (2015b). Impact of varying irradiance on vegetation indices and chlorophyll fluorescence derived from spectroscopy data. *Remote Sensing of Environment*, *156*, 202–215.

Dash, J., Curran, P., Tallis, M. J., Llewellyn, G., Taylor, G., & Snoeij, P. (2010). Validating the meris terrestrial chlorophyll index (mtci) with ground chlorophyll content data at meris spatial resolution. *International Journal of Remote Sensing*, *31*(20), 5513–5532.

Dash, J., & Curran, P. J. (2004). The meris terrestrial chlorophyll index. *International Journal of Remote Sensing*, *25*(23), 5403–5413.

Dash, J., & Curran, P. J. (2007). Evaluation of the meris terrestrial chlorophyll index (mtci). *Advances in Space Research*, *39*(1), 100–104.

Demarty, J., Chevallier, F., Friend, A. D., Viovy, N., Piao, S., & Ciais, P. (2007). Assimilation of global modis leaf area index retrievals within a terrestrial biosphere model. *Geophysical Research Letters*, *34*(15).

Deming, W. E. (1943). Statistical adjustment of data.

Desai, A. R., Bolstad, P. V., Cook, B. D., Davis, K. J., & Carey, E. V. (2005). Comparing net ecosystem exchange of carbon dioxide between an old-growth and mature forest in the upper midwest, usa. *Agricultural and Forest Meteorology*, *128*(1-2), 33–55.

Desai, A. R., Richardson, A. D., Moffat, A. M., Kattge, J., Hollinger, D. Y., Barr, A., Falge, E., Noormets, A., Papale, D., Reichstein, M., & Stauch, V. J. (2008). Cross-site evaluation of eddy covariance gpp and re decomposition techniques. *Agricultural and Forest Meteorology*, *148*(6-7), 821–838.

Dijkstra, P., Hymus, G., Colavito, D., Vieglais, D. A., Cundari, C. M., Johnson, D. P., Hungate, B. A., Hinkle, C. R., & Drake, B. G. (2002). Elevated atmospheric co2 stimulates aboveground biomass in a fire-regenerated scrub-oak ecosystem. *Global Change Biology*, *8*(1), 90–103.

Dolman, A. J., Moors, E. J., & Elbers, J. A. (2002). The carbon uptake of a mid latitude pine forest growing on sandy soil. *Agricultural and Forest Meteorology*, *111*(3), 157–170.

Dong, J., Xiao, X., Wagle, P., Zhang, G., Zhou, Y., Jin, C., Torn, M. S., Meyers, T. P., Suyker, A. E., Wang, J., Yan, H., Biradar, C., & Moore Iii, B. (2015). Comparison of four evi-based models for estimating gross primary production of maize and soybean croplands and tallgrass prairie under severe drought. *Remote Sensing of Environment*, *162*(0), 154–168.

Dore, S., Kolb, T. E., Montes-Helu, M., Sullivan, B. W., Winslow, W. D., Hart, S. C., Kaye, J. P., Koch, G. W., & Hungate, B. A. (2008). Long-term impact of a stand-replacing fire on ecosystem co(2) exchange of a ponderosa pine forest. *Global Change Biology*, *14*(8), 1801–1820.

Easterling, D. R., Evans, J., Groisman, P. Y., Karl, T., Kunkel, K. E., & Ambenje, P. (2000a). Observed variability and trends in extreme climate events: A brief review*. *Bulletin of the American Meteorological Society*, *81*(3), 417–425.

Easterling, D. R., Meehl, G. A., Parmesan, C., Changnon, S. A., Karl, T. R., & Mearns, L. O. (2000b). Climate extremes: observations, modeling, and impacts. *Science*, *289*(5487), 2068–2074.

Eder, F., Schmidt, M., Damian, T., Träumner, K., & Mauder, M. (2015). Mesoscale eddies affect near-surface turbulent exchange: evidence from lidar and tower measurements. *Journal of Applied Meteorology and Climatology*, *54*(1), 189–206.

Elsobky, N. M. (2015). *Variation and uncertainty in MERIS sensor land biophysical variables at global scale.* Thesis.

Epron, D., Bosc, A., Bonal, D., & Freycon, V. (2006). Spatial variation of soil respiration across a topographic gradient in a tropical rain forest in french guiana. *Journal of Tropical Ecology*, *22*, 565–574.

Epstein, H. E., Calef, M. P., Walker, M. D., Chapin, F. S., & Starfield, A. M. (2004). Detecting changes in arctic tundra plant communities in response to warming over decadal time scales. *Global Change Biology*, *10*(8), 1325–1334.

Falge, E., Baldocchi, D., Tenhunen, J., Aubinet, M., Bakwin, P., Berbigier, P., Bernhofer, C., Burba, G., Clement, R., Davis, K. J., Elbers, J. A., Goldstein, A. H., Grelle, A., Granier, A., Guomundsson, J., Hollinger, D., Kowalski, A. S., Katul, G., Law, B. E., Malhi, Y., Meyers, T., Monson, R. K., Munger, J. W., Oechel, W., Paw, K. T., Pilegaard, K., Rannik, U., Rebmann, C., Suyker, A., Valentini, R., Wilson, K., & Wofsy, S. (2002). Seasonality of ecosystem respiration and gross primary production as derived from fluxnet measurements. *Agricultural and Forest Meteorology*, *113*(1-4), 53–74.

Farquhar, G. D., Caemmerer, S. V., & Berry, J. A. (1980). A biochemical-model of photosynthetic co2 assimilation in leaves of c-3 species. *Planta*, *149*(1), 78–90.

Fensholt, R., Sandholt, I., & Rasmussen, M. S. (2004). Evaluation of modis lai, fapar and the relation between fapar and ndvi in a semi-arid environment using in situ measurements. *Remote Sensing of Environment*, *91*(3-4), 490–507.

Ferrea, C., Zenone, T., Comolli, R., & Seufert, G. (2012). Estimating heterotrophic and autotrophic soil respiration in a semi-natural forest of lombardy, italy. *Pedobiologia*, *55*(6), 285–294.

Field, C. B., Ball, J. T., & Berry, J. A. (2000). *Photosynthesis: principles and field techniques*, (pp. 209–253). Springer.

Findell, K. L., Gentine, P., Lintner, B. R., & Kerr, C. (2011). Probability of afternoon precipitation in eastern united states and mexico enhanced by high evaporation. *Nature Geoscience*, *4*(7), 434.

Fiora, A., & Cescatti, A. (2006). Diurnal and seasonal variability in radial distribution of sap flux density: implications for estimating stand transpiration. *Tree Physiology*, *26*(9), 1217–1225.

Fischer, E. M., Seneviratne, S. I., Vidale, P. L., Lüthi, D., & Schär, C. (2007a). Soil moisture–atmosphere interactions during the 2003 european summer heat wave. *Journal of Climate*, *20*(20), 5081–5099.

Fischer, M. L., Billesbach, D. P., Berry, J. A., Riley, W. J., & Torn, M. S. (2007b). Spatiotemporal variations in growing season exchanges of co2, h2o, and sensible heat in agricultural fields of the southern great plains. *Earth Interactions*, *11*.

Flexas, J., Briantais, J.-M., Cerovic, Z., Medrano, H., & Moya, I. (2000). Steady-state and maximum chlorophyll fluorescence responses to water stress in grapevine leaves: a new remote sensing system. *Remote Sensing of Environment*, *73*(3), 283–297.

Flexas, J., & Medrano, H. (2002). DroughtâĂŘinhibition of photosynthesis in c3 plants: stomatal and nonâĂŘstomatal limitations revisited. *Annals of Botany*, *89*(2), 183–189.

Forkel, M., Carvalhais, N., Rodenbeck, C., Keeling, R., Heimann, M., Thonicke, K., Zaehle, S., & Reichstein, M. (2016). Enhanced seasonal co2 exchange caused by amplified plant productivity in northern ecosystems. *Science*, *351*(6274), 696–699.

Frank, D., Reichstein, M., Bahn, M., Frank, D., Mahecha, M. D., Smith, P., Thonicke, K., van der Velde, M., Vicca, S., Babst, F., Beer, C., Buchmann, N., Canadell, J. G., Ciais, P., Cramer, W., Ibrom, A., Miglietta, F., Poulter, B., Rammig, A., Seneviratne, S. I., Walz, A., Wattenbach, M., Zavala, M. A., & Zscheischler, J. (2015). Effects of climate extremes on the terrestrial carbon cycle: concepts, processes and potential future impacts. *Global Change Biology*, (pp. n/a–n/a).

Frankenberg, C., Fisher, J. B., Worden, J., Badgley, G., Saatchi, S. S., Lee, J. E., Toon, G. C., Butz, A., Jung, M., Kuze, A., & Yokota, T. (2011). New global observations of the terrestrial carbon cycle from gosat: Patterns of plant fluorescence with gross primary productivity. *Geophysical Research Letters*, *38*(17), L17706.

Frankenberg, C., O'Dell, C., Berry, J., Guanter, L., Joiner, J., Köhler, P., Pollock, R., & Taylor, T. E. (2014). Prospects for chlorophyll fluorescence remote sensing from the orbiting carbon observatory-2. *Remote Sensing of Environment*, *147*, 1–12.

Friedl, M. A., Sulla-Menashe, D., Tan, B., Schneider, A., Ramankutty, N., Sibley, A., & Huang, X. M. (2010). Modis collection 5 global land cover: Algorithm refinements and characterization of new datasets. *Remote Sensing of Environment*, *114*(1), 168–182.

Fritsche, J., Wohlfahrt, G., Ammann, C., Zeeman, M., Hammerle, A., Obrist, D., & Alewell, C. (2008). Summertime elemental mercury exchange of temperate grasslands on an ecosystem-scale. *Atmospheric Chemistry and Physics*, *8*(24), 7709–7722.

Fu, Y. H., Piao, S., Zhao, H., Jeong, S. J., Wang, X., Vitasse, Y., Ciais, P., & Janssens, I. A. (2014). Unexpected role of winter precipitation in determining heat requirement for spring vegetation green-up at northern middle and high latitudes. *Globe Change Biology*, *20*(12), 3743–55.

Fu, Y. H., Zhao, H., Piao, S., Peaucelle, M., Peng, S., Zhou, G., Ciais, P., Huang, M., Menzel, A., Peñuelas, J., Song, Y., Vitasse, Y., Zeng, Z., & Janssens, I. A. (2015). Declining global warming effects on the phenology of spring leaf unfolding. *Nature*, *526*, 104–107.

Galvagno, M., Wohlfahrt, G., Cremonese, E., Rossini, M., Colombo, R., Filippa, G., Julitta, T., Manca, G., Siniscalco, C., di Cella, U. M., & Migliavacca, M. (2013). Phenology and carbon dioxide source/sink strength of a subalpine grassland in response to an exceptionally short snow season. *Environmental Research Letters*, *8*(2).

Gamon, J., Serrano, L., & Surfus, J. (1997). The photochemical reflectance index: an optical indicator of photosynthetic radiation use efficiency across species, functional types, and nutrient levels. *Oecologia*, *112*(4), 492–501.

Gamon, J. A., Huemmrich, K. F., Wong, C. Y., Ensminger, I., Garrity, S., Hollinger, D. Y., Noormets, A., & Penuelas, J. (2016). A remotely sensed pigment index reveals photosynthetic phenology in evergreen conifers. *Proceedings of the National Academy of Sciences of the United States of America*.

Gamon, J. A., Peñuelas, J., & Field, C. B. (1992). A narrow-waveband spectral index that tracks diurnal changes in photosynthetic efficiency. *Remote Sensing of Environment*, *41*(1), 35–44.

Garbulsky, M. F., Penuelas, J., Papale, D., & Filella, I. (2008). Remote estimation of carbon dioxide uptake by a mediterranean forest. *Global Change Biology*, *14*(12), 2860–2867.

Genty, B., Briantais, J.-M., & Baker, N. R. (1989). The relationship between the quantum yield of photosynthetic electron transport and quenching of chlorophyll fluorescence. *Biochimica et Biophysica Acta (BBA)-General Subjects*, *990*(1), 87–92.

Gilmanov, T. G., Verma, S. B., Sims, P. L., Meyers, T. P., Bradford, J. A., Burba, G. G., & Suyker, A. E. (2003). Gross primary production and light response parameters of four southern plains ecosystems estimated using long-term co2-flux tower measurements. *Global Biogeochemical Cycles*, *17*(2).

Gitelson, A. A., Buschmann, C., & Lichtenthaler, H. K. (1999). The chlorophyll fluorescence ratio f 735/f 700 as an accurate measure of the chlorophyll content in plants. *Remote Sensing of Environment*, *69*(3), 296–302.

Gitelson, A. A., & Gamon, J. A. (2015). The need for a common basis for defining light-use efficiency: Implications for productivity estimation. *Remote Sensing of Environment*, *156*, 196–201.

Gitelson, A. A., Peng, Y., Arkebauer, T. J., & Schepers, J. (2014). Relationships between gross primary production, green lai, and canopy chlorophyll content in maize: Implications for remote sensing of primary production. *Remote Sensing of Environment*, *144*, 65–72.

Gitelson, A. A., Viña, A., Verma, S. B., Rundquist, D. C., Arkebauer, T. J., Keydan, G., Leavitt, B., Ciganda, V., Burba, G. G., & Suyker, A. E. (2006). Relationship between gross primary production and chlorophyll content in crops: Implications for the synoptic monitoring of vegetation productivity. *Journal of Geophysical Research*, *111*(D8).

Goldstein, A. H., Hultman, N. E., Fracheboud, J. M., Bauer, M. R., Panek, J. A., Xu, M., Qi, Y., Guenther, A. B., & Baugh, W. (2000). Effects of climate variability on the carbon dioxide, water, and sensible heat fluxes above a ponderosa pine plantation in the sierra nevada (ca). *Agricultural and Forest Meteorology*, *101*(2-3), 113–129.

Gough, C. M., Vogel, C. S., Schmid, H. P., Su, H. B., & Curtis, P. S. (2008). Multi-year convergence of biometric and meteorological estimates of forest carbon storage. *Agricultural and Forest Meteorology*, *148*(2), 158–170.

Goulas, Y., Fournier, A., Daumard, F., Champagne, S., Ounis, A., Marloie, O., & Moya, I. (2017). Gross primary production of a wheat canopy relates stronger to far red than to red solar-induced chlorophyll fluorescence. *Remote Sensing*, *9*(1), 97.

Goulden, M. L., Munger, J. W., Fan, S. M., Daube, B. C., & Wofsy, S. C. (1996). Measurements of carbon sequestration by long-term eddy covariance: Methods and a critical evaluation of accuracy. *Global Change Biology*, *2*(3), 169–182.

Goulden, M. L., Winston, G. C., McMillan, A. M. S., Litvak, M. E., Read, E. L., Rocha, A. V., & Elliot, J. R. (2006). An eddy covariance mesonet to measure the effect of forest age on land-atmosphere exchange. *Global Change Biology*, *12*(11), 2146–2162.

Govindjee, G. (2004). Chlorophyll a fluorescence: a bit of basics and history. *Chlorophyll a fluorescence: a signature of photosynthesis. Springer, Dordrecht*, (pp. 1–42).

Granier, A., Breda, N., Longdoz, B., Gross, P., & Ngao, J. (2008). Ten years of fluxes and stand growth in a young beech forest at hesse, north-eastern france. *Annals of Forest Science*, *65*(7).

Grassi, G., & Magnani, F. (2005). Stomatal, mesophyll conductance and biochemical limitations to photosynthesis as affected by drought and leaf ontogeny in ash and oak trees. *Plant, Cell and Environment*, *28*(7), 834–849.

Graven, H. D., Keeling, R. F., Piper, S. C., Patra, P. K., Stephens, B. B., Wofsy, S. C., Welp, L. R., Sweeney, C., Tans, P. P., Kelley, J. J., Daube, B. C., Kort, E. A., Santoni, G. W., & Bent, J. D. (2013). Enhanced seasonal exchange of co2 by northern ecosystems since 1960. *Science*, *341*(6150), 1085–9.

Gray, J. M., Frolking, S., Kort, E. A., Ray, D. K., Kucharik, C. J., Ramankutty, N., & Friedl, M. A. (2014). Direct human influence on atmospheric co2 seasonality from increased cropland productivity. *Nature*, *515*(7527), 398–401.

Griffis, T. J., Baker, J. M., & Zhang, J. (2005). Seasonal dynamics and partitioning of isotopic co2 exchange in c-3/c-4 managed ecosystem. *Agricultural and Forest Meteorology*, *132*(1-2), 1–19.

Grunwald, T., & Bernhofer, C. (2007). A decade of carbon, water and energy flux measurements of an old spruce forest at the anchor station tharandt. *Tellus Series B-Chemical and Physical Meteorology*, *59*(3), 387–396.

Gu, L., Baldocchi, D., Verma, S. B., Black, T. A., Vesala, T., Falge, E. M., & Dowty, P. R. (2002). Advantages of diffuse radiation for terrestrial ecosystem productivity. *Journal of Geophysical Research: Atmospheres*, *107*(D6), ACL 2–1–ACL 2–23.

Gu, L. H., Meyers, T., Pallardy, S. G., Hanson, P. J., Yang, B., Heuer, M., Hosman, K. P., Riggs, J. S., Sluss, D., & Wullschleger, S. D. (2006). Direct and indirect effects of atmospheric conditions and soil moisture on surface energy partitioning revealed by a prolonged drought at a temperate forest site. *Journal of Geophysical Research-Atmospheres*, *111*(D16).

Gu, Y., Brown, J. F., Verdin, J. P., & Wardlow, B. (2007). A fiveâĂŘyear analysis of modis ndvi and ndwi for grassland drought assessment over the central great plains of the united states. *Geophysical Research Letters*, *34*(6).

Guan, K., Berry, J. A., Zhang, Y., Joiner, J., Guanter, L., Badgley, G., & Lobell, D. B. (2016). Improving the monitoring of crop productivity using spaceborne solar-induced fluorescence. *Globe Change Biology*, *22*(2), 716–726.

Guan, K., Pan, M., Li, H., Wolf, A., Wu, J., Medvigy, D., Caylor, K. K., Sheffield, J., Wood, E. F., Malhi, Y., Liang, M., Kimball, J. S., Saleska, S. R., Berry, J., Joiner, J., & Lyapustin, A. I. (2015). Photosynthetic seasonality of global tropical forests constrained by hydroclimate. *Nature Geoscience*, *8*, 284–289.

Guan, K., Wu, J., Kimball, J. S., Anderson, M. C., Frolking, S., Li, B., Hain, C. R., & Lobell, D. B. (2017). The shared and unique values of optical, fluorescence, thermal and microwave satellite data for estimating large-scale crop yields. *Remote Sensing of Environment*, *199*, 333–349.

Guanter, L., Aben, I., Tol, P., Krijger, J. M., Hollstein, A., Kohler, P., Damm, A., Joiner, J., Frankenberg, C., & Landgraf, J. (2015). Potential of the tropospheric monitoring instrument (tropomi) onboard the sentinel-5 precursor for the monitoring of terrestrial chlorophyll fluorescence. *Atmospheric Measurement Techniques*, *8*(3), 1337–1352.

Guanter, L., Frankenberg, C., Dudhia, A., Lewis, P. E., Gomez-Dans, J., Kuze, A., Suto, H., & Grainger, R. G. (2012). Retrieval and global assessment of terrestrial chlorophyll fluorescence from gosat space measurements. *Remote Sensing of Environment*, *121*, 236–251.

Guanter, L., Rossini, M., Colombo, R., Meroni, M., Frankenberg, C., Lee, J.-E., & Joiner, J. (2013). Using field spectroscopy to assess the potential of statistical approaches for the retrieval of sun-induced chlorophyll fluorescence from ground and space. *Remote Sensing of Environment*, *133*, 52–61.

Guanter, L., Zhang, Y., Jung, M., Joiner, J., Voigt, M., Berry, J. A., Frankenberg, C., Huete, A. R., Zarco-Tejada, P., Lee, J. E., Moran, M. S., Ponce-Campos, G., Beer, C., Camps-Valls, G., Buchmann, N., Gianelle, D., Klumpp, K., Cescatti, A., Baker, J. M., & Griffis, T. J. (2014). Global and time-resolved monitoring of crop photosynthesis with chlorophyll fluorescence. *Proceedings of the National Academy of Sciences of the United States of America*, *111*(14), E1327–33.

Guerschman, J. P., Hill, M. J., Renzullo, L. J., Barrett, D. J., Marks, A. S., & Botha, E. J. (2009). Estimating fractional cover of photosynthetic vegetation, non-photosynthetic vegetation and bare soil in the australian tropical savanna region upscaling the eo-1 hyperion and modis sensors. *Remote Sensing of Environment*, *113*(5), 928–945.

Hagen, S. C., Braswell, B. H., Linder, E., Frolking, S., Richardson, A. D., & Hollinger, D. Y. (2006). Statistical uncertainty of eddy flux-based estimates of gross ecosystem carbon exchange at howland forest, maine. *Journal of Geophysical Research-Atmospheres*, *111*(D8).

Hahn-Schofl, M., Zak, D., Minke, M., Gelbrecht, J., Augustin, J., & Freibauer, A. (2011). Organic sediment formed during inundation of a degraded fen grassland emits large fluxes of ch4 and co2. *Biogeosciences*, *8*(6), 1539–1550.

Harris, I., Jones, P., Osborn, T., & Lister, D. (2014). Updated highâĂŘresolution grids of monthly climatic observations–the cru ts3. 10 dataset. *International Journal of Climatology*, *34*(3), 623–642.

He, H. L., Liu, M., Xiao, X. M., Ren, X. L., Zhang, L., Sun, X. M., Yang, Y. H., Li, Y. N., Zhao, L., Shi, P. L., Du, M. Y., Ma, Y. M., Ma, M. G., Zhang, Y., & Yu, G. R. (2014). Large-scale estimation and uncertainty analysis of gross primary production in

tibetan alpine grasslands. *Journal of Geophysical Research-Biogeosciences, 119*(3), 466–486.

Heinsch, F. A., Heilman, J. L., McInnes, K. J., Cobos, D. R., Zuberer, D. A., & Roelke, D. L. (2004). Carbon dioxide exchange in a high marsh on the texas gulf coast: effects of freshwater availability. *Agricultural and Forest Meteorology*, *125*(1-2), 159–172.

Hetherington, A. M., & Woodward, F. I. (2003). The role of stomata in sensing and driving environmental change. *Nature*, *424*(6951), 901–908.

Hilker, T., Coops, N. C., Wulder, M. A., Black, T. A., & Guy, R. D. (2008). The use of remote sensing in light use efficiency based models of gross primary production: A review of current status and future requirements. *Science of the Total Environment*, *404*(2-3), 411–423.

Hollinger, D. Y., Aber, J., Dail, B., Davidson, E. A., Goltz, S. M., Hughes, H., Leclerc, M. Y., Lee, J. T., Richardson, A. D., Rodrigues, C., Scott, N. A., Achuatavarier, D., & Walsh, J. (2004). Spatial and temporal variability in forest-atmosphere co2 exchange. *Global Change Biology*, *10*(10), 1689–1706.

Hollinger, S. E., Bernacchi, C. J., & Meyers, T. P. (2005). Carbon budget of mature no-till ecosystem in north central region of the united states. *Agricultural and Forest Meteorology*, *130*(1-2), 59–69.

Huang, J., Yu, H., Guan, X., Wang, G., & Guo, R. (2015). Accelerated dryland expansion under climate change. *Nature Climate Change*, *6*(2), 166–171.

Huete, A., Didan, K., Miura, T., Rodriguez, E. P., Gao, X., & Ferreira, L. G. (2002). Overview of the radiometric and biophysical performance of the modis vegetation indices. *Remote Sensing of Environment*, *83*(1), 195–213.

Huete, A. R., Didan, K., Shimabukuro, Y. E., Ratana, P., Saleska, S. R., Hutyra, L. R., Yang, W., Nemani, R. R., & Myneni, R. (2006). Amazon rainforests greenâĂŘup with sunlight in dry season. *Geophysical Research Letters*, *33*(6).

Huntzinger, D. N., Post, W. M., Wei, Y., Michalak, A. M., West, T. O., Jacobson, A. R., Baker, I. T., Chen, J. M., Davis, K. J., Hayes, D. J., Hoffman, F. M., Jain, A. K., Liu, S., McGuire, A. D., Neilson, R. P., Potter, C., Poulter, B., Price, D., Raczka, B. M., Tian, H. Q., Thornton, P., Tomelleri, E., Viovy, N., Xiao, J., Yuan, W., Zeng, N., Zhao, M., & Cook, R. (2012). North american carbon program (nacp) regional interim synthesis: Terrestrial biospheric model intercomparison. *Ecological Modelling*, *232*, 144–157.

Hussain, M. Z., Grunwald, T., Tenhunen, J. D., Li, Y. L., Mirzae, H., Bernhofer, C., Otieno, D., Dinh, N. Q., Schmidt, M., Wartinger, M., & Owen, K. (2011). Summer drought influence on co2 and water fluxes of extensively managed grassland in germany. *Agriculture Ecosystems Environment*, *141*(1-2), 67–76.

Huxman, T. E., Smith, M. D., Fay, P. A., Knapp, A. K., Shaw, M. R., Loik, M. E., Smith, S. D., Tissue, D. T., Zak, J. C., Weltzin, J. F., Pockman, W. T., Sala, O. E., Haddad, B. M., Harte, J., Koch, G. W., Schwinning, S., Small, E. E., & Williams, D. G. (2004). Convergence across biomes to a common rain-use efficiency. *Nature*, *429*(6992), 651–654.

Illston, B. G., Basara, J. B., Fiebrich, C. A., Crawford, K. C., Hunt, E., Fisher, D. K., Elliott, R., & Humes, K. (2008). Mesoscale monitoring of soil moisture across a statewide network. *Journal of Atmospheric and Oceanic Technology*, *25*(2), 167–182.

IPCC (2013). The physical science basis. contribution of working group i to the fifth assessment report of the intergovernmental panel on climate change. *K., Tignor, M., Allen, SK, Boschung, J., Nauels, A., Xia, Y., Bex, V., Midgley, PM, Eds*, (p. 1535).

Ito, A. (2008). The regional carbon budget of east asia simulated with a terrestrial ecosystem model and validated using asiaflux data. *Agricultural and Forest Meteorology*, *148*(5), 738–747.

Janssens, I. A., Kowalski, A. S., & Ceulemans, R. (2001). Forest floor co2 fluxes estimated by eddy covariance and chamber-based model. *Agricultural and Forest Meteorology*, *106*(1), 61–69.

Jenkins, J. P., Richardson, A. D., Braswell, B. H., Ollinger, S. V., Hollinger, D. Y., & Smith, M. L. (2007). Refining light-use efficiency calculations for a deciduous forest canopy using simultaneous tower-based carbon flux and radiometric measurements. *Agricultural and Forest Meteorology*, *143*(1-2), 64–79.

Jeong, S.-J., Schimel, D., Frankenberg, C., Drewry, D. T., Fisher, J. B., Verma, M., Berry, J. A., Lee, J.-E., & Joiner, J. (2017). Application of satellite solar-induced chlorophyll fluorescence to understanding large-scale variations in vegetation phenology and function over northern high latitude forests. *Remote Sensing of Environment*, *190*, 178–187.

Ji, L., & Peters, A. J. (2003). Assessing vegetation response to drought in the northern great plains using vegetation and drought indices. *Remote Sensing of Environment*, *87*(1), 85–98.

Jin, C., Xiao, X., Wagle, P., Griffis, T., Dong, J., Wu, C., Qin, Y., & Cook, D. R. (2015). Effects of in-situ and reanalysis climate data on estimation of cropland gross primary production using the vegetation photosynthesis model. *Agricultural and Forest Meteorology*, *213*, 240–250.

Jin, C., Xiao, X. M., Merbold, L., Arneth, A., Veenendaal, E., & Kutsch, W. L. (2013). Phenology and gross primary production of two dominant savanna woodland ecosystems in southern africa. *Remote Sensing of Environment*, *135*, 189–201.

Joiner, J., Guanter, L., Lindstrot, R., Voigt, M., Vasilkov, A. P., Middleton, E. M., Huemmrich, K. F., Yoshida, Y., & Frankenberg, C. (2013). Global monitoring of terrestrial chlorophyll fluorescence from moderate-spectral-resolution near-infrared satellite measurements: methodology, simulations, and application to gome-2. *Atmospheric Measurement Techniques*, *6*(10), 2803–2823.

Joiner, J., Yoshida, Y., Guanter, L., & Middleton, E. (2016). New methods for retrieval of chlorophyll red fluorescence from hyper-spectral satellite instruments: simulations and application to gome-2 and sciamachy. *Atmospheric Measurement Techniques*, *9*, 3939–3967.

Joiner, J., Yoshida, Y., Vasilkov, A. P., Middleton, E. M., Campbell, P. K. E., Yoshida, Y., Kuze, A., & Corp, L. A. (2012). Filling-in of near-infrared solar lines by terrestrial fluorescence and other geophysical effects: simulations and space-based observations from sciamachy and gosat. *Atmospheric Measurement Techniques*, *5*(4), 809–829.

Joiner, J., Yoshida, Y., Vasilkov, A. P., Schaefer, K., Jung, M., Guanter, L., Zhang, Y., Garrity, S., Middleton, E. M., Huemmrich, K. F., Gu, L., & Belelli Marchesini, L. (2014). The seasonal cycle of satellite chlorophyll fluorescence observations and its relationship to vegetation phenology and ecosystem atmosphere carbon exchange. *Remote Sensing of Environment*, *152*, 375–391.

Jung, M., Reichstein, M., & Bondeau, A. (2009). Towards global empirical upscaling of fluxnet eddy covariance observations: validation of a model tree ensemble approach using a biosphere model. *Biogeosciences*, *6*(10), 2001–2013.

Jung, M., Reichstein, M., Margolis, H. A., Cescatti, A., Richardson, A. D., Arain, M. A., Arneth, A., Bernhofer, C., Bonal, D., Chen, J. Q., Gianelle, D., Gobron, N., Kiely, G., Kutsch, W., Lasslop, G., Law, B. E., Lindroth, A., Merbold, L., Montagnani, L., Moors, E. J., Papale, D., Sottocornola, M., Vaccari, F., & Williams, C. (2011). Global patterns of land-atmosphere fluxes of carbon dioxide, latent heat, and sensible heat derived from eddy covariance, satellite, and meteorological observations. *Journal of Geophysical Research-Biogeosciences*, *116*.

Jung, M., Reichstein, M., Schwalm, C. R., Huntingford, C., Sitch, S., Ahlstrom, A., Arneth, A., Camps-Valls, G., Ciais, P., Friedlingstein, P., Gans, F., Ichii, K., Jain, A. K., Kato, E., Papale, D., Poulter, B., Raduly, B., Rodenbeck, C., Tramontana, G., Viovy, N., Wang, Y. P., Weber, U., Zaehle, S., & Zeng, N. (2017). Compensatory water effects link yearly global land co2 sink changes to temperature. *Nature*, *541*, 516–520.

Kalfas, J. L., Xiao, X., Vanegas, D. X., Verma, S. B., & Suyker, A. E. (2011). Modeling gross primary production of irrigated and rain-fed maize using modis imagery and co2 flux tower data. *Agricultural and Forest Meteorology*, *151*(12), 1514–1528.

Kato, E., Kinoshita, T., Ito, A., Kawamiya, M., & Yamagata, Y. (2013). Evaluation of spatially explicit emission scenario of land-use change and biomass burning using a process-based biogeochemical model. *Journal of Land Use Science*, *8*(1), 104–122.

Kato, T., Tang, Y. H., Gu, S., Hirota, M., Du, M. Y., Li, Y. N., & Zhao, X. Q. (2006). Temperature and biomass influences on interannual changes in co2 exchange in an alpine meadow on the qinghai-tibetan plateau. *Global Change Biology*, *12*(7), 1285–1298.

Kattge, J., Knorr, W., Raddatz, T., & Wirth, C. (2009). Quantifying photosynthetic capacity and its relationship to leaf nitrogen content for global-scale terrestrial biosphere models. *Global Change Biology*, *15*(4), 976–991.

Keeling, C. D., Chin, J. F. S., & Whorf, T. P. (1996). Increased activity of northern vegetation inferred from atmospheric co2 measurements. *Nature*, *382*(6587), 146–149.

Keenan, T. F., Baker, I., Barr, A., Ciais, P., Davis, K., Dietze, M., Dragoni, D., Gough, C. M., Grant, R., Hollinger, D., Hufkens, K., Poulter, B., McCaughey, H., Raczka, B., Ryu, Y., Schaefer, K., Tian, H., Verbeeck, H., Zhao, M., & Richardson, A. D. (2012). Terrestrial biosphere model performance for inter-annual variability of land-atmosphere co2 exchange. *Global Change Biology*, *18*(6), 1971–1987.

Keenan, T. F., Hollinger, D. Y., Bohrer, G., Dragoni, D., Munger, J. W., Schmid, H. P., & Richardson, A. D. (2013). Increase in forest water-use efficiency as atmospheric carbon dioxide concentrations rise. *Nature*, *499*(7458), 324–7.

Keenan, T. F., Prentice, I. C., Canadell, J. G., Williams, C. A., Wang, H., Raupach, M., & Collatz, G. J. (2016). Recent pause in the growth rate of atmospheric co2 due to enhanced terrestrial carbon uptake. *Nature Communications*, *7*, 13428.

Knapp, A. K., & Smith, M. D. (2001). Variation among biomes in temporal dynamics of aboveground primary production. *Science*, *291*(5503), 481–484.

Koffi, E. N., Rayner, P. J., Norton, A. J., Frankenberg, C., & Scholze, M. (2015). Investigating the usefulness of satellite-derived fluorescence data in inferring gross primary productivity within the carbon cycle data assimilation system. *Biogeosciences*, *12*(13), 4067–4084.

Köhler, P., Guanter, L., & Joiner, J. (2015). A linear method for the retrieval of sun-induced chlorophyll fluorescence from gome-2 and sciamachy data. *Atmospheric Measurement Techniques*, *8*(6), 2589–2608.

Kooten, O., & Snel, J. F. (1990). The use of chlorophyll fluorescence nomenclature in plant stress physiology. *Photosynthesis Research*, *25*(3), 147–150.

Koster, R. D., & Suarez, M. J. (1999). A simple framework for examining the interannual variability of land surface moisture fluxes. *Journal of Climate*, *12*(7), 1911–1917.

Kraft, S., Bézy, J., Del Bello, U., Berlich, R., Drusch, M., Franco, R., Gabriele, A., Harnisch, B., Meynart, R., & Silvestrin, P. (2013). Floris: Phase a status of the fluorescence imaging spectrometer of the earth explorer mission candidate flex. In *Proc. SPIE*, vol. 8889, (p. 88890T).

Krause, G., & Weis, E. (1991). Chlorophyll fluorescence and photosynthesis: the basics. *Annual review of plant biology*, *42*(1), 313–349.

Krinner, G., Viovy, N., de Noblet-Ducoudre, N., Ogee, J., Polcher, J., Friedlingstein, P., Ciais, P., Sitch, S., & Prentice, I. C. (2005). A dynamic global vegetation model for studies of the coupled atmosphere-biosphere system. *Global Biogeochemical Cycles*, *19*(1).

Kross, A., Seaquist, J. W., & Roulet, N. T. (2016). Light use efficiency of peatlands: Variability and suitability for modeling ecosystem production. *Remote Sensing of Environment*, *183*, 239–249.

Kurbatova, J., Li, C., Varlagin, A., Xiao, X., & Vygodskaya, N. (2008). Modeling carbon dynamics in two adjacent spruce forests with different soil conditions in russia. *Biogeosciences*, *5*(4), 969–980.

Kutzbach, L., Wille, C., & Pfeiffer, E. M. (2007). The exchange of carbon dioxide between wet arctic tundra and the atmosphere at the lena river delta, northern siberia. *Biogeosciences*, *4*(5), 869–890.

Lasslop, G., Reichstein, M., Papale, D., Richardson, A. D., Arneth, A., Barr, A., Stoy, P., & Wohlfahrt, G. (2010). Separation of net ecosystem exchange into assimilation and respiration using a light response curve approach: critical issues and global evaluation. *Global Change Biology*, *16*(1), 187–208.

Law, B. E., Turner, D., Campbell, J., Sun, O. J., Van Tuyl, S., Ritts, W. D., & Cohen, W. B. (2004). Disturbance and climate effects on carbon stocks and fluxes across western oregon usa. *Global Change Biology*, *10*(9), 1429–1444.

Law, B. E., Williams, M., Anthoni, P. M., Baldocchi, D. D., & Unsworth, M. H. (2000). Measuring and modelling seasonal variation of carbon dioxide and water vapour exchange of a pinus ponderosa forest subject to soil water deficit. *Global Change Biology*, *6*(6), 613–630.

Le Quéré, C., Andrew, R. M., Canadell, J. G., Sitch, S., Korsbakken, J. I., Peters, G. P., Manning, A. C., Boden, T. A., Tans, P. P., Houghton, R. A., Keeling, R. F., Alin, S., Andrews, O. D., Anthoni, P., Barbero, L., Bopp, L., Chevallier, F., Chini, L. P., Ciais, P., Currie, K., Delire, C., Doney, S. C., Friedlingstein, P., Gkritzalis, T., Harris, I., Hauck, J., Haverd, V., Hoppema, M., Klein Goldewijk, K., Jain, A. K., Kato, E., Körtzinger, A., Landschützer, P., Lefèvre, N., Lenton, A., Lienert, S., Lombardozzi, D., Melton, J. R., Metzl, N., Millero, F., Monteiro, P. M. S., Munro, D. R., Nabel, J. E. M. S., Nakaoka, S.-i., amp, apos, Brien, K., Olsen, A., Omar, A. M., Ono, T., Pierrot, D., Poulter, B., Rödenbeck, C., Salisbury, J., Schuster, U., Schwinger, J., Séférian, R., Skjelvan, I., Stocker, B. D., Sutton, A. J., Takahashi, T., Tian, H., Tilbrook, B., van der Laan-Luijkx, I. T., van der Werf, G. R., Viovy, N., Walker, A. P., Wiltshire, A. J., & Zaehle, S. (2016). Global carbon budget 2016. *Earth System Science Data*, *8*(2), 605–649.

Le Quéré, C., Moriarty, R., Andrew, R. M., Canadell, J. G., Sitch, S., Korsbakken, J. I., Friedlingstein, P., Peters, G. P., Andres, R. J., Boden, T. A., Houghton, R. A., House, J. I., Keeling, R. F., Tans, P., Arneth, A., Bakker, D. C. E., Barbero, L., Bopp, L., Chang, J., Chevallier, F., Chini, L. P., Ciais, P., Fader, M., Feely, R. A., Gkritzalis, T., Harris, I., Hauck, J., Ilyina, T., Jain, A. K., Kato, E., Kitidis, V., Klein Goldewijk, K., Koven, C., Landschützer, P., Lauvset, S. K., Lefèvre, N., Lenton, A., Lima, I. D., Metzl, N., Millero, F., Munro, D. R., Murata, A., Nabel, J. E. M. S., Nakaoka, S., Nojiri, Y., O'Brien, K., Olsen, A., Ono, T., Pérez, F. F., Pfeil, B., Pierrot, D., Poulter, B., Rehder, G., Rödenbeck, C., Saito, S., Schuster, U., Schwinger, J., Séférian, R., Steinhoff, T., Stocker, B. D., Sutton, A. J., Takahashi, T., Tilbrook, B., van der Laan-Luijkx, I. T., van der Werf, G. R., van Heuven, S., Vandemark, D., Viovy, N., Wiltshire, A., Zaehle, S., & Zeng, N. (2015). Global carbon budget 2015. *Earth System Science Data*, *7*(2), 349–396.

Lee, J. E., Berry, J. A., van der Tol, C., Yang, X., Guanter, L., Damm, A., Baker, I., & Frankenberg, C. (2015). Simulations of chlorophyll fluorescence incorporated into the community land model version 4. *Globe Change Biology*, *21*, 3469–3477.

Leuning, R., Cleugh, H. A., Zegelin, S. J., & Hughes, D. (2005). Carbon and water fluxes over a temperate eucalyptus forest and a tropical wet/dry savanna in

australia: measurements and comparison with modis remote sensing estimates. *Agricultural and Forest Meteorology*, *129*(3-4), 151–173.

Lhomme, J. P., Rocheteau, A., Ourcival, J. M., & Rambal, S. (2001). Non-steady-state modelling of water transfer in a mediterranean evergreen canopy. *Agricultural and Forest Meteorology*, *108*(1), 67–83.

Li, D., Pan, M., Cong, Z., Zhang, L., & Wood, E. (2013). Vegetation control on water and energy balance within the budyko framework. *Water Resources Research*, *49*(2), 969–976.

Li, X., Zhu, Z., Zeng, H., & Piao, S. (2016). Estimation of gross primary production in china (1982–2010) with multiple ecosystem models. *Ecological Modelling*, *324*, 33–44.

Lichtenthaler, H. K., & Rinderle, U. (1988). The role of chlorophyll fluorescence in the detection of stress conditions in plants. *CRC Critical Reviews in Analytical Chemistry*, *19*(sup1), S29–S85.

Lin, X., Chen, B., Chen, J., Zhang, H., Sun, S., Xu, G., Guo, L., Ge, M., Qu, J., Li, L., & Kong, Y. (2017). Seasonal fluctuations of photosynthetic parameters for light use efficiency models and the impacts on gross primary production estimation. *Agricultural and Forest Meteorology*, *236*, 22–35.

Lin, Y.-S., Medlyn, B. E., Duursma, R. A., Prentice, I. C., Wang, H., Baig, S., Eamus, D., de Dios, V. R., Mitchell, P., Ellsworth, D. S., de Beeck, M. O., Wallin, G., Uddling, J., Tarvainen, L., Linderson, M.-L., Cernusak, L. A., Nippert, J. B., Ocheltree, T. W., Tissue, D. T., Martin-StPaul, N. K., Rogers, A., Warren, J. M., De Angelis, P., Hikosaka, K., Han, Q., Onoda, Y., Gimeno, T. E., Barton, C. V. M., Bennie, J., Bonal, D., Bosc, A., Löw, M., Macinins-Ng, C., Rey, A., Rowland, L., Setterfield, S. A., Tausz-Posch, S., Zaragoza-Castells, J., Broadmeadow, M. S. J., Drake, J. E., Freeman, M., Ghannoum, O., Hutley, L. B., Kelly, J. W., Kikuzawa, K., Kolari, P., Koyama, K., Limousin, J.-M., Meir, P., Lola da Costa, A. C., Mikkelsen, T. N., Salinas, N., Sun, W., & Wingate, L. (2015). Optimal stomatal behaviour around the world. *Nature Climate Change*.

Lindauer, M., Schmid, H. P., Grote, R., Mauder, M., Steinbrecher, R., & Wolpert, B. (2014). Net ecosystem exchange over a non-cleared wind-throw-disturbed upland spruce forest-measurements and simulations. *Agricultural and Forest Meteorology*, *197*, 219–234.

Liu, L., Guan, L., & Liu, X. (2017a). Directly estimating diurnal changes in gpp for c3 and c4 crops using far-red sun-induced chlorophyll fluorescence. *Agricultural and Forest Meteorology*, *232*, 1–9.

Liu, L., Liu, X., Hu, J., & Guan, L. (2017b). Assessing the wavelength-dependent ability of solar-induced chlorophyll fluorescence to estimate the gpp of winter wheat at the canopy level. *International Journal of Remote Sensing*, *38*(15), 4396–4417.

Liu, Y. Y., van Dijk, A. I. J. M., de Jeu, R. A. M., Canadell, J. G., McCabe, M. F., Evans, J. P., & Wang, G. (2015). Recent reversal in loss of global terrestrial biomass. *Nature Climate Change*.

Liu, Y. Y., van Dijk, A. I. J. M., McCabe, M. F., Evans, J. P., & de Jeu, R. A. M. (2013). Global vegetation biomass change (1988-2008) and attribution to environmental and human drivers. *Global Ecology and Biogeography*, *22*(6), 692–705.

Lohila, A., Aurela, M., Tuovinen, J. P., & Laurila, T. (2004). Annual co2 exchange of a peat field growing spring barley or perennial forage grass. *Journal of Geophysical Research-Atmospheres*, *109*(D18).

Los, S. O., North, P. R. J., Grey, W. M. F., & Barnsley, M. J. (2005). A method to convert avhrr normalized difference vegetation index time series to a standard viewing and illumination geometry. *Remote Sensing of Environment*, *99*(4), 400–411.

Loubet, B., Laville, P., Lehuger, S., Larmanou, E., Flechard, C., Mascher, N., Genermont, S., Roche, R., Ferrara, R. M., Stella, P., Personne, E., Durand, B., Decuq, C., Flura, D., Masson, S., Fanucci, O., Rampon, J. N., Siemens, J., Kindler, R., Gabrielle, B., Schrumpf, M., & Cellier, P. (2011). Carbon, nitrogen and greenhouse gases budgets over a four years crop rotation in northern france. *Plant and Soil*, *343*(1-2), 109–137.

Lund, M., Falk, J. M., Friborg, T., Mbufong, H. N., Sigsgaard, C., Soegaard, H., & Tamstorf, M. P. (2012). Trends in co2 exchange in a high arctic tundra heath, 2000-2010. *Journal of Geophysical Research-Biogeosciences*, *117*.

Luo, Y., Ogle, K., Tucker, C., Fei, S., Gao, C., LaDeau, S., Clark, J. S., & Schimel, D. S. (2011). Ecological forecasting and data assimilation in a dataâĂŘrich era. *Ecological Applications*, *21*(5), 1429–1442.

Luo, Y. Q., Randerson, J. T., Abramowitz, G., Bacour, C., Blyth, E., Carvalhais, N., Ciais, P., Dalmonech, D., Fisher, J. B., Fisher, R., Friedlingstein, P., Hibbard, K., Hoffman, F., Huntzinger, D., Jones, C. D., Koven, C., Lawrence, D., Li, D. J., Mahecha, M., Niu, S. L., Norby, R., Piao, S. L., Qi, X., Peylin, P., Prentice, I. C., Riley, W., Reichstein, M., Schwalm, C., Wang, Y. P., Xia, J. Y., Zaehle, S., & Zhou, X. H. (2012). A framework for benchmarking land models. *Biogeosciences*, *9*(10), 3857–3874.

Luo, Y. Q., Wan, S. Q., Hui, D. F., & Wallace, L. L. (2001). Acclimatization of soil respiration to warming in a tall grass prairie. *Nature*, *413*(6856), 622–625.

Lyapustin, A. I., Wang, Y., Laszlo, I., Hilker, T., Hall, F. G., Sellers, P. J., Tucker, C. J., & Korkin, S. V. (2012). Multi-angle implementation of atmospheric correction for modis (maiac): 3. atmospheric correction. *Remote Sensing of Environment*, *127*, 385–393.

Ma, S. Y., Baldocchi, D. D., Xu, L. K., & Hehn, T. (2007). Inter-annual variability in carbon dioxide exchange of an oak/grass savanna and open grassland in california. *Agricultural and Forest Meteorology*, *147*(3-4), 157–171.

Ma, X., Huete, A., Yu, Q., Restrepo-Coupe, N., Beringer, J., Hutley, L. B., Kanniah, K. D., Cleverly, J., & Eamus, D. (2014). Parameterization of an ecosystem light-use-efficiency model for predicting savanna gpp using modis evi. *Remote Sensing of Environment*, *154*, 253–271.

Mahadevan, P., Wofsy, S. C., Matross, D. M., Xiao, X. M., Dunn, A. L., Lin, J. C., Gerbig, C., Munger, J. W., Chow, V. Y., & Gottlieb, E. W. (2008). A satellite-based biosphere parameterization for net ecosystem co2 exchange: Vegetation photosynthesis and respiration model (vprm). *Global Biogeochemical Cycles*, *22*(2).

Mao, J., Ribes, A., Yan, B., Shi, X., Thornton, P. E., Seferian, R., Ciais, P., Myneni, R. B., Douville, H., Piao, S., Zhu, Z., Dickinson, R. E., Dai, Y., Ricciuto, D. M., Jin, M., Hoffman, F. M., Wang, B., Huang, M., & Lian, X. (2016). Human-induced greening of the northern extratropical land surface. *Nature Climate Change*, *6*(10), 959–963.

Marcolla, B., Cescatti, A., Manca, G., Zorer, R., Cavagna, M., Fiora, A., Gianelle, D., Rodeghiero, M., Sottocornola, M., & Zampedri, R. (2011). Climatic controls and ecosystem responses drive the inter-annual variability of the net ecosystem exchange of an alpine meadow. *Agricultural and Forest Meteorology*, *151*(9), 1233–1243.

Marcolla, B., Cescatti, A., Montagnani, L., Manca, G., Kerschbaumer, G., & Minerbi, S. (2005). Importance of advection in the atmospheric co2 exchanges of an alpine forest. *Agricultural and Forest Meteorology*, *130*(3-4), 193–206.

Marek, M. V., Janous, D., Taufarova, K., Havrankova, K., Pavelka, M., Kaplan, V., & Markova, I. (2011). Carbon exchange between ecosystems and atmosphere in the czech republic is affected by climate factors. *Environmental Pollution*, *159*(5), 1035–1039.

Martinez-Vilalta, J., & Garcia-Forner, N. (2017). Water potential regulation, stomatal behaviour and hydraulic transport under drought: deconstructing the iso/anisohydric concept. *Plant Cell and Environment*, *40*(6), 962–976.

Matamala, R., Jastrow, J. D., Miller, R. M., & Garten, C. T. (2008). Temporal changes in c and n stocks of restored prairie: Implications for c sequestration strategies. *Ecological Applications*, *18*(6), 1470–1488.

McCallum, I., Wagner, W., Schmullius, C., Shvidenko, A., Obersteiner, M., Fritz, S., & Nilsson, S. (2009). Satellite-based terrestrial production efficiency modeling. *Carbon Balance and Management*, *4*(1), 8.

McCaughey, J. H., Pejam, M. R., Arain, M. A., & Cameron, D. A. (2006). Carbon dioxide and energy fluxes from a boreal mixedwood forest ecosystem in ontario, canada. *Agricultural and Forest Meteorology*, *140*(1-4), 79–96.

McGuire, A. D., Melillo, J., Joyce, L., Kicklighter, D., Grace, A., Moore, B., & Vorosmarty, C. (1992). Interactions between carbon and nitrogen dynamics in estimating net primary productivity for potential vegetation in north america. *Global Biogeochemical Cycles*, *6*(2), 101–124.

Merbold, L., Eugster, W., Stieger, J., Zahniser, M., Nelson, D., & Buchmann, N. (2014). Greenhouse gas budget (co2, ch4 and n2o) of intensively managed grassland following restoration. *Global Change Biology*, *20*(6), 1913–1928.

Merbold, L., Ziegler, W., Mukelabai, M. M., & Kutsch, W. L. (2011). Spatial and temporal variation of co2 efflux along a disturbance gradient in a miombo woodland in western zambia. *Biogeosciences*, *8*(1), 147–164.

Mercado, L. M., Bellouin, N., Sitch, S., Boucher, O., Huntingford, C., Wild, M., & Cox, P. M. (2009). Impact of changes in diffuse radiation on the global land carbon sink. *Nature*, *458*(7241), 1014–1017.

Meroni, M., Rossini, M., Guanter, L., Alonso, L., Rascher, U., Colombo, R., & Moreno, J. (2009). Remote sensing of solar-induced chlorophyll fluorescence: Review of methods and applications. *Remote Sensing of Environment*, *113*(10), 2037–2051.

Mesinger, F., DiMego, G., Kalnay, E., Mitchell, K., Shafran, P. C., Ebisuzaki, W., Jovic, D., Woollen, J., Rogers, E., Berbery, E. H., Ek, M. B., Fan, Y., Grumbine, R., Higgins, W., Li, H., Lin, Y., Manikin, G., Parrish, D., & Shi, W. (2006). North american regional reanalysis. *Bulletin of the American Meteorological Society*, *87*(3), 343–+.

Middleton, N., & Thomas, D. (1997). *World atlas of desertification*. Arnold, Hodder Headline, PLC.

Migliavacca, M., Meroni, M., Manca, G., Matteucci, G., Montagnani, L., Grassi, G., Zenone, T., Teobaldelli, M., Goded, I., Colombo, R., & Seufert, G. (2009). Seasonal and interannual patterns of carbon and water fluxes of a poplar plantation under peculiar eco-climatic conditions. *Agricultural and Forest Meteorology*, *149*(9), 1460–1476.

Migliavacca, M., Reichstein, M., Richardson, A. D., Mahecha, M. D., Cremonese, E., Delpierre, N., Galvagno, M., Law, B. E., Wohlfahrt, G., Andrew Black, T., Carvalhais, N., Ceccherini, G., Chen, J., Gobron, N., Koffi, E., William Munger, J., Perez-Priego, O., Robustelli, M., Tomelleri, E., & Cescatti, A. (2015). Influence of physiological phenology on the seasonal pattern of ecosystem respiration in deciduous forests. *Globe Change Biology*, *21*(1), 363–76.

Misson, L., Tang, J. W., Xu, M., McKay, M., & Goldstein, A. (2005). Influences of recovery from clear-cut, climate variability, and thinning on the carbon balance of a young ponderosa pine plantation. *Agricultural and Forest Meteorology*, *130*(3-4), 207–222.

Monteith, J. L. (1972). Solar-radiation and productivity in tropical ecosystems. *Journal of Applied Ecology*, *9*(3), 747–766.

Morton, D. C., Nagol, J., Carabajal, C. C., Rosette, J., Palace, M., Cook, B. D., Vermote, E. F., Harding, D. J., & North, P. R. J. (2014). Amazon forests maintain consistent canopy structure and greenness during the dry season. *Nature*, *506*(7487), 221–224.

Moureaux, C., Debacq, A., Bodson, B., Heinesch, B., & Aubinet, M. (2006). Annual net ecosystem carbon exchange by a sugar beet crop. *Agricultural and Forest Meteorology*, *139*(1-2), 25–39.

Mu, Q., Heinsch, F. A., Zhao, M., & Running, S. W. (2007). Development of a global evapotranspiration algorithm based on modis and global meteorology data. *Remote Sensing of Environment*, *111*(4), 519–536.

Mu, Q. Z., Zhao, M. S., & Running, S. W. (2011). Improvements to a modis global terrestrial evapotranspiration algorithm. *Remote Sensing of Environment*, *115*(8), 1781–1800.

Mund, M., Kutsch, W. L., Wirth, C., Kahl, T., Knohl, A., Skomarkova, M. V., & Schulze, E. D. (2010). The influence of climate and fructification on the inter-annual variability of stem growth and net primary productivity in an old-growth, mixed beech forest. *Tree Physiology*, *30*(6), 689–704.

Myneni, R. B., Hoffman, S., Knyazikhin, Y., Privette, J. L., Glassy, J., Tian, Y., Wang, Y., Song, X., Zhang, Y., Smith, G. R., Lotsch, A., Friedl, M., Morisette, J. T., Votava, P., Nemani, R. R., & Running, S. W. (2002). Global products of vegetation leaf area and fraction absorbed par from year one of modis data. *Remote Sensing of Environment*, *83*(1-2), 214–231.

Myneni, R. B., Yang, W., Nemani, R. R., Huete, A. R., Dickinson, R. E., Knyazikhin, Y., Didan, K., Fu, R., Juárez, N., & Robinson, I. (2007). Large seasonal swings in leaf

area of amazon rainforests. *Proceedings of the National Academy of Sciences of the United States of America*.

Nagy, Z., Czobel, S., Balogh, J., Horvath, L., Foti, S., Pinter, K., Weidinger, T., Csintalan, Z., & Tuba, Z. (2005). Some preliminary results of the hungarian grassland ecological research: Carbon cycling and greenhouse gas balances under changing. *Cereal Research Communications*, *33*(1), 279–281.

Nave, L. E., Gough, C. M., Maurer, K. D., Bohrer, G., Hardiman, B. S., Le Moine, J., Munoz, A. B., Nadelhoffer, K. J., Sparks, J. P., Strahm, B. D., Vogel, C. S., & Curtis, P. S. (2011). Disturbance and the resilience of coupled carbon and nitrogen cycling in a north temperate forest. *Journal of Geophysical Research-Biogeosciences*, *116*.

Noormets, A., Gavazzi, M. J., Mcnulty, S. G., Domec, J. C., Sun, G., King, J. S., & Chen, J. Q. (2010). Response of carbon fluxes to drought in a coastal plain loblolly pine forest. *Global Change Biology*, *16*(1), 272–287.

Noormets, A., McNulty, S. G., DeForest, J. L., Sun, G., Li, Q., & Chen, J. (2008). Drought during canopy development has lasting effect on annual carbon balance in a deciduous temperate forest. *New Phytologist*, *179*(3), 818–828.

Nouvellon, Y., Begue, A., Moran, M. S., Lo Seen, D., Rambal, S., Luquet, D., Chehbouni, G., & Inoue, Y. (2000). Par extinction in shortgrass ecosystems: effects of clumping, sky conditions and soil albedo. *Agricultural and Forest Meteorology*, *105*(1-3), 21–41.

Novick, K. A., Miniat, C. F., & Vose, J. M. (2016). Drought limitations to leaf-level gas exchange: results from a model linking stomatal optimization and cohesion-tension theory. *Plant Cell and Environment*, *39*(3), 583–596.

Oleson, K., Lawrence, D., Bonan, G., Drewniak, B., Huang, M., Koven, C., Levis, S., Li, F., Riley, W., & Subin, Z. (2013). Technical description of version 4.5 of the community land model (clm). ncar tech. Report, Note NCAR/TN-503+ STR. National Center for Atmospheric Research, Boulder, CO, 422 pp. doi: 10.5065/D6RR1W7M.

Ollinger, S. V., Richardson, A. D., Martin, M. E., Hollinger, D. Y., Frolking, S. E., Reich, P. B., Plourde, L. C., Katul, G. G., Munger, J. W., Oren, R., Smithb, M. L., U, K. T. P., Bolstad, P. V., Cook, B. D., Day, M. C., Martin, T. A., Monson, R. K., & Schmid, H. P. (2008). Canopy nitrogen, carbon assimilation, and albedo in temperate and boreal forests: Functional relations and potential climate feedbacks. *Proceedings of the National Academy of Sciences of the United States of America*, *105*(49), 19336–19341.

Oren, R., Sperry, J. S., Katul, G. G., Pataki, D. E., Ewers, B. E., Phillips, N., & Schafer, K. V. R. (1999). Survey and synthesis of intra- and interspecific variation in stomatal sensitivity to vapour pressure deficit. *Plant Cell and Environment*, *22*(12), 1515–1526.

Parazoo, N. C., Bowman, K., Fisher, J. B., Frankenberg, C., Jones, D. B., Cescatti, A., Perez-Priego, O., Wohlfahrt, G., & Montagnani, L. (2014). Terrestrial gross primary production inferred from satellite fluorescence and vegetation models. *Globe Change Biology*, *20*(10), 3103–21.

Peng, C., Ma, Z., Lei, X., Zhu, Q., Chen, H., Wang, W., Liu, S., Li, W., Fang, X., & Zhou, X. (2011a). A drought-induced pervasive increase in tree mortality across canada's boreal forests. *Nature Climate Change*, *1*(9), 467–471.

Peng, C. H., Guiot, J., Wu, H. B., Jiang, H., & Luo, Y. Q. (2011b). Integrating models with data in ecology and palaeoecology: advances towards a model-data fusion approach. *Ecology Letters*, *14*(5), 522–536.

Piao, S., Fang, J., Zhou, L., Ciais, P., & Zhu, B. (2006). Variations in satellite-derived phenology in china's temperate vegetation. *Global Change Biology*, *12*(4), 672–685.

Piao, S., Friedlingstein, P., Ciais, P., Viovy, N., & Demarty, J. (2007). Growing season extension and its impact on terrestrial carbon cycle in the northern hemisphere over the past 2 decades. *Global Biogeochemical Cycles*, *21*(3), n/a–n/a.

Piao, S., Sitch, S., Ciais, P., Friedlingstein, P., Peylin, P., Wang, X., Ahlstrom, A., Anav, A., Canadell, J. G., Cong, N., Huntingford, C., Jung, M., Levis, S., Levy, P. E., Li, J., Lin, X., Lomas, M. R., Lu, M., Luo, Y., Ma, Y., Myneni, R. B., Poulter, B., Sun, Z., Wang, T., Viovy, N., Zaehle, S., & Zeng, N. (2013). Evaluation of terrestrial carbon cycle models for their response to climate variability and to co2 trends. *Globe Change Biology*, *19*(7), 2117–32.

Pilegaard, K., Hummelshoj, P., Jensen, N. O., & Chen, Z. (2001). Two years of continuous co2 eddy-flux measurements over a danish beech forest. *Agricultural and Forest Meteorology*, *107*(1), 29–41.

Porcar-Castell, A., Bäck, J., Juurola, E., & Hari, P. (2006). Dynamics of the energy flow through photosystem ii under changing light conditions: a model approach. *Functional Plant Biology*, *33*(3), 229–239.

Porcar-Castell, A., Tyystjarvi, E., Atherton, J., van der Tol, C., Flexas, J., Pfundel, E. E., Moreno, J., Frankenberg, C., & Berry, J. A. (2014). Linking chlorophyll a fluorescence to photosynthesis for remote sensing applications: mechanisms and challenges. *Journal of Experimental Botany*, *65*(15), 4065–4095.

Potter, C. S., Randerson, J. T., Field, C. B., Matson, P. A., Vitousek, P. M., Mooney, H. A., & Klooster, S. A. (1993). Terrestrial ecosystem production - a process model-based on global satellite and surface data. *Global Biogeochemical Cycles*, *7*(4), 811–841.

Poulter, B., Frank, D., Ciais, P., Myneni, R. B., Andela, N., Bi, J., Broquet, G., Canadell, J. G., Chevallier, F., Liu, Y. Y., Running, S. W., Sitch, S., & van der Werf, G. R. (2014). Contribution of semi-arid ecosystems to interannual variability of the global carbon cycle. *Nature*, *509*(7502), 600–3.

Prentice, I., Kelley, D., Foster, P., Friedlingstein, P., Harrison, S., & Bartlein, P. (2011). Modeling fire and the terrestrial carbon balance. *Global Biogeochemical Cycles*, *25*(3).

Prescher, A.-K., Grünwald, T., & Bernhofer, C. (2010). Land use regulates carbon budgets in eastern germany: from nee to nbp. *Agricultural and Forest Meteorology*, *150*(7), 1016–1025.

Prince, S. D., & Goward, S. N. (1995). Global primary production: a remote sensing approach. *Journal of Biogeography*, (pp. 815–835).

Raddatz, T., Reick, C., Knorr, W., Kattge, J., Roeckner, E., Schnur, R., Schnitzler, K.-G., Wetzel, P., & Jungclaus, J. (2007). Will the tropical land biosphere dominate the climate–carbon cycle feedback during the twenty-first century? *Climate Dynamics*, *29*(6), 565–574.

Raich, J., Rastetter, E., Melillo, J., Kicklighter, D., Steudler, P., Peterson, B., Grace, A., Moore Iii, B., & Vorosmarty, C. (1991). Potential net primary productivity in south america: application of a global model. *Ecological Applications*, *1*(4), 399–429.

Rayner, P., Scholze, M., Knorr, W., Kaminski, T., Giering, R., & Widmann, H. (2005). Two decades of terrestrial carbon fluxes from a carbon cycle data assimilation system (ccdas). *Global Biogeochemical Cycles*, *19*(2).

Reichstein, M., Bahn, M., Ciais, P., Frank, D., Mahecha, M. D., Seneviratne, S. I., Zscheischler, J., Beer, C., Buchmann, N., Frank, D. C., Papale, D., Rammig, A., Smith, P., Thonicke, K., van der Velde, M., Vicca, S., Walz, A., & Wattenbach, M. (2013). Climate extremes and the carbon cycle. *Nature*, *500*(7462), 287–95.

Reichstein, M., Ciais, P., Papale, D., Valentini, R., Running, S., Viovy, N., Cramer, W., Granier, A., Ogee, J., Allard, V., Aubinet, M., Bernhofer, C., Buchmann, N., Carrara, A., Grunwald, T., Heimann, M., Heinesch, B., Knohl, A., Kutsch, W., Loustau, D., Manca, G., Matteucci, G., Miglietta, F., Ourcival, J. M., Pilegaard, K., Pumpanen, J., Rambal, S., Schaphoff, S., Seufert, G., Soussana, J. F., Sanz, M. J., Vesala, T., & Zhao, M. (2007). Reduction of ecosystem productivity and respiration during the

european summer 2003 climate anomaly: a joint flux tower, remote sensing and modelling analysis. *Global Change Biology*, *13*(3), 634–651.

Reichstein, M., Falge, E., Baldocchi, D., Papale, D., Aubinet, M., Berbigier, P., Bernhofer, C., Buchmann, N., Gilmanov, T., Granier, A., Grunwald, T., Havrankova, K., Ilvesniemi, H., Janous, D., Knohl, A., Laurila, T., Lohila, A., Loustau, D., Matteucci, G., Meyers, T., Miglietta, F., Ourcival, J.-M., Pumpanen, J., Rambal, S., Rotenberg, E., Sanz, M., Tenhunen, J., Seufert, G., Vaccari, F., Vesala, T., Yakir, D., & Valentini, R. (2005). On the separation of net ecosystem exchange into assimilation and ecosystem respiration: review and improved algorithm. *Global Change Biology*, *11*(9), 1424–1439.

Reichstein, M., Stoy, P. C., Desai, A. R., Lasslop, G., & Richardson, A. D. (2012). *Partitioning of net fluxes*, (pp. 263–289). Springer.

Reichstein, M., Tenhunen, J. D., Roupsard, O., Ourcival, J., Rambal, S., Miglietta, F., Peressotti, A., Pecchiari, M., Tirone, G., & Valentini, R. (2002). Severe drought effects on ecosystem co2 and h2o fluxes at three mediterranean evergreen sites: revision of current hypotheses? *Global Change Biology*, *8*(10), 999–1017.

Reverter, B. R., Sanchez-Canete, E. P., Resco, V., Serrano-Ortiz, P., Oyonarte, C., & Kowalski, A. S. (2010). Analyzing the major drivers of nee in a mediterranean alpine shrubland. *Biogeosciences*, *7*(9), 2601–2611.

Rey, A., Pegoraro, E., Tedeschi, V., De Parri, I., Jarvis, P. G., & Valentini, R. (2002). Annual variation in soil respiration and its components in a coppice oak forest in central italy. *Global Change Biology*, *8*(9), 851–866.

Rossini, M., Cogliati, S., Meroni, M., Migliavacca, M., Galvagno, M., Busetto, L., Cremonese, E., Julitta, T., Siniscalco, C., di Cella, U. M., & Colombo, R. (2012). Remote sensing-based estimation of gross primary production in a subalpine grassland. *Biogeosciences*, *9*(7), 2565–2584.

Rossini, M., Nedbal, L., Guanter, L., Ač, A., Alonso, L., Burkart, A., Cogliati, S., Colombo, R., Damm, A., Drusch, M., Hanus, J., Janoutova, R., Julitta, T., Kokkalis, P., Moreno, J., Novotny, J., Panigada, C., Pinto, F., Schickling, A., Schüttemeyer, D., Zemek, F., & Rascher, U. (2015). Red and far-red sun-induced chlorophyll fluorescence as a measure of plant photosynthesis. *Geophysical Research Letters*, (pp. n/a–n/a).

Ruehr, N. K., Martin, J. G., & Law, B. E. (2012). Effects of water availability on carbon and water exchange in a young ponderosa pine forest: Above- and belowground responses. *Agricultural and Forest Meteorology*, *164*, 136–148.

Running, S. W., Nemani, R. R., Heinsch, F. A., Zhao, M. S., Reeves, M., & Hashimoto, H. (2004). A continuous satellite-derived measure of global terrestrial primary production. *BioScience*, *54*(6), 547–560.

Ryu, Y., Baldocchi, D. D., Black, T. A., Detto, M., Law, B. E., Leuning, R., Miyata, A., Reichstein, M., Vargas, R., Ammann, C., Beringer, J., Flanagan, L. B., Gu, L. H., Hutley, L. B., Kim, J., McCaughey, H., Moors, E. J., Rambal, S., & Vesala, T. (2012). On the temporal upscaling of evapotranspiration from instantaneous remote sensing measurements to 8-day mean daily-sums. *Agricultural and Forest Meteorology*, *152*, 212–222.

Saatchi, S., Asefi-Najafabady, S., Malhi, Y., Aragão, L. E., Anderson, L. O., Myneni, R. B., & Nemani, R. (2013). Persistent effects of a severe drought on amazonian forest canopy. *Proceedings of the National Academy of Sciences of the United States of America*, *110*(2), 565–570.

Sabbatini, S., Arriga, N., Bertolini, T., Castaldi, S., Chiti, T., Consalvo, C., Njakou Djomo, S., Gioli, B., Matteucci, G., & Papale, D. (2016). Greenhouse gas balance of cropland conversion to bioenergy poplar short-rotation coppice. *Biogeosciences*, *13*(1), 95–113.

Saleska, S. R., Didan, K., Huete, A. R., & Da Rocha, H. R. (2007). Amazon forests green-up during 2005 drought. *Science*, *318*(5850), 612–612.

Sanz, M., Carrara, A., Gimeno, C., Bucher, A., & Lopez, R. (2004). Effects of a dry and warm summer conditions on co2 and energy fluxes from three mediterranean ecosystems. In *Geophys. Res. Abstr*, vol. 6, (p. 3239).

Schaefer, K., Schwalm, C. R., Williams, C., Arain, M. A., Barr, A., Chen, J. M., Davis, K. J., Dimitrov, D., Hilton, T. W., Hollinger, D. Y., Humphreys, E., Poulter, B., Raczka, B. M., Richardson, A. D., Sahoo, A., Thornton, P., Vargas, R., Verbeeck, H., Anderson, R., Baker, I., Black, T. A., Bolstad, P., Chen, J., Curtis, P. S., Desai, A. R., Dietze, M., Dragoni, D., Gough, C., Grant, R. F., Gu, L., Jain, A., Kucharik, C., Law, B., Liu, S., Lokipitiya, E., Margolis, H. A., Matamala, R., McCaughey, J. H., Monson, R., Munger, J. W., Oechel, W., Peng, C., Price, D. T., Ricciuto, D., Riley, W. J., Roulet, N., Tian, H., Tonitto, C., Torn, M., Weng, E., & Zhou, X. (2012). A model-data comparison of gross primary productivity: Results from the north american carbon program site synthesis. *Journal of Geophysical Research*, *117*(G3).

Schar, C., Vidale, P. L., Luthi, D., Frei, C., Haberli, C., Liniger, M. A., & Appenzeller, C. (2004). The role of increasing temperature variability in european summer heatwaves. *Nature*, *427*(6972), 332–336.

Schimel, D., Pavlick, R., Fisher, J. B., Asner, G. P., Saatchi, S., Townsend, P., Miller, C., Frankenberg, C., Hibbard, K., & Cox, P. (2015). Observing terrestrial ecosystems and the carbon cycle from space. *Global Change Biology*, *21*, 1762–1776.

Schmid, H. P., Grimmond, C. S. B., Cropley, F., Offerle, B., & Su, H. B. (2000). Measurements of co2 and energy fluxes over a mixed hardwood forest in the mid-western united states. *Agricultural and Forest Meteorology*, *103*(4), 357–374.

Schneider, J., Fisher, D., Elliott, R., Brown, G., & Bahrmann, C. (2003). Spatiotemporal variations in soil water: First results from the arm sgp cart network. *Journal of Hydrometeorology*, *4*(1), 106–120.

Schneider, U., Becker, A., Finger, P., Meyer-Christoffer, A., Rudolf, B., & Ziese, M. (2011). Gpcc full data reanalysis version 6.0 at 0.5: monthly land-surface precipitation from rain-gauges built on gts-based and historic data. doi: 10.5676/dwd$_g pcc. FD_{MV} 6_0 50$.

Schreiber, U., Bilger, W., & Neubauer, C. (1995). *Chlorophyll fluorescence as a nonintrusive indicator for rapid assessment of in vivo photosynthesis*, (pp. 49–70). Springer.

Scott, R. L., Hamerlynck, E. P., Jenerette, G. D., Moran, M. S., & Barron-Gafford, G. A. (2010). Carbon dioxide exchange in a semidesert grassland through drought-induced vegetation change. *Journal of Geophysical Research-Biogeosciences*, *115*.

Scott, R. L., Huxman, T. E., Cable, W. L., & Emmerich, W. E. (2006). Partitioning of evapotranspiration and its relation to carbon dioxide exchange in a chihuahuan desert shrubland. *Hydrological Processes*, *20*(15), 3227–3243.

Scott, R. L., Jenerette, G. D., Potts, D. L., & Huxman, T. E. (2009). Effects of seasonal drought on net carbon dioxide exchange from a woody-plant-encroached semiarid grassland. *Journal of Geophysical Research-Biogeosciences*, *114*.

Serrano-Ortiz, P., Kowalski, A. S., Domingo, F., Rey, A., Pegoraro, E., Villagarcia, L., & Alados-Arboledas, L. (2007). Variations in daytime net carbon and water exchange in a montane shrubland ecosystem in southeast spain. *Photosynthetica*, *45*(1), 30–35.

Shao, C. L., Chen, J. Q., & Li, L. H. (2013). Grazing alters the biophysical regulation of carbon fluxes in a desert steppe. *Environmental Research Letters*, *8*(2).

Shi, H., Li, L., Eamus, D., Huete, A., Cleverly, J., Tian, X., Yu, Q., Wang, S., Montagnani, L., Magliulo, V., Rotenberg, E., Pavelka, M., & Carrara, A. (2017). Assessing the ability of modis evi to estimate terrestrial ecosystem gross primary production of multiple land cover types. *Ecological Indicators*, *72*, 153–164.

Sims, D., Rahman, A., Cordova, V., Elmasri, B., Baldocchi, D., Bolstad, P., Flanagan, L., Goldstein, A., Hollinger, D., & Misson, L. (2008). A new model of gross primary productivity for north american ecosystems based solely on the enhanced vegetation index and land surface temperature from modis. *Remote Sensing of Environment*, *112*(4), 1633–1646.

Sims, D. A., Brzostek, E. R., Rahman, A. F., Dragoni, D., & Phillips, R. P. (2014). An improved approach for remotely sensing water stress impacts on forest c uptake. *Globe Change Biology*, *20*(9), 2856–66.

Sims, D. A., & Gamon, J. A. (2002). Relationships between leaf pigment content and spectral reflectance across a wide range of species, leaf structures and developmental stages. *Remote Sensing of Environment*, *81*(2), 337–354.

Sims, D. A., Rahman, A. F., Cordova, V. D., Baldocchi, D. D., Flanagan, L. B., Goldstein, A. H., Hollinger, D. Y., Misson, L., Monson, R. K., Schmid, H. P., Wofsy, S. C., & Xu, L. K. (2005). Midday values of gross co2 flux and light use efficiency during satellite overpasses can be used to directly estimate eight-day mean flux. *Agricultural and Forest Meteorology*, *131*(1-2), 1–12.

Sims, D. A., Rahman, A. F., Cordova, V. D., El-Masri, B. Z., Baldocchi, D. D., Flanagan, L. B., Goldstein, A. H., Hollinger, D. Y., Misson, L., Monson, R. K., Oechel, W. C., Schmid, H. P., Wofsy, S. C., & Xu, L. K. (2006). On the use of modis evi to assess gross primary productivity of north american ecosystems. *Journal of Geophysical Research-Biogeosciences*, *111*(G4).

Sitch, S., Friedlingstein, P., Gruber, N., Jones, S. D., Murray-Tortarolo, G., Ahlström, A., Doney, S. C., Graven, H., Heinze, C., Huntingford, C., Levis, S., Levy, P. E., Lomas, M., Poulter, B., Viovy, N., Zaehle, S., Zeng, N., Arneth, A., Bonan, G., Bopp, L., Canadell, J. G., Chevallier, F., Ciais, P., Ellis, R., Gloor, M., Peylin, P., Piao, S. L., Le Quéré, C., Smith, B., Zhu, Z., & Myneni, R. (2015). Recent trends and drivers of regional sources and sinks of carbon dioxide. *Biogeosciences*, *12*(3), 653–679.

Sitch, S., Huntingford, C., Gedney, N., Levy, P. E., Lomas, M., Piao, S. L., Betts, R., Ciais, P., Cox, P., Friedlingstein, P., Jones, C. D., Prentice, I. C., & Woodward, F. I. (2008). Evaluation of the terrestrial carbon cycle, future plant geography and climate-carbon cycle feedbacks using five dynamic global vegetation models (dgvms). *Global Change Biology*, *14*(9), 2015–2039.

Sitch, S., Smith, B., Prentice, I. C., Arneth, A., Bondeau, A., Cramer, W., Kaplan, J. O., Levis, S., Lucht, W., Sykes, M. T., Thonicke, K., & Venevsky, S. (2003). Evaluation of ecosystem dynamics, plant geography and terrestrial carbon cycling in the lpj dynamic global vegetation model. *Global Change Biology*, *9*(2), 161–185.

Smith, B., Prentice, I. C., & Sykes, M. T. (2001). Representation of vegetation dynamics in the modelling of terrestrial ecosystems: comparing two contrasting approaches within european climate space. *Global Ecology and Biogeography*, *10*(6), 621–637.

Song, C. H., Dannenberg, M. P., & Hwang, T. (2013). Optical remote sensing of terrestrial ecosystem primary productivity. *Progress in Physical Geography*, *37*(6), 834–854.

Soukupová, J., Cséfalvay, L., Urban, O., Košvancová, M., Marek, M., Rascher, U., & Nedbal, L. (2008). Annual variation of the steady-state chlorophyll fluorescence emission of evergreen plants in temperate zone. *Functional Plant Biology*, *35*(1), 63–76.

Spinoni, J., Vogt, J., Naumann, G., Carrao, H., & Barbosa, P. (2015). Towards identifying areas at climatological risk of desertification using the köppen-geiger classification and fao aridity index. *International Journal of Climatology*, *35*(9), 2210–2222.

Steininger, M. K. (2004). Net carbon fluxes from forest clearance and regrowth in the amazon. *Ecological Applications*, *14*(4), S313–S322.

Sulman, B. N., Desai, A. R., Cook, B. D., Saliendra, N., & Mackay, D. S. (2009). Contrasting carbon dioxide fluxes between a drying shrub wetland in northern wisconsin, usa, and nearby forests. *Biogeosciences*, *6*(6), 1115–1126.

Sun, G., Alstad, K., Chen, J. Q., Chen, S. P., Ford, C. R., Lin, G. H., Liu, C. F., Lu, N., McNulty, S. G., Miao, H. X., Noormets, A., Vose, J. M., Wilske, B., Zeppel, M., Zhang, Y., & Zhang, Z. Q. (2011). A general predictive model for estimating monthly ecosystem evapotranspiration. *Ecohydrology*, *4*(2), 245–255.

Sun, G., Noormets, A., Chen, J., & McNulty, S. G. (2008). Evapotranspiration estimates from eddy covariance towers and hydrologic modeling in managed forests in northern wisconsin, usa. *Agricultural and Forest Meteorology*, *148*(2), 257–267.

Sun, Y., Fu, R., Dickinson, R., Joiner, J., Frankenberg, C., Gu, L., Xia, Y., & Fernando, N. (2015). Drought onset mechanisms revealed by satellite solar-induced chlorophyll fluorescence: Insights from two contrasting extreme events. *Journal of Geophysical Research: Biogeosciences*, *120*(11), 2427–2440.

Sun, Y., Piao, S., Huang, M., Ciais, P., Zeng, Z., Cheng, L., Li, X., Zhang, X., Mao, J., Peng, S., Poulter, B., Shi, X., Wang, X., Wang, Y.-P., & Zeng, H. (2016). Global patterns and climate drivers of water-use efficiency in terrestrial ecosystems deduced from satellite-based datasets and carbon cycle models. *Global Ecology and Biogeography*, *25*(3), 311–323.

Suni, T., Rinne, J., Reissell, A., Altimir, N., Keronen, P., Rannik, U., Dal Maso, M., Kulmala, M., & Vesala, T. (2003). Long-term measurements of surface fluxes above a scots pine forest in hyytiala, southern finland, 1996-2001. *Boreal Environment Research*, *8*(4), 287–301.

Suyker, A. E., Verma, S. B., Burba, G. G., & Arkebauer, T. J. (2005). Gross primary production and ecosystem respiration of irrigated maize and irrigated soybean during a growing season. *Agricultural and Forest Meteorology*, *131*(3-4), 180–190.

Suyker, A. E., Verma, S. B., Burba, G. G., Arkebauer, T. J., Walters, D. T., & Hubbard, K. G. (2004). Growing season carbon dioxide exchange in irrigated and rainfed maize. *Agricultural and Forest Meteorology*, *124*(1-2), 1–13.

Tedeschi, V., Rey, A., Manca, G., Valentini, R., Jarvis, P. G., & Borghetti, M. (2006). Soil respiration in a mediterranean oak forest at different developmental stages after coppicing. *Global Change Biology*, *12*(1), 110–121.

Teuling, A. J., Seneviratne, S. I., Stöckli, R., Reichstein, M., Moors, E., Ciais, P., Luyssaert, S., van den Hurk, B., Ammann, C., Bernhofer, C., Dellwik, E., Gianelle, D., Gielen, B., Grünwald, T., Klumpp, K., Montagnani, L., Moureaux, C., Sottocornola, M., & Wohlfahrt, G. (2010). Contrasting response of european forest and grassland energy exchange to heatwaves. *Nature Geoscience*, *3*(10), 722–727.

Tramontana, G., Jung, M., Schwalm, C. R., Ichii, K., Camps-Valls, G., Raduly, B., Reichstein, M., Arain, M. A., Cescatti, A., Kiely, G., Merbold, L., Serrano-Ortiz, P., Sickert, S., Wolf, S., & Papale, D. (2016). Predicting carbon dioxide and energy fluxes across global fluxnet sites with regression algorithms. *Biogeosciences*, *13*(14), 4291–4313.

Trenberth, K. E., Dai, A., van der Schrier, G., Jones, P. D., Barichivich, J., Briffa, K. R., & Sheffield, J. (2013). Global warming and changes in drought. *Nature Climate Change*, *4*(1), 17–22.

Turner, D., Ritts, W., Styles, J., Yang, Z., Cohen, W., Law, B., & Thornton, P. (2006). A diagnostic carbon flux model to monitor the effects of disturbance and interannual variation in climate on regional nep. *Tellus B*, *58*(5), 476–490.

Urbanski, S., Barford, C., Wofsy, S., Kucharik, C., Pyle, E., Budney, J., McKain, K., Fitzjarrald, D., Czikowsky, M., & Munger, J. W. (2007). Factors controlling co2 exchange on timescales from hourly to decadal at harvard forest. *Journal of Geophysical Research-Biogeosciences*, *112*(G2).

Vaccari, F. P., Lugato, E., Gioli, B., D'Acqui, L., Genesio, L., Toscano, P., Matese, A., & Miglietta, F. (2012). Land use change and soil organic carbon dynamics in mediterranean agro-ecosystems: The case study of pianosa island. *Geoderma*, *175*, 29–36.

van der Molen, M. K., Dolman, A. J., Ciais, P., Eglin, T., Gobron, N., Law, B. E., Meir, P., Peters, W., Phillips, O. L., Reichstein, M., Chen, T., Dekker, S. C., Doubková, M., Friedl, M. A., Jung, M., van den Hurk, B. J. J. M., de Jeu, R. A. M., Kruijt, B., Ohta, T., Rebel, K. T., Plummer, S., Seneviratne, S. I., Sitch, S., Teuling, A. J., van der Werf, G. R., & Wang, G. (2011). Drought and ecosystem carbon cycling. *Agricultural and Forest Meteorology*, *151*(7), 765–773.

van der Tol, C., Berry, J. A., Campbell, P. K. E., & Rascher, U. (2014). Models of fluorescence and photosynthesis for interpreting measurements of solar-induced chlorophyll fluorescence. *Journal of Geophysical Research-Biogeosciences*, *119*(12), 2312–2327.

van der Tol, C., Verhoef, W., Timmermans, J., Verhoef, A., & Su, Z. (2009). An integrated model of soil-canopy spectral radiances, photosynthesis, fluorescence, temperature and energy balance. *Biogeosciences*, *6*(12), 3109–3129.

van Huissteden, J., Maximov, T. C., & Dolman, A. J. (2005). High methane flux from an arctic floodplain (indigirka lowlands, eastern siberia). *Journal of Geophysical Research-Biogeosciences*, *110*(G2).

Van Wittenberghe, S., Alonso, L., Verrelst, J., Moreno, J., & Samson, R. (2015). Bidirectional sun-induced chlorophyll fluorescence emission is influenced by leaf structure and light scattering properties — a bottom-up approach. *Remote Sensing of Environment*, *158*, 169–179.

Vanderhoof, M., Williams, C., Pasay, M., & Ghimire, B. (2013). Controls on the rate of co2 emission from woody debris in clearcut and coniferous forest environments. *Biogeochemistry*, *114*(1-3), 299–311.

Vankooten, O., & Snel, J. F. H. (1990). The use of chlorophyll fluorescence nomenclature in plant stress physiology. *Photosynthesis Research*, *25*(3), 147–150.

Verhoef, W. (1984). Light-scattering by leaf layers with application to canopy reflectance modeling - the sail model. *Remote Sensing of Environment*, *16*(2), 125–141.

Verhoef, W., & Bach, H. (2007). Coupled soil–leaf-canopy and atmosphere radiative transfer modeling to simulate hyperspectral multi-angular surface reflectance and toa radiance data. *Remote Sensing of Environment*, *109*(2), 166–182.

Verma, M., Friedl, M. A., Law, B. E., Bonal, D., Kiely, G., Black, T. A., Wohlfahrt, G., Moors, E. J., Montagnani, L., Marcolla, B., Toscano, P., Varlagin, A., Roupsard, O., Cescatti, A., Arain, M. A., & D'Odorico, P. (2015). Improving the performance of remote sensing models for capturing intra- and inter-annual variations in daily gpp: An analysis using global fluxnet tower data. *Agricultural and Forest Meteorology*, *214-215*, 416–429.

Verma, M., Friedl, M. A., Richardson, A. D., Kiely, G., Cescatti, A., Law, B. E., Wohlfahrt, G., Gielen, B., Roupsard, O., Moors, E. J., Toscano, P., Vaccari, F. P., Gianelle, D., Bohrer, G., Varlagin, A., Buchmann, N., van Gorsel, E., Montagnani, L., & Propastin, P. (2014). Remote sensing of annual terrestrial gross primary productivity from modis: an assessment using the fluxnet la thuile data set. *Biogeosciences*, *11*(8), 2185–2200.

Vermote, E., & Vermeulen, A. (1999). Atmospheric correction algorithm: spectral reflectances (mod09). *ATBD version, 4*.

Verrelst, J., Rivera, J. P., van der Tol, C., Magnani, F., Mohammed, G., & Moreno, J. (2015). Global sensitivity analysis of the scope model: What drives simulated canopy-leaving sun-induced fluorescence? *Remote Sensing of Environment*, *166*, 8–21.

Verrelst, J., van der Tol, C., Magnani, F., Sabater, N., Rivera, J. P., Mohammed, G., & Moreno, J. (2016). Evaluating the predictive power of sun-induced chlorophyll fluorescence to estimate net photosynthesis of vegetation canopies: A scope modeling study. *Remote Sensing of Environment*, *176*, 139–151.

Vetter, M., Churkina, G., Jung, M., Reichstein, M., Zaehle, S., Bondeau, A., Chen, Y., Ciais, P., Feser, F., Freibauer, A., Geyer, R., Jones, C., Papale, D., Tenhunen, J., Tomelleri, E., Trusilova, K., Viovy, N., & Heimann, M. (2008). Analyzing the causes and spatial pattern of the european 2003 carbon flux anomaly using seven models. *Biogeosciences*, *5*(2), 561–583.

Viovy, N., Arino, O., & Belward, A. (1992). The best index slope extraction (bise): A method for reducing noise in ndvi time-series. *International Journal of Remote Sensing*, *13*(8), 1585–1590.

Vuolo, F., Dash, J., Curran, P. J., Lajas, D., & Kwiatkowska, E. (2012). Methodologies and uncertainties in the use of the terrestrial chlorophyll index for the sentinel-3 mission. *Remote Sensing*, *4*(5), 1112–1133.

Wagle, P., Xiao, X., & Suyker, A. E. (2015). Estimation and analysis of gross primary production of soybean under various management practices and drought conditions. *ISPRS Journal of Photogrammetry and Remote Sensing*, *99*, 70–83.

Wagle, P., Xiao, X., Torn, M. S., Cook, D. R., Matamala, R., Fischer, M. L., Jin, C., Dong, J., & Biradar, C. (2014). Sensitivity of vegetation indices and gross primary production of tallgrass prairie to severe drought. *Remote Sensing of Environment*, *152*, 1–14.

Wagle, P., Zhang, Y., Jin, C., & Xiao, X. (2016). Comparison of solar-induced chlorophyll fluorescence, light-use efficiency, and process-based gpp models in maize. *Ecological Applications*, *26*(4), 1211–1222.

Walther, S., Voigt, M., Thum, T., Gonsamo, A., Zhang, Y., Koehler, P., Jung, M., Varlagin, A., & Guanter, L. (2016). Satellite chlorophyll fluorescence measurements reveal large-scale decoupling of photosynthesis and greenness dynamics in boreal evergreen forests. *Globe Change Biology*, *22*(9), 2979–2996.

Wan, Z., Wang, P., & Li, X. (2004). Using modis land surface temperature and normalized difference vegetation index products for monitoring drought in the southern great plains, usa. *International Journal of Remote Sensing*, *25*(1), 61–72.

Wang, C. K., Bond-Lamberty, B., & Gower, S. T. (2002). Environmental controls on carbon dioxide flux from black spruce coarse woody debris. *Oecologia*, *132*(3), 374–381.

Wang, L., Zhu, H., Lin, A., Zou, L., Qin, W., & Du, Q. (2017). Evaluation of the latest modis gpp products across multiple biomes using global eddy covariance flux data. *Remote Sensing*, *9*(5), 418.

Wang, X., Piao, S., Xu, X., Ciais, P., MacBean, N., Myneni, R. B., & Li, L. (2015). Has the advancing onset of spring vegetation green-up slowed down or changed abruptly over the last three decades? *Global Ecology and Biogeography*, (pp. n/a–n/a).

Westergaard-Nielsen, A., Lund, M., Hansen, B. U., & Tamstorf, M. P. (2013). Camera derived vegetation greenness index as proxy for gross primary production in a low arctic wetland area. *ISPRS Journal of Photogrammetry and Remote Sensing*, *86*, 89–99.

Wicke, W., & Bernhofer, C. (1996). Energy balance comparison of the hartheim forest and an adjacent grassland site during the hartx experiment. *Theoretical and applied climatology*, *53*(1-3), 49–58.

Williams, C. A., Hanan, N., Scholes, R. J., & Kutsch, W. (2009). Complexity in water and carbon dioxide fluxes following rain pulses in an african savanna. *Oecologia*, *161*(3), 469–480.

Wilson, T. B., & Meyers, T. P. (2007). Determining vegetation indices from solar and photosynthetically active radiation fluxes. *Agricultural and Forest Meteorology*, *144*(3-4), 160–179.

Wohlfahrt, G., & Gu, L. (2015). The many meanings of gross photosynthesis and their implication for photosynthesis research from leaf to globe. *Plant Cell and Environment*, *38*(12), 2500–7.

Wohlfahrt, G., Hammerle, A., Haslwanter, A., Bahn, M., Tappeiner, U., & Cernusca, A. (2008). Seasonal and inter-annual variability of the net ecosystem co2 exchange of a temperate mountain grassland: Effects of weather and management. *Journal of Geophysical Research-Atmospheres*, *113*(D8).

Wolf, S., Eugster, W., Potvin, C., & Buchmann, N. (2011). Strong seasonal variations in net ecosystem co 2 exchange of a tropical pasture and afforestation in panama. *Agricultural and Forest Meteorology*, *151*(8), 1139–1151.

Wright, J. S., Fu, R., Worden, J. R., Chakraborty, S., Clinton, N. E., Risi, C., Sun, Y., & Yin, L. (2017). Rainforest-initiated wet season onset over the southern amazon. *Proceedings of the National Academy of Sciences of the United States of America*.

Wu, C., & Chen, J. M. (2013). Deriving a new phenological indicator of interannual net carbon exchange in contrasting boreal deciduous and evergreen forests. *Ecological Indicators*, *24*, 113–119.

Wu, C. Y., Munger, J. W., Niu, Z., & Kuang, D. (2010a). Comparison of multiple models for estimating gross primary production using modis and eddy covariance data in harvard forest. *Remote Sensing of Environment*, *114*(12), 2925–2939.

Wu, C. Y., Niu, Z., & Gao, S. A. (2010b). Gross primary production estimation from modis data with vegetation index and photosynthetically active radiation in maize. *Journal of Geophysical Research-Atmospheres*, *115*.

Wu, J., Albert, L. P., Lopes, A. P., Restrepo-Coupe, N., Hayek, M., Wiedemann, K. T., Guan, K., Stark, S. C., Christoffersen, B., & Prohaska, N. (2016). Leaf development and demography explain photosynthetic seasonality in amazon evergreen forests. *Science*, *351*(6276), 972–976.

Wu, J., Serbin, S. P., Xu, X., Albert, L. P., Chen, M., Meng, R., Saleska, S. R., & Rogers, A. (2017). The phenology of leaf quality and its withinâĂŘcanopy variation are essential for accurate modeling of photosynthesis in tropical evergreen forests. *Global Change Biology*.

Wu, X., & Liu, H. (2013). Consistent shifts in spring vegetation green-up date across temperate biomes in china, 1982-2006. *Globe Change Biology*, *19*(3), 870–80.

Wullschleger, S. D. (1993). Biochemical limitations to carbon assimilation in c3 plants—a retrospective analysis of the a/ci curves from 109 species. *Journal of Experimental Botany*, *44*(5), 907–920.

Xia, J., Chen, J., Piao, S., Ciais, P., Luo, Y., & Wan, S. (2014). Terrestrial carbon cycle affected by non-uniform climate warming. *Nature Geoscience*, *7*(3), 173–180.

Xiao, J., Zhuang, Q., Law, B. E., Chen, J., Baldocchi, D. D., Cook, D. R., Oren, R., Richardson, A. D., Wharton, S., & Ma, S. (2010). A continuous measure of gross primary production for the conterminous united states derived from modis and ameriflux data. *Remote Sensing of Environment*, *114*(3), 576–591.

Xiao, J. F., Ollinger, S. V., Frolking, S., Hurtt, G. C., Hollinger, D. Y., Davis, K. J., Pan, Y. D., Zhang, X. Y., Deng, F., Chen, J. Q., Baldocchi, D. D., Law, B. E., Arain, M. A., Desai, A. R., Richardson, A. D., Sun, G., Amiro, B., Margolis, H., Gu, L. H., Scott, R. L., Blanken, P. D., & Suyker, A. E. (2014). Data-driven diagnostics of terrestrial carbon dynamics over north america. *Agricultural and Forest Meteorology*, *197*, 142–157.

Xiao, X., Boles, S., Frolking, S., Salas, W., Moore, B., Li, C., He, L., & Zhao, R. (2002). Observation of flooding and rice transplanting of paddy rice fields at the site to landscape scales in china using vegetation sensor data. *International Journal of Remote Sensing*, *23*(15), 3009–3022.

Xiao, X., Hagen, S., Zhang, Q., Keller, M., & Moore, B. (2006). Detecting leaf phenology of seasonally moist tropical forests in south america with multi-temporal modis images. *Remote Sensing of Environment*, *103*(4), 465–473.

Xiao, X., Hollinger, D., Aber, J., Goltz, M., Davidson, E. A., Zhang, Q., & Moore, B. (2004a). Satellite-based modeling of gross primary production in an evergreen needleleaf forest. *Remote Sensing of Environment*, *89*(4), 519–534.

Xiao, X., Zhang, Q., Braswell, B., Urbanski, S., Boles, S., Wofsy, S., Moore, B., & Ojima, D. (2004b). Modeling gross primary production of temperate deciduous broadleaf forest using satellite images and climate data. *Remote Sensing of Environment*, *91*(2), 256–270.

Xiao, X. M., Zhang, Q. Y., Hollinger, D., Aber, J., & Moore, B. (2005a). Modeling gross primary production of an evergreen needleleaf forest using modis and climate data. *Ecological Applications*, *15*(3), 954–969.

Xiao, X. M., Zhang, Q. Y., Saleska, S., Hutyra, L., De Camargo, P., Wofsy, S., Frolking, S., Boles, S., Keller, M., & Moore, B. (2005b). Satellite-based modeling of gross primary production in a seasonally moist tropical evergreen forest. *Remote Sensing of Environment*, *94*(1), 105–122.

Xu, L., & Baldocchi, D. D. (2003). Seasonal trends in photosynthetic parameters and stomatal conductance of blue oak (quercus douglasii) under prolonged summer drought and high temperature. *Tree Physiology*, *23*(13), 865–877.

Xu, L. K., & Baldocchi, D. D. (2004). Seasonal variation in carbon dioxide exchange over a mediterranean annual grassland in california. *Agricultural and Forest Meteorology*, *123*(1-2), 79–96.

Yan, K., Park, T., Yan, G., Liu, Z., Yang, B., Chen, C., Nemani, R. R., Knyazikhin, Y., & Myneni, R. B. (2016). Evaluation of modis lai/fpar product collection 6. part 2: Validation and intercomparison. *Remote Sensing*, *8*(6), 460.

Yang, F. H., Ichii, K., White, M. A., Hashimoto, H., Michaelis, A. R., Votava, P., Zhu, A. X., Huete, A., Running, S. W., & Nemani, R. R. (2007). Developing a continental-scale measure of gross primary production by combining modis and ameriflux data through support vector machine approach. *Remote Sensing of Environment*, *110*(1), 109–122.

Yang, H., Yang, D., Lei, Z., & Sun, F. (2008). New analytical derivation of the mean annual water-energy balance equation. *Water Resources Research*, *44*(3).

Yang, H., Yang, X., Zhang, Y., Heskel, M. A., Lu, X., Munger, J. W., Sun, S., & Tang, J. (2016). Chlorophyll fluorescence tracks seasonal variations of photosynthesis from leaf to canopy in a temperate forest. *Globe Change Biology*.

Yang, X., Tang, J., Mustard, J. F., Lee, J.-E., Rossini, M., Joiner, J., Munger, J. W., Kornfeld, A., & Richardson, A. D. (2015). Solar-induced chlorophyll fluorescence correlates with canopy photosynthesis on diurnal and seasonal scales in a temperate deciduous forest. *Geophysical Research Letters*, *42*(8), 2977–2987.

Yu, G., Chen, Z., Piao, S., Peng, C., Ciais, P., Wang, Q., Li, X., & Zhu, X. (2014). High carbon dioxide uptake by subtropical forest ecosystems in the east asian monsoon region. *Proceedings of the National Academy of Sciences of the United States of America*, *111*(13), 4910–4915.

Yu, G. R., Zhu, X. J., Fu, Y. L., He, H. L., Wang, Q. F., Wen, X. F., Li, X. R., Zhang, L. M., Zhang, L., Su, W., Li, S. G., Sun, X. M., Zhang, Y. P., Zhang, J. H., Yan, J. H., Wang, H. M., Zhou, G. S., Jia, B. R., Xiang, W. H., Li, Y. N., Zhao, L., Wang, Y. F., Shi, P. L., Chen, S. P., Xin, X. P., Zhao, F. H., Wang, Y. Y., & Tong, C. L. (2013). Spatial patterns and climate drivers of carbon fluxes in terrestrial ecosystems of china. *Global Change Biology*, *19*(3), 798–810.

Yuan, W., Cai, W., Liu, S., Dong, W., Chen, J., Arain, M. A., Blanken, P. D., Cescatti, A., Wohlfahrt, G., Georgiadis, T., Genesio, L., Gianelle, D., Grelle, A., Kiely, G., Knohl, A., Liu, D., Marek, M. V., Merbold, L., Montagnani, L., Panferov, O., Peltoniemi, M., Rambal, S., Raschi, A., Varlagin, A., & Xia, J. (2014a). Vegetation-specific model parameters are not required for estimating gross primary production. *Ecological Modelling*, *292*, 1–10.

Yuan, W., Cai, W., Nguy-Robertson, A. L., Fang, H., Suyker, A. E., Chen, Y., Dong, W., Liu, S., & Zhang, H. (2015). Uncertainty in simulating gross primary production of cropland ecosystem from satellite-based models. *Agricultural and Forest Meteorology*, *207*(0), 48–57.

Yuan, W., Cai, W., Xia, J., Chen, J., Liu, S., Dong, W., Merbold, L., Law, B., Arain, A., Beringer, J., Bernhofer, C., Black, A., Blanken, P. D., Cescatti, A., Chen, Y., Francois, L., Gianelle, D., Janssens, I. A., Jung, M., Kato, T., Kiely, G., Liu, D., Marcolla, B., Montagnani, L., Raschi, A., Roupsard, O., Varlagin, A., & Wohlfahrt, G. (2014b). Global comparison of light use efficiency models for simulating terrestrial vegetation gross primary production based on the lathuile database. *Agricultural and Forest Meteorology*, *192-193*, 108–120.

Yuan, W., Chen, Y., Xia, J., Dong, W., Magliulo, V., Moors, E., Olesen, J. E., & Zhang, H. (2016). Estimating crop yield using a satellite-based light use efficiency model. *Ecological Indicators*, *60*, 702–709.

Yuan, W., Liu, S., Zhou, G., Zhou, G., Tieszen, L. L., Baldocchi, D., Bernhofer, C., Gholz, H., Goldstein, A. H., Goulden, M. L., Hollinger, D. Y., Hu, Y., Law, B. E., Stoy, P. C., Vesala, T., & Wofsy, S. C. (2007). Deriving a light use efficiency model from eddy covariance flux data for predicting daily gross primary production across biomes. *Agricultural and Forest Meteorology*, *143*(3-4), 189–207.

Zaehle, S., & Friend, A. D. (2010). Carbon and nitrogen cycle dynamics in the o-cn land surface model: 1. model description, site-scale evaluation, and sensitivity to parameter estimates. *Global Biogeochemical Cycles*, *24*.

Zaitchik, B. F., Macalady, A. K., Bonneau, L. R., & Smith, R. B. (2006). Europe's 2003 heat wave: A satellite view of impacts and land-atmosphere feedbacks. *International Journal of Climatology*, *26*(6), 743–769.

Zeng, N., Mariotti, A., & Wetzel, P. (2005). Terrestrial mechanisms of interannual co(2) variability. *Global Biogeochemical Cycles*, *19*(1).

Zeng, N., Zhao, F., Collatz, G. J., Kalnay, E., Salawitch, R. J., West, T. O., & Guanter, L. (2014). Agricultural green revolution as a driver of increasing atmospheric co2 seasonal amplitude. *Nature*, *515*(7527), 394–397.

Zhang, F., Xing, Z., Rees, H. W., Dong, Y., Li, S., & Meng, F. (2014a). Assessment of effects of two runoff control engineering practices on soil water and plant growth for afforestation in a semi-arid area after 10 years. *Ecological Engineering*, *64*, 430–442.

Zhang, G., Xiao, X., Dong, J., Kou, W., Jin, C., Qin, Y., Zhou, Y., Wang, J., Menarguez, M. A., & Biradar, C. (2015a). Mapping paddy rice planting areas through time series analysis of modis land surface temperature and vegetation index data. *ISPRS Journal of Photogrammetry and Remote Sensing*, *106*, 157–171.

Zhang, G., Zhang, Y., Dong, J., & Xiao, X. (2013a). Green-up dates in the tibetan plateau have continuously advanced from 1982 to 2011. *Proceedings of the National Academy of Sciences of the United States of America*, *110*(11), 4309–4314.

Zhang, L., Dawes, W. R., & Walker, G. R. (2001). Response of mean annual evapotranspiration to vegetation changes at catchment scale. *Water Resources Research*, *37*(3), 701–708.

Zhang, L., Luo, Y. Q., Yu, G. R., & Zhang, L. M. (2010). Estimated carbon residence times in three forest ecosystems of eastern china: Applications of probabilistic inversion. *Journal of Geophysical Research-Biogeosciences*, *115*.

Zhang, Q., Middleton, E. M., Cheng, Y.-B., Huemmrich, K. F., Cook, B. D., Corp, L. A., Kustas, W. P., Russ, A. L., Prueger, J. H., & Yao, T. (2016a). Integrating chlorophyll fapar and nadir photochemical reflectance index from eo-1/hyperion to predict cornfield daily gross primary production. *Remote Sensing of Environment*, *186*, 311–321.

Zhang, Q., Xiao, X., Braswell, B., Linder, E., Baret, F., & Mooreiii, B. (2005). Estimating light absorption by chlorophyll, leaf and canopy in a deciduous broadleaf forest using modis data and a radiative transfer model. *Remote Sensing of Environment*, *99*(3), 357–371.

Zhang, Q. Y., Middleton, E. M., Margolis, H. A., Drolet, G. G., Barr, A. A., & Black, T. A. (2009). Can a satellite-derived estimate of the fraction of par absorbed by chlorophyll (fapar(chl)) improve predictions of light-use efficiency and ecosystem photosynthesis for a boreal aspen forest? *Remote Sensing of Environment*, *113*(4), 880–888.

Zhang, X. Y., Friedl, M. A., Schaaf, C. B., Strahler, A. H., Hodges, J. C. F., Gao, F., Reed, B. C., & Huete, A. (2003). Monitoring vegetation phenology using modis. *Remote Sensing of Environment*, *84*(3), 471–475.

Zhang, Y., Guanter, L., Berry, J. A., Joiner, J., van der Tol, C., Huete, A., Gitelson, A., Voigt, M., & Kohler, P. (2014b). Estimation of vegetation photosynthetic capacity from space-based measurements of chlorophyll fluorescence for terrestrial biosphere models. *Globe Change Biology*, *20*(12), 3727–42.

Zhang, Y., Guanter, L., Berry, J. A., van der Tol, C., Yang, X., Tang, J., & Zhang, F. (2016b). Model-based analysis of the relationship between sun-induced chlorophyll fluorescence and gross primary production for remote sensing applications. *Remote Sensing of Environment*, *187*, 145–155.

Zhang, Y., Li, W. Z., Zhu, Q., Chen, H., Fang, X. Q., Zhang, T. L., Zhao, P. X., & Peng, C. H. (2015b). Monitoring the impact of aerosol contamination on the drought-induced decline of gross primary productivity. *International Journal of Applied Earth Observation and Geoinformation*, *36*, 30–40.

Zhang, Y., Peng, C., Li, W., Tian, L., Zhu, Q., Chen, H., Fang, X., Zhang, G., Liu, G., Mu, X., Li, Z., Li, S., Yang, Y., Wang, J., & Xiao, X. (2016c). Multiple afforestation programs accelerate the greenness in the 'three north' region of china from 1982 to 2013. *Ecological Indicators*, *61*, 404–412.

Zhang, Y., Peng, C. H., Li, W. Z., Fang, X. Q., Zhang, T. L., Zhu, Q. A., Chen, H., & Zhao, P. X. (2013b). Monitoring and estimating drought-induced impacts on forest structure, growth, function, and ecosystem services using remote-sensing data: recent progress and future challenges. *Environmental Reviews*, *21*(2), 103–115.

Zhang, Y., Song, C., Sun, G., Band, L. E., Noormets, A., & Zhang, Q. (2015c). Understanding moisture stress on light use efficiency across terrestrial ecosystems based on global flux and remote-sensing data. *Journal of Geophysical Research: Biogeosciences*, *120*(10), 2053–2066.

Zhang, Y., Xiao, X., Guanter, L., Zhou, S., Ciais, P., Joiner, J., Sitch, S., Wu, X., Nabel, J., Dong, J., Kato, E., Jain, A. K., Wiltshire, A., & Stocker, B. D. (2016d). Precipitation and carbon-water coupling jointly control the interannual variability of global land gross primary production. *Scientific Reports*, *6*, 39748.

Zhang, Y., Xiao, X., Jin, C., Dong, J., Zhou, S., Wagle, P., Joiner, J., Guanter, L., Zhang, Y., Zhang, G., Qin, Y., Wang, J., & Moore, B. I. (2016e). Consistency between sun-induced chlorophyll fluorescence and gross primary production of vegetation in north america. *Remote Sensing of Environment*, *183*, 154–169.

Zhang, Y., Xiao, X. M., Zhou, S., Ciais, P., McCarthy, H., & Luo, Y. Q. (2016f). Canopy and physiological controls of gpp during drought and heat wave. *Geophysical Research Letters*, *43*(7), 3325–3333.

Zhao, M., Heinsch, F. A., Nemani, R. R., & Running, S. W. (2005). Improvements of the modis terrestrial gross and net primary production global data set. *Remote Sensing of Environment*, *95*(2), 164–176.

Zhao, M., & Running, S. W. (2010). Drought-induced reduction in global terrestrial net primary production from 2000 through 2009. *Science*, *329*(5994), 940–943.

Zhao, M., Running, S. W., & Nemani, R. R. (2006). Sensitivity of moderate resolution imaging spectroradiometer (modis) terrestrial primary production to the accuracy of meteorological reanalyses. *Journal of Geophysical Research-Biogeosciences*, *111*(G1).

Zhou, S., Yu, B., Huang, Y., & Wang, G. (2015a). The complementary relationship and generation of the budyko functions. *Geophysical Research Letters*, *42*(6), 1781–1790.

Zhou, S., Zhang, Y., Caylor, K. K., Luo, Y., Xiao, X., Ciais, P., Huang, Y., & Wang, G. (2016). Explaining inter-annual variability of gross primary productivity from plant phenology and physiology. *Agricultural and Forest Meteorology*, *226-227*, 246–256.

Zhou, Y., Wu, X., Ju, W., Chen, J. M., Wang, S., Wang, H., Yuan, W., Black, A., Jassal, R., & Ibrom, A. (2015b). Global parameterization and validation of a twoâĂŘleaf light use efficiency model for predicting gross primary production across fluxnet sites. *Journal of Geophysical Research: Biogeosciences*.

Zhu, Z., Piao, S., Myneni, R. B., Huang, M., Zeng, Z., Canadell, J. G., Ciais, P., Sitch, S., Friedlingstein, P., Arneth, A., Cao, C., Cheng, L., Kato, E., Koven, C., Li, Y., Lian,

X., Liu, Y., Liu, R., Mao, J., Pan, Y., Peng, S., Peñuelas, J., Poulter, B., Pugh, T. A. M., Stocker, B. D., Viovy, N., Wang, X., Wang, Y., Xiao, Z., Yang, H., Zaehle, S., & Zeng, N. (2016). Greening of the earth and its drivers. *Nature Climate Change*, *6*, 791–795.

Zscheischler, J., Mahecha, M. D., von Buttlar, J., Harmeling, S., Jung, M., Rammig, A., Randerson, J. T., Schölkopf, B., Seneviratne, S. I., Tomelleri, E., Zaehle, S., & Reichstein, M. (2014a). A few extreme events dominate global interannual variability in gross primary production. *Environmental Research Letters*, *9*(3), 035001.

Zscheischler, J., Reichstein, M., von Buttlar, J., Mu, M., Randerson, J. T., & Mahecha, M. D. (2014b). Carbon cycle extremes during the 21st century in cmip5 models: Future evolution and attribution to climatic drivers. *Geophysical Research Letters*, *41*(24), 8853–8861.